Chemical dynamics using wavepacket methods

Abigail J. Dobbyn

Thesis for Ph.D.

University of Durham Chemistry Department

Chemical Dynamics Using Wavepacket Methods

Abigail J. Dobbyn

September 1993

Abstract of Thesis for Ph.D.,

"Chemical Dynamics Using Wavepacket Methods."

Abigail J. Dobbyn, Durham University, September 1993.

This thesis is concerned with studying chemical dynamics using time-dependent quantum mechanics and in particular using the Fourier method.

Various ways of implementing the Fourier method are described, both for calculations in one dimension and for those in many dimensions.

The Fourier method is then used to simulate time-resolved femtosecond and picosecond pump-probe experiments, which investigate the B state of the sodium trimer. The simulation is divided into three stages: the initial wavefunction is generated by modelling the effect of the pump laser pulse on the ground state wavefunction of the X state of the sodium trimer; the wavepacket now on the B state is propagated in time; the observables are extracted from the time-dependent wavefunction. The calculations are carried out initially in two dimensions, corresponding to the bending and asymmetric stretch normal modes, and then in three dimensions, i.e. including the symmetric stretch normal mode.

The simulation of the time-resolved experiments produced physically plausible results. The correspondence with the experimental results was only fair, but this could be mostly accounted for by the poor quality of the potential energy surfaces used. Thus, even the relatively simple model used to simulate the time-resolved experiments is useful to gain both a qualitative explanation of the results of these experiments and an insight into the dynamics of systems which are in non-stationary states.

Acknowledgements.

I would like to acknowledge the help and guidance of my supervisor Dr. Jeremy M. Hutson. I would also like to thank S.E.R.C. who have supported my studies.

Statement.

No part of this thesis has previously been submitted by me for a degree to any university. Every effort has been made to ensure that all work which is not original to the author has been properly credited. I place no restriction upon access to, or copying of, this thesis.

Contents

1: Introduction

In order to understand the mechanisms by which chemical reactions occur, it is necessary to consider the motion of nuclei and electrons within reacting species. This is the subject of chemical dynamics calculations. Chemical dynamics can be investigated using quantum mechanical methods in a variety of ways. These methods can be crudely divided into time-independent methods, e.g. diagonalising the Hamiltonian matrix or solving the coupled channel equations, and time-dependent or wavepacket methods, which solve the time-dependent Schrödinger equation.

The time-dependent Schrödinger equation (T.D.S.E.):

$$i\hbar\frac{\partial\Psi}{\partial t} = \hat{H}\Psi, \tag{1}$$

can be solved by finding the initial state of the system under consideration, i.e. the wavefunction at zero time, and then propagating this in time.

Apart from these quantum mechanical methods, classical trajectory calculations and semiclassical methods, which are also time-dependent, can be used. There is a variety of these time-dependent semiclassical methods or Gaussian wavepacket methods, e.g. those using frozen Gaussians or thawed Gaussians [1]. One major advantage of the time-dependent quantum mechanical method over the semiclassical methods that have been developed so far is that potentials of arbitrary complexity can be treated.

Chemical reactions have a beginning and an end that are separated in time. Thus they are a time-dependent phenomenon. It would seem natural then to study chemical dynamics within this framework. However, it is only in the recent past that time-dependent methods have become popular. This is mainly because of the large computational resources required for the calculations, as well as the difficulty in relating the results to spectroscopic observables.

Early studies used an implicit time propagator to numerically integrate the time-dependent Schrödinger equation; the finite-difference method was used, which defines the wavefunction on a grid, to calculate the spatial derivatives in the Hamiltonian operator [2]. Later an explicit time propagator, using second-order differencing, was introduced [3]. This improved the scaling of the method from $O(N^2)$ to $O(N)$, where N is the number of grid points used. The use of the finite-differencing algorithm, which has very poor convergence with respect to grid size, meant that only qualitative results were produced. Other early attempts to study chemical dynamics problems in the time domain involved the expansion

of the initial state in terms of the stationary state solutions, which can be propagated analytically [4].

In 1983 Kosloff introduced the Fourier, or Pseudospectral, method [5]. In this method the spatial derivatives in the Hamiltonian operator are calculated by the use of forward and backward discrete Fourier transformations of the wavefunction. The wavefunction is defined on a grid in the same way as in the finite-difference method. The Fourier method produces results of very high accuracy, due to the exponential convergence of the method with respect to grid size. The use of Fast Fourier Transforms makes this method extremely efficient, scaling as $O(N \log N)$. Subsequently, the method has been enhanced even further, particularly with the introduction of a variety of new propagators [6].

Advances have also been made in methods to obtain observables from time-dependent calculations. In 1978 Heller introduced a formula for the total photodissociation cross section [7], which is simply related to the absorption spectrum. This stated that 'the total photodissociation cross section is given by a Fourier transform of the overlap between the propagated and unpropagated initial vibrational wavefunction times the transition dipole'. Later a strategy was introduced for calculating the partial cross sections [8]. This was done by projecting the propagated wavefunction, once it had reached the asymptotic regions of configuration space, onto simple asymptotic outgoing states. This formalism has been extended to a variety of different applications in all areas of chemical dynamics. More recently a new method for the calculation of partial cross sections has been developed [9]. This method analyses the propagating wavepacket at a particular cut in configuration space and then uses the results of this analysis to form the partial cross sections.

It is not the intention here to give a complete review of the various physical problems to which time-dependent methods have been successfully applied. Some of these include: photodissociation on a single two-dimensional potential energy surface, e.g. H_2S [9] and ICN [10] (this study also explicitly treats the absorption process); photodissociation on a single three-dimensional surface, e.g. O_3 [11]; predissociation on a single three-dimensional adiabatic surface, e.g. Van der Waals molecules [12]; predissociation in three dimensions using vibronically coupled surfaces, e.g. HCN^+ [13]; atom-molecule scattering, e.g. a model implementation for inelastic collisions [14]; reactive scattering, e.g. two-dimensional studies on $HD + H \rightarrow H_2 + D$ [15] [16] as well as three-dimensional studies on $F + H_2 \rightarrow HF + H$ [17] which use an extension to the theory derived for atom-molecule elastic scattering [18]; and gas-surface scattering, e.g. H_2 from flat or corrugated surfaces [19] [20]. Some reviews exist, including one on time-dependent wavepacket calculations of molecular scattering from surfaces [21], and another on quantal wavepacket calculations of reactive scattering [22]. Recently there has been a thematic issue of Computer Physics Reports on time-dependent

methods for quantum dynamics [23]. What follows, instead of a comprehensive review, is a brief discussion of some areas in which time-dependent methods show a large advantage over time-independent methods, so that their application is particularly useful. Also, some of the methods that have been introduced to extend the use of the Fourier method are included in this discussion.

Consider first those chemical reactions which are difficult to study with time-independent methods because these methods are only used to solve two-point boundary value problems. Such chemical reactions include those which have multiple continua, i.e. those reactions whose final products consist of three or more fragments, making the construction of boundary conditions impossible, because of the practical difficulty in partitioning the kinetic energy between the fragments. The time-dependent method allows a simple treatment of continua and of the rearrangement problem in reactive scattering, because this method solves initial value, rather than two-point boundary value, problems. An example is the study of the dissociation dynamics of vibrationally excited Van der Waals clusters: $I_2XY \rightarrow I_2 + X + Y$ $(X, Y = He, Ne)$ [24] and other similar systems [25]. However for problems of this sort, i.e. double continuum processes, the wavefunction explores a large volume in configuration space, making exact quantum methods prohibitively expensive to apply. A class of approximation methods has arisen which deals with this, and other computationally intractable problems. These are the time-dependent self-consistent field (T.D.S.C.F.) schemes [26]. In this approximation the wavefunction is represented by a product of one-dimensional wavefunctions associated with each quantum mode (or dimension). The wavefunction is then substituted into the T.D.S.E. and a set of coupled single-mode S.C.F. field equations is obtained. The potential for each mode in these equations is the total potential for the system averaged over the other modes. This potential allows energy to be transferred between different modes, and is time-dependent. A variety of these schemes exist, including single-configuration T.D.S.C.F., configuration interaction T.D.S.C.F., and those which treat one or more of the modes semiclassically or classically.

Now consider those chemical reactions which are difficult to study with time-independent methods because the calculations with these methods are computationally too intensive. Obviously, this will apply to very large problems, where many states or dimensions have to considered. The time-dependent method is useful here because it can be in many cases computationally more efficient. This can come about in two ways. The first arises because a wavepacket can correspond to a wide range of energies, so that a single calculation can yield results for many energies. Thus the columns of the S-matrix corresponding to the states of interest, e.g. those most directly corresponding to the experiment, can be found from one calculation. A good example of this is the calculation

of partial photodissociation cross sections for all photon energies by a single calculation. That a single calculation can provide all the information of interest about a system has been shown explicitly for the calculation of the partial cross sections of H_2S [9]. It has also been shown for the calculation of the partial cross sections of reactive scattering, in particular for the reaction $F + H_2 \rightarrow HF + H$ [27].

The second reason why time-dependent calculations can be computationally more efficient is because the computational scaling laws can be favourable. For example, the computational effort in time-dependent methods scales as the number of grid points squared (N^2), in contrast to time-independent coupled channel methods in which the computational effort scales as the number of channels cubed (N^3) [28]. These advantageous scaling laws have made the solution of several problems possible, e.g. the scattering of atoms and molecules from surfaces, where very many dimensions must be considered for even the simplest study [11][19][29]. The difficulties involved with generalising the Fourier method to coordinate systems other than Cartesian are avoided in these calculations since for these calculations a good coordinate system to use is Cartesian. Also, the periodic nature of the Fourier transform can be used to great advantage to match the surface unit cell. Calculations which aim to extend these studies further and to study the energy transfer between the surface and the incoming molecule have been carried out. These have to use some approximations in order that the computation is feasible. T.D.S.C.F. calculations have been used, where the surface and molecule motions are separated [21]. In another related method, the surface is modelled using the stochastic generalised Langevin equation formalism. With this method the surface is treated as heat bath, and is modelled using a chain of atoms coupled together with harmonic forces [30] [31] [32] [33]. The parameters used to describe the chain are derived from considering autocorrelation functions and their relation to the spectral density of the solid; the spectral density is often taken to the Debye model spectrum. In order to model a heat bath it would be necessary to use an infinite chain of atoms. This is not computationally possible, so simple fictional damping and white noise terms are added to the equations of motion for the last atom in the chain [34]. The motion of the surface atoms is then solved classically. The motion of the surface atom or the 'top' atom in the chain is used as a parameter in the potential for the equations of motion of the molecule approaching the surface.

As well as these computational advantages, the algorithms used in time-dependent methods are highly vectorisable, which is particularly important since modern computers gain their speed from parallel and vector type architectures [6][35]. In particular, for multi-dimensional problems, many mutually independent Fourier transforms may be performed

in parallel [36]. This has been demonstrated on both the S.I.M.D. and M.I.M.D. † type parallel processing computers. For machines with distributed memory, the implementation is not as obvious as initially appears, due to necessity of transposing the wavefunction which can involve a great deal of time consuming message passing [37]. For the S.I.M.D. architecture, it has been shown that almost every step of the grid algorithms can be executed concurrently for each grid site, and for those steps which cannot excellent parallel schemes exist for their execution [38].

The numerical advantage gained by time-dependent calculations is particularly obvious when the 'events' of interest in the system are fast, e.g. photodissociation which occurs via a direct mechanism, so that the T.D.S.E. has only to be propagated for relatively few, short timesteps.

It is clear then that the time-dependent method is important in studying chemical reactions because of certain advantages in the structure of the method, i.e. it is an initial value problem with favourable scaling laws. Now consider the advantage that the *time-dependence* gives to these calculations. First, the results, i.e. the wavefunction at a series of timesteps, can easily be interpreted to give direct insight into a reaction's mechanism. Secondly, problems with an explicit time-dependence, i.e. a time-dependent Hamiltonian, can be treated straightforwardly.

The study of photodissociation is a good example of a physical process where the results of time-dependent calculations are particularly useful in understanding the reaction mechanism. The results of time-dependent calculations, obtained recently for a series of molecules of the type RNO, have shown how much physical insight can be gained. These calculations are a systematic study of the dissociation of RNO molecules, using accurate *ab-initio* potential energy surfaces. They have shown how the dissociation dynamics changes from being fast and direct in the case of $FNO(S_2)$ to slow, occurring by vibrational predissociation, in the case of $CH_3ONO(S_1)$, depending on the topology of the potential energy surface [39]. In the first case, the wavepacket on the excited state moved quickly from the Franck-Condon region, where it was initially promoted by a laser pulse, down a repulsive surface to form the free fragments. In the second case, the wavepacket on the excited state was at least partially trapped by a well in the surface in the Franck-Condon region and only managed to escape after several periods of vibrational motion.

The pictures of the wavefunction at a series of timesteps can lead to a variety of ways of describing the dynamics on the potential energy surface, and so help to substantiate general theories of unimolecular reactions. One description of the dynamics could be in

† These are single instruction multiple data and multiple instruction multiple data architectures.

terms of energy flow through the bonds of a molecule, i.e. intramolecular redistribution of vibrational energy (I.V.R.) from one mode, or bond, to the rest of the molecule. Consider the extensive study of the overtone excitation in CHX_3 molecules (X = D, F, Cl, Br, CF_3). An overtone of the CH bond stretching motion is excited and due to its coupling to the bending motion, i.e. Fermi resonance, energy is transferred from the stretch to the bend, and so to the rest of the molecule [39]. For the CHF_3 molecule, to take one example, the transfer of this energy has been studied by following a wavepacket in two dimensions on an anharmonic potential energy surface [40]. For short times, less than 70 fs, there is a quasiperiodic motion in the stretch, but for later times the wavepacket spreads out over the whole of the space, and apart from some recurrence phenomena, the wavepacket remains delocalised. Studies of this type on the dynamics of unimolecular reactions can help to categorise the reaction in terms of R.R.K.M. or non-R.R.K.M. (e.g. Slater) like behaviour, i.e. whether or not the energy is almost instantaneously distributed to all bonds in the molecule.

Another area of study, which is connected to theories of unimolecular reactions, is that of quantum chaos and the dynamics of a pair of coupled non-linear oscillators. These have been studied in a time-dependent frame by examining the variation in the autocorrelation function of the wavefunction [41]. For example wavepacket dynamics on the Hénon-Heiles potential has been studied. In this study, the phase space volume over which initial wavepackets spread was taken to be a measure of chaos [42]. The study of quantum chaos is particularly interesting because of the ease with which the results of time-dependent calculations can be compared to those from classical trajectory calculations, which can lead to a better understanding of quantum/classical correspondence, especially concerning the origin of classical chaos.

The study of I.V.R., R.R.K.M. and chaos can be seen to be closely related. If I.V.R. is found to be fast, i.e. the rates can be described by R.R.K.M. theory and the wavefunction is quickly delocalised over all of the available phase space (and thus chaotic), then rate constants will be found to depend only on the energy of the initial state, and not on any other detail of the state.

Thus, the detailed understanding of chemical reaction mechanisms, which the results of time-dependent calculations can supply, gives rise to/dashes the hope of controlling the outcome of unimolecular reaction by exciting particular modes in specific ways [43]. An excellent example of this is the systematic study of the dynamics of photodissociation in H_2O and then in HOD. This enabled a two-photon scheme, by which the branching ratio (H + OD)/(D + OH) could be controlled, to be presented [44]. However, more general schemes have also been suggested. Consider a reaction which occurs on a ground electronic state,

and which has two possible asymptotic channels, corresponding to two different reaction products. It has been shown that promoting a wavepacket to an excited state using a pump laser pulse, leaving it to evolve for a specified time delay and then using a dump laser pulse to return the wavepacket to the ground state in a particular configuration, or channel, can influence product formation [45]. Thus it is hoped that by optimising the parameters of the dump laser pulse, e.g. the field amplitude, laser carrier frequency, phase and pulse duration, i.e. laser shaping, as well as by optimising the length of the time delay between the pump and dump lasers, the progress of a reaction can be controlled. Variational schemes to optimise these parameters have been formulated [46]. Another scheme has been proposed [47], which employs a series of ultrashort infrared laser pulses with analytical shapes, either Gaussian or sine squared. Each pulse selectively induces a vibrational transition. The whole series yields the desired sequence of transitions, from the ground state of the reactants via a transition state to a vibrationally excited product state. The final transition stabilises the products, from a vibrationally highly excited state to a lower level. In this scheme the molecule remains in the ground electronic state throughout. This scheme has been used to show the possible control of the isomerisation of organic molecules, e.g. the semibullvalenes [48]. It has also been used to show isotopomer selective isomerisations and bond-fissions in organometallic compounds [49].

The detailed time-dependent study of the dynamics of chemical reactions is no longer only of *theoretical* interest. Experiments that study molecular reaction dynamics in real time have recently been introduced. Information about the detailed mechanism can be obtained, which cannot be inferred from the more usual study of the rovibrational distributions of the product fragments. This is in direct analogy to the fact that time-dependent calculations can give substantially more insight into mechanisms than time-independent calculations. In these experiments the system is prepared in a particular state, by a pump laser pulse, or a combination of such pulses. The time evolution of the state is followed by a probe laser pulse, which produces either multiphoton ionisation or laser induced fluorescence, so that the population on the excited state can be monitored. The experiment is repeated many times for different known time delays between the pump and probe laser pulses. Thus the results are the magnitude of a signal at various delay times.

The first experiments of this type used picosecond lasers. These experiments have been used extensively to study I.V.R. and related phenomena in isolated large polyatomic molecules in supersonic beams [50]. Some of these studies were of: quantum beats and coherence spectroscopy of, amongst others, anthracene, stilbene and pyrazine; laser induced isomerisation in e.g. stilbene, going from the cis to the trans isomer, and hydrogen bonded systems, such as salicylate, where a hydrogen atom is transferred; lastly, I.V.R. was followed

explicitly by selective chromophore excitation in suitable molecules, e.g. Anthracene-CH_2-CH_2-CH_2-Aniline where the anthracene is excited and then fluorescence from the aniline is monitored.

However experiments are now possible using femtosecond laser pulses. These pulses are shorter ($10-100$ femtoseconds) than even the fastest of vibrational motions or dissociation reactions, ensuring that all these motions can be resolved, and the dynamics is followed in real time [51]. The ultrashort laser pulses can be obtained by compressing the pulses produced by 'a colliding-pulse mode-locked ring dye laser'.

Experiments using femtosecond laser pulses were first introduced in the study of transition states during direct dissociation reactions, e.g. in the study of $ICN^* \rightarrow [I\cdots CN]^{\dagger *} \rightarrow I + CN$ [52]. In these experiments the fragments are followed in two ways [53]. In the first the probe laser is set at a frequency corresponding to the energy required to promote one of the *completely* separated fragments to an excited state (it is on-resonance). The fragment in its excited state can then be detected, and in the case of CN this is done by monitoring fluorescence from an excited electronic state. The signal at different time delays shows, after an initial lag, a steady rise which eventually levels off. This is equivalent to 'clocking' the reaction, and the time delay at which the signal is turned on gives a measure of the time to break the bond. In the second case the probe laser is set at various frequencies corresponding to lower energies (it is off-resonance), so that the fragment will be excited while still interacting with the other fragments. This signal shows a steady rise but later decreases. The rise and fall in the signal occurs as the fragment enters the region where the probe laser can promote it to the excited state, but then at greater time delays leaves it. Analysis of these signals gives information about the potential energy surface in the region of the transition state [54]. In the case of direct dissociation there are no oscillations or recurrences in the signals since the potential surfaces are purely repulsive.

Since these early experiments the use of femtosecond laser pulses has been extended to the study of a variety of different systems, and a few examples follow. In reactions where more than one degree of freedom is involved, either vibrational or electronic, the adiabatic potential energy surface may not be purely repulsive and wells may exist leading to complex dissociation mechanisms, i.e. there are resonances. The dissociation of alkali halides, $NaX^* \rightarrow [Na\cdots X]^{\dagger *} \rightarrow Na + X$, (X = I, Br), occurs by such a complex mechanism, due to the crossing of the ionic ground state and the covalent excited state [55]. The on and off-resonance time-delay signals have been measured, using laser induced fluorescence from the Na atom. The on-resonance signal was similar to that for direct dissociation initially, but instead of levelling off, the signal then increased in a series of progressively smaller steps. The off-resonance signal was again similar to that for direct dissociation initially,

but after the decrease, then proceeded to increase and decrease in a series of oscillations. The results confirmed the complex dissociation mechanism, i.e. that some of the molecules were being trapped in a well formed by the avoided crossing of the two adiabatic potential energy surfaces. Analysis of the results gave the time to traverse the well, together with the probability of escaping from this well, and hence the coupling between the two surfaces [56]. The dissociation of HgI_2 also takes place via a complex mechanism: $IHgI^* \rightarrow [IHgI]^{\dagger *} \rightarrow HgI + I$. For this reaction, this occurs because it is necessary to consider two coordinates, which are symmetrical, giving rise to a potential energy surface (P.E.S.) which has a saddle point. The results, although more complicated than for the alkali halides, show similar features [57]. The predissociation of a Rydberg state of CH_3I, into CH_3 and I, has also been studied. Here the probe pulse ionises the iodine fragment, thus the I^+ mass signal, as a function of delay time, has been analysed to gain information about the crossing from the Rydberg bound state to the continuum [58].

In systems with bound potential energy surfaces, wavepacket motion can be viewed directly, e.g. for I_2 [59]. In this experiment a pump laser prepares a coherent superposition of a few vibrational states. This gives rise to a wavepacket moving on the bound P.E.S. A probe laser is then used to excite the molecule to an upper fluorescent state. For a probe laser at a particular frequency the transition is only resonant when the molecule is in a certain configuration, or the wavepacket is in a particular position on the P.E.S. Thus the time-delay signal is oscillatory with a period depending on the motion of the wavepacket and so on the details of the P.E.S., which can be obtained from these results.

Bimolecular reactions are much more difficult to study experimentally due to the difficulty of defining a zero of reaction time. This is because although the reactants can be prepared at a particular time by using ultrafast laser pulses it is not possible to say how long it takes for the reactants to 'meet', and so to have the opportunity to start to react. In order to surmount this problem ingenious experimental methods have been developed. These methods involve the formation of a Van der Waals cluster of the reagents. For example for the reaction $H + CO_2 \rightarrow HO + CO$, the complex $HI\cdots CO_2$ is formed in a supersonic beam. The HI is then dissociated by a femtosecond pump laser which establishes the zero of time. This is possible since the reactants are now so close that there is no time lapse before they meet. The reaction complex so formed can now be studied using the same methods as previously described [60]. Similiar studies have been carried out on the reaction $Br + I_2 \rightarrow BrI + I$, where the Van der Waals complex formed is $HBr\cdots I_2$ [61].

The study of more complicated systems is now being attempted, e.g. surface chemistry, chemistry in solution, hydrogen atom transfer and isomerisation reactions [62].

New techniques have been introduced to complement these experiments [51]. One

involves the use of phase-locked pulses, so that the two laser pulses used, separated by a time delay, have definite a phase relative to each other [63]. Therefore these experiments involve the preparation and quantum interference of two nuclear wavepackets. The result of this interference is detected by measuring the fluorescence from the excited state. Thus it was demonstrated that by varying the relative phase of the two pulses and/or the time delay between them it was possible, for I_2, to control the prepared wavepacket on the excited potential energy surface. Another technique aims to obtain the time *and* frequency resolved response of a molecule, in just one experiment, by monitoring the spectrum of the probe laser after it has passed through the sample [64].

There has been a great deal of theoretical work done on modelling these ultrafast pump/probe experiments. The modelling of these experiments involves finding methods to describe the effect of the laser pulses. The laser pulses have been described using first or second order perturbation theory [65], i.e. assuming a weak field limit. This method of modelling the experiments has been used successfully for a variety of different systems, e.g. the dissociation of ICN [66] and of NaI [67]. Obviously the explicit time dependence of the problem makes the use of time-dependent methods imperative here.

From the above it can be seen that the time-dependent approach to studying chemical dynamics is a useful tool for studying reactions. Practical methods have been developed to solve the T.D.S.E., which have been used widely in many applications. The approach has many advantages, perhaps the most important of which is the ability to *see* a reaction proceed in time, particularly since the development of experiments which can do the same!

This thesis is divided into seven chapters. The first chapter has been a short introduction to chemical dynamics using wavepacket methods, including the history and a brief survey of the applications of the wavepacket method, as well as a discussion of some relevant experiments. The second chapter gives an introduction to the Fourier method. The third chapter investigates some of the various ways of implementing the Fourier method. The fourth chapter shows how this method can be extended to problems with more than one dimension. The fifth and sixth chapters are a theoretical study of the wavepacket dynamics of the sodium trimer and include a comparison with the results of femtosecond pump/probe experiments carried out by Gerber's group in Freiburg, and the picosecond experiments carried out by Wöste's group in Berlin. The final chapter is a summary and conclusion of the thesis.

2: The Method

Solving the time-dependent Schrödinger equation can be divided into three parts. The first involves selecting an initial wavefunction; this is not always straightforward. The second or spatial part requires the Hamiltonian operator:

$$\hat{H} = \frac{\hat{p}^2}{2m} + \hat{V}, \tag{2}$$

and its operation on Ψ, $\hat{H}\Psi$, to be calculated. The third or temporal part is the propagation of the wavefunction in time.

In the Fourier method, both the first and the second stages of the solution of the T.D.S.E. rely on the discretisation of coordinate space. That is the wavefunction and the operators are represented on a regular grid, with sampling points $x_j = (j-1)\Delta x$. Although the use of a grid apparently implies no connection with basis set methods, this is in fact a pseudospectral method, in which an implicit basis is used. This implicit basis is used to represent the kinetic energy on the grid; it is necessary because of the non-local nature of the kinetic energy operator. For a grid with N points, the N implicit basis functions used are:

$$g_k(x) = \exp[ikx], \qquad k = -\frac{(N/2-1)\pi}{(N/2)\Delta x}, \ldots, 0, \ldots, \frac{\pi}{\Delta x}, \tag{3}$$

so that there is also a discretisation of momentum space. There is a great deal of erudite discussion in the literature about the representation of the wavefunction and the operators in such a discretised space [6], but it need only be of concern here in the most practical of ways. Consider first the representation of the wavefunction and the potential operator on a *finite* grid. In order that this grid can properly represent the wavefunction and the potential operator, it must be ensured that the grid is large enough to include all the important parts of the potential and wavefunction. Consider next the representation of the kinetic energy operator by a *finite* number of implicit basis functions. Here in order that the kinetic energy operator can be properly represented, it must be ensured that the highest energy components of the wavefunction can be included. This will be discussed later.

The third stage relies on discretisation in time. It will be seen later that this has implications for the stability and accuracy of the propagation methods.

2.1 The Initial Wavefunction

The T.D.S.E. is a first order differential equation. Hence the initial state, for a given potential energy surface, determines completely the subsequent time evolution. Thus, it is

obviously important to determine this as accurately, and as suitably, as possible.

The choice of the initial wavefunction depends on the purpose of the calculation. Usually, a Gaussian wavepacket can be used for the translational degree of freedom. The width of the packet will determine the range of energies to be considered, the narrower the packet the wider the energy range. For example, in the simulation of a gas-surface collision, the width can be chosen to match the energy spread of the experimental supersonic beam. For vibrational and rotational dimensions, it is customary to choose an eigenstate of some zeroth-order problem as the initial state. The total initial wavefunction will then be a product of the terms for each of the dimensions [68].

However, various other ways of chosing the initial state have been used. For example, it has been found that, for certain applications, chosing an initial wavefunction which has the same symmetry as the Hamiltonian under consideration will enable states of particular symmetry to be isolated and so increase the accuracy of the solutions [36]. Another example is the study of the long-time decay of a particular metastable state. Here, it is obviously most appropriate to consider an initial state as similar to this metastable state as possible. An example of this is the study of the fragmentation of $NeCl_2$ [12]. In this study, the lifetime of the cluster, for a particular vibrational level of the chlorine molecule, e.g. $v = 9$, is to be calculated. Thus, the initial state is chosen to be one of the stabilised eigenvectors of the Hamiltonian corresponding to this state. It is interesting to note that in this case it is not necessary to have a highly accurate initial wavefunction, because although it is helpful to have an initial state near to the state being considered, it is still possible to obtain useful information when the state differs slightly. This is because the state being considered is metastable, i.e. it will be longer living than any other states which may be present in the initial state. Thus, if the initial transitory behaviour is ignored, and the wavepacket at later times analysed, a true picture of the dynamics will emerge, regardless of the exact nature of the initial state.

2.2 The Spatial Part

The Hamiltonian is partitioned into two parts, the potential part and the kinetic part:

$$\hat{H} = \hat{T} + \hat{V}. \tag{4}$$

The potential part of the Hamiltonian, which is calculated theoretically or by fitting of experimental measurements, is local in coordinate space, and therefore its operation is simply a multiplication of $\Psi(x_j)$ by $V(x_j)$ [6].

2.3 The Fourier Method

The kinetic part of the Hamiltonian cannot be calculated so simply because it is a non-local operator in coordinate space [5]. The solution is then to transform the wavefunction into momentum space, in which the operator is local, and its operation is then a multiplication by the kinetic energy spectrum:

$$T(k) = \frac{\hbar^2 k^2}{2m}, \tag{5}$$

where k is given by the relation $p = \hbar k$. The transformation into (and out of) momentum space is achieved using a Fourier transformation [69]:

$$\Psi(x) \Longleftrightarrow \Psi(k), \tag{6}$$

which means,

$$\Psi(k) = \int_{-\infty}^{\infty} e^{-ikx}\Psi(x)\,dx \tag{7}$$

$$\Psi(x) = \frac{1}{2\pi}\int_{-\infty}^{\infty} e^{ikx}\Psi(k)\,dk. \tag{8}$$

So that,

$$\hat{T}\Psi(x) = \frac{1}{2\pi}\int_{-\infty}^{\infty} e^{ikx}\left[\frac{\hbar^2 k^2}{2m}\Psi(k)\right]\,dk. \tag{9}$$

To summarise, the kinetic energy operator is calculated by transforming the wavefunction to momentum space by a forward Fourier transformation, multiplying by $T(k)$, and performing an inverse Fourier transformation back to coordinate space.

This series of operations can be understood from a purely mathematical point of view. The kinetic energy operator requires the calculation of the second derivative of $\Psi(x)$ with respect to x:

$$\hat{T} = \frac{-\hbar^2}{2m}\frac{d^2}{dx^2}. \tag{10}$$

Let $\Psi(x) \Longleftrightarrow \Psi(k)$, as before, and

$$\frac{d^2\Psi(x)}{dx^2} \Longleftrightarrow \Psi_2(k). \tag{11}$$

Writing this out explicitly:

$$\Psi_2(k) = \int_{-\infty}^{\infty} e^{-ikx}\frac{d^2\Psi(x)}{dx^2}\,dx, \tag{12}$$

which can be integrated by parts successively to give:

$$\Psi_2(k) = (-ik)^2\Psi(k), \tag{13}$$

provided $\Psi(x) \rightarrow 0$ as $x \rightarrow \pm\infty$, which it must do in order to be square-integrable (a requirement for all wavefunctions). Therefore,

$$\frac{d^2\Psi(x)}{dx^2} = \frac{1}{2\pi}\int_{-\infty}^{\infty} e^{ikx}\left[-k^2\Psi(k)\right]\,dk, \tag{14}$$

and the calculation of $\hat{T}\Psi(x)$ becomes obvious.

2.3. 1 The Discrete Fourier Transform

All the above applies to continuous space, whilst the space to be considered in numerical calculations is discrete. This means that a discrete Fourier transformation must be used:

$$\Psi(x_j) \Longleftrightarrow \Psi(k_j), \tag{15}$$

which means,

$$\Psi(k_j) \approx \sum_{l=0}^{N-1} e^{-ik_j x_l/N}\Psi(x_l)\Delta x \tag{16}$$

$$\Psi(x_l) \approx \frac{1}{2\pi}\sum_{j=0}^{N-1} e^{ik_j x_l/N}\Psi(k_j)\Delta k, \tag{17}$$

where N is the number of grid points, Δx is the spacing between the points of the grid in coordinate space and Δk is the spacing in momentum space.

Consider the position/momentum phase-space. It extends a distance $N\Delta x$ along the position axis and from $-p_{\max}$ to $p_{\max}$ along the momentum axis, so that the volume of the space is $2p_{\max}N\Delta x$. Phase space is divided up into cells each of volume h, i.e. $\delta x \delta p = h$ [70]. It can be shown that phase space can be accurately represented with as little as one point per unit volume [6]. Thus, since there are N points on the grid, the maximum volume of phase space that can be represented is Nh. Equating these two volumes:

$$Nh = 2p_{\max}N\Delta x,$$

gives $p_{\max}$ equal to $h/2\Delta x$. Therefore $k_{\max}$ equals $\pi/\Delta x$, as $p = \hbar k$, and the range of k is $2\pi/\Delta x$; Δk is $2\pi/(N\Delta x)$. It can be seen that the discretisation of coordinate space leads to a maximum value for the kinetic energy that can be represented.

Now consider this problem in a slightly different way. The implicit basis functions used are of the form $\exp[ikx]$. Obviously these are just combinations of sine and cosine functions. Thus the functions which are represented are of the form $\sin kx$ and $\cos kx$. Another way of writing these is as $\sin \pi n/(N\Delta x)$ and $\cos \pi n/(N\Delta x)$, where n is an integer. Thus k is equal to $\pi n/(N\Delta x)$. In order to accurately represent $\sin \pi n/(N\Delta x)$, or $\cos \pi n/(N\Delta x)$, on a grid of N points, the maximum value that n can take is N, i.e. N points are needed to represent N functions. Thus the maximum value that k can have, $k_{\max}$, is $\pi/\Delta x$.

The question then arises as to the accuracy of this approximation, i.e. using a phase space whose volume is bounded (this is a consequence of using a discretised space). One way to consider this is to think about the range of kinetic energies which have to be accommodated on the grid. Given a spacing in coordinate space of Δx then the maximum kinetic energy that can be accommodated is $\hbar^2 k_{\max}^2/2m$, where $k_{\max}$ is given above. This means that the wavefunction must be bounded in momentum space or equivalently the Fourier transform of the wavefunction must be band limited, in order to ensure the accuracy of the approximation.

What then is the consequence if the wavefunction is not bounded in momentum space? Consider the following sampling theorem. For any sampling interval Δt , there is a special frequency f_c, called the Nyquist critical frequency, given by:

$$f_c = \frac{1}{2\Delta t}. \tag{18}$$

(In this case the phase space considered is energy/time, and $E = hf$.) If the function $g(t)$ is band-width limited to frequencies smaller in magnitude than f_c, i.e. $G(f) = 0$ for all $|f| > f_c$, then the function $g(t)$ is completely determined by its sample $g(t_i)$. This would correspond to a wavefunction whose maximum kinetic energy was less than that allowed on the grid. However, if the function is not band-width limited to less than the Nyquist critical frequency, then all of the power spectral density which lies outside of the frequency range $-f_c < f < f_c$ is spuriously moved into that range. This is called aliasing, and will obviously occur in the case under consideration if the kinetic energy of the wavefunction is too large to be accommodated on the grid [71].

It is not always possible to know at the outset of a calculation what the maximum kinetic energy will be, so it is necessary to monitor the Fourier transform to ensure that it is small at the edges of the grid in momentum space. It is important to try to obtain an optimum grid spacing because this will minimise the computational effort, i.e. it will minimise the number of grid points required, whilst still ensuring the accuracy of the Fourier transform.

There is another problem with using the discrete Fourier transform. Consider a finite grid, $x_j, j = 0, 1, \ldots, (N-1)$. When carrying out Fourier transforms, one tacitly assumes that $\Psi(x)$ is periodic, with x_0 and $x_{N-1} + \Delta x$ being the same point. This means that wavepackets can spuriously come out one end of the grid and enter the other end. If the potential is very large at the edges, e.g. for a harmonic potential, then this will not be a problem since the wavefunction will be very small in this region. However, in this case it is then possible to get reflection at the boundaries, that is if the potential is very large at x_0, there may be reflection at x_{N-1}. There are two ways to deal with this problem [72].

First, use a large enough grid so that significant reflection does not occur within the time of the propagation; this will be computationally expensive. Secondly, an absorbing boundary can be used so that the outgoing amplitude is effectively destroyed before it reaches the boundary; this will be discussed later.

2.3. 2 The Fast Fourier Transform

In practice, the discrete Fourier transform is carried out using a *Fast Fourier Transform* (F.F.T.) [71]. This is an algorithm which can be computed in $O(N \log_2 N)$ operations rather than $O(N^2)$ which is required by the more traditional methods. The sequence used here is called *a decimation-in-time* or *Cooley-Tukey* F.F.T. algorithm [71]. It is the use of this algorithm which makes the Fourier Method, and so the time-dependent methods, viable.

2.3. 3 Two-Dimensional Fourier Transforms

A wavefunction which depends on more than one spatial variable, say two, has a many-dimensional, say two-dimensional, Fourier transform:

$$\Psi(k_x, k_y) = \int_{-\infty}^{\infty} \int_{-\infty}^{\infty} e^{-i(k_x x + k_y y)} \Psi(x, y)\, dx dy. \tag{19}$$

The two-dimensional Fourier transform $\Psi(k_x, k_y)$ can be viewed as two successive one-dimensional transforms. The last equation can be written as:

$$\Psi(k_x, k_y) = \int_{-\infty}^{\infty} e^{-ik_y y} \left[\int_{-\infty}^{\infty} e^{-ik_x x} \Psi(x, y)\, dx \right] dy. \tag{20}$$

Note that the term in brackets is simply the one-dimensional Fourier transform of $\Psi(x, y)$ with respect to x, that is,

$$\Psi(k_x, y) = \int_{-\infty}^{\infty} e^{-ik_x x} \Psi(x, y)\, dx. \tag{21}$$

Using this, equation (19) can be rewritten as:

$$\Psi(k_x, k_y) = \int_{-\infty}^{\infty} e^{-ik_y y} \Psi(k_x, y)\, dy. \tag{22}$$

Thus $\Psi(k_x, k_y)$ is the one-dimensional transform of $\Psi(k_x, y)$ with respect to y.

Now consider the discrete Fourier transform:

$$\Psi(k_{xi}, k_{yj}) \approx \sum_{l=0}^{M-1} e^{-ik_{yj} y_l / M} \left[\sum_{p=0}^{N-1} e^{-ik_{xi} x_p / N} \Psi(x_p, y_l) \right] \Delta x \Delta y, \tag{23}$$

where N and M are the number of grid points in the x and y directions respectively. The term in brackets is a one-dimensional discrete Fourier transform of $\Psi(x_p, y_l)$, and has to

be calculated M times, i.e. for each value of y_l, to produce $\Psi(k_{xi}, y_l)$, which in turn will be Fourier transformed N times, i.e. for each value of k_{xi}, to produce $\Psi(k_{xi}, k_{yj})$.

Hence, it is clear that the two-dimensional Fourier transform can be interpreted as two successive transforms, and so the methods used to calculate the one-dimensional transforms can be extended for use with two-dimensional transforms.

Similar results apply to the inverse Fourier transforms. Thus it is clear that the application of the Fourier method to two and more dimensions is quite straightforward.

It can be seen that the algorithm for the two-dimensional discrete Fourier transform is highly parallelizable since the M Fourier transforms in the first stage are independent of each other, as are the N Fourier transforms in the second stage.

2.4 The Temporal Part

The time-dependent Schrödinger equation is:

$$i\hbar\frac{\partial\Psi}{\partial t} = \hat{H}\Psi. \tag{24}$$

In the last section it was seen how $\hat{H}\Psi$ can be calculated using the Fourier method. This will now be used in the time-dependent Schrödinger equation to propagate the wavefunction in time. The solution of the T.D.S.E. can be written in the form:

$$\Psi(t) = \hat{U}(t)\Psi(0) = \hat{T}\exp\left[\frac{-i}{\hbar}\int_0^t \hat{H}\,dt'\right]\Psi(0), \tag{25}$$

where $\hat{T}$ is the time-ordering operator.

The various methods for propagating the initial wavefunction can be divided into two groups [6]:

1. The short-time propagators, which propagate the wavefunction using a series of short timesteps, and can be used for both time-dependent and time-independent Hamiltonians. This is equivalent to dividing $\hat{U}(t)$ into short segments:

$$\hat{U}(t) = \prod_{n=0}^{N-1} \hat{U}((n+1)\Delta t, n\,\Delta t), \tag{26}$$

where $\Delta t = t/N$. If these timesteps are short enough that the Hamiltonian does not change significantly in Δt then the time ordering operator can effectively be ignored, even for time-dependent Hamiltonians. This is the first Magnus approximation [73]. In each short segment the time-evolution operator $\hat{U}((n+1)\Delta t, n\,\Delta t)$ used is of the form:

$$\hat{U}((n+1)\Delta t, n\,\Delta t) \approx \exp\left[\frac{-i}{\hbar}\int_{n\Delta t}^{(n+1)\Delta t} \hat{H}(t')\,dt'\right]. \tag{27}$$

If the time segments are so short, i.e. they are short compared to any time-dependence in the Hamiltonian, that the Hamiltonian does not change significantly in Δt then the time-evolution operator is simply:

$$\hat{U}((n+1)\Delta t, n\,\Delta t) \approx \exp\left[\frac{-i}{\hbar}\hat{H}(t)\,\Delta t\right]. \tag{28}$$

This is the form of the propagation operator which will be used throughout the work which follows.

Alternatively, if the timesteps are not short enough that the Hamiltonian does not change significantly in Δt, i.e. if the Hamiltonian is strongly time-dependent, it may be necessary to use the second Magnus approximation, where the time-evolution operator used is of the form:

$$\begin{aligned}&\hat{U}((n+1)\Delta t, n\,\Delta t)\\ &\approx \exp\left[\frac{-i}{\hbar}\int_{n\Delta t}^{(n+1)\Delta t}\hat{H}(t')\,dt' - \frac{i}{2\hbar^2}\int_{n\Delta t}^{(n+1)\Delta t}dt'\int_{n\Delta t}^{t'}[\hat{H}(t'),\hat{H}(t'')]\,dt''\right].\end{aligned} \tag{29}$$

From this it becomes clear that in the first Magnus approximation it is the assertion that the commutator $[\hat{H}(t'),\hat{H}(t'')]$ is approximately zero which determines how short the timestep used must be.

2. The global propagators use a polynomial expansion of $\hat{U}(t)$, where the form of the time-evolution operator is given by:

$$\Psi(t) = \hat{U}(t)\Psi(0) = \exp\left[\frac{-i}{\hbar}\hat{H}\,t\right]\Psi(0), \tag{30}$$

so that either, $\hat{H}$ is time-independent or, the time over which the propagator is used is very short compared to any time-dependence of the Hamiltonian, ensuring that the time-ordering operator can be ignored, as for the short-time propagators discussed above. An expansion of the type:

$$\hat{U}(t) \approx \sum_{k=0}^{N} p_k P_k(-i\hat{H}t/\hbar), \tag{31}$$

is used. These propagators divide into two groups, low-order and high-order polynomial approximations. Essentially, the first group use short timesteps and the second long timesteps. This implies that high-order polynomial approximations can only be used for time-independent Hamiltonians, (i.e. $\hat{T}$ can be omitted regardless of how long the timestep used in the propagation is), whilst the low-order approximations can be used for both time-dependent and independent Hamiltonians.

2.5 Global Propagators

The question which must be addressed is: what is the optimal choice of polynomial expansion? The aim is to find the best form for the polynomials P_k used in the expansion of the time-evolution operator [74]. In general any function can be approximated using the Newtonian formulation of the interpolation polynomial [75]:

$$F(x) = \sum_{k=0}^{N} a_k \prod_{j=0}^{k-1} (x - x_j), \tag{32}$$

where a_k are the divided difference coefficients and x_j are the interpolation points. A similar expression can be given for the approximation of the time-evolution operator by an interpolation polynomial. This interpolation polynomial is a function of the Hamiltonian operator:

$$F\left(\frac{-i}{\hbar}\hat{H}\Delta t\right) = \sum_{k=0}^{N} a_k \prod_{j=0}^{k-1} \left(\frac{-i}{\hbar}\hat{H}\Delta t - x_j\hat{I}\right). \tag{33}$$

In this expansion, if the interpolation points are chosen in the region where the eigenvalues lie, i.e. the x_j are the eigenvalues of $-i\hat{H}\Delta t/\hbar$, then the convergence of the above expression will be greatly improved [74]. This can be proved by showing that this problem reduces to approximating the scalar function $e^{\lambda'}$ by the polynomial expansion, where λ' belongs to the domain which includes all the eigenvalues of the operator $-i\hat{H}\Delta t/\hbar$. This can be understood by recalling the definition of a function of an operator:

$$e^{\hat{B}}\underline{b}_j = e^{b_j}\underline{b}_j \tag{34}$$

where $\hat{B}$ has the eigenvector $\underline{b}_j$ with eigenvalue b_j.

The error in an interpolation polynomial is given by:

$$E(x) = a_{N+1}(x) \prod_{j=0}^{N} (x - x_j). \tag{35}$$

One method by which this error can be minimised takes no account of its relative magnitude in the interval, i.e. the error is minimised regardless of how important the error at x_1 is relative to the error at x_2. This can be done by choosing the interpolation points x_j such that $\prod_{j=0}^{N}(x - x_j)$ is minimum for arbitrary x in the interval. The Chebyshev polynomials have uniform magnitude across the interval, i.e. $\prod_{j=0}^{N}(x - x_j)$ is a minimum. Hence if these polynomials are used $E(x)$ is minimised. Thus, the Chebyshev polynomials are used in this expansion because they provide an approximation which is *almost* as good as the *best approximation*, or minimax polynomial, which has the smallest deviation from the true function. An important aspect of this minimisation is that the error is uniformly distributed over all the range of eigenvalues.

In solving the T.D.S.E. the time-evolution operator is applied to an initial wavefunction, $\Psi(0)$. Thus it might be better to try to minimise the error in $U(t)\Psi(0)$ rather than in $U(t)$. This error can be written as:

$$R = a_{N+1}\left(\frac{-i}{\hbar}\hat{H}\Delta t\right)\prod_{j=0}^{N}\left(\frac{-i}{\hbar}\hat{H}\Delta t - x_j\hat{I}\right)\Psi(0). \tag{36}$$

Full minimisation of R is extremely complicated due to dependence of a_{N+1} on $\frac{-i}{\hbar}\hat{H}\Delta t$. Thus only the minimisation of $(\frac{-i}{\hbar}\hat{H}\Delta t - x_j\hat{I})\Psi(0)$ is considered. It has been shown that the polynomials generated by the Lanczos recurrence scheme satisfy this condition [73]. Another method of minimising the error can be used which assumes a functional form for $a_{N+1}(\frac{-i}{\hbar}\hat{H}\Delta t)$ and then does a full minimisation of R [73]. For both these minimisations of R, the error will not be uniform across the range of eigenvalues. This however *may* not be a disadvantage. This algorithm tailors the polynomial approximation to the particular wavefunction which is to be propagated. It can be thought of as putting the interpolation points most densely in the areas of the domain where they are most needed, i.e. those corresponding to the eigenvalues of the predominant eigenvectors which make up the wavefunction.

2.5. 1 The Chebyshev Propagator

This propagator expands the time-evolution operator using the complex Chebyshev polynomials [76] [77]. These polynomials are a complex version of the Chebyshev polynomials and are defined as:

$$\phi_k(\omega) = (i)^k T_k(-i\omega), \qquad \omega \in [-i, i], \tag{37}$$

and the T_k are the Chebyshev polynomials and are defined as:

$$T_k(x) = \cos(k \arccos(x)). \tag{38}$$

The ϕ_k are orthogonal on the imaginary interval $[-i, i]$ with respect to the following inner product:

$$\langle f, g\rangle = -i\int_{-i}^{i}\frac{f(\omega)g^*(\omega)}{\sqrt{1-|\omega|^2}}\,d\omega. \tag{39}$$

The Chebyshev polynomials can be calculated using the recurrence relation:

$$T_k(x) = 2xT_{k-1}(x) + T_{k-2}(x) \tag{40}$$

with

$$T_0(x) = 1, \qquad T_1(x) = x. \tag{41}$$

A related recurrence exists for the complex Chebyshev polynomials.

In order to use these polynomials the Hamiltonian must be scaled and shifted. This is necessary because the complex polynomials are only defined on the range $[-i, i]$. It was stated previously that an interpolation polynomial will have the best convergence when the interpolation points are in the region of the eigenvalues. Thus, it would be useful to scale and shift the Hamiltonian so that its eigenvalues fall in the range $[-i, i]$, i.e. in the region of the interpolation points. To do this the range of eigenvalues of $-i\hat{H}\Delta t/\hbar$ must be calculated. This can be done as follows. The maximum kinetic energy that can be represented on the grid is $\hbar^2 k_{max}^2/2m$ where k_{max} is $\pi/\Delta x$. If then V_{min} and V_{max} are the minimum and maximum of the potential represented on the grid, the range of the eigenvalues of $\hat{H}$ is:

$$\lambda \in \left[V_{min}, V_{max} + \frac{\pi^2\hbar^2}{2m(\Delta x)^2}\right], \tag{42}$$

so that the range of $-i\hat{H}\Delta t/\hbar$ is $-i\lambda\Delta t/\hbar$. A normalised Hamiltonian can now be defined:

$$\hat{H}_{\text{norm}} = \frac{\hat{H}\Delta t - (R+G)}{R}, \tag{43}$$

where

$$R = \frac{\Delta t\left(V_{max} + \frac{\pi^2\hbar^2}{2m(\Delta x)^2} - V_{min}\right)}{2} \tag{44}$$

and

$$G = \Delta t V_{min}. \tag{45}$$

Here $\hbar$ has not been explicitly included in the definition of $\hat{H}_{\text{norm}}$, equation (43), since as it is present in both the numerator and the denominator, it will cancel. Thus,

$$\exp\left[\frac{-i}{\hbar}\hat{H}\Delta t\right] = \exp\left[-i\hat{H}_{\text{norm}}R/\hbar\right]\exp\left[-i(R+G)/\hbar\right], \tag{46}$$

and the term $\exp\left[-i\hat{H}_{\text{norm}}R/\hbar\right]$ will be approximated using the Chebyshev expansion:

$$\exp\left[-i\hat{H}_{\text{norm}}R/\hbar\right] \approx \sum_{k=0}^{N} a_k(R/\hbar)\phi_k(-i\hat{H}_{\text{norm}}). \tag{47}$$

The coefficients $a_k(R/\hbar)$ are now needed,

$$a_k(R/\hbar) = -i\int_{-i}^{i} \frac{\exp\left[-i\hat{H}_{\text{norm}}R/\hbar\right]\phi_k(-i\hat{H}_{\text{norm}})}{\sqrt{1-|\hat{H}_{\text{norm}}|^2}}\, d(-i\hat{H}_{\text{norm}}) \tag{48}$$

$$= c_k J_k(R/\hbar), \tag{49}$$

where $c_k = 1$ for $k = 0$, $c_k = 2$ for $k > 0$, and $J_k(R/\hbar)$ are Bessel functions. Now substituting these coefficients into the Chebyshev expansion:

$$\exp\left[-i\hat{H}_{\rm norm}R/\hbar\right] \approx \sum_{k=0}^{N} c_k J_k(R/\hbar)\phi_k(-i\hat{H}_{\rm norm}). \tag{50}$$

Hence the time-evolution operator can be approximated as:

$$\exp\left[\frac{-i}{\hbar}\hat{H}\Delta t\right] \approx \exp\left[-i(R+G)/\hbar\right] \sum_{k=0}^{N} c_k J_k(R/\hbar)\phi_k(-i\hat{H}_{\rm norm}). \tag{51}$$

This then requires the evaluation of R and G, and so $\hat{H}_{\rm norm}$, which is then used in the recurrence relation (given above) to calculate the Chebyshev polynomials. In fact the calculation is actually of $\hat{U}(t)\Psi(0)$ so that the recurrence becomes:

$$\phi_k(-i\hat{H}_{\rm norm})\Psi(0) = 2(-i\hat{H}_{\rm norm})\phi_{k-1}(-i\hat{H}_{\rm norm})\Psi(0) + \phi_{k-2}(-i\hat{H}_{\rm norm})\Psi(0) \tag{52}$$

with

$$\phi_0(-i\hat{H}_{\rm norm})\Psi(0) = \Psi(0), \qquad \phi_1(-i\hat{H}_{\rm norm})\Psi(0) = -i\hat{H}_{\rm norm}\Psi(0). \tag{53}$$

The Bessel function coefficients, $J_k(R/\hbar)$, are calculated for $k = 0$ and 1 using, depending on the magnitude of $R/\hbar$, either a polynomial expansion or rational functions of their argument $R/\hbar$. For $k > 1$ a recurrence relation upward on k from J_0 and J_1 is used, but will only remain stable whilst $k < R/\hbar$. For $k > R/\hbar$, Miller's algorithm is used [71]. This involves applying the recurrence downward from some arbitrary starting value and making use of the upward-unstable nature of the recurrence to put the value of the function onto the correct solution. Whilst this recurrence downward is carried out, the value of $J_k(R/\hbar)$, i.e. the required value of the kth Bessel function, is saved. Once J_0 is reached, $J_k(R/\hbar)$ is normalised with the sum accumulated along the way [71]. This normalisation is done using the following summation:

$$1 = J_0(R/\hbar) + 2J_2(R/\hbar) + 2J_4(R/\hbar) + 2J_6(R/\hbar) + \cdots \tag{54}$$

The number of expansion terms, N, needed for convergence is determined by the size of $R/\hbar$, or more precisely the size of the time-energy phase space. When $k > R/\hbar$ the Bessel functions $J_k(R/\hbar)$ decay exponentially, so that the number of terms in the expansion, N, has only to be slightly larger than $R/\hbar$. The amount by which N exceeds $R/\hbar$ will determine how accurate the calculation will be. This means that, in a practical implementation, the number of expansion terms, N, can be chosen such that the accuracy of the summation is dominated by the accuracy of the computer. The total number of terms is usually taken to be $\alpha R/\hbar$ where $\alpha = 1.3$.

One drawback of the global evolution is that information about intermediate results is not obtained. There are two ways to remedy this, though for both it must be realised that the practical lower limit of the number of terms in the Chebyshev expansion is of the order of 40 [6]. The reason for this lower limit, or minimum number of terms, is that the extra terms above $k = R/\hbar$ which are needed to converge the sum begin to dominate, making the approximation inefficient. The two methods are then:

1. In equation (51), consider that only the expansion coefficients are time dependent, i.e. $J_k(R/\hbar)$, since $R/\hbar$ depends on Δt. The Chebyshev polynomial operations, $\phi_k(-i\hat{H}_{\text{norm}})\Psi(0)$, which require most of the calculation effort, are time independent. This means that the expansion coefficients $J_k(R/\hbar)$ can be recalculated for many intermediate times. This method is probably the most accurate of the two, but the repeated calculation of the coefficients can be computational expensive, and the method is very unstable when an imaginary potential is introduced. This then is a high-order polynomial approximation, i.e. the total timestep which is propagated is very long requiring a large number of terms in the polynomial expansion.
2. The other method is simply to split the propagation into smaller intervals, so that in some ways the propagator becomes like a short-time propagator though the timestep used has no limit. It is this method which is particularly sensitive to the lower limit of the number of terms in the Chebyshev expansion. This is because the extra computational effort required to calculate the terms above $\alpha R/\hbar$ becomes prohibitive when repeated for many timesteps. This is a *lower*-order polynomial approximation. Whether or not it will actually be a low-order polynomial approximation, with which a time-dependent Hamiltonian can be used, will depend on the particular problem and the shortest reasonable timestep that can be used without the calculation becoming too expensive.

2.5. 2 The Short Iterative Lanczos (S.I.L.)

This propagator expands the time-evolution operator using a basis of polynomials which are generated with the Lanczos recursion [6][78]. This expansion is not done explicitly as for the Chebyshev propagator. However, a M dimensional Krylov basis set is constructed, using the Lanczos recurrence scheme. This is initialised using:

$$\begin{aligned} q_0 &= \Psi(0) \\ \hat{H}q_0 &= \alpha_0 q_0 + \beta_0 q_1 \end{aligned} \tag{55}$$

and the recurrence formula used is:

$$\hat{H}q_j = \beta_{j-1}q_{j-1} + \alpha q_j + \beta_j q_{j+1}, \tag{56}$$

where

$$\alpha_j = \langle q_j|\hat{H}|q_j\rangle \tag{57}$$

and

$$\beta_{j-1} = \langle q_{j-1}|\hat{H}|q_j\rangle. \tag{58}$$

(β_j is obtained by the normalisation requirement $\langle q_{j+1}|q_{j+1}\rangle = 1$.) Thus, the polynomials q_j, which form an orthogonal basis, are constructed using this scheme. The matrix of the Hamiltonian operator is then formed using these polynomials. In this basis the Hamiltonian operator is tridiagonal and so its diagonalisation is relatively easy, i.e. it does not scale as $O(M^3)$:

$$H_M = \begin{pmatrix} \alpha_0 & \beta_0 & 0 & \cdots & \cdots & \cdots & 0 \\ \beta_0 & \alpha_1 & \beta_1 & 0 & \cdots & \cdots & 0 \\ 0 & \beta_1 & \alpha_2 & \beta_2 & 0 & \cdots & 0 \\ \vdots & \vdots & \ddots & \ddots & \vdots & \vdots & 0 \\ 0 & \cdots & \cdots & \cdots & \beta_{M-3} & \alpha_{M-2} & \beta_{M-2} \\ 0 & \cdots & \cdots & \cdots & 0 & \beta_{M-2} & \alpha_{M-1} \end{pmatrix} \tag{59}$$

The Hamiltonian matrix, H_M, is diagonalised in this basis to yield a set of eigenvalues and eigenvectors which describe the diagonal matrix, D_M, and the matrix of the eigenvectors, Z. These are then used in the propagation of the wavefunction.

The propagation scheme is then:

1. The Krylov basis is constructed; the matrix H_M formed, and then diagonalised.
2. The wavefunction is transformed into the space described by the eigenvectors of the Hamiltonian, using the matrix Z. These eigenvectors will be simple combinations of the Krylov basis functions.
3. The transformed wavefunction is then propagated using the diagonal time-evolution operator, $\exp(\frac{-i}{\hbar}D_M\Delta t)$. Since the Hamiltonian is diagonal in the space described by its eigenvectors, the propagation is as simple as for any eigenfunction of a Hamiltonian.
4. The propagated wavefunction is then back-transformed as a reverse of the second step.

Thus, the time-evolution operator can be expressed as:

$$U(\Delta t) = Z^\dagger \exp(\frac{-i}{\hbar}D_M\Delta t)Z, \tag{60}$$

so that the time-dependent wavefunction can be written as:

$$\Psi(\Delta t) = Z^\dagger \exp(\frac{-i}{\hbar}D_M\Delta t)Zq_0 = \sum_{i=0}^{M-1} u_{li}q_i, \tag{61}$$

from which it is clear that the time-evolution operator can be expressed as an expansion in the polynomials generated by the Lanczos recursion.

It can be seen that at zero time the wavefunction is given by the zeroth-order vector in the Krylov basis set. As time evolves amplitude will be transferred to higher-order vectors. The error in this time-evolution propagator occurs because amplitude in the last vector q_{M-1} cannot escape to the next vector q_M, as the basis set has a limited size. This error is given by the expression [79]:

$$\text{error} \approx \left[\frac{(\Delta t/\hbar)^{M-1}}{(M-1)!} \prod_{k}^{M-2} \beta_k \right]^{1/2} . \tag{62}$$

Thus the accuracy depends on the order of the expansion and the length of the time step. If a calculation is required to a particular accuracy equation (62) can be used to decide on a suitable time step and size of the Krylov basis. Certain situations may minimise this error, e.g. when the initial wavefunction is an approximate eigenfunction of the Hamiltonian [80].

However, other errors do arise from the scheme used to obtain the orthogonal vectors. For this reason the method must have a limited size of basis set and so a limited time step [78]. Thus this propagator is the *Short* Iterative Lanczos.

2.6 Short-Time Propagators

Short-time propagators are conceptually much easier to understand than global propagators, since they do not rely on any complicated expansions of the time-evolution operator. Also, it is essential to use them in certain physical situations, where time-dependent Hamiltonians are used, e.g. motion in laser fields, motion under thermal agitation, or the T.D.S.C.F. (time-dependent self-consistent field) approximation. There are two main propagators, *The Second-Order-Differencing Scheme* (S.O.D.) [5][6], and *The Split Time Propagator Scheme* (Feit and Fleck) [36][81].

2.6. 1 The Second-Order-Differencing Scheme (S.O.D.)

For the S.O.D. scheme, the time-evolution operator is expanded in a Taylor series. However, this cannot be done without considering time reversal, since if it is ignored the expansion is not stable. Thus consider the symmetric relation:

$$\Psi(t+\Delta t) - \Psi(t-\Delta t) = \left(\exp\left[-i\hat{H}\Delta t/\hbar\right] - \exp\left[i\hat{H}\Delta t/\hbar\right] \right) \Psi(t); \tag{63}$$

and then the expansion of the exponential terms in a Taylor series:

$$\Psi(t+\Delta t) \approx \Psi(t-\Delta t) - 2i\Delta t\hat{H}\Psi(t)/\hbar; \tag{64}$$

this is the second-order-differencing scheme.

This propagating scheme, however, is only stable for timesteps smaller than the stability limit, Δt_s:

$$\Delta t_s = \frac{\hbar}{E_{\max}}, \tag{65}$$

where $E_{\max}$ can be calculated in a similar way to R and G in equations (44) and (45), so that $E_{\max} = (2R + G)$. This stability limit can be thought of as arising from the time-uncertainty principle, and obviously affects the way in which time is discretised.

This scheme rigorously preserves both norm and energy, so that error accumulates in the phase:

$$\text{error} \approx \frac{(\Delta t E_m)^3}{3\hbar^3}. \tag{66}$$

It can be seen that the error is worse at higher eigenvalues, in contrast to the Chebyshev propagator which has its error evenly distributed across the range. Propagating N times, this error accumulates N times. This means that the error can be minimised by choosing a smaller timestep and propagating for longer times. For example, it is usual to choose a timestep five times smaller than the stability limit, and to propagate for $5N$ timesteps. In this way the error is reduced by a factor of $5/5^3 = 1/25$, (compared to the propagation at the longer timestep), and allows longer times for propagation before errors in the phase become appreciable. It is also possible to shift the energy by adding a constant to the Hamiltonian, so that the energy range for which there is minimum error can be chosen to coincide with the most appropriate energy range for the calculation being done. Another way to increase the accuracy of the calculation, without reducing the timestep, is to use a bounded potential. For example, at very small displacements a Morse potential will be very large, so that Δt_s will be very small. However, the wavefunction does not penetrate far into this region, so that if the potential is *cut-off* at some value Δt_s will be increased, without affecting the wavefunction unduly. Besides improving the accuracy, the speed of the calculation can also be improved, since the number of timesteps can be reduced.

Consider again the S.O.D. scheme; it can be seen to require the wavefunction at *two* previous timesteps. At the start of the propagation only the initial wavefunction is available. Thus the propagation of the first step is done using a second-order *Runge-Kutta* scheme, which only requires one previous value of the wavefunction [71]. This scheme is an extension of the Euler method, which estimates the next point on a curve simply as:

$$y_{n+1} \approx y_n + \frac{dy(x_n)}{dx} dx. \tag{67}$$

In the second-order Runge-Cutta scheme, a trial point is considered:

$$y(x_n + \frac{1}{2}dx) \approx y_n + \frac{dy(x_n)}{dx}\frac{dx}{2}, \tag{68}$$

and then the required point is calculated using the derivative of the curve at this trial point:

$$y_{n+1} \approx y_n + \frac{dy(x_n + \frac{1}{2}dx)}{dx}dx. \tag{69}$$

Thus in the case of the time propagation:

$$\Psi(\Delta t) \approx \Psi(0) - \frac{i}{\hbar}\hat{H}\Psi(\Delta t/2)\Delta t, \tag{70}$$

where

$$\Psi(\Delta t/2) \approx \Psi(0) - \frac{i}{\hbar}\hat{H}\Psi(0)\Delta t/2, \tag{71}$$

since

$$\frac{\partial\Psi(t)}{\partial t} = -\frac{i}{\hbar}\hat{H}\Psi(0). \tag{72}$$

2.6. 2 The Split Time Propagating Scheme

For this propagation scheme, the Hamiltonian is split into its constituent parts:

$$\hat{H} = \hat{T} + \hat{V}, \tag{73}$$

so that the time-evolution operator can be approximated as:

$$\exp\left[\frac{-i\hat{H}\Delta t}{\hbar}\right] \approx \exp\left[\frac{-i\hat{T}\Delta t}{2\hbar}\right]\exp\left[\frac{-i\hat{V}\Delta t}{\hbar}\right]\exp\left[\frac{-i\hat{T}\Delta t}{2\hbar}\right]. \tag{74}$$

Thus the time-evolution operator is symmetrically split in a way which can be shown be of second-order accuracy [81].

This propagator is intrinsically stable, so there is no restriction on the magnitude of the timestep on these grounds. However, it has been suggested that if the timestep exceeds the stability limit, Δt_s given above, the results become meaningless because the phase of the propagation operator is greater than 2π. However, if only eigenstates below a certain energy bound are required, e.g. when bound states are of interest, it is possible to choose a timestep governed by this bounded energy range, rather than considering the entire energy range supported on the grid. Thus in the example given, the time step would be chosen according to the binding energy. In this way the bound states would have the correct phase, whilst the continuum states would be out of phase.

The errors which arise in the split time propagator are due to the fact that the operators $\hat{T}$ and $\hat{V}$ do not commute. Hence the error is given in terms of the commutators of these operators:

$$\text{error} \approx \max\left[-i\frac{\Delta t^3}{16m}\left[\hat{V},\left[\hat{V},\hat{P}^2\right]\right], -i\frac{\Delta t^3}{32m^2}\left[\hat{P}^2,\left[\hat{P}^2,\hat{V}\right]\right]\right]/\hbar^3, \tag{75}$$

where $\hat{P}^2 = 2m\hat{T}$.

The norm of the wavefunction is rigorously preserved so that the error accumulates in both the phase and the energy of the wavefunction. As with the S.O.D., the errors are of $O(\Delta t^3)$. Again as with the S.O.D., the timestep can be reduced to reduce the error, and the degree to which this is done depends on the accuracy required. Also, the error is not distributed uniformly, and can be expected to be worst in the region of the most rapidly fluctuating potential.

Consider now how this propagation is carried out. The right-hand side of equation (74) is equivalent to free-particle propagation over a half timestep. This free-particle propagation is carried out by transforming the wavefunction into momentum space by a F.F.T. procedure and then multiplying each grid point by $\exp\left[-i(k_l^2/2m)(\Delta t/2\hbar)\right]$; the wavefunction is then transformed back to coordinate space by an inverse F.F.T. procedure. The next term in equation (74) corresponds to a phase change from the action of the potential applied over the whole timestep. This phase change is carried out simply by multiplying the wavefunction by $\exp\left[-iV_l(\Delta t/\hbar)\right]$. Finally the last term corresponds to an additional free-particle propagation over a half timestep. This propagation is carried out in the same way as the first.

If the propagation is applied many times in sequence, which is likely because propagations of long time intervals are nearly always required, pairs of half-step free-particle propagations combine into full-step propagations. The computation thus proceeds as a succession of full-step propagations, applied in momentum space, alternating with phase changes of the wavefunction executed in coordinate space. The exceptions to this rule are the half timesteps applied at the beginning and end of the calculation, and at those intermediate times where the wavefunction is required, e.g. when studying the mechanism of a reaction not only the final wavefunction is of interest.

2.7 Aside—The Calculation of Eigenvalues and Eigenfunctions

The wavefunction at zero time can always be written as a combination of the eigenfunctions, u_i, of the Hamiltonian, since the eigenfunctions will form a complete basis, so that:

$$\Psi(0) = \sum_{i=1}^{N} a_i u_i, \tag{76}$$

and in general the time-dependent wavefunction can be written as:

$$\Psi(t) = \sum_{i=1}^{N} a_i e^{-iE_i t/\hbar} u_i, \tag{77}$$

where E_i is the eigenvalue corresponding to the eigenfunction u_i. If the autocorrelation

function is formed:

$$\langle \Psi(0)|\Psi(t)\rangle = \sum_{i=1}^{N} |a_i|^2 e^{-iE_i t/\hbar}, \tag{78}$$

and then Fourier transformed, an energy spectrum is produced:

$$P(E) = \sum_{i=1}^{N} |a_i|^2 \delta(E - E_i). \tag{79}$$

This gives then the eigenvalues weighted by the coefficients $|a_i|^2$ [36]. If the autocorrelation function does not die off significantly, so that the time for which the wavefunction is propagated, T, cannot be taken to be infinite, it may be necessary to use windowing functions [36][71]. If these are not used and the function is cut off in such a way that the function is no longer periodic then the spectrum produced by the Fourier transform will have many unphysical artifacts.

The eigenfunctions can be found by considering the expansion of the wavefunction in two ways. The first method, which is only suitable to find the ground state, propagates the wavefunction in imaginary time. It can be seen from equation (77) that $\Psi(t)$ will converge to the ground state at a rate depending on the difference between the ground state energy and the other eigenvalues [74].

The second method, which in theory may be used to calculate all the eigenfunctions, involves taking the Fourier transform of $\Psi(t)$:

$$\Psi(t) \Longleftrightarrow \Psi(E) = \sum_{i=1}^{N} a_i u_i \delta(E - E_i) \tag{80}$$

so that at E equal to E_n, $\Psi(E)$ will be proportional to u_n [36]. The above implies that T can be taken to be infinite and that there no overlapping resonances. If this is not the case the use of lineshaping techniques will be necessary in order to calculate all the eigenfunctions. For the resolution of eigenfunctions, which have eigenvalues separated by an amount ΔE (in atomic units), it is necessary to propagate the wavefunction $\Psi(t)$ for a time T of at least $\pi/\Delta E$.

2.8 Absorbing Boundaries

As was hinted at earlier in this chapter, problems of wrap-around and reflection can arise at the edge of the grid. In essence these occur because a *finite* grid is used. Obviously, in real physical situations space is not bounded in this way, and so the problem can be thought of as trying to imitate infinite space. The mechanism by which the boundary effects occur is through the use of the F.F.T., which discretises both coordinate and momentum space with periodic boundary conditions.

The problem can be approached in two ways: either to use a very large grid; or somehow to achieve an absorbing boundary so that the outgoing amplitude is effectively destroyed before it arrives at the boundary. The first of these two methods is simple, but computationally expensive. The second is less straightforward, but more efficient. Again this can be done in two ways:

1. At regular time intervals the wavefunction is *damped* down, from a point suitably far from the edge R_{abs} [12]. Thus a function of the following type:

$$\begin{aligned} &\Psi(R) \rightarrow \Psi(R), \qquad R \leq R_{\text{abs}} \\ &\Psi(R) \rightarrow \Psi(R) \exp\left[-a(R - R_{\text{abs}})^2\right], \qquad R > R_{\text{abs}}, \end{aligned} \tag{81}$$

   is used. The parameters R_{abs} and a, can be altered depending on the frequency with which the function is applied, for example, if it is applied after every timestep, rather than say every thousandth, a need only be quite small.

2. An imaginary potential can be included in the Hamiltonian. The sign of this potential will be negative. The magnitude will be zero for $R < R_{\text{abs}}$. The introduction of an imaginary potential will have the same effect as the damping described above, but is carried out during every timestep, i.e. each time the Hamiltonian is used. The total potential of the system becomes:

$$V(R) = V_0(R) - iV_I(R). \tag{82}$$

   However, a *CAREFUL* choice of a time integration scheme is required to ensure numerical stability [72]. The reason for this warning is that most of the propagation schemes previously described are for Hamiltonians which are Hermitian, which will not be the case when an imaginary potential is included. This last point will be discussed in greater detail later.

2.8. 1 Imaginary Potentials

The question now arises as to the form and magnitude of the imaginary potential required.

It has been suggested that the magnitude of the imaginary potential required can be estimated by the following relation [82]:

$$\hbar E^{\frac{1}{2}}/(\Delta R\sqrt{8m}) < |V_{IB}| < (\Delta R\sqrt{8m}E^{\frac{3}{2}})/\hbar, \tag{83}$$

where E is the translational energy of the system, ΔR is the length of the part of the grid which is being used as the absorbing boundary, m the mass of the system under

consideration and V_{IB} is the magnitude of the potential at the very edge of the grid. The strengths of the inequalities in equation (83) have been investigated using the semiclassical J.W.K.B. approximation [83].

Two different forms of the potential have been suggested, linear [82] or with exponential terms [72]. For a linear imaginary potential one form which has been used is:

$$V_I = \begin{cases} V_{IB}\frac{R-R_{\text{abs}}}{\Delta R}, & R_{\text{abs}} \leq R \leq R_{\text{edge}}, \\ 0, & \text{otherwise.} \end{cases} \tag{84}$$

For an imaginary potential with exponential terms, one form which has been used is:

$$V_I = \begin{cases} \frac{V_{IB}}{\cosh^2[(R_{\text{edge}}-R)/\alpha]}, & R_{\text{abs}} \leq R \leq R_{\text{edge}}, \\ 0, & \text{otherwise.} \end{cases} \tag{85}$$

i.e. inverse of a squared hyperbolic cosine. Another form is the inverse of a non-squared hyperbolic cosine:

$$V_I = \begin{cases} \frac{V_{IB}}{\cosh[(R_{\text{edge}}-R)/\alpha]}, & R_{\text{abs}} \leq R \leq R_{\text{edge}}, \\ 0, & \text{otherwise.} \end{cases} \tag{86}$$

Here α is adjusted depending on the value of ΔR.

Recently an investigation into the best form of the imaginary potential has been carried out, again using the semiclassical J.W.K.B. approximation. This recommended that a complex absorbing potential of the form $V(x) = -iA\exp(-B/x)$ be used. Also a scaled version of the Schrödinger equation was derived, ensuring that the optimised parameters obtained under particular conditions could be scaled, and so be suitable for use under different conditions [84] [85].

2.8. 2 Aside—The Interaction Picture

Another completely different approach to the problems caused by the use of a finite grid is to use the interaction picture [86]. This picture is in between the Schrödinger picture and the Heisenberg picture. In the Schrödinger picture the dynamical variables or the operators are constant in time except for an explicit time dependence, but the state vector or wavefunction changes in time (this is the picture utilised here). In the Heisenberg picture the wavefunction is constant in time, but the operators change. The interaction picture, in which both the operators and the wavefunction have some time dependence, can be used so that the movement or spreading of the wavepacket in time is minimised, and the size of grid required is minimised too. The wavefunction will be given by:

$$\Psi_I(t) = \exp\left[i\hat{H}_0 t/\hbar\right]\Psi_S(t), \tag{87}$$

where $\hat{H}_0$ is the kinetic part of the Hamiltonian, i.e. $\hat{T}$. This implies the wavefunctions in the two different pictures are the same at time zero. The last equation can be rewritten as:

$$\Psi_I(t) = \exp\left[i\hat{H}_0 t/\hbar\right]\exp\left[-i\hat{H}t/\hbar\right]\Psi_S(0). \tag{88}$$

The physical meaning of this is that $\Psi_I(t)$ is obtained by propagating the wavefunction from time zero to time t under the action of the full Hamiltonian, and then propagating backwards to $t = 0$ under the action of the free Hamiltonian. Thus, the difference between $\Psi_I(t)$ and $\Psi_S(t)$ at time t will be purely due to the dynamical influence the system experiences from time zero through t. Therefore, the use of this picture eliminates effects such as spreading and oscillation.

In the interaction picture the T.D.S.E. becomes:

$$i\hbar\frac{\partial\Psi_I(t)}{\partial t} = \hat{H}_I\Psi_I(t), \tag{89}$$

where

$$\hat{H}_I(t) = \exp\left[i\hat{H}_0 t/\hbar\right]\hat{V}\exp\left[-i\hat{H}_0 t/\hbar\right], \tag{90}$$

and $\Psi_I(t)$ has been defined previously.

For some calculations this may be very useful. For example, consider the calculation of the S matrix elements. The elements are independent of the picture and so there is no need to transform back to the Schrödinger picture to obtain the required information. Also, in general, in scattering calculations the interaction picture will be useful because there are large parts of the grid where the potential is very small, which this picture can treat efficiently.

2.9 Summary

In this chapter the Fourier method for studying one-dimensional problems has been introduced. The nature of the initial wavefunction to be used has been discussed. It has been shown how the Hamiltonian and its operation on the wavefunction can be calculated, and then used to propagate the wavefunction in time. Several different methods for the propagation of the T.D.S.E. have been described. Various types of absorbing boundaries have also been described. The use of these different propagation schemes, and different types of absorbing boundaries, will be investigated in the next chapter.

3: Topics Investigated

There are many methods that can be used for propagating the T.D.S.E., and various different forms of imaginary potentials that can be used to set up an absorbing boundary. It was felt that a systematic investigation of these was necessary to make informed decisions about which methods were suitable for the applications of interest in the present work.

3.1 Propagating Schemes

All the propagation schemes described in the previous chapter were investigated, with the exception of the Short Iterative Lanczos. Recently a comparison of different propagation schemes has been reported in the literature [78]; this is a thorough investigation into the accuracy, numerical efficiency and stability of all the propagation schemes described in Chapter 2.

3.1. 1 Method

In order to investigate the various propagators, a simple problem was set up whose solution was known analytically. The problem used was that of an eigenfunction propagating in a harmonic well. The solution was obtained using the propagators and then compared to the analytical solution. Atomic units are used throughout this chapter; these are described in Appendix A.

A purely harmonic potential was used,

$$\hat{V}(x) = \frac{1}{2}k(x-a)^2 \tag{91}$$

with values of the parameters, k and a, appropriate for the hydrogen molecule. The force constant k can be calculated from the frequency of vibration of the hydrogen molecule, $\nu = (1/2\pi)\sqrt{k/m}$; a is the equilibrium bond length of the hydrogen molecule.

A variety of different initial wavefunctions was used, corresponding to the eigenfunctions of this potential. For $n = 0$, the initial wavefunction was a Gaussian centred at the equilibrium bond length of hydrogen:

$$\Psi_{n=0}(x,0) = \frac{\alpha^{1/2}}{\pi^{1/4}} \exp\left[-\alpha^2(x-a)^2/2\right], \tag{92}$$

where $\alpha^4 = mk/\hbar^2$. The higher eigenfunctions were described by the product of this Gaussian with an Hermite polynomial, $H_n(\alpha x)$ (given in table 1), where n is the index of the energy level.

Table 1. Hermite polynomials.

$H_0(\alpha x) = 1$
$H_1(\alpha x) = 2\alpha x$
$H_2(\alpha x) = 4(\alpha x)^2 - 2$
$H_3(\alpha x) = 8(\alpha x)^3 - 12\alpha x$
$H_4(\alpha x) = 16(\alpha x)^4 - 48(\alpha x)^2 + 12$

The error in the propagation was estimated by the deviation from the analytic solution:

$$\text{error}(t) = \int |\Psi_{\text{anal}}(x,t) - \Psi_{\text{cal}}(x,t)|^2 \, dx, \tag{93}$$

where the analytical solutions, Ψ_{anal}, are simply the initial wavefunctions multiplied by a phase factor:

$$\Psi_{\text{anal},n}(x,t) = \Psi_n(x,0) \exp\left[-i(n+1/2)\omega t\right], \tag{94}$$

where ω is the angular frequency of the hydrogen bond vibration. The S.O.D. and Chebyshev propagators can have their error estimated in this way. However, for the Feit/Fleck propagator error accumulates in both energy and phase so that this method is not completely reliable [6].

As well as this error, the norm:

$$\text{norm}(t) = \int \Psi(x,t)^* \Psi(x,t) \, dx \tag{95}$$

and the energy:

$$\text{energy}(t) = \int \Psi(x,t)^* \hat{H} \Psi(x,t) \, dx \tag{96}$$

were monitored. These should, of course, stay constant. Since, for the specific case of the harmonic oscillator, the eigenfunctions are invariant to the Feit/Fleck propagator, a good method to test the error is to follow the energy deviation from the initial value [6].

The computer time used for the calculations was recorded.

A grid of 64 points was used in the calculation, with $\Delta x = 0.031250$ Å, so that the grid ranged from $x = 0.010$ Å to $x = 2.01$ Å, with $a = 0.74144$ Å. The total propagation time was $T = 20\tau$, where τ is the period of vibration of H_2 and is equal to the reciprocal of the vibrational frequency of H_2. The timestep, Δt, was varied. To keep the total propagation time constant, the total number of propagation steps, N_T, was varied accordingly. The ratio of the timestep used to the stability timestep defined in Chapter 2, was denoted by R (this is not the same R as was used in the discussion of the Chebyshev propagator):

$$R = \frac{\Delta t}{\Delta t_s}. \tag{97}$$

Thus, in order to vary the timestep, the calculations were carried out for different values of R. This is only relevant for the short-time propagators.

In fact, the grid used here is not particularly efficient. The range of kinetic energy available on the grid is much larger than the range of potential energy. Whilst in certain situations this might be useful, in this case a harmonic oscillator is being considered, which is known to have equal amounts of average kinetic and potential energy. Thus, a grid which was better balanced would be more suitable in this case. However, this in no way affects the comparison of the different time propagators.

3.1. 2 Results

The results for the computer time, the norm, the energy deviation, and the error are presented for each propagator.

Time

Consider the computer time taken to propagate the eigenstate $n = 4$ for a total propagation time of T with $R = 0.21$ on a Sun Sparcstation IPC workstation. The computer times for each propagator are shown in table 2.

Table 2. Timings for the various propagation schemes.

Propagation Scheme	Time/s
S.O.D.	1622.08
Feit/Fleck	2010.15
Chebyshev-stepping	254.55
Chebyshev-global	3315.27
Chebyshev-global†	707.71

†—No intermediate results obtained.

First, it is immediately obvious that the Chebyshev-stepping method is superior to the Chebyshev-global propagator if intermediate results are required. It appears that the substantially longer times for the calculations using the Chebyshev-global propagator arise because of the limited RAM on the machine on which the calculations were carried out. The Chebyshev-global propagator requires that many functions be held in the memory. Another factor could be the necessity of calculating very many time-dependent coefficients, i.e. Bessel functions, for the global version of the Chebyshev propagator.

Secondly, it can be seen that the short-time propagators are a great deal slower than the Chebyshev-stepping propagator for the value of R used. A small value of R was chosen since this gives comparable accuracy for the various propagators; a value any higher would have made the comparison meaningless. The reason for the disparity in propagation times becomes obvious when the number of calls to the Hamiltonian, N_C, is considered. For the S.O.D., as for all short-time propagators, the number of calls to the Hamiltonian is equal to the number of timesteps, N_T. Thus, as $N_T \times \Delta t = T$:

$$N_C \times \Delta t = T. \tag{98}$$

Now, Δt is restricted, due to the constraints of stability and accuracy, by the relation (in atomic units):

$$\frac{\Delta t}{R} = \Delta t_s = \frac{1}{\Delta E}, \tag{99}$$

since ΔE is equal to $E_{\max}$ here, so that:

$$\Delta t = \frac{R}{\Delta E}. \tag{100}$$

Thus

$$N_C = \frac{T}{(R/\Delta E)} = \frac{T\Delta E}{R} \tag{101}$$

For the Chebyshev scheme, the number of calls, N_C, is equal to the number of terms in the polynomial expansion:

$$N_C = \frac{\Delta E \times T}{2} \times 1.3, \tag{102}$$

where the value 1.3 refers to the factor by which the minimum number of terms in the expansion must be multiplied in order to obtain machine accuracy. (This discussion concerning the number of calls to the Hamiltonian does not change when the Chebyshev propagator is used in a stepping manner.) Therefore, the ratio of N_C for the two propagation schemes is:

$$\text{Ratio} = \frac{2}{1.3 \times R} \tag{103}$$

which in this case gives Ratio $\approx$ 7.3, which compares well to a value of 6.3 (that is comparing S.O.D. and Chebyshev-stepping) obtained above. The discrepancy is probably due to the neglect of the time required for the calculation of the Bessel coefficients.

Norm

Analysis of the conservation of the norm revealed nothing interesting.

The norm was conserved better for the short-time propagators than the global propagator because the former are unitary transformations, but the norm was still conserved to 8 decimal places for the Chebyshev propagator. However, when R approaches 1 the S.O.D. propagator becomes unstable and the norm becomes extremely large.

Error

Now consider the error as defined above in equation (93). The results for the various propagators are shown in figures 1 $\rightarrow$ 10.

For the S.O.D. propagator the error may be clearly seen to increase with both R, i.e. Δt, and n, i.e. energy (figures 1 $\rightarrow$ 2).

Given the way error accumulates for the Feit/Fleck propagator, i.e. in both phase and energy, the results here for that propagator may be only of limited significance for use in comparison with the other propagators. However it can be seen that the error increases with R, i.e. Δt (figures 3 $\rightarrow$ 6).

For the Chebyshev propagators (figures 7 $\rightarrow$ 10) the error does not depend on n as expected, in fact the error seems to decrease as n increases. The global propagator appears to be more accurate than the stepping propagator. Since error accumulates for each

timestep, for the stepping propagator and all short-time propagators, the greater accuracy of the global propagator is expected.

It also can be clearly seen that for all except the lowest values of R and n, the Chebyshev propagator is the most accurate of all the propagation schemes. In any calculation of significance there will be a wide range of energies involved, thus it can be seen that in general the Chebyshev propagator will yield the most accurate results.

Energy

Energy was conserved better for the S.O.D. propagator than the Chebyshev propagator, while R was small, but the opposite was true as R approached 1. There was not a significant difference in the results at different values of n. For both, the deviations showed little need for concern.

Table 3. The dependence of the error in the Feit/Fleck propagator on R and n.

Initial energy $= 0.0099861127453796\,E_h$, $n = 0$	
R	Deviation of energy/E_h
0.21	−0.0000000000001960
0.95	−0.0000000000000476
1.14	−0.0000000000000425
4.20	−0.0000000000000039
8.40	−0.0000000000040607
Initial energy $= 0.049930563726905\,E_h$, $n = 2$	
R	Deviation of energy/E_h
0.21	−0.000000000001075
0.95	−0.000000000000241
1.14	−0.000000000000195
4.20	−0.000000000000007
Initial energy $= 0.089875014711377\,E_h$, $n = 4$	
R	Deviation of energy /E_h
0.21	−0.00000000003137
0.95	−0.00000000000778
1.14	−0.00000000000276
3.80	−0.00000000061170
7.60	−0.00000022168605

For the Feit/Fleck propagator the energy conservation deteriorated when R was very large, but appeared to be best for intermediate values of R (see table 3). For the Feit/Fleck propagator it is not necessary for R to be less than 1 in these calculations; this is in contrast to the requirements for the S.O.D. propagator. This is because a wavepacket with considerably less energy than the total available on the grid is being propagated. Thus, although the phase of higher energy wavepackets would become meaningless, the phase of the low energy wavepacket used in this calculation is not affected by such errors, until a particular limiting value of R is reached.

The results are not those expected since the error, which is taken here to be the error in the energy, is for this method proportional to Δt^3. Hence the error should increase with R. In fact it appears as if the error increases with the number of steps propagated, i.e. inversely proportional to R for a constant total propagation time.

The dependence of the error on the energy, or n, has been reported to be linear in the quantum number n [6]. It is not completely clear in the work done in this chapter what the dependence is, though there is certainly a marked increase at $n = 4$, so maybe this is an indication of the error being proportional to the energy, although this is more likely due to the limiting value of R having been reached. It appears that using the conservation of energy as a measure of the error for this propagator is not particularly useful.

The results obtained here for the performance of the various propagators are mostly those expected from a consideration of the properties of the propagators, which were discussed in the last chapter, as well as extensively in the literature [6]. At this stage it appears that, on the grounds of conservation of energy and accuracy the Chebyshev-stepping propagator is the 'best' for our purposes.

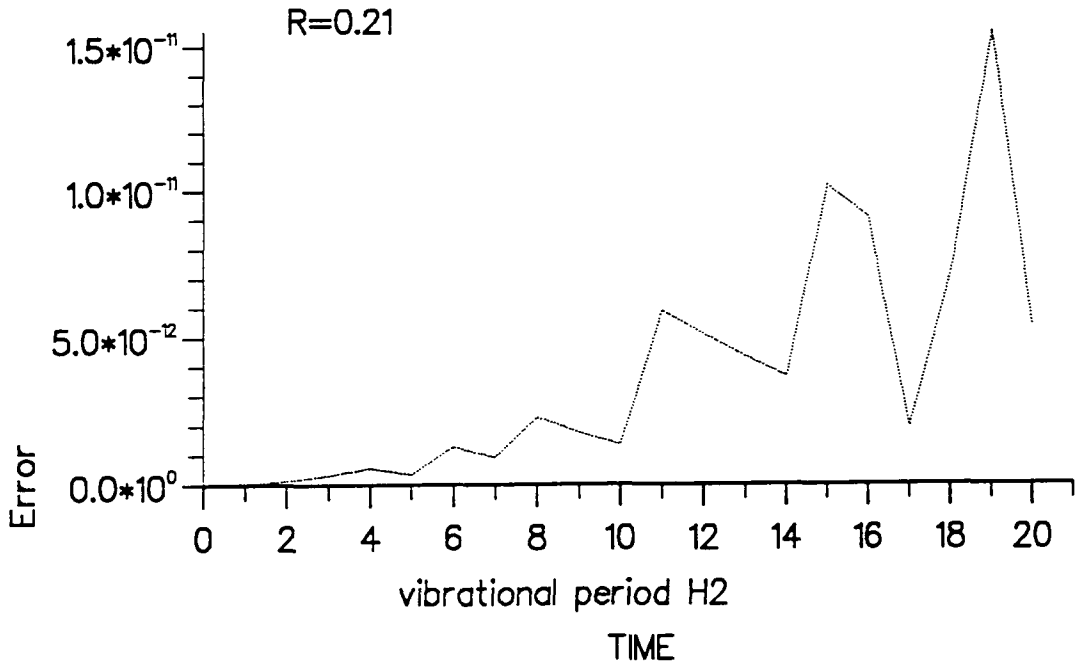

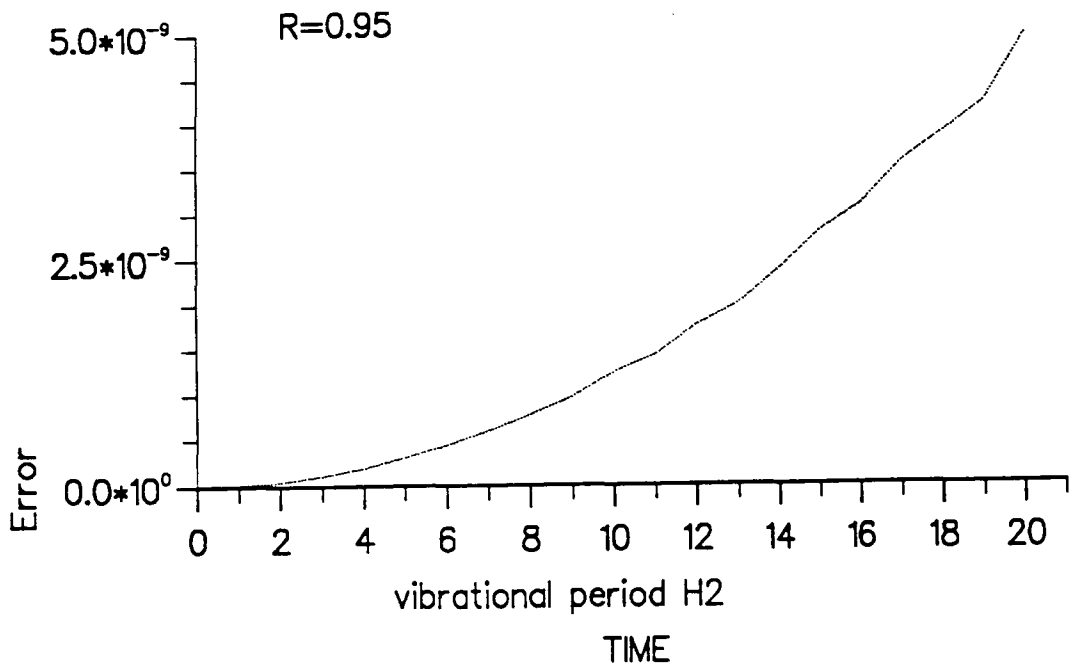

Fig. 1. Graphs of error against time for the second-order differencing propagator, for $n = 0$.

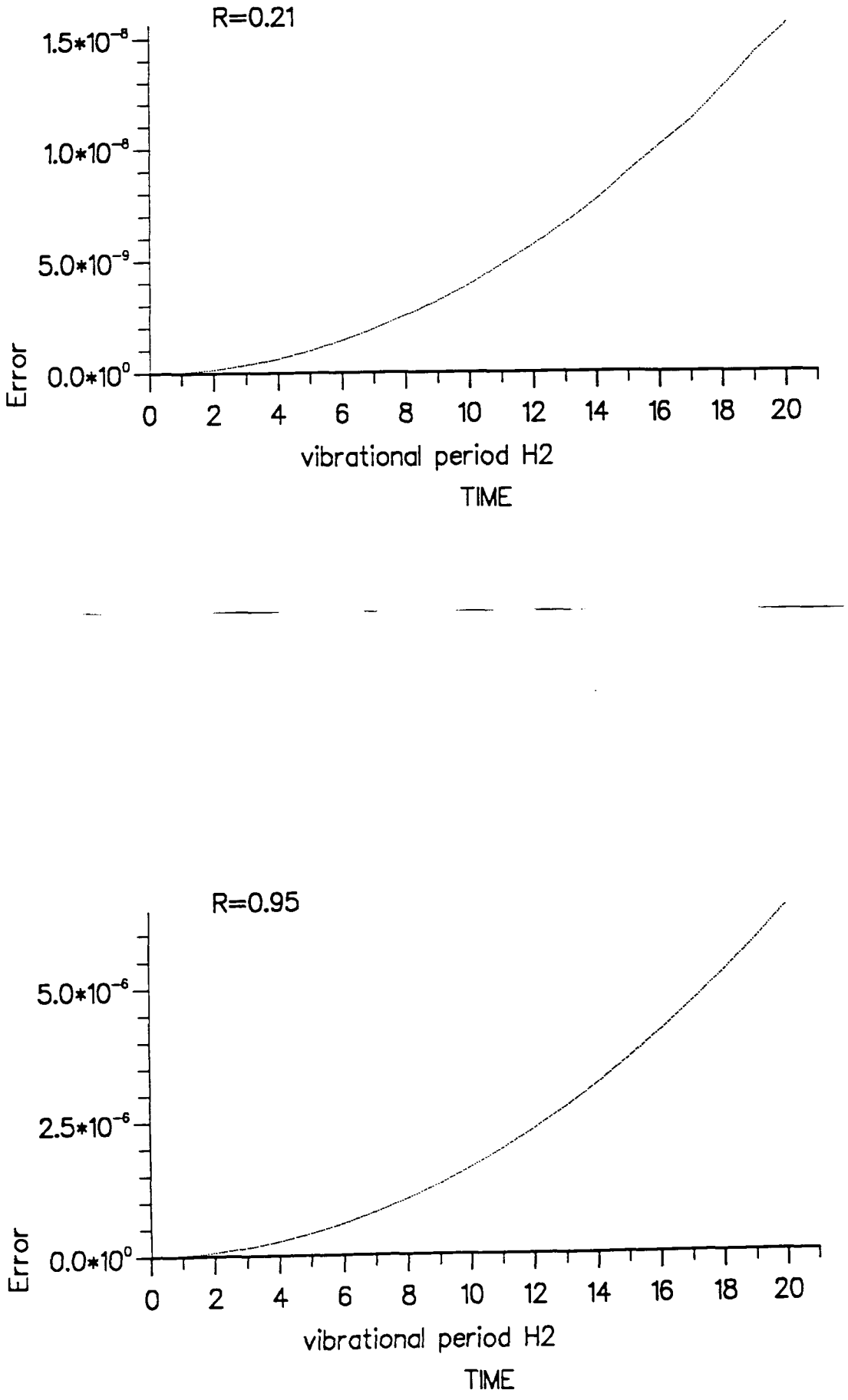

Fig. 2. Graphs of error against time for the second-order differencing propagator, for $n = 4$.

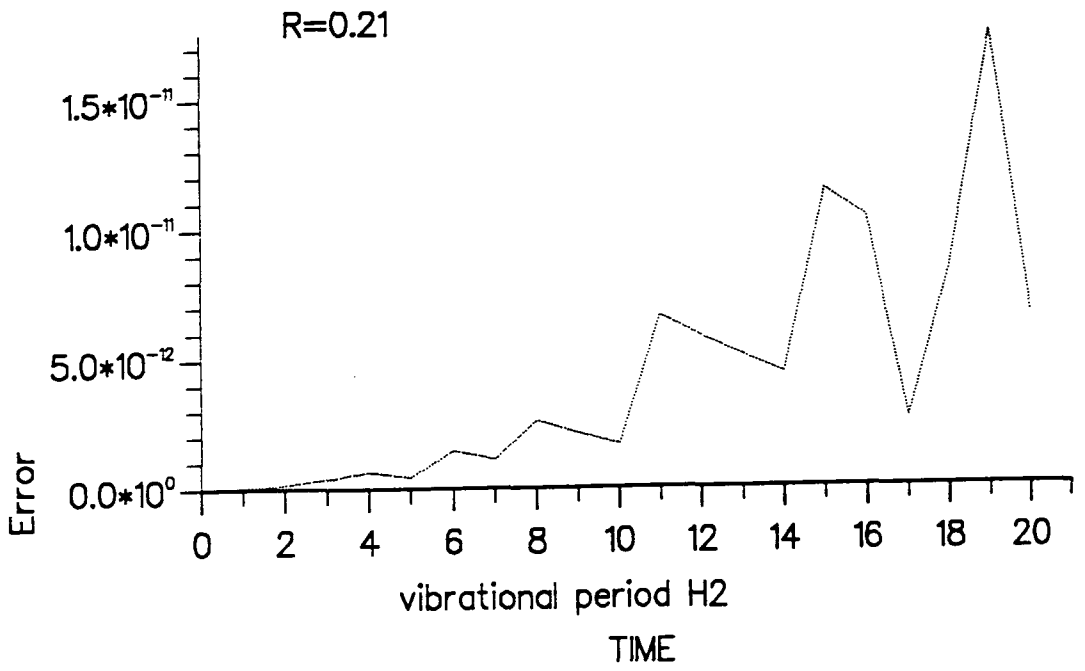

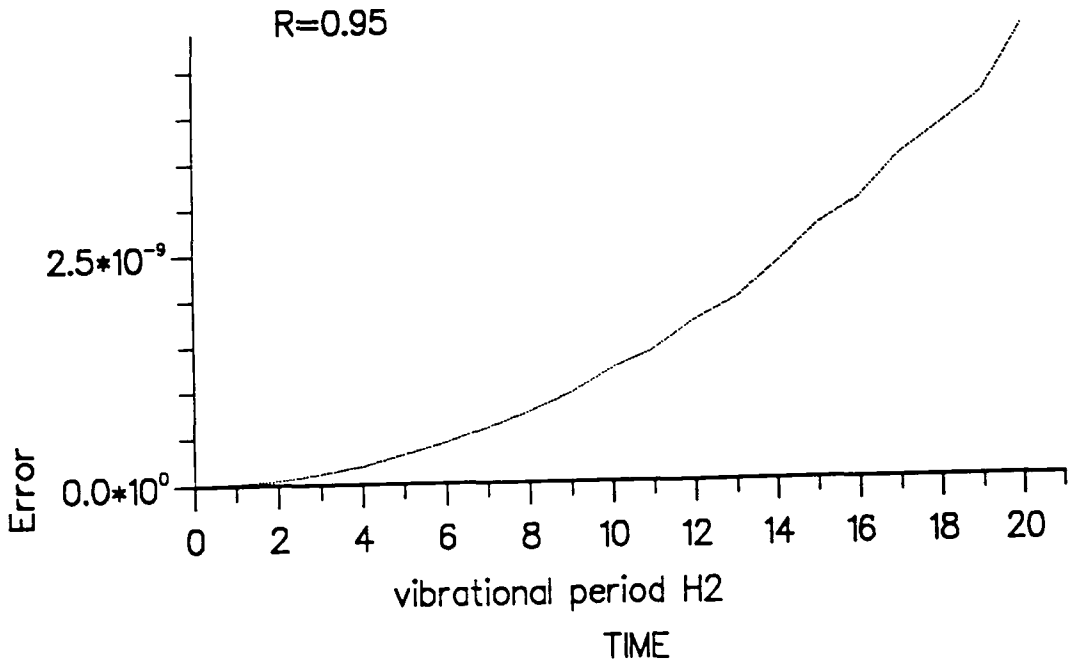

Fig. 3. Graphs of error against time for the Feit/Fleck propagator, for $n = 0$.

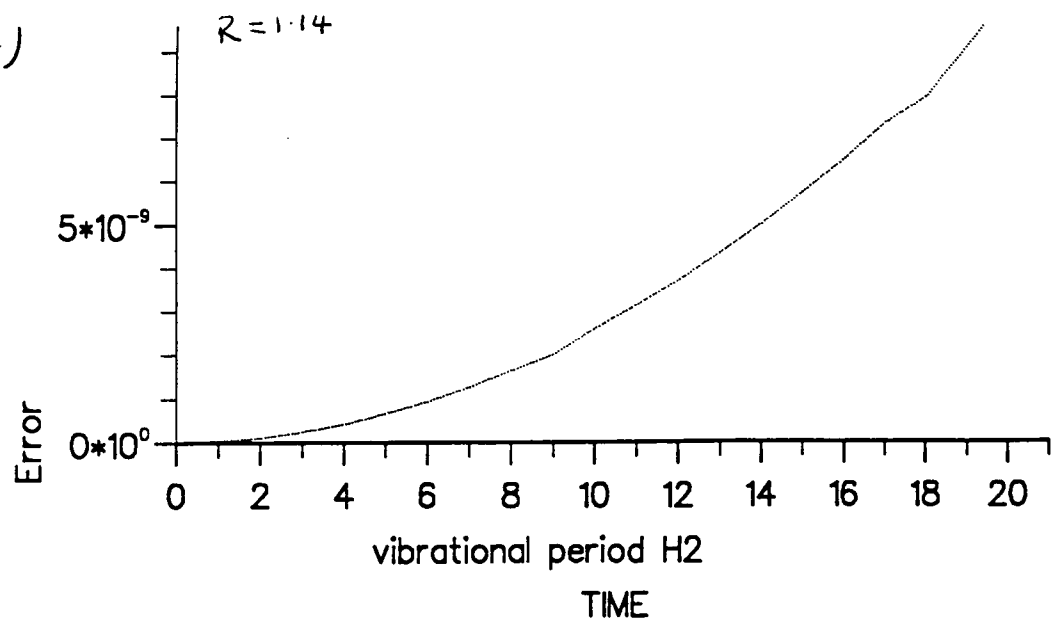
R=1.14
5*10^-9
0*10^0
Error
0
2
4
6
8
10
12
14
16
18
20
vibrational period H2
TIME

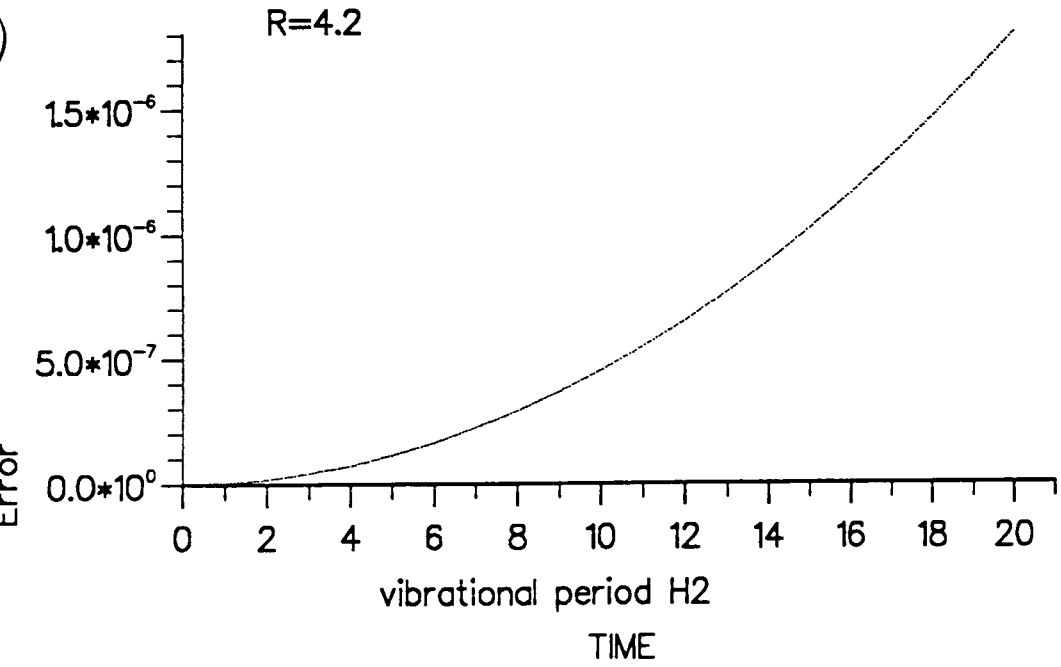
R=4.2
1.5*10^-6
1.0*10^-6
5.0*10^-7
0.0*10^0
Error
0
2
4
6
8
10
12
14
16
18
20
vibrational period H2
TIME

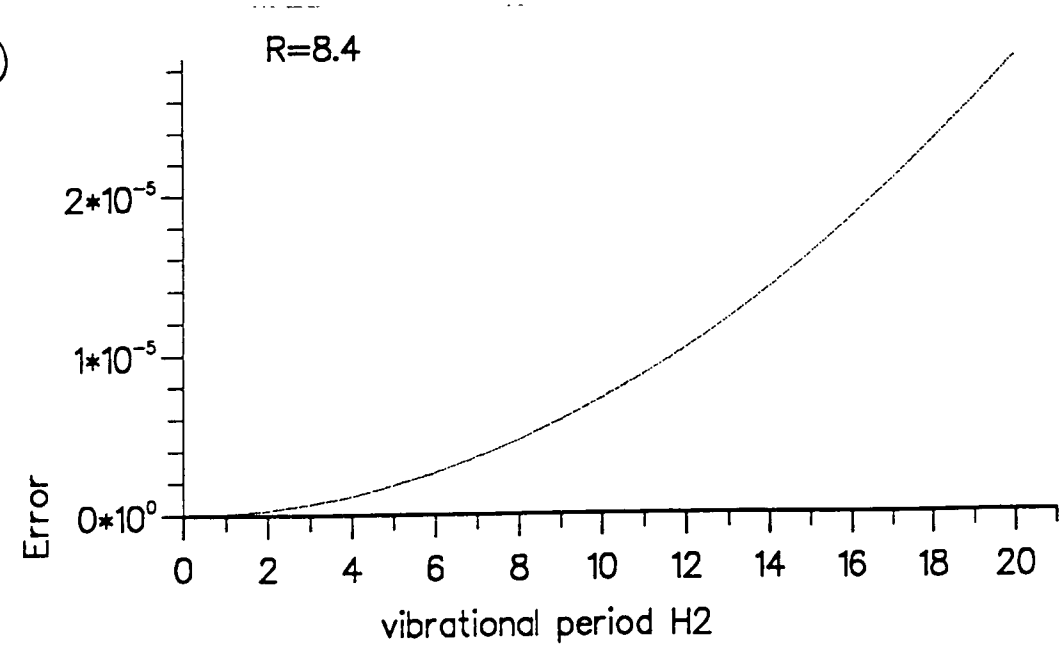
R=8.4
2*10^-5
1*10^-5
0*10^0
Error
0
2
4
6
8
10
12
14
16
18
20
vibrational period H2

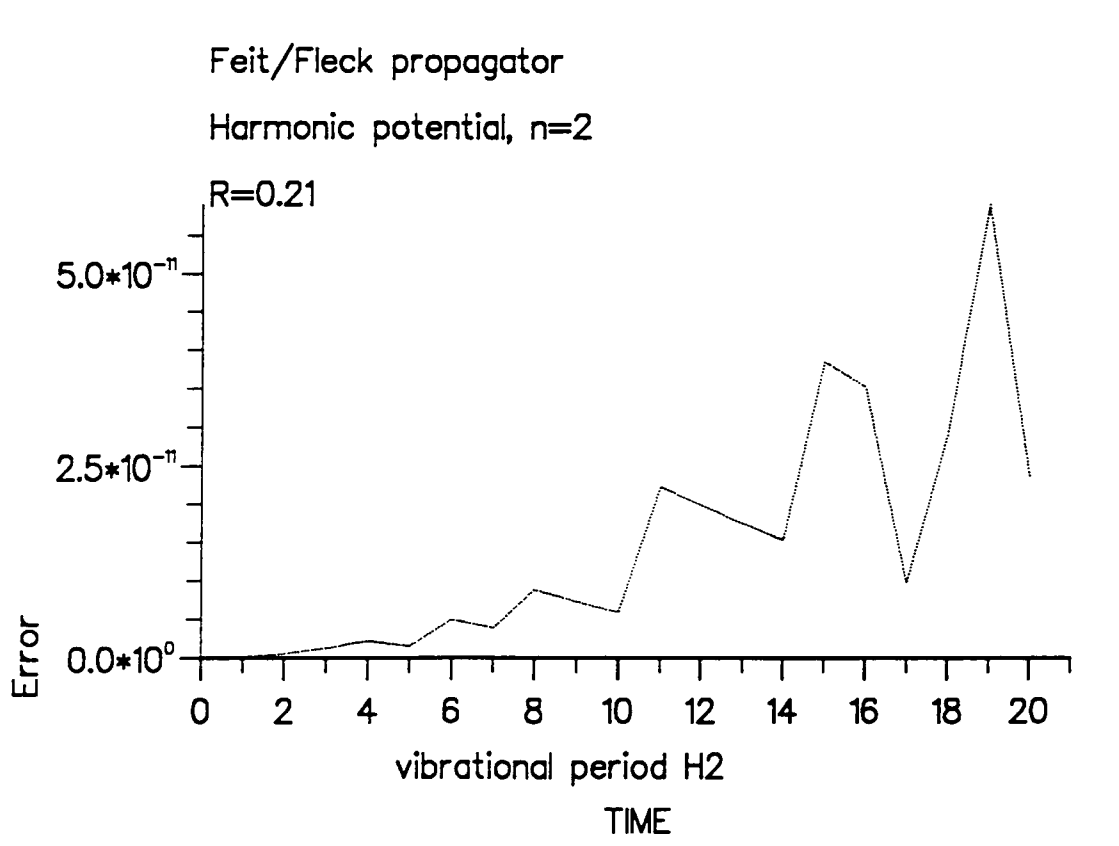

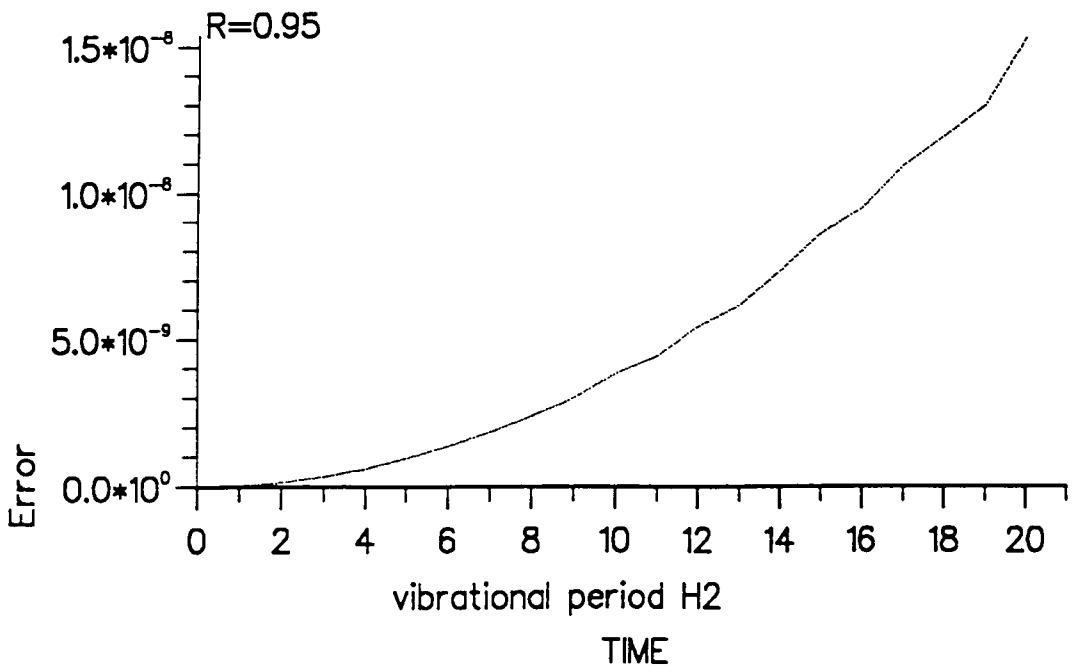

Fig. 4. Graphs of error against time for the Feit/Fleck propagator, for $n = 2$.

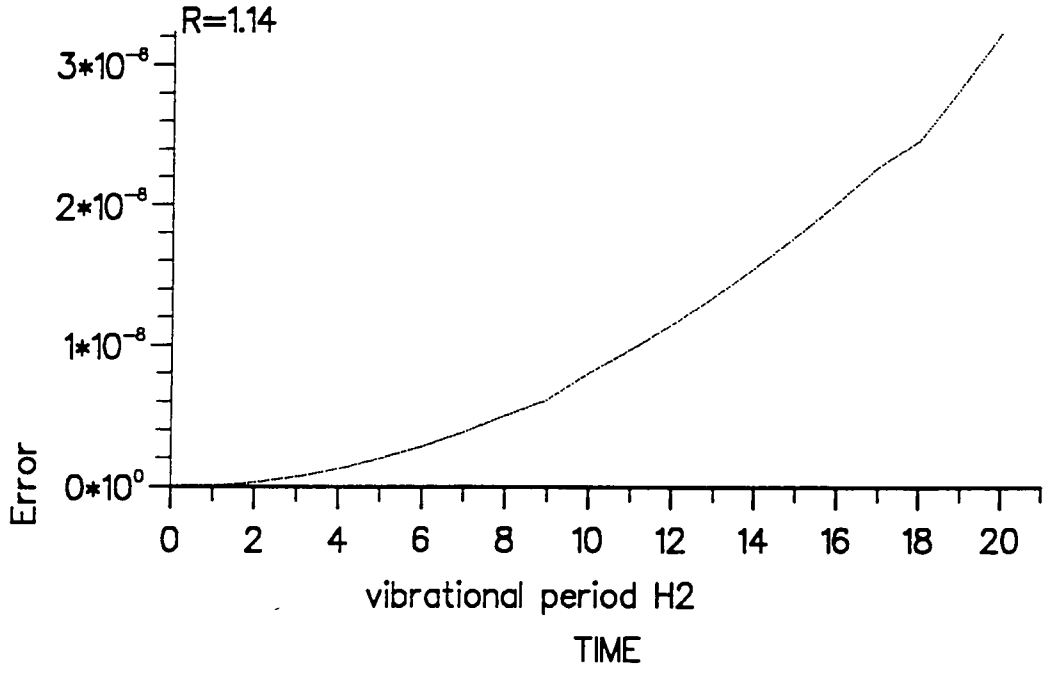
R=1.14
3*10⁻⁸
2*10⁻⁸
1*10⁻⁸
0*10⁰
Error
0 2 4 6 8 10 12 14 16 18 20
vibrational period H2
TIME

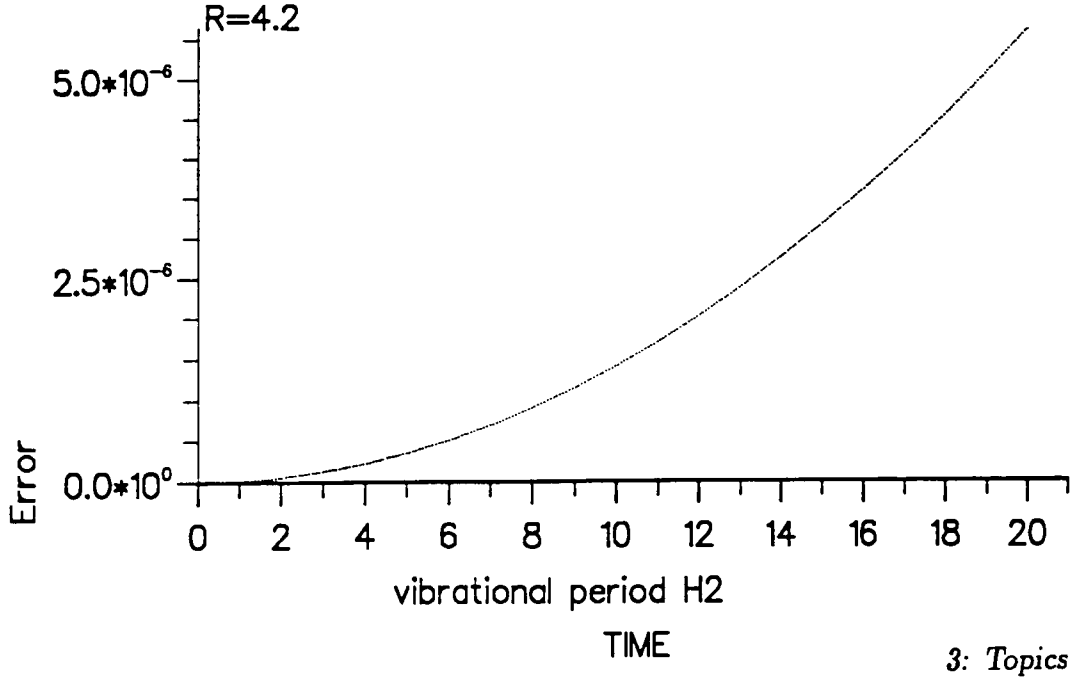
R=4.2
5.0*10⁻⁶
2.5*10⁻⁶
0.0*10⁰
Error
0 2 4 6 8 10 12 14 16 18 20
vibrational period H2
TIME

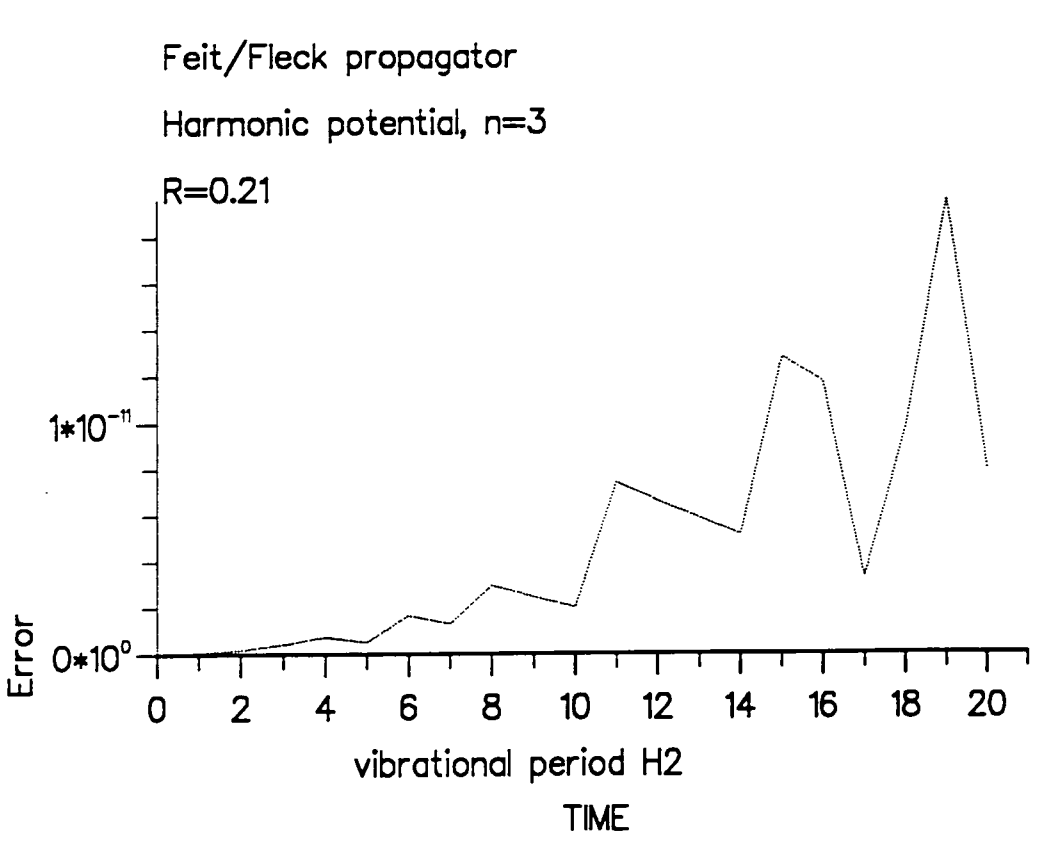

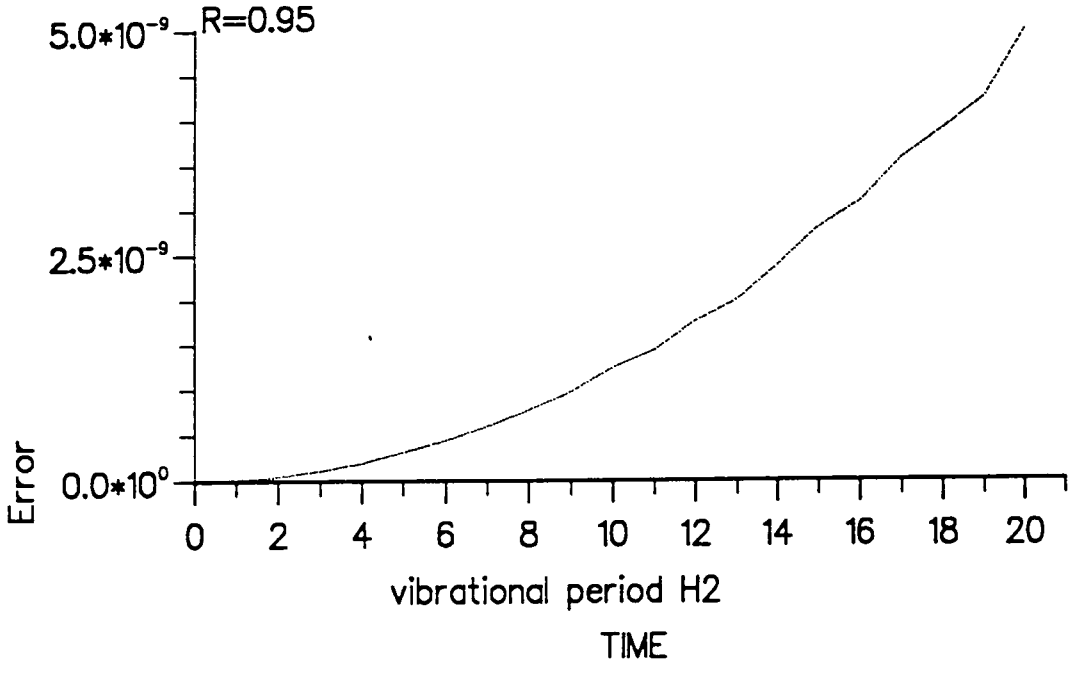

Fig. 5. Graphs of error against time for the Feit/Fleck propagator, for $n = 3$.

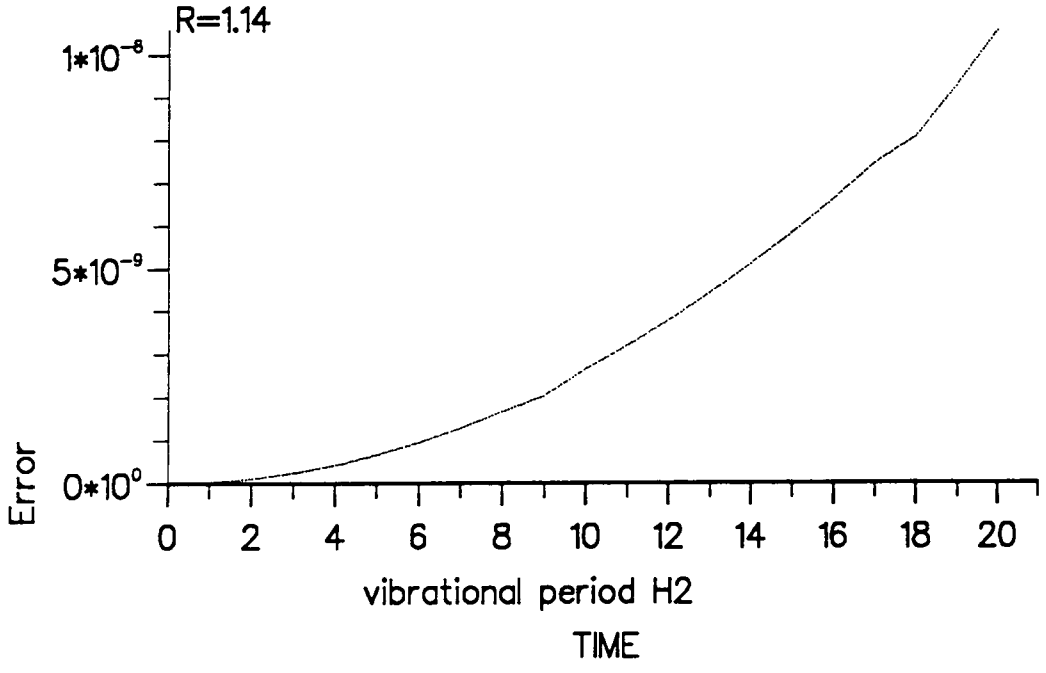
R=1.14
1*10⁻⁸
5*10⁻⁹
0*10⁰
Error
0 2 4 6 8 10 12 14 16 18 20
vibrational period H2
TIME

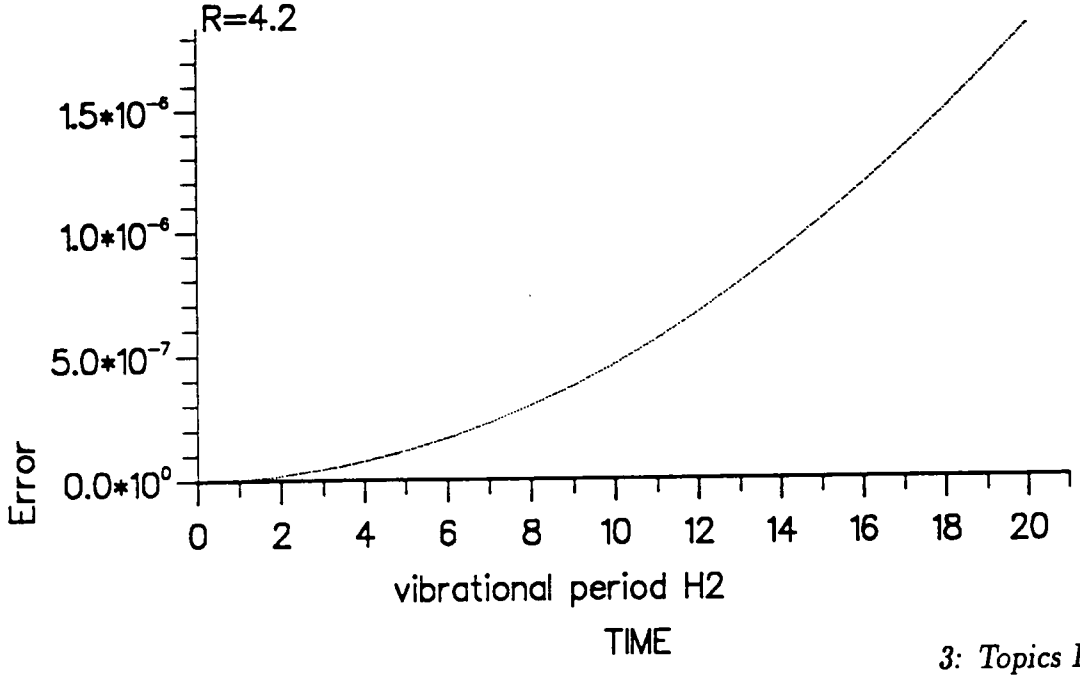
R=4.2
1.5*10⁻⁶
1.0*10⁻⁶
5.0*10⁻⁷
0.0*10⁰
Error
0 2 4 6 8 10 12 14 16 18 20
vibrational period H2
TIME

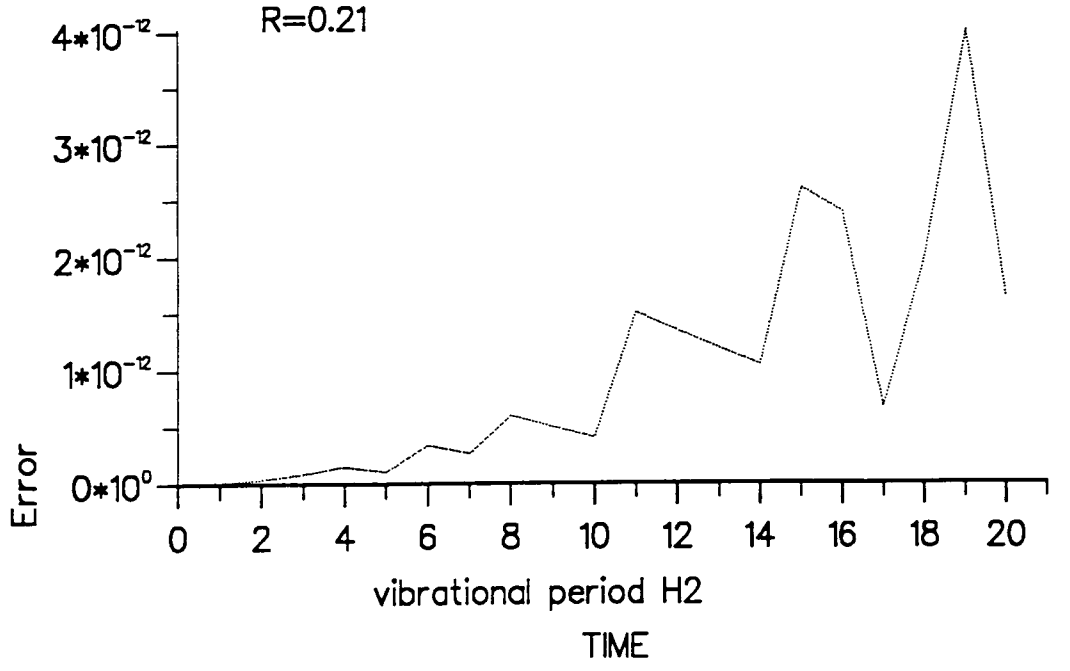

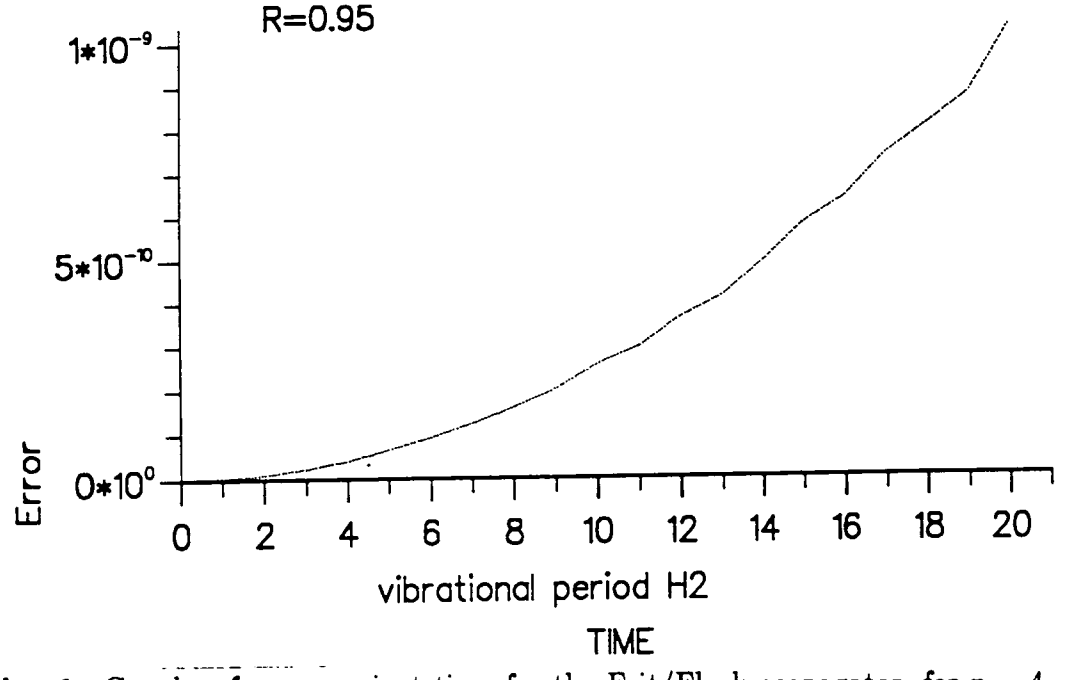

Fig. 6. Graphs of error against time for the Feit/Fleck propagator, for $n = 4$.

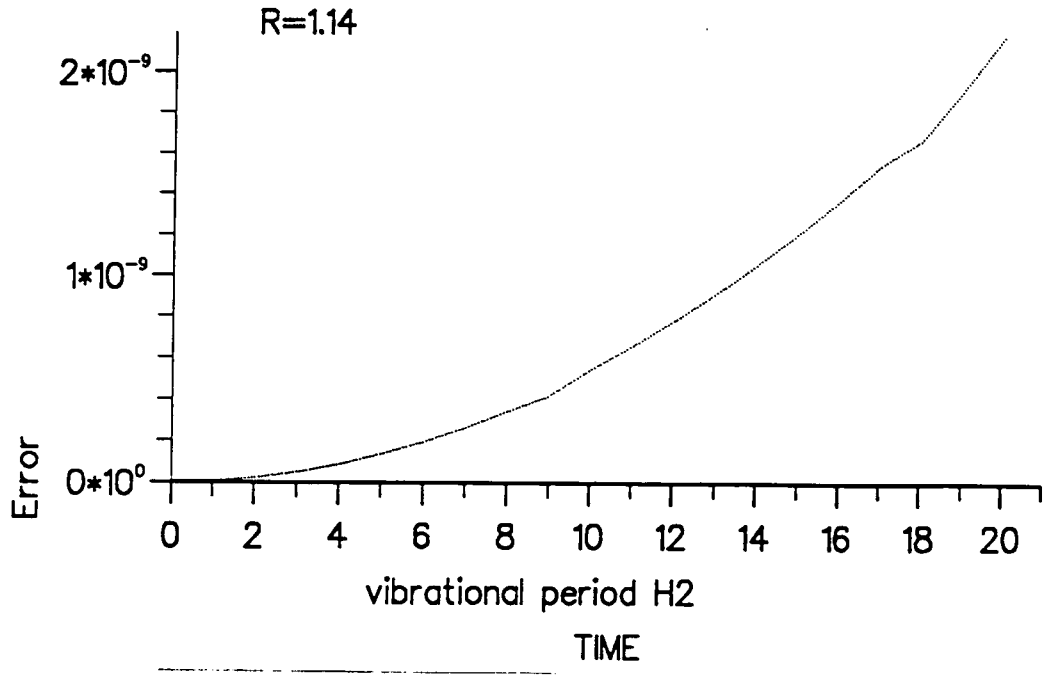
R=1.14
2*10^-9
1*10^-9
0*10^0
Error
0 2 4 6 8 10 12 14 16 18 20
vibrational period H2
TIME

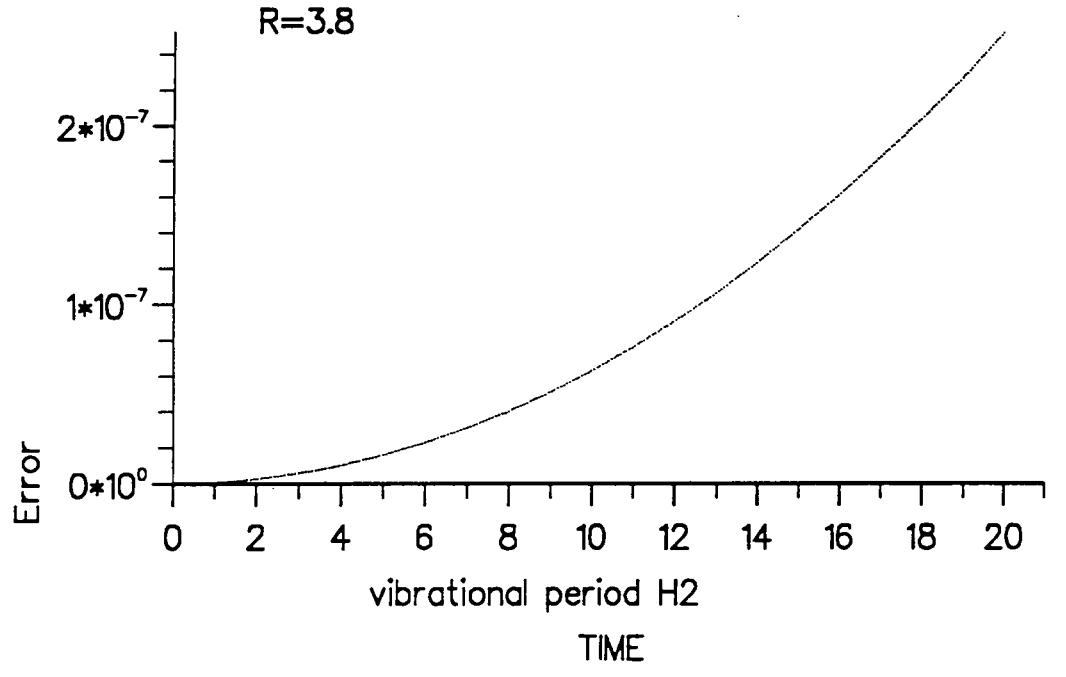
R=3.8
2*10^-7
1*10^-7
0*10^0
Error
0 2 4 6 8 10 12 14 16 18 20
vibrational period H2
TIME

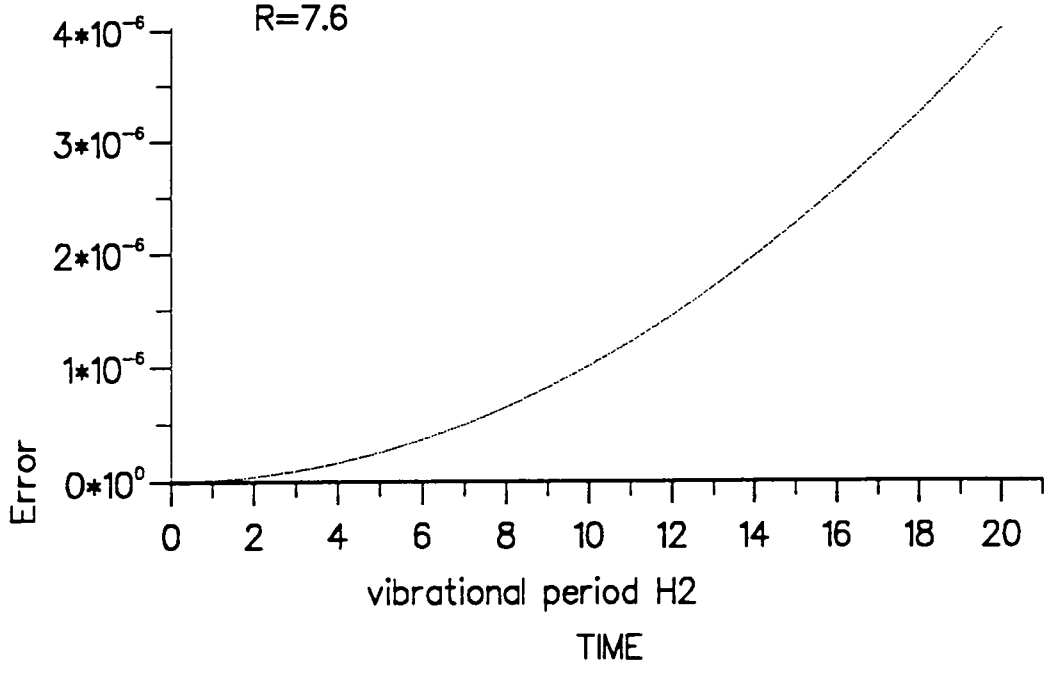
R=7.6
4*10^-6
3*10^-6
2*10^-6
1*10^-6
0*10^0
Error
0 2 4 6 8 10 12 14 16 18 20
vibrational period H2
TIME

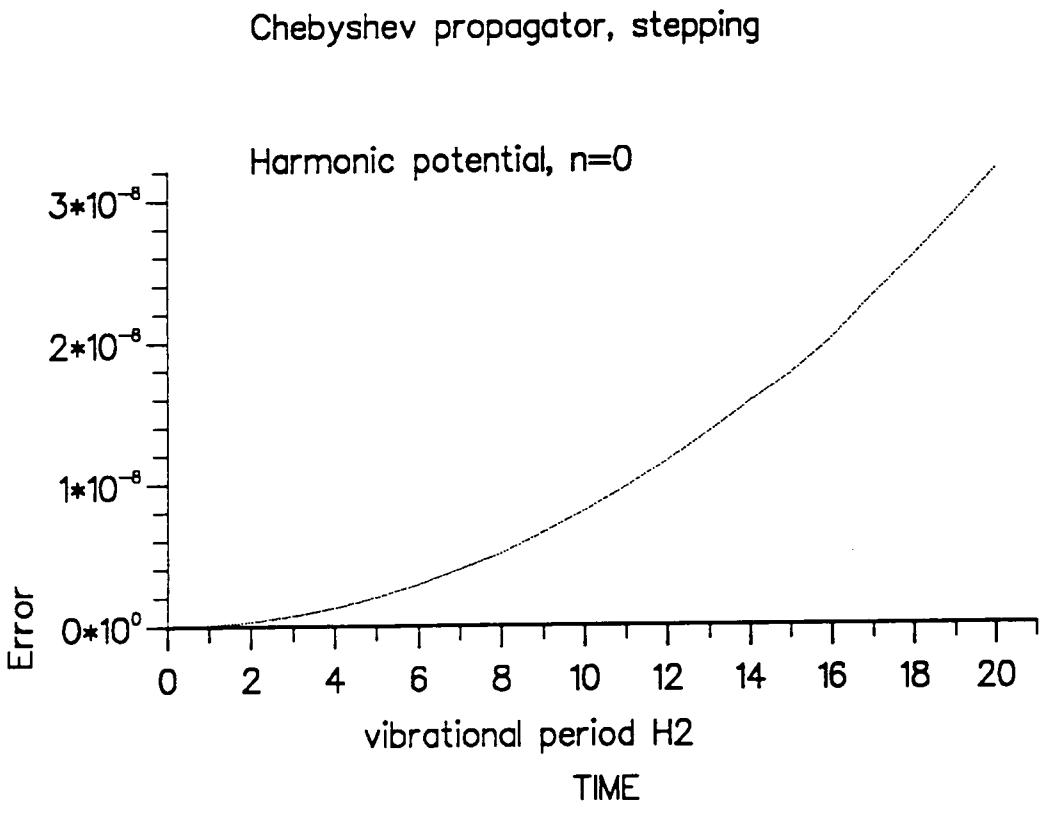

Fig. 7. Graphs of error against time for the Chebyshev stepping propagator, $n = 0$.

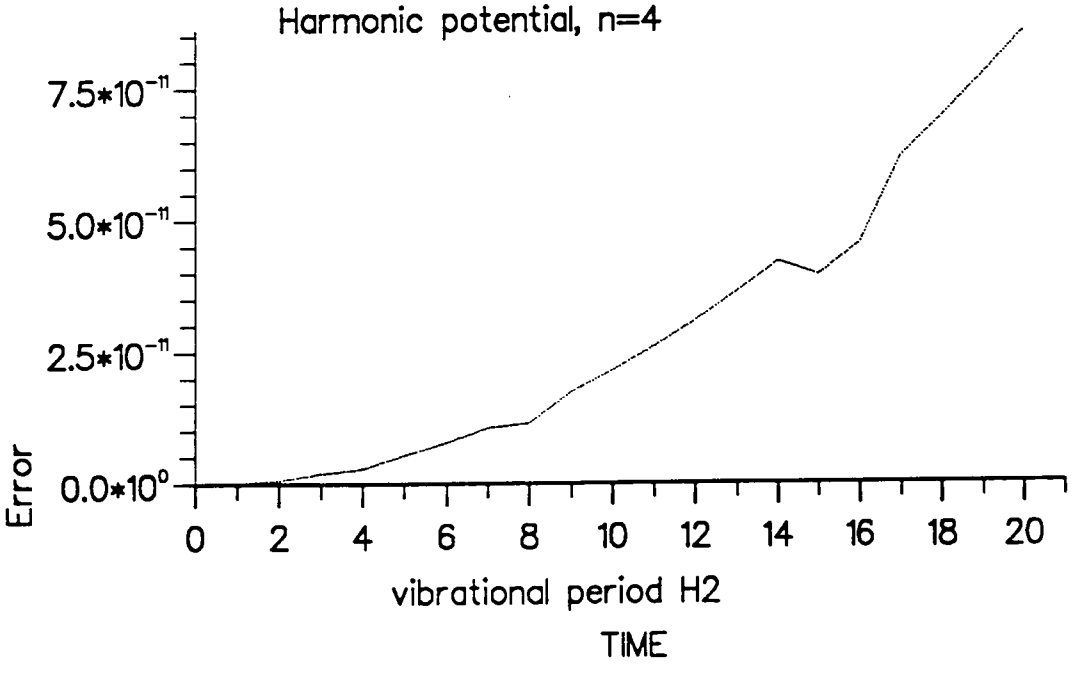

Fig. 8. Graphs of error against time for the Chebyshev stepping propagator, $n = 4$.

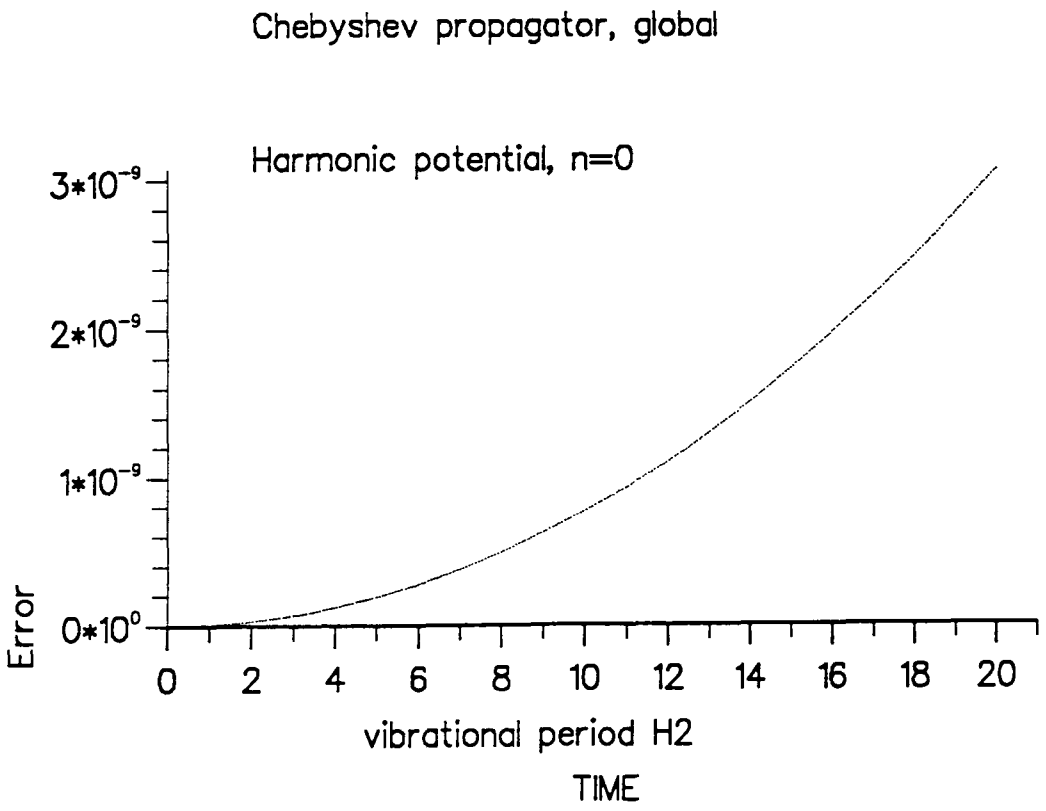

Fig. 9. Graphs of error against time for the Chebyshev global propagator, $n = 0$.

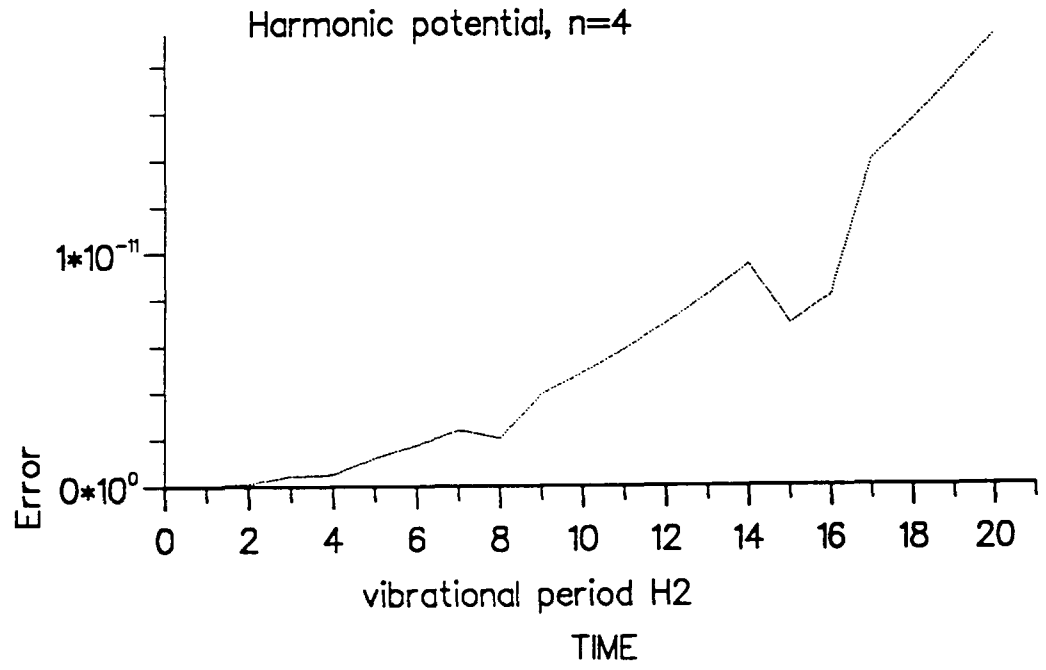

Fig. 10. Graphs of error against time for the Chebyshev global propagator, $n = 4$.

3.2 Imaginary Potentials

The optimal magnitude and functional form of imaginary potentials, required for use as absorbing boundaries, were investigated. Also, the stability of the various propagators with non-Hermitian Hamiltonians was investigated.

3.2. 1 Method

In order to investigate the use of imaginary potentials a moving Gaussian was set up on a grid with a potential barrier. The motion of the wavepacket after contact with the barrier, as it approached the edge of the grid, was monitored.

A square potential barrier was used. The barrier height was 2×10^4 cm^{-1} (9.13×10^{-2} E_h) and its width was five grid points on a grid of 64 points. The barrier started at grid point number 40.

The initial wavefunction was a moving Gaussian, i.e. it was of the form:

$$\Psi(x,0) = e^{-ikx} e^{\alpha^2 (x-a)^2/2}, \tag{104}$$

where a determines the initial position of the Gaussian (at approximately grid point 12) and α determines its width (the values for H_2, given earlier in this chapter, were used for these two parameters). The wave vector k determines the speed with which the Gaussian moves. A value for k must be chosen which can be represented on a grid with the spacing $\Delta x = 0.0625$ Å; in this case a value of -10.5 a.u. was used.

The transmitted probability of the wavepacket through the square potential barrier, or total flux, was obtained from the flux $j(x,t)$ at a particular point $x = x_f$ [82]. The point x_f must be beyond the potential barrier, but not too near the boundary; in this case it is at grid point number 48. The flux is given by:

$$j(x_f,t) = \frac{1}{2m} \left(\Psi^* \frac{d\Psi}{dx} - \Psi \frac{d\Psi^*}{dx} \right)_{x=x_f}. \tag{105}$$

This flux was integrated over time to give the total flux. If there is no absorbing potential at the boundary, then the total flux will initially increase as the wavepacket passes through the potential barrier, but will then decrease as the wavepacket is reflected back by the boundary. However, if there is a suitable absorbing boundary then the total flux will reach a maximum value and will then remain constant.

The magnitude of the imaginary potential required and the best functional form were investigated using the Feit/Fleck propagator which is stable for non-Hermitian Hamiltonians. The magnitude of the potential was varied within the range:

$$V_1 < |V_{IB}| < V_2, \tag{106}$$

where V_1 and V_2 were defined in the last chapter in equation (83). The value for $|V_{IB}|$ is given by:

$$|V_{IB}| = V_1 + M_V(V_2 - V_1), \tag{107}$$

so that the parameter M_V is altered in order to vary the magnitude of the imaginary potential. Several different functional forms for the imaginary potential were investigated, e.g. with linear or with exponential terms. These were described in Chapter 2 in equations (84), (85) and (86).

In these examples the absorbing potential was applied over approximately 10% of the grid so that R_{abs}, from equations (84), (85) and (86), is at grid point number 58. The value of α in the exponential form of the imaginary potential was set to 1/2. The total propagation time was 20τ, where τ was defined earlier in this chapter; for the short-time propagators the value of R used was approximately 0.25.

3.2. 2 Results

The optimal magnitude and form of the imaginary potential

The results of the calculations for the different magnitudes and forms of the imaginary potential are shown in figures 11 → 12.

It can be seen from these figures that the imaginary potential should be slightly above the bottom of the range, $M_V \approx 0.03$, to get full absorption. Even potentials well above the range do not cause significant reflection from the potential itself (see figures $11d, 12d, 12h$). There is very little difference between the various functional forms, that is the linear and the exponential (both the inverse squared and non-squared hyperbolic cosine forms), since they both appear to need the same magnitude of imaginary potential to be effective. (Note that in the figures, the potentials with the exponential terms are referred to as the exponential and the squared exponential for the inverse hyperbolic cosine and inverse squared hyperbolic cosine forms respectively.)

It has been suggested by Child [83] that the strengths of the inequalities in equation (83) are such that M_V would need only to be very small to achieve complete absorption. This agrees well with the result obtained here. However, it also implies that the value of M_V should perhaps have been varied by much smaller amounts to investigate properly the magnitude of imaginary potential required for full absorption.

It has been reported by Neuhauser and Baer [82] that the linear form of the imaginary potential is more efficient than the other forms used here. It has also been reported [84] [85] that the form of the potential can be an extremely important factor in determining the efficiency of an absorbing potential. This is not what has been found here. The reason

for this could be that the magnitude of the imaginary potential was varied too rapidly to see the effect that the form can have on the efficiency of absorption.

The effect of an imaginary potential on the propagators

Consider first the S.O.D. propagator (see figures $13a \rightarrow d$). For very small values of M_V the propagation is stable but for for $M_V > 0.02$ this is no longer true. It was found that as the time of the propagation increased the instability worsened (see figure $13c$). For the S.O.D., in general, if the timestep is reduced, and the number of propagation steps increased to compensate, the error is reduced. Thus here the propagation was done with the timestep halved and N_T doubled. The results were effectively the same. This means that the instability introduced by the imaginary potential is linear in the timestep, and in the number of timesteps. The above makes it difficult to see how this propagator could be used effectively in real problems, when an imaginary potential is used.

Now consider the Chebyshev propagator. (Note that the imaginary potential has to be included in the shifting and scaling necessary in the use of the Chebyshev propagation scheme.) First, consider this propagator when it is used in its truly global sense (see figures $14a, b$). Effectively, the propagation is completely unstable. This is because the polynomial expansion in the Chebyshev polynomials is only stable while the imaginary part of the eigenvalues is kept very small. However, in a global calculation of this type the eigenvalues are continually becoming more and more complex in nature. Second, consider the Chebyshev stepping propagator (see figures $15a \rightarrow f$). Even for quite large values of the imaginary potential the propagation is stable, though for M_V very large the propagation scheme does break down (see figure $15e$). This need not be of concern since the absorbing boundary is effective for quite small values of M_V. However, in this case if the timestep was doubled then the propagation became unstable for quite small values of M_V (see figure $15f$). There exists a complex relationship therefore between the length of each timestep and the amount of imaginary potential which can be allowed without causing instability. This relationship was investigated but no clear pattern was found. This probably is not of great concern since the effect is obvious when it does occur, and should not therefore produce uncertainties in the results of a propagation.

There is very little, if any, warning in the literature about the instability of many of the propagators when an imaginary potential is included in the Hamiltonian.

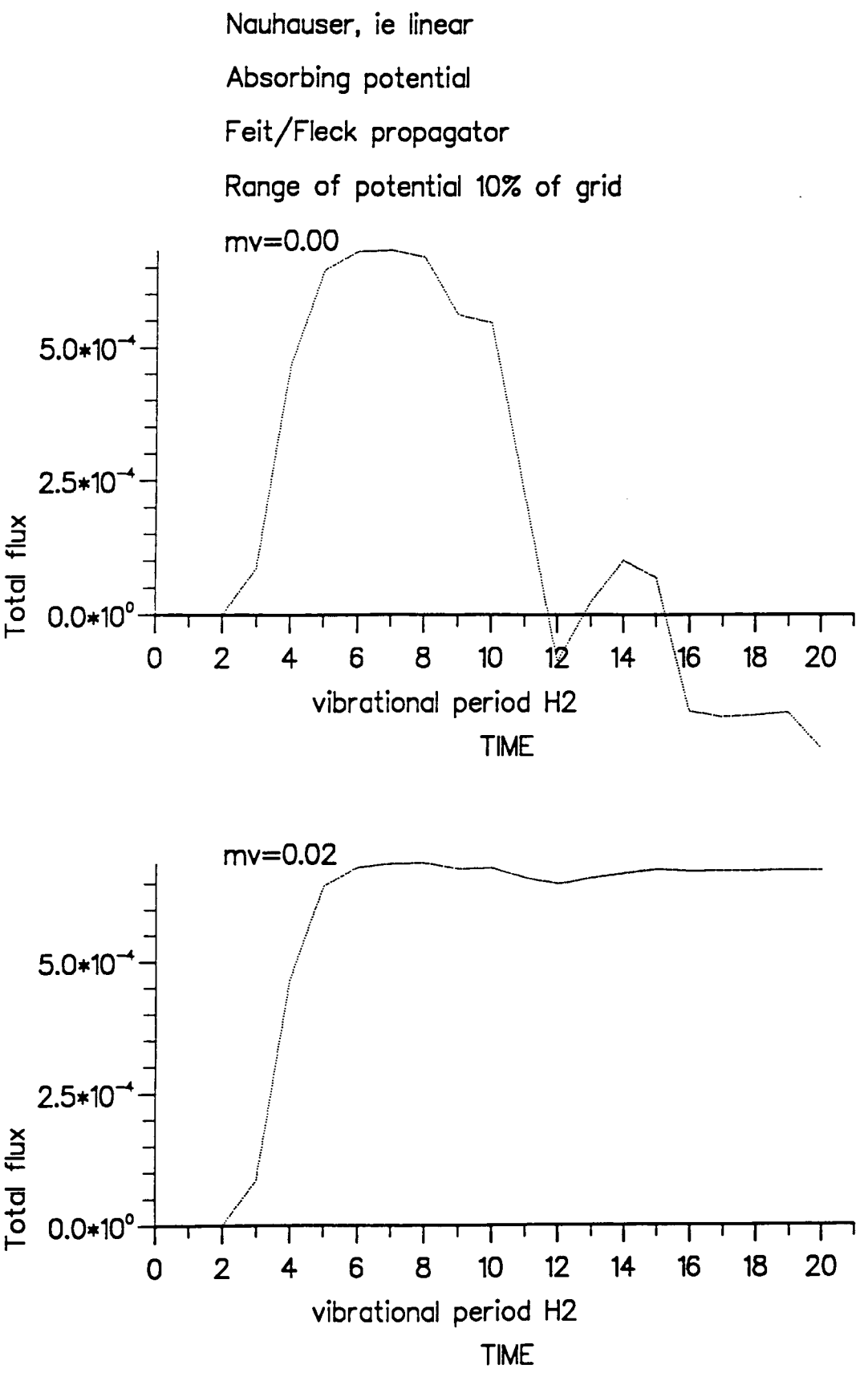

Fig. 11. Graphs of total flux against time for the linear form of the absorbing potential over 10% of the grid, using the Feit/Fleck propagator.

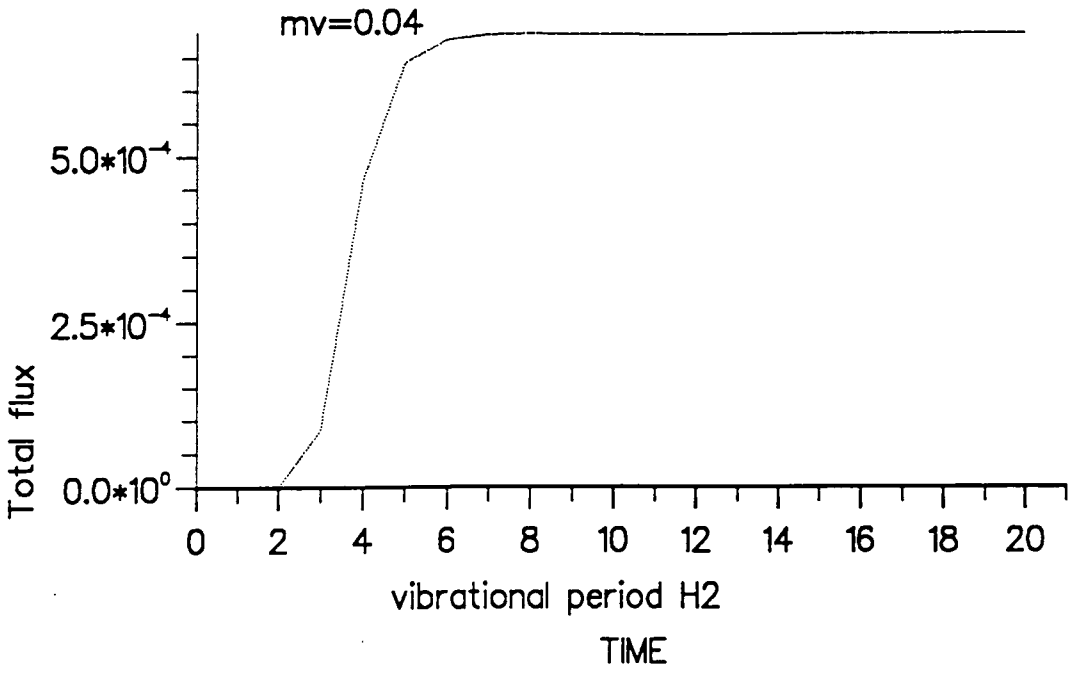
mv=0.04
5.0*10⁻⁴
2.5*10⁻⁴
0.0*10⁰
Total flux
0 2 4 6 8 10 12 14 16 18 20
vibrational period H2
TIME

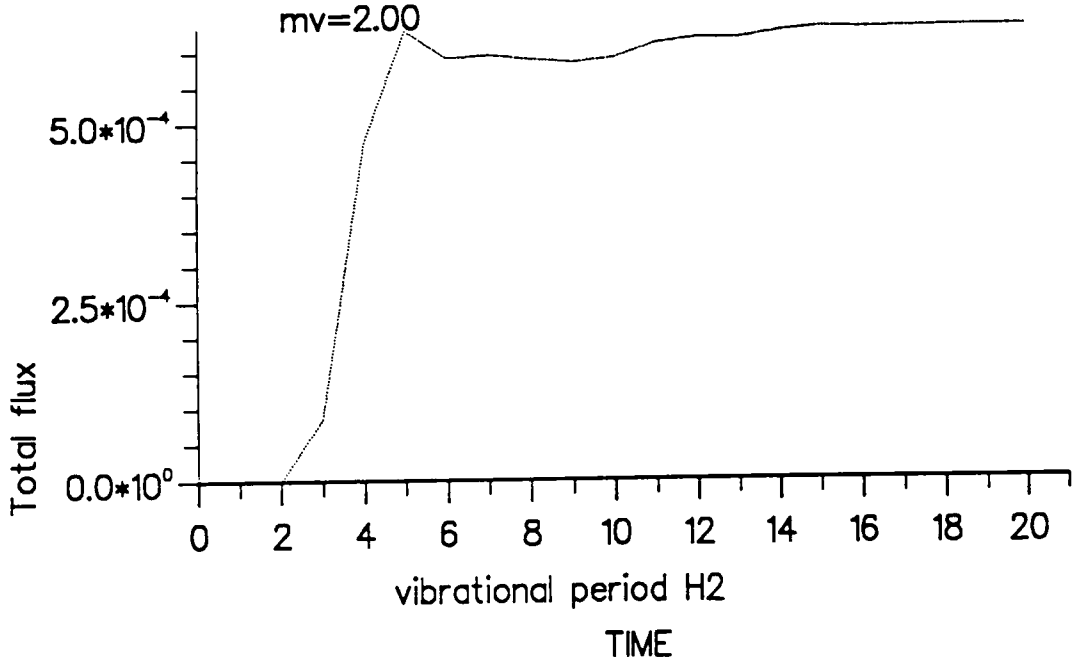
mv=2.00
5.0*10⁻⁴
2.5*10⁻⁴
0.0*10⁰
Total flux
0 2 4 6 8 10 12 14 16 18 20
vibrational period H2
TIME

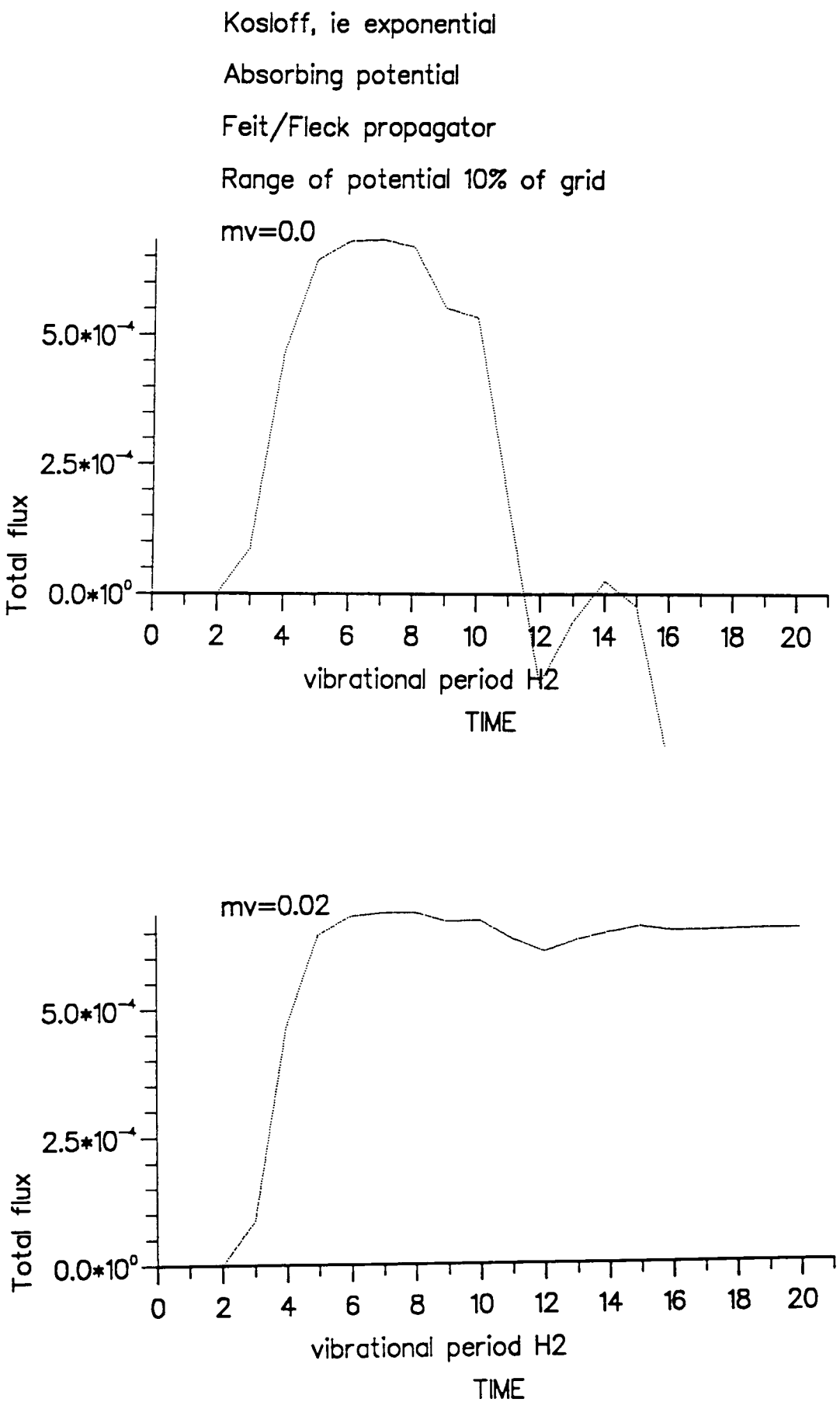

Fig. 12. Graphs of total flux against time for the exponential form of the absorbing potential over 10% of the grid, using the Feit/Fleck propagator.

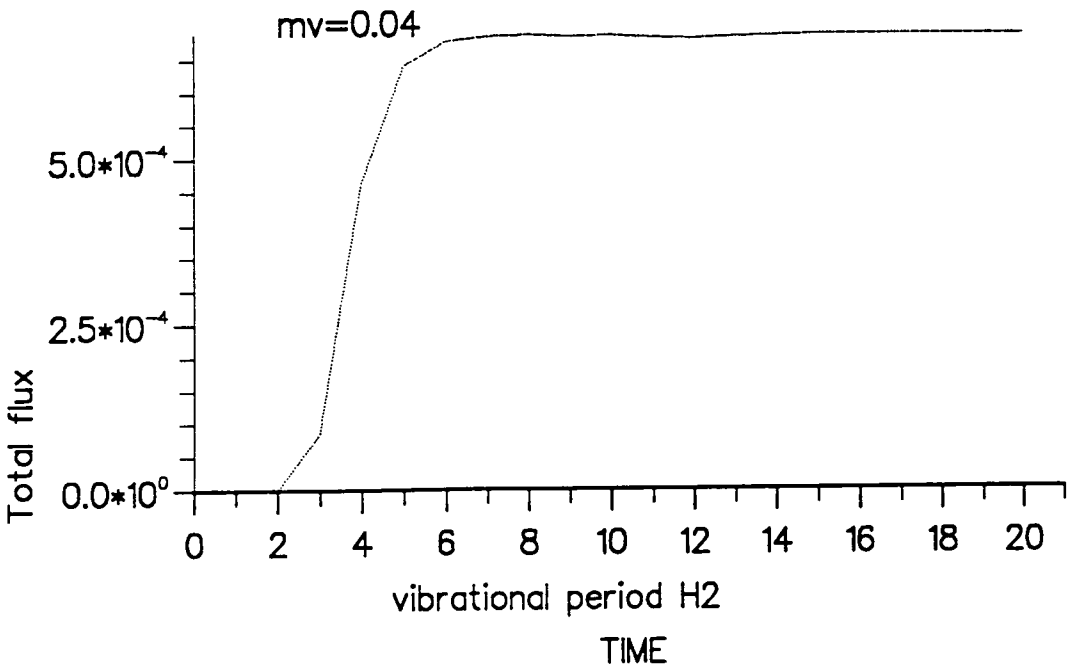
mv=0.04
5.0*10⁻⁴
2.5*10⁻⁴
0.0*10⁰
Total flux
0 2 4 6 8 10 12 14 16 18 20
vibrational period H2
TIME

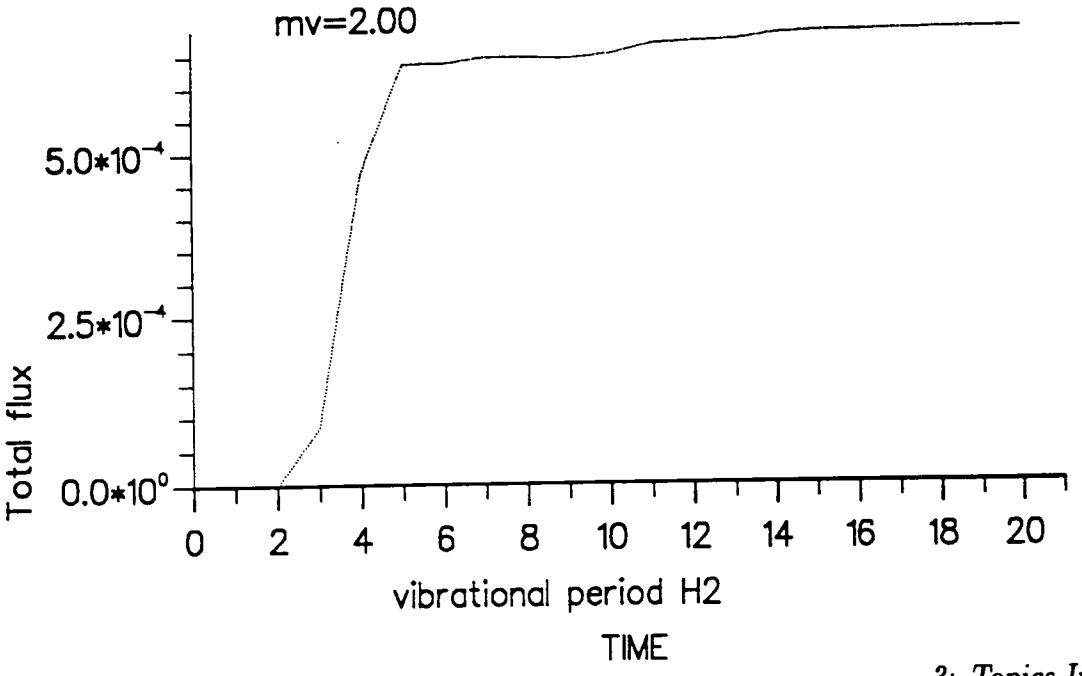
mv=2.00
5.0*10⁻⁴
2.5*10⁻⁴
0.0*10⁰
Total flux
0 2 4 6 8 10 12 14 16 18 20
vibrational period H2
TIME

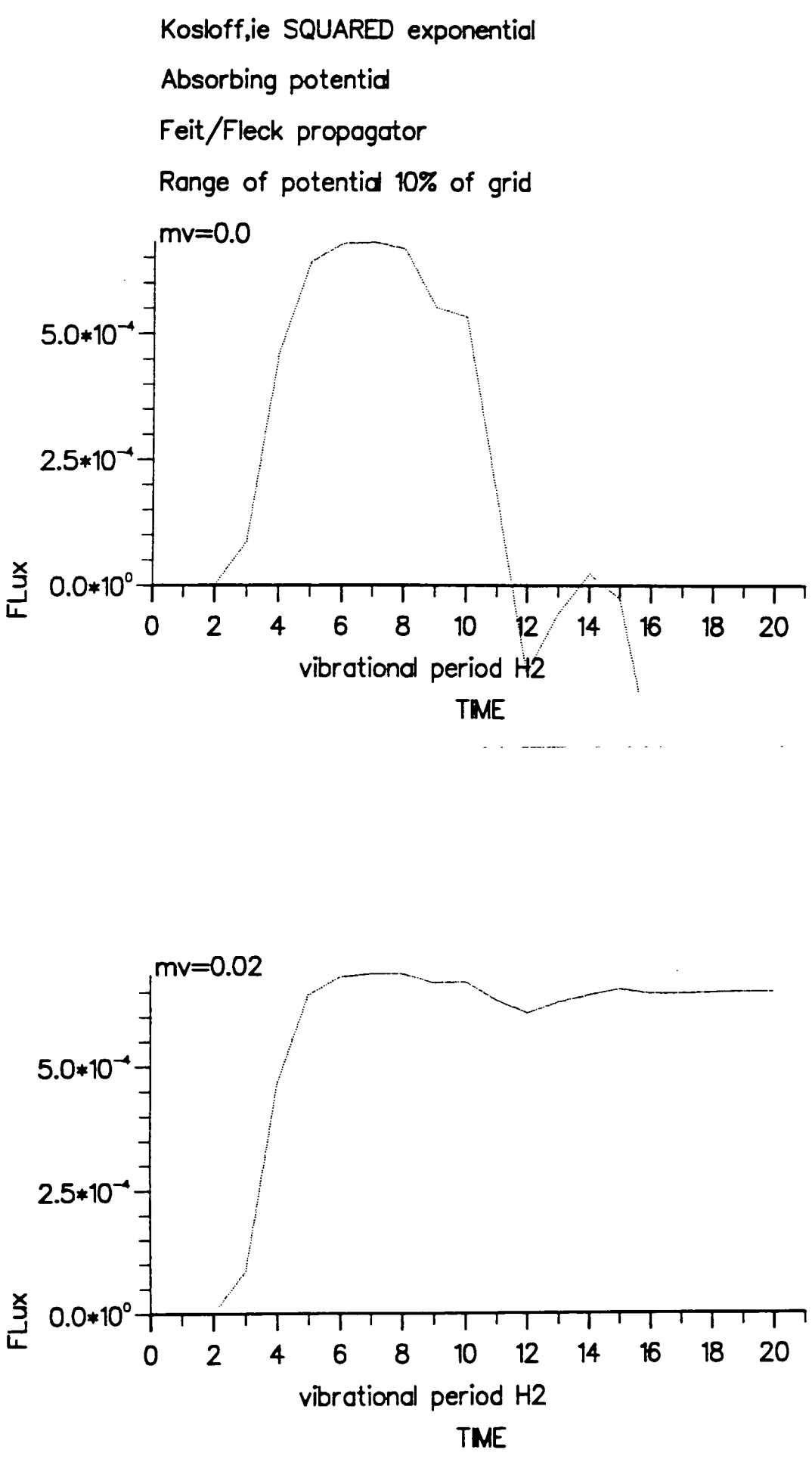

Graphs of total flux against time for the squared exponential form of the absorbing potential over 10% of the grid, using the Feit/Fleck propagator.

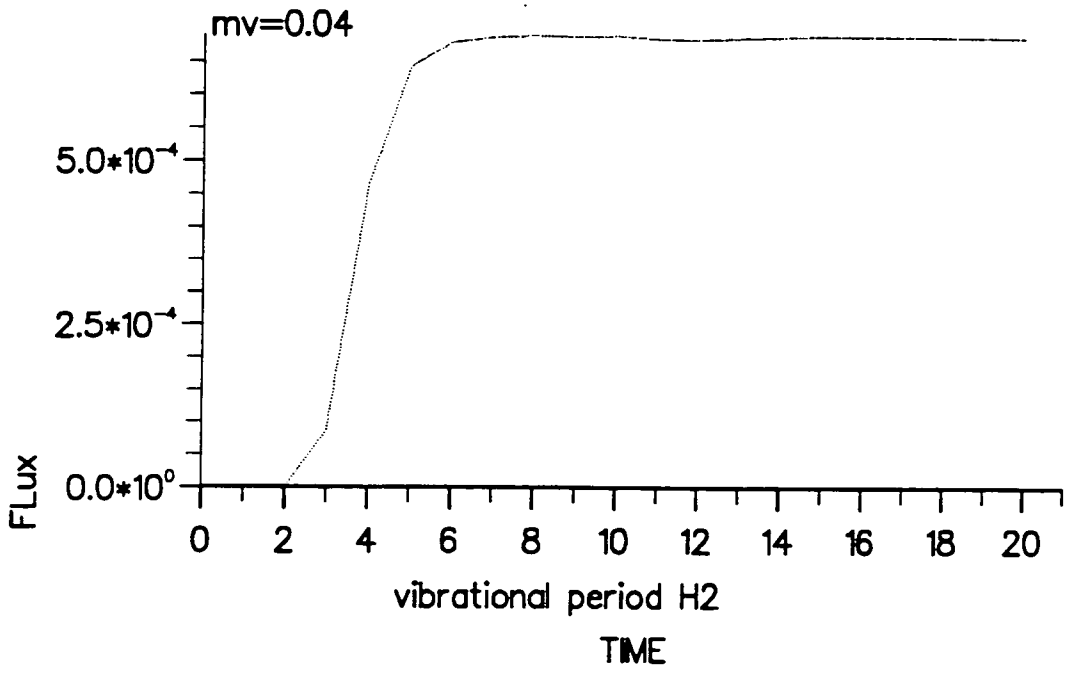
mv=0.04
5.0*10⁻⁴
2.5*10⁻⁴
0.0*10⁰
FLux
0 2 4 6 8 10 12 14 16 18 20
vibrational period H2
TIME

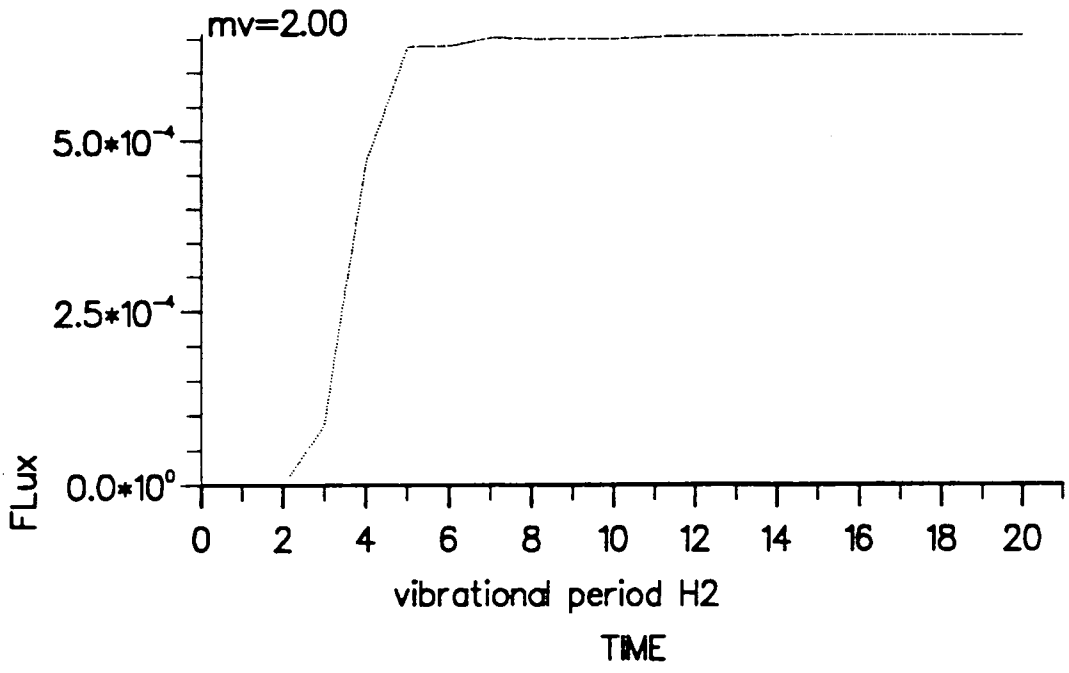
mv=2.00
5.0*10⁻⁴
2.5*10⁻⁴
0.0*10⁰
FLux
0 2 4 6 8 10 12 14 16 18 20
vibrational period H2
TIME

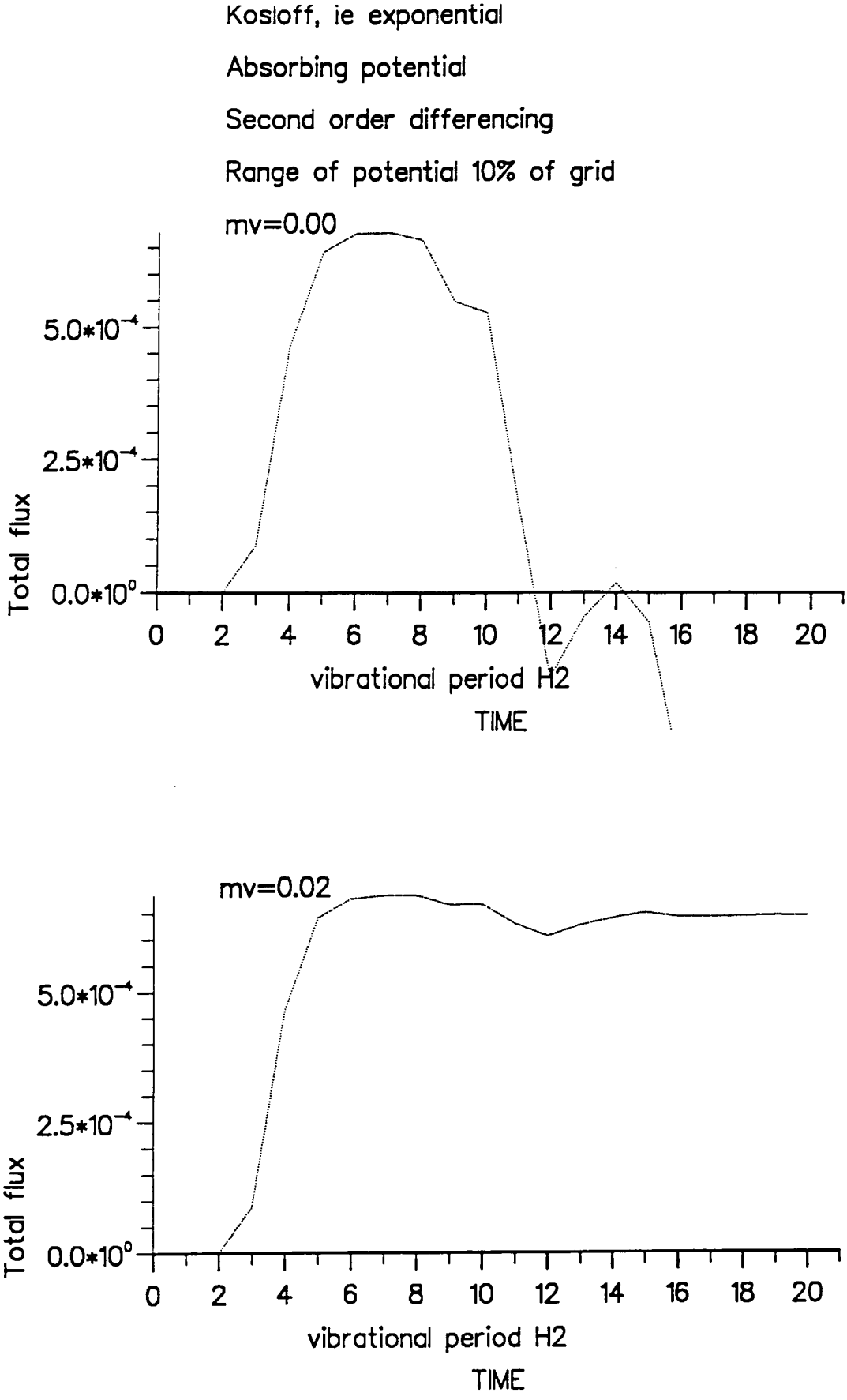

Fig. 13. Graphs of total flux against time for the exponential form of the absorbing potential over 10% of the grid, using the S.O.D. propagator.

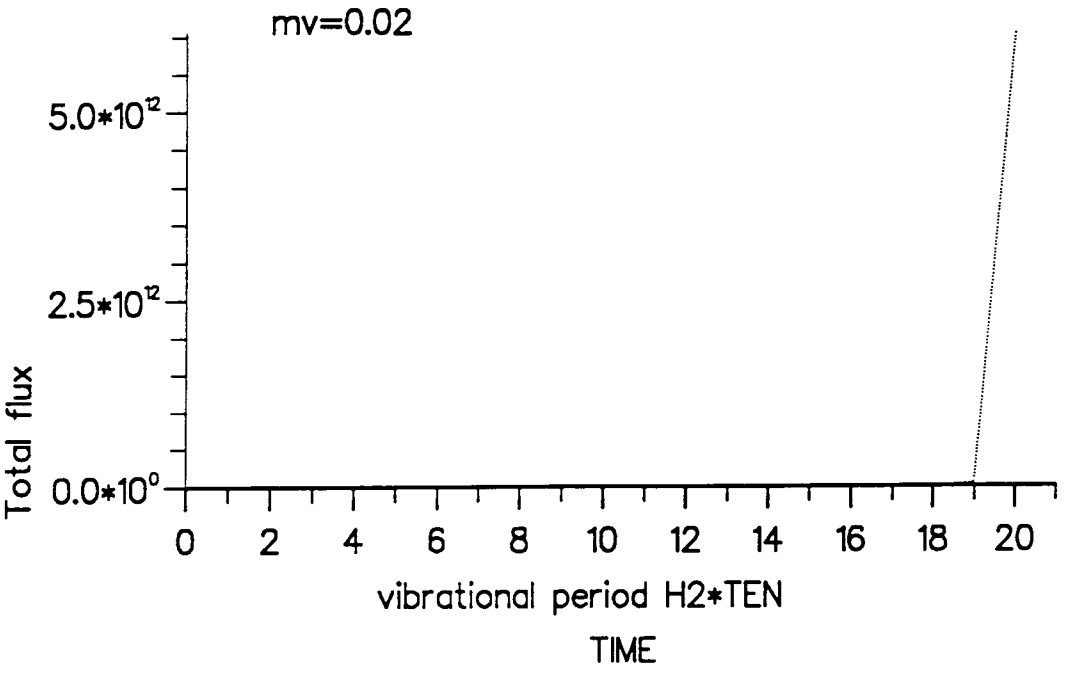
mv=0.02
5.0*10^12
2.5*10^12
0.0*10^0
Total flux
0 2 4 6 8 10 12 14 16 18 20
vibrational period H2*TEN
TIME

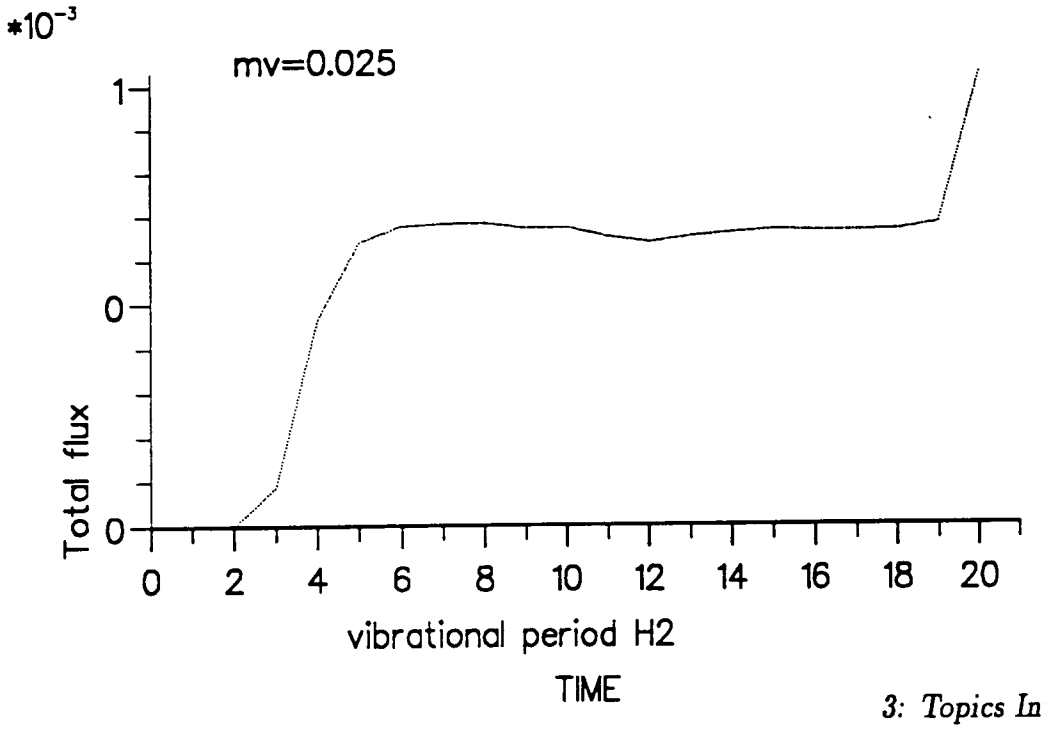
*10^-3
mv=0.025
1
0
0
Total flux
0 2 4 6 8 10 12 14 16 18 20
vibrational period H2
TIME

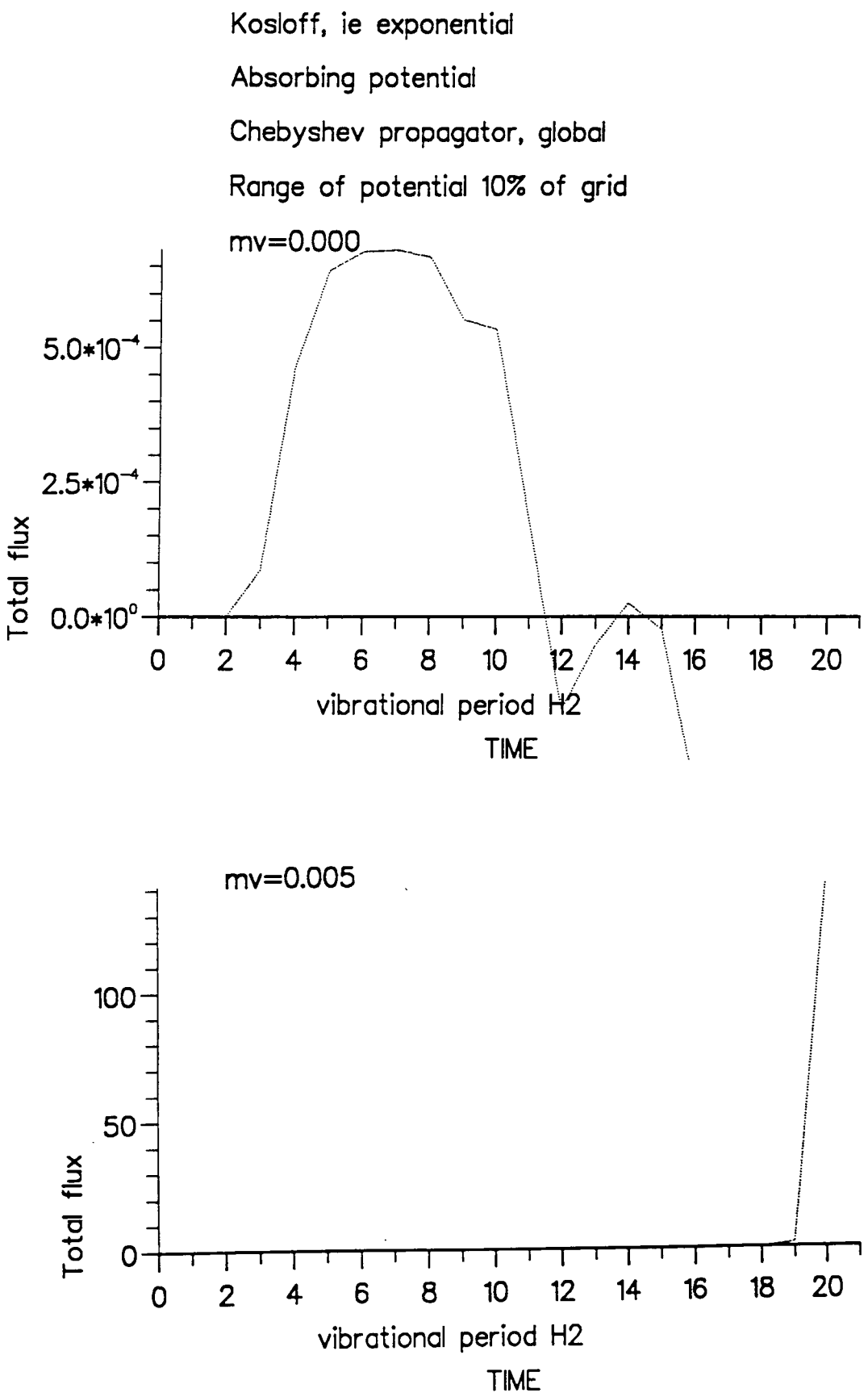

Fig. 14. Graphs of total flux against time for the exponential form of the absorbing potential over 10% of the grid, using the Chebyshev global propagator.

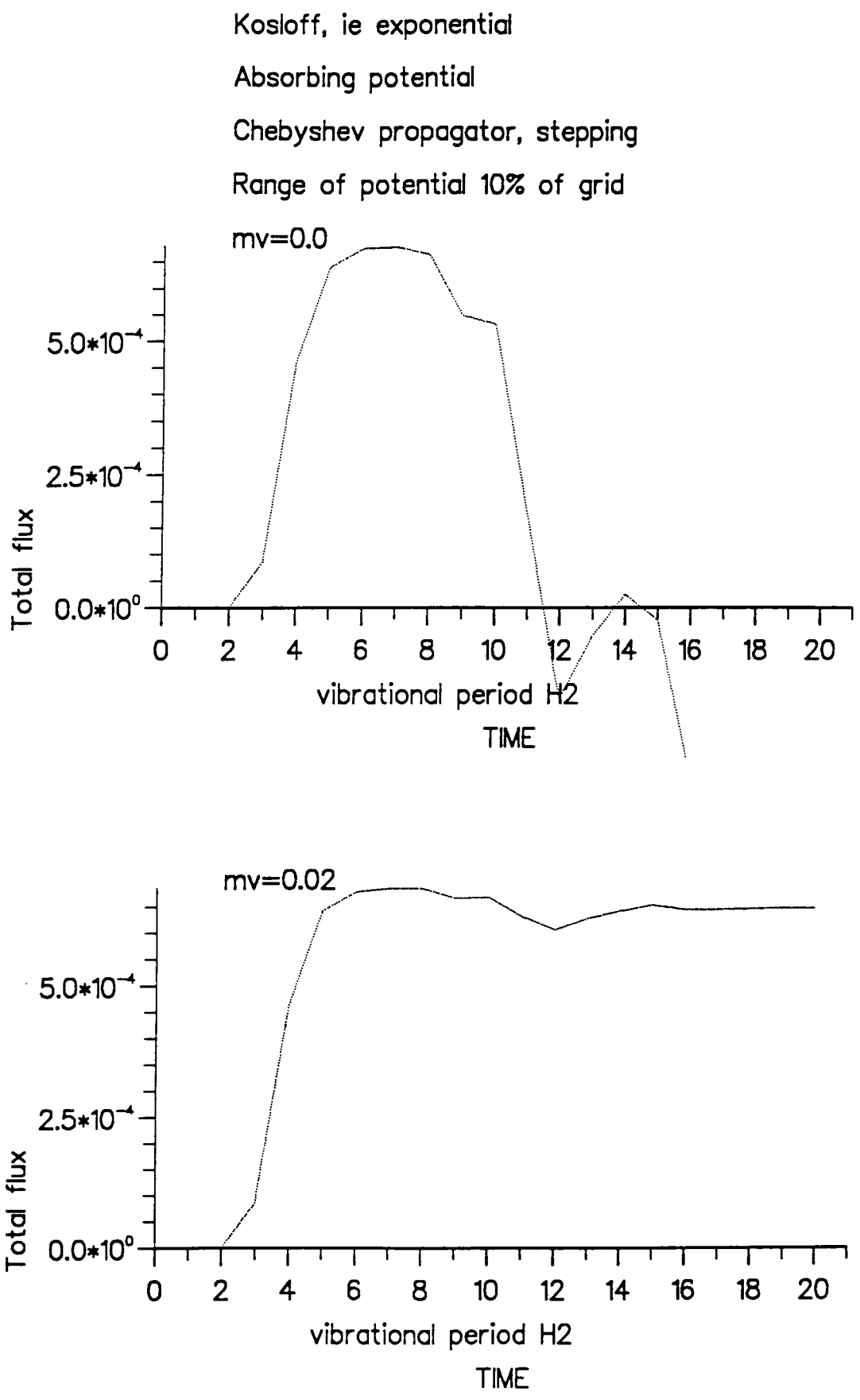

Fig. 15. Graphs of total flux against time for the exponential form of the absorbing potential over 10% of the grid, using the Chebyshev stepping propagator.

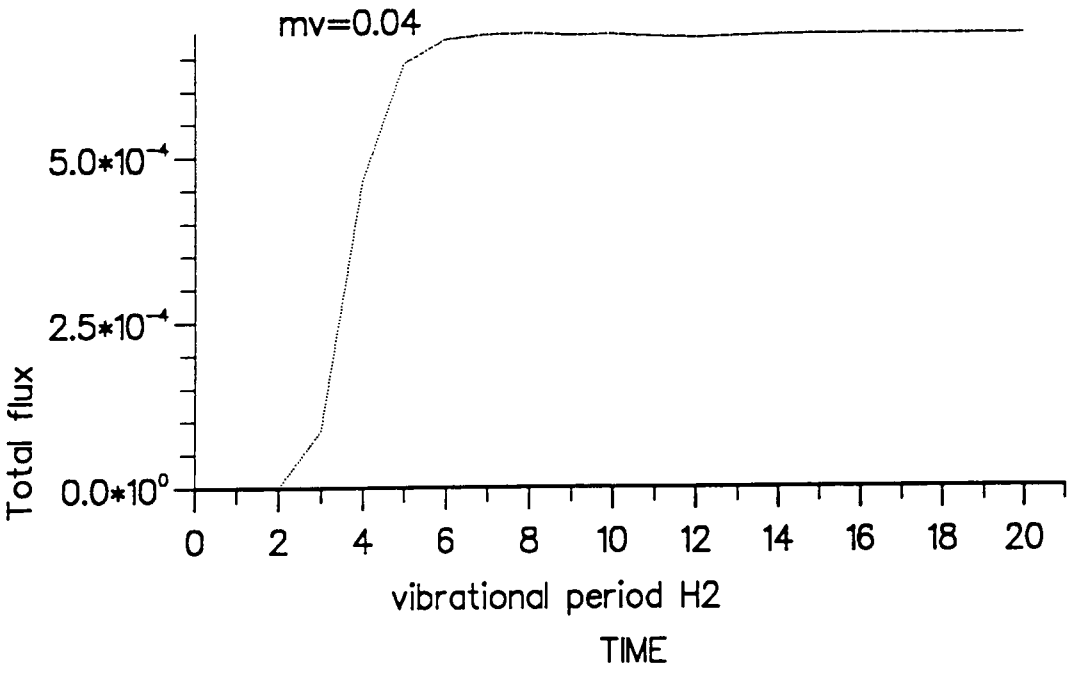
mv=0.04
5.0*10⁻⁴
2.5*10⁻⁴
0.0*10⁰
Total flux
0 2 4 6 8 10 12 14 16 18 20
vibrational period H2
TIME

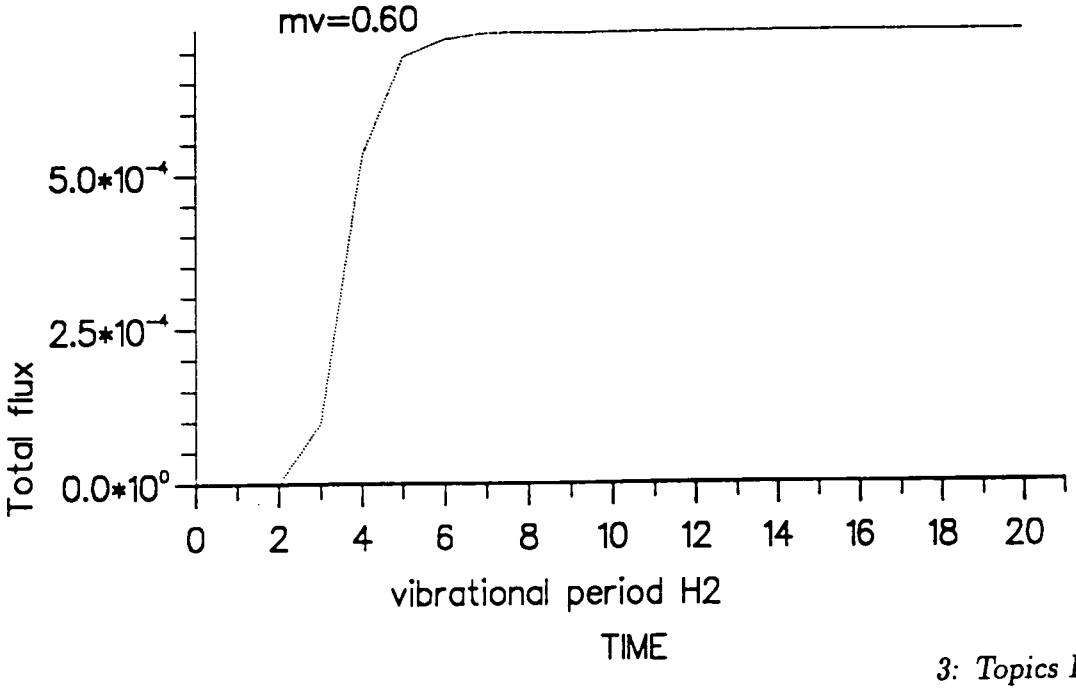
mv=0.60
5.0*10⁻⁴
2.5*10⁻⁴
0.0*10⁰
Total flux
0 2 4 6 8 10 12 14 16 18 20
vibrational period H2
TIME

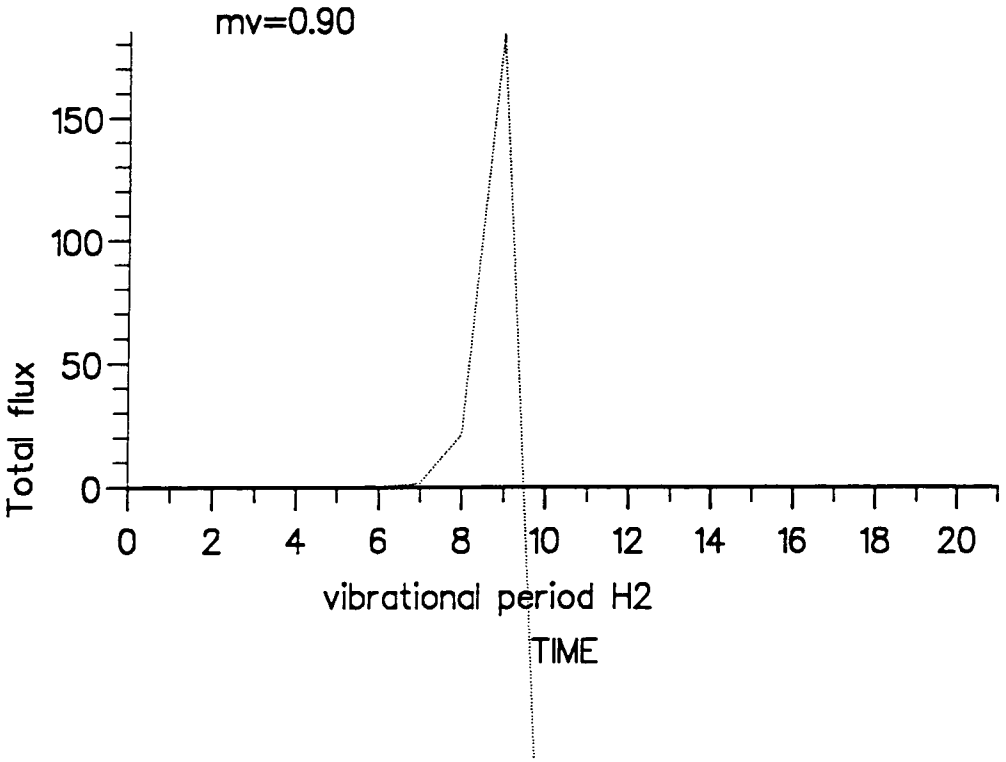
mv=0.90
150
100
50
0
Total flux
0 2 4 6 8 10 12 14 16 18 20
vibrational period H2
TIME

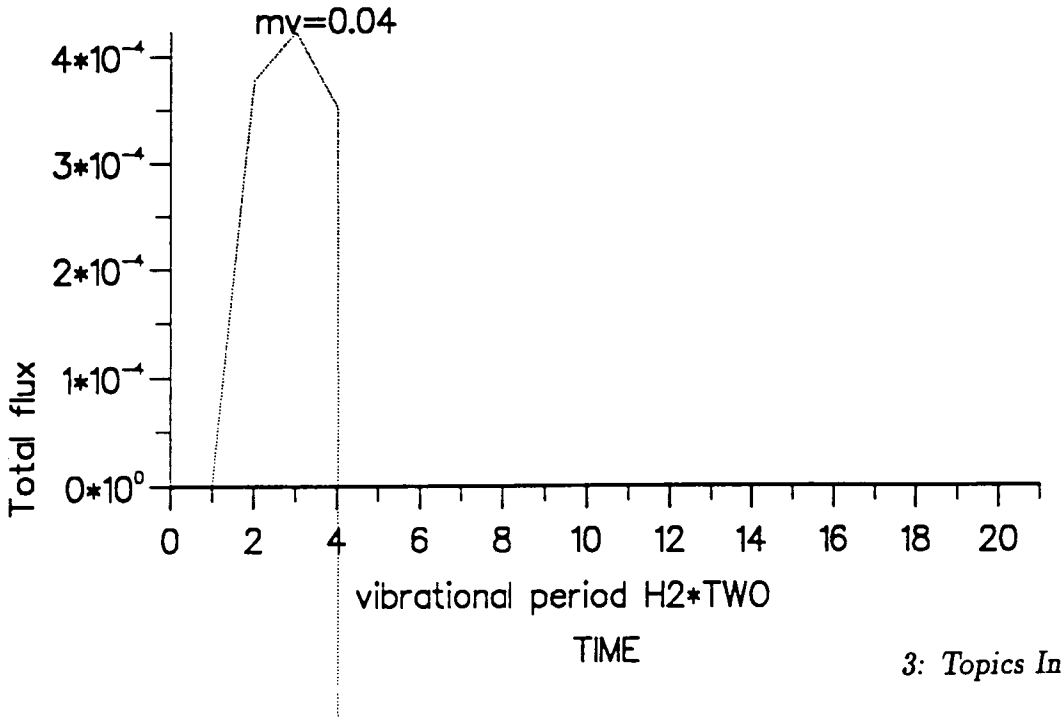
mv=0.04
4*10⁻⁴
3*10⁻⁴
2*10⁻⁴
1*10⁻⁴
0*10⁰
Total flux
0 2 4 6 8 10 12 14 16 18 20
vibrational period H2*TWO
TIME

3.3 Conclusions

The Fourier Method of studying time-dependent quantum mechanics has been investigated. The various propagators, i.e. the Chebyshev, S.O.D. and Feit/Fleck, have all been applied to a simple one-dimensional problem. It was found that the Chebyshev propagator is the most accurate and efficient, especially when used as a stepping rather than a truly global propagator. However care is needed when using imaginary potentials, so that in some cases it may be preferable to use the Feit/Fleck propagator. Although these tests were carried out in one dimension, the results apply to two or more dimensions. However, it is not always straightforward to use the Feit/Fleck propagator with the Fourier/Basis set method for solving multi-dimensional problems (see later), so that the stability advantage that this propagator shows for imaginary potentials cannot always be exploited.

4: Multi-Dimensional Problems

In order to gain some insight into chemical processes it is usually necessary to consider as many degrees of freedom as is computationally feasible. Thus it is very important that any method of studying chemical dynamics can be extended easily to multi-dimensional problems. This chapter is concerned with ways in which the one-dimensional Fourier method can be extended for use with multi-dimensional problems.

4.1 A Simple Extension

The simplest generalisation of the Fourier method to many dimensions uses a multi-dimensional regular grid and calculates the kinetic energy of the wavefunction using a multi-dimensional Fourier transform.

In Cartesian coordinates the kinetic energy operator is separable:

$$\hat{T} = \sum_{i=1}^{D} \frac{-\hbar^2}{2m_i} \frac{d^2}{dx_i^2} \tag{108}$$

where D is the total number of dimensions. Thus the kinetic part of the Hamiltonian is simply the sum of the kinetic energy in each dimension [6]. In Chapter 2 it was seen that the kinetic energy is easily calculated with the use of Fourier transforms:

$$\hat{T}\Psi(x) = \frac{1}{2\pi} \int_{-\infty}^{\infty} e^{ikx} \left[\frac{\hbar^2 k^2}{2m} \Psi(k) \right] dk. \tag{109}$$

When more than one dimension is to be considered in a calculation, the multi-dimensional Fourier transform is used, and the kinetic energy is again easily calculated:

$$\hat{T}\Psi(x,y) = \left(\frac{1}{2\pi}\right)^2 \int_{-\infty}^{\infty} \int_{-\infty}^{\infty} e^{ik_x x} e^{ik_y y} \left[\frac{\hbar^2 (k_x^2 + k_y^2)}{2m} \Psi(k_x, k_y) \right] dk_x dk_y. \tag{110}$$

The use of multi-dimensional transforms was discussed previously and it was seen that their use is just a simple extension of the one-dimensional transform.

However, the above only applies to *Cartesian* coordinates, in which regular grids are used. In other coordinate systems, such as polar or spherical coordinates, the effect of the kinetic energy operator is not as easily calculated. This is because the Laplacian is not simply in terms of the second derivatives of the functions, with respect to the various coordinates, but can be a combination of first and second derivatives. Other problems which present greater difficulties are the singularities which exist at certain points in space, and in some coordinate systems the non-periodic nature of particular coordinates, e.g. θ in spherical coordinates.

The use of reduced wavefunctions can help in certain coordinate systems. In the case of polar coordinates the Laplacian can be simplified by using a modified wavefunction such that:

$$\Psi(r,\theta) = \frac{\Psi_m(r,\theta)}{r^{1/2}}, \tag{111}$$

so that the Laplacian,

$$\nabla^2 = \frac{d^2}{dr^2} + \frac{1}{r}\frac{d}{dr} + \frac{1}{r^2}\frac{d^2}{d\theta^2}, \tag{112}$$

becomes equal to:

$$\frac{1}{4r^2} + \frac{d^2}{dr^2} + \frac{1}{r^2}\frac{d^2}{d\theta^2}. \tag{113}$$

A wavefunction normalised with integration measure $dr d\theta$, rather than $r\,dr d\theta$, is then consistent with the original wavefunction. Similarly in Jacobi coordinates it is useful to use a modified wavefunction such that:

$$\Psi(R,r,\theta) = \frac{\Psi_m(R,r,\theta)}{Rr}, \tag{114}$$

so that the radial momentum operators become Cartesian-like, and are given by $-id/dr$ and $-id/dR$, and the wavefunction is normalised with integration measure $\sin\theta\, d\theta dr dR$ [12].

4.1. 1 A Test Case

In order to investigate (and check) calculations carried out in more than one dimension, a test case very similar to the one-dimensional case was used. A two-dimensional harmonic oscillator with the parameters of the hydrogen molecule was used. The results are shown in figure 16, for the S.O.D. propagator. Although the error appears to be very small it must be noted that the propagation time was short because of the long times necessary to run the program, but it can be seen that the calculation is producing reasonably accurate results.

4.2 Different Approaches

Another very different approach to multi-dimensional problems is to consider the use of different transforms, i.e. the use of different implicit basis functions [6]. Consider the kinetic energy operator in spherical coordinates:

$$\frac{\hat{P}}{2m} = \frac{-\hbar^2}{2m}\left[\frac{1}{r^2}\frac{d}{dr}r^2\frac{d}{dr} + \frac{1}{r^2\sin\theta}\frac{d}{d\theta}\sin\theta\frac{d}{d\theta} + \frac{1}{r^2\sin^2\theta}\frac{d^2}{d\phi^2}\right]. \tag{115}$$

This can be divided into radial and angular parts.

For the radial part of the Laplacian, if a reduced wavefunction (similar to those described above) is used, the Bessel function $J_{1/2}(kr)$ is a solution, i.e. an eigenfunction

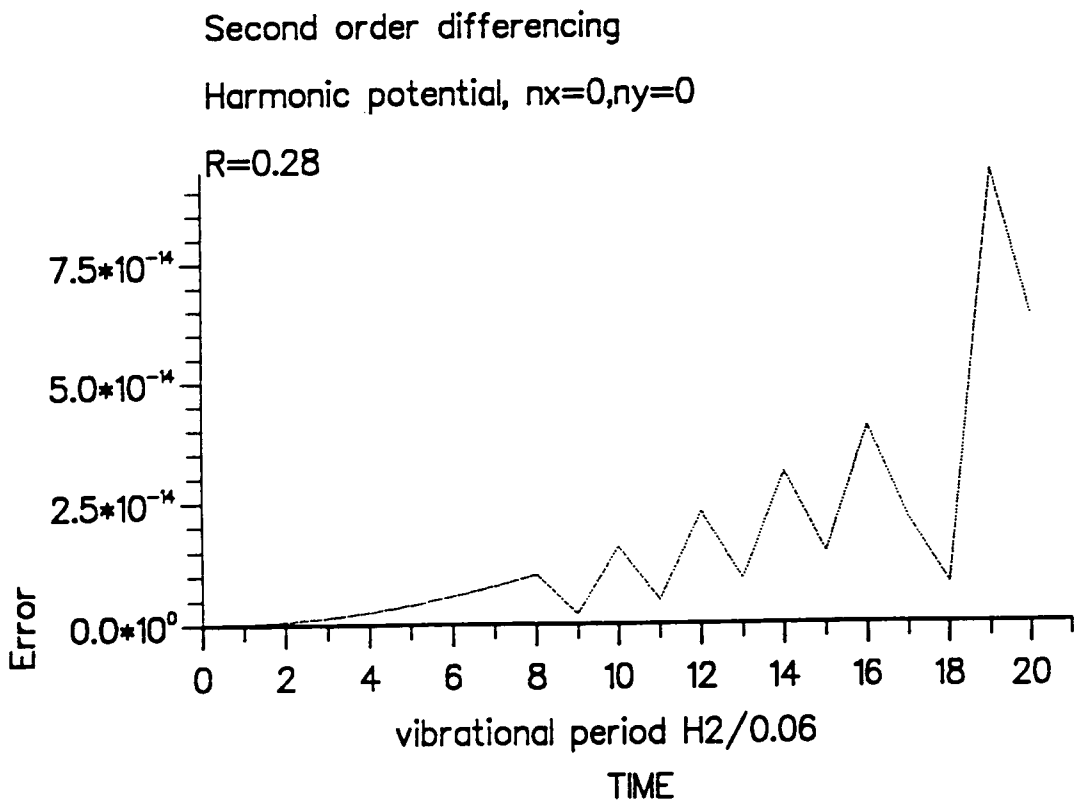

Fig. 16. Graph of error against time for S.O.D. propagator for a two-dimensional harmonic oscillator.

with eigenvalue $-k^2$. This means that the wavefunction can be transformed, using the Fourier-Bessel (or Hankel) transform of order 1/2, into a space where the radial part of the Laplacian is now a local operator with the spectrum $-k^2$. This is very similar to the one-dimensional case using the Fourier transform. A fast Hankel transform has been described by Bisseling and Kosloff [87]. For polar coordinates a similar method can be used for the radial part of the Laplacian; in this case the Bessel function of order 0 is a solution, so that a Hankel transform of order 0 is used. The use of the Hankel transform can be extended to Hamiltonians with centrifugal terms, m/r^2, by the use of a transform of order m, for polar coordinates, and $m + 1/2$, for spherical coordinates.

For the ϕ variable the Fourier method is applicable, though care must be taken to avoid the singularity in $\sin\theta$ at 0 and π by suitable choice of the grid points in the θ variable [29].

For the θ part of the Laplacian, i.e. the second term, the Legendre polynomials, $P_l(\cos\theta)$, are eigenfunctions with eigenvalues $l(l+1)$. Thus, it has been suggested that a discrete variable representation with Gauss-Legendre quadrature points is appropriate, i.e. a Legendre transformation [11]. For Hamiltonians which have centrifugal terms, $K^2/\sin^2\theta$, a basis of spherical harmonics, $Y_{lK}(\theta, \phi = 0)$, could be used. Another way in which these

centrifugal terms have been treated is the use of a modified wavefunction such that [88]:

$$\Psi = (\sin\theta)^K \Psi_m. \tag{116}$$

Unfortunately there is no fast Legendre transform reported in the literature. This has led to a variety of other methods to treat this coordinate being used. In several [29][88], the product is differentiated generating two terms, one in the first derivative of θ, the other in the second derivative. These derivatives are then calculated directly using the Fourier method. This has two disadvantages: first, four F.F.T. are required, forward and backwards for each derivative; secondly, the grid has to be artificially extended to include all θ values from 0 to 2π (rather than π). The reason for the latter is that in the Fourier method the coordinate is assumed to be periodic, and in this case the period of the coordinate is 2π. Recently a method which uses a fast cosine transform has been described which overcomes these two disadvantages [89].

4.3 Fourier Method/Basis Set Expansion

The Fourier Method can be used in conjunction with a more standard basis set expansion. This is sometimes called the close coupled wavepacket (C.C.W.P.) method. Given the complications which can arise when non-Cartesian coordinates are used (see above), the extensive development of this hybrid method is not unexpected. In this method the time-dependent wavefunction is expanded in a basis set of functions in one or more of the coordinates. This wavefunction is substituted into the T.D.S.E. to derive a set of coupled equations. The solution of this set of coupled equations produces the time evolution of the coefficients in the expansion. The basis functions used are usually eigenfunctions of the part of the Hamiltonian which describes the particular coordinate.

Obviously this method will be best suited to problems where there is only a weak coupling to the coordinate described by the basis set, ensuring that only a few functions are required to model the system accurately. An excellent example of this is given by the study of the dissociation of Van der Waals molecules, where a diatomic molecule is only weakly bound, by the very nature of such molecules, to another atom. An expansion in the coordinate which describes the internal motion of the diatomic molecule will only require a few functions, since this coordinate will be only very weakly coupled to the dissociation coordinate [12][90] [91]. Gray and co-workers have done three-dimensional calculations on the fragmentation of halogen molecules weakly bound to rare gas atoms. In these calculations the wavefunction was expanded in functions which described the vibration and rotation of the halogen molecule within the complex, and the coupled channel equations were solved to obtain the evolution of a wavepacket in the dissociation coordinate.

Although computationally more expensive, the C.C.W.P. method has been found to work very successfully for problems which require very many expansion functions, rather than just a few, to model the system. The long-lived resonance states in molecule-surface scattering have been extensively studied by Mowrey and Kouri, with a rotational basis set as well as a basis set in the translational motion parallel to the surface [19][20]. Atom-diatom scattering has been studied by this group using similar methods [14]. The photodissociation of very many different molecules has also been studied using this method, using an expansion in the functions which describe the angular momentum of one of the fragments [92].

In all of the above applications the major advantages of the Fourier method are retained. In particular, the motion in the key coordinate(s), i.e. the movement of the wavepacket, can still be easily visualised to obtain an insight into the reaction mechanism.

4.3. 1 An Example Problem

In order to investigate the use of this method a simple two-dimensional problem was studied, i.e. the fragmentation of a Van der Waals molecule. The expansion of the wavefunction using a specific basis set and the use of a particular Hamiltonian means that the set of coupled equations derived in the following are only relevant to the specific problem under consideration [12]. The Van der Waals fragmentation reaction to be studied is:

$$\mathrm{XBC}(v) \rightarrow \mathrm{X} + \mathrm{BC}(v') \qquad v' = v-1, v-2, \ldots$$

where v denotes some metastable initial state of the Van der Waals complex, in which the molecule BC is vibrationally excited, which fragments to form a rare gas atom, X, and a halogen molecule, BC, in vibrational state v'.

If the XBC system is constrained at a T-shaped geometry, so that the rotational motion is not included, the Hamiltonian is given by:

$$\hat{H} = \frac{\hat{P}_R^2}{2\mu} + \frac{\hat{p}_r^2}{2m} + \hat{V}_{BC}(r) + \hat{V}(R,r) \tag{117}$$

where μ is the reduced mass of the whole cluster and m is the reduced mass of the BC molecule. The coordinates are defined so that R is the distance between X and the centre of mass of BC and r is the BC internuclear distance, i.e. Jacobi coordinates are used. As was suggested previously in this chapter, a modified definition of Ψ is used (equation (114)) so that $\hat{P}_R$ and $\hat{p}_r$ have simple Cartesian forms.

$\Psi(t)$ is expanded in a basis set as follows:

$$\Psi(t) = \sum_{v'} C_{v'}(R,t)\psi_{v'}(r) \tag{118}$$

where the functions $\psi_{v'}$ represent the BC vibrational states, and are solutions of:

$$\left(\frac{\hat{p}_r^2}{2m} + \hat{V}_{BC}(r)\right)\psi_v = E_v\psi_v(r) \tag{119}$$

Inserting $\hat{H}$ and Ψ into the T.D.S.E., left-multipling both sides by $\psi^*_{v''}$, and integrating over r leads to the coupled equations:

$$i\frac{\partial C_{v'}(R,t)}{\partial t} = \frac{\hat{P}_R^2}{2\mu}C_{v'}(R,t) + E_{v'}C_{v'}(R,t) + \sum_{v''}\langle v''|V(R,r)|v'\rangle C_{v''}(R,t). \tag{120}$$

This set of equations describes the evolution of the *channel* wavepackets $C_{v'}(R,t)$, the appropriate weighted sum of which determines the full wavepacket $\Psi(t)$. Thus once the initial states for each channel, $C_{v'}(R,0)$, are found the set of equations is used to propagate the channel wavepackets in time using the methods described in Chapter 2. The only unfamiliar aspect to this equation is the potential part which requires a sum over the matrix elements $\langle v''|V(R,r)|v'\rangle$ for each channel. This is the essential part of any coupled channel method. The matrix elements can be calculated using a Gauss-like quadrature scheme [93] so that,

$$\langle v''|V(R,r)|v'\rangle = \sum_{j=1}^{N}\psi_{v''}(r_j)V(R,r_j)\psi_{v'}(r_j)w_j. \tag{121}$$

The abscissae, r_j, are the zeroes of a high vibrational wavefunction for the potential curve concerned, and the weights, w_j, are defined so that integrals over low-order wavefunctions are evaluated exactly.

For multi-channel problems, the Feit/Fleck or split propagator method becomes cumbersome to use because of the need to diagonalise the potential at each grid point [6]. For the Chebyshev method, some thought is needed to decide the range of the eigenvalues, required for the calculation of the number of terms in the polynomial expansion. The range of the eigenvalues must include a term for the vibrational energy, $E_{v_{max}}$. The maximum of the potential part, i.e. the matrix elements of the potential operator, is found from the spectral radius of the matrix; this is calculated by computing the sum of the moduli of the matrix elements in each row for each grid point and choosing the maximum [20].

The initial state

The initial state used in the Van der Waals predissociation problem is a metastable state of the Hamiltonian given above (equation (117)). It can be thought of as the specific state under investigation, e.g. a particular vibrational state of the BC molecule in the Van der Waals complex, so that the decay of this particular state can be studied. These metastable states are not the true stationary states of the Hamiltonian since the energy regime of interest is in the continuum, and the true stationary states are scattering states.

The initial state, Ψ_m, is expanded as follows:

$$\Psi_m(R,r) = \sum_{v,n} a_{vn}\psi_v(r)\chi_n(R), \tag{122}$$

where the functions $\psi_v(r)$ were defined above and $\chi_n(R)$ are effective Van der Waals stretching eigenfunctions, and are given by the solutions of:

$$\left[\frac{\hat{P}_R^2}{2\mu} + \hat{V}_R(R)\right]\chi_n(R) = E_n\chi_n(R), \tag{123}$$

where $\hat{V}_R(R)$ is a suitably chosen potential, and in this case is $\hat{V}(R,r_e)$ where r_e is the equilibrium value of r. This wavefunction, Ψ_m, and the Hamiltonian are substituted into the S.E. equation, $\hat{H}\Psi = E\Psi$, to give:

$$\sum_{v,n}\left[\frac{\hat{P}_R^2}{2\mu} + \frac{\hat{p}_r^2}{2m} + \hat{V}_{BC}(r) + \hat{V}(R,r)\right] a_{vn}\psi_v(r)\chi_n(R) = E\Psi_m. \tag{124}$$

This is then left-multiplied on both sides by $\psi^*_{v'}(r)\chi^*_{n'}(R)$ and integrated over R and r to give:

$$\sum_{v,n} a_{vn}\langle\psi_{v'}\chi_{n'}|\frac{\hat{P}_R^2}{2\mu} + \frac{\hat{p}_r^2}{2m} + \hat{V}_{BC}(r) + \hat{V}(R,r)|\psi_v\chi_n\rangle = \sum_{v,n} E_{v',n'}a_{v'n'}\delta_{v,v'}\delta_{n,n'}. \tag{125}$$

This can be expressed as:

$$\left(\underline{\underline{H}} - E\underline{\underline{I}}\right)\underline{a} = 0, \tag{126}$$

where

$$\underline{\underline{H}} = \langle\psi_{v'}\chi_{n'}|\hat{H}|\psi_v\chi_n\rangle, \tag{127}$$

and

$$H_{v'n',vn} = E_v\delta_{v'v,n'n} + E_n\delta_{v'v,n'n} + \langle\psi_{v'}\chi_{n'}|\hat{V}(R,r) - \hat{V}_R(R)|\psi_v\chi_n\rangle. \tag{128}$$

Hence in order to find a_{vn}, and so Ψ_m, the matrix $\underline{\underline{H}}$ must be diagonalised. Therefore the matrix elements of the Hamiltonian must be calculated; in order to calculate these matrix elements it is necessary to solve equations (119) and (123) to find E_v, E_n, ψ_v and χ_n. This just involves solving the one-dimensional S.E. and can be done using Cooley's method (Numerov integration) [94]. The matrix elements of the potential part involve a double integration; the integration over r is done using the Gauss-like quadrature described above, whilst the integration over R is done using the trapezium rule (the anharmonicity in this variable makes it inappropriate to use the Gaussian quadrature scheme).

The potentials

For the BC molecule potential, $\hat{V}_{BC}(r)$, a Morse function is used. For the interaction potential, $\hat{V}(R,r)$, a pairwise-additive function is used, i.e. two Morse functions are added together, one for X-C and one for X-B. A long-range attractive tail region may be included.

Extracting observables from the wavepackets

It is useful at this point to describe the experiment which the theory hopes to model. The cluster is prepared in a supersonic beam in the state $|v_x = n_x = 0\rangle$, where v_x is an effective vibrational quantum number for BC in the X electronic state and n_x denotes an effective Van der Waals stretching quantum number. A narrow-frequency band laser, with frequency ω, is applied to the system. This frequency corresponds to an electronic transition from the X state to an excited electronic state, B. In general the molecule BC in the electronically excited cluster will also be vibrationally excited so that v_x is equal to v. The excited cluster, which has a resonance energy depending on v, then dissociates with a particular lifetime, into a certain product distribution of the halogen molecule; all of these variables can in principle be determined experimentally.

These experimental observables, i.e. the resonance energy, the lifetime and the product distribution, have then to be extracted from the *time-dependent* wavefunction. The information of main interest here is the lifetime of the cluster, though the resonance energy and the product distribution of the halogen molecule after fragmentation can also be obtained. The extraction of the observables from the time-dependent wavefunction can be done using either Fourier Analysis or the MUSIC frequency estimator [95]. The second method can yield more information given a shorter time of propagation because it assumes a certain model and then, given a data sample of limited duration, determines the best fit to this model.

For the dissociation of many Van der Waals clusters, it can be assumed that only one resonance dominates the dynamics of the cluster and so the lifetime, τ, can be inferred as the reciprocal of the slope of a plot of $\ln|\langle\Psi(0)|\Psi(t)\rangle|^2$ against t. The autocorrelation function is easily calculated from the channel wavepackets as the sum of the squares of the autocorrelation functions of the packets; this is because the 'weighting' functions, ψ_v, are orthonormal.

Test cases

The C.C.W.P. method was used to investigate the fragmentation of both $NeCl_2$ and HeI_2. Figures 17 and 18 show the $\ln(A_c)$, where A_c is the square modulus of the autocorrelation function, against time.

Consider first the system $NeCl_2$. This problem has been studied in three dimensions

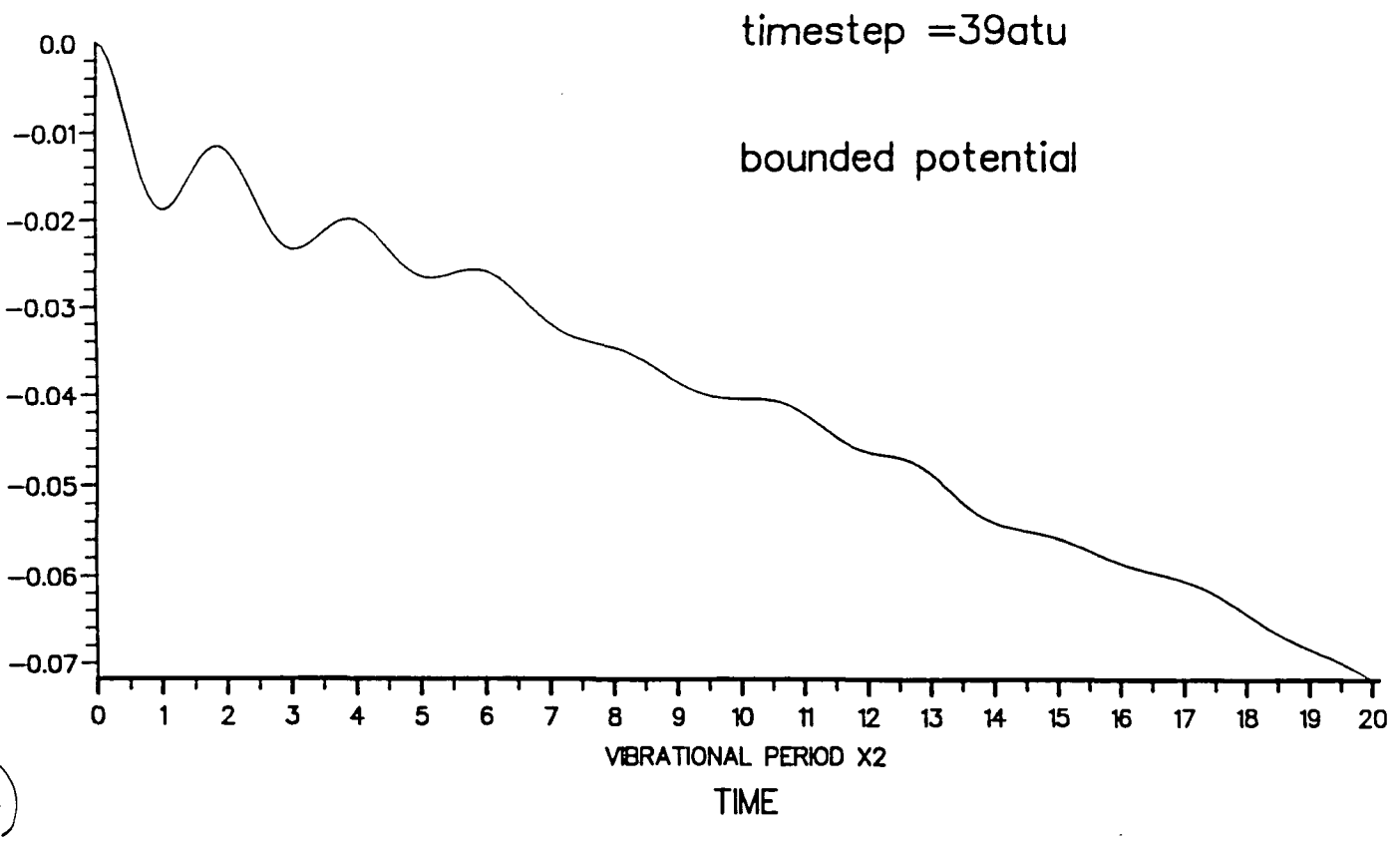

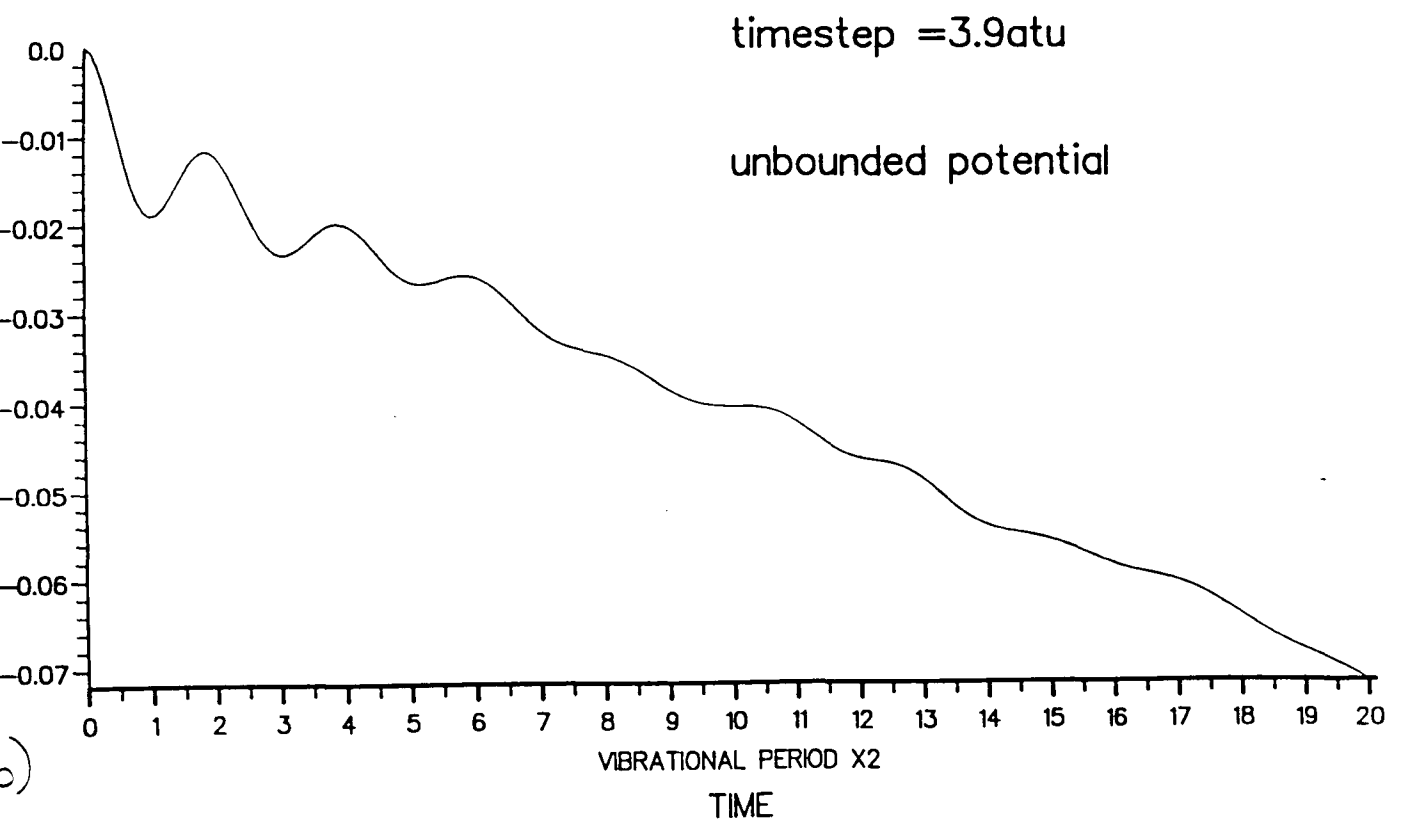

Fig. 17. a). $\ln(A_c)$ against time for the dissociation of $NeCl_2$ $v = 11$, using the bounded potential and the longer timestep. b). $\ln(A_c)$ against time for the dissociation of $NeCl_2$ $v = 11$, using the short timestep.

by Gray et al. [12]. In order to check that the calculations done in this work yield sensible results, these were compared to those obtained by Gray et al. As an aside it is interesting to note some points in their implementation of the C.C.W.P. method, which were also utilised in this work:

1. A bounded potential is used which enables the use of a longer timestep for the S.O.D. than would be allowed by the stability limit, if an unbounded potential was used. Figure $17a, b$ shows two graphs of the $\ln(A_c)$ against time, obtained for the two-dimensional calculations described earlier, one with a short timestep and the unaltered potential and the other with the longer timestep and the bounded potential. They look identical.
2. The energies of the vibrational channels are taken relative to the initial channel, i.e. relative to the chosen vibrational state of the BC molecule in the excited cluster, or Ψ_m. This shifts the region where minimum error occurs, hence improving the accuracy of the calculation.

The figures $17a, b$ suggest a lifetime of approximately 70 ps, (the vibrational period of Cl_2 is 0.245 ps). This is smaller than the three-dimensional value, given by Gray as 120 ps. (Note the potential referred to as surface 2, with initial vibrational level $v = 11$, is being used). This is not the expected result, which is that the T-shaped molecule should be less likely to fall apart than the molecule free to rotate, but it does not give rise to great concern.

Consider next the system HeI_2. Again the results obtained in this work were compared to those reported in the literature in order to check the reliability of the calculations done here. Two-dimensional studies on HeI_2 have been done which help to make the comparison of results more meaningful. One of these studies by Gray [96] uses a periodically forced oscillator model (P.F.O.) and the wavepacket method. Although this is only a one-dimensional study, it is suggested that 'the P.F.O. model is indeed typical of the original 2D problem'. The graphs presented in the paper are of $\ln(P_s)$ against t where P_s is the survival probability. The definition of P_s:

$$P_s(t) = \sum_n |\langle \chi_n | \Psi(t) \rangle|^2, \tag{129}$$

differs from the observable used in the present work, which is the square modulus of the autocorrelation function. However, in the calculations done in the present work, the magnitude of the wavefunction in the $v-1$ and $v-2$ channels is small compared to that in the v channel, so that the autocorrelation can be approximated by $|\langle C_v(R,0)|C_v(R,t)\rangle|$; also the initial wavefunction corresponds almost exactly with $n = 0$ in the Van der Waals stretching mode. This implies that $C_v(R,0) \approx \chi_0(R)$, and so the autocorrelation function can be given by $|\langle \chi_0(R)|C_v(R,t)\rangle|$. In the Gray paper the dominant contribution to P_s is

thought to originate from P_0, i.e. from the wavefunction in the $n = 0$ mode. This implies that $P_s(t) \approx |\langle\chi_0|\Psi(t)\rangle|^2$. Given these analyses of the observables used in each of the calculations, the observable used in the Gray work, i.e. P_s, can be seen to correspond reasonably well to the observable used in this work, i.e. the square modulus of the autocorrelation function. Figures $18a, b$ show two graphs for $v = 20$ and $v = 30$. They reproduce those shown in the Gray paper quite well, although the slopes are too steep by approximately 15%.

4.4 Conclusions

The extension of the Fourier method to multi-dimensional problems has been described. It was seen that there are many different approaches possible, some of which are similar to the one-dimensional Fourier method, others of which are quite different.

The C.C.W.P. method has been used to describe the fragmentation of Van der Waals molecules. It was seen that the derivation of the set of coupled equations was straightforward. The solution of the equations and the extraction of observables from the channel wavepackets was no more complicated than for the Fourier method. Thus it can be seen that this hybrid method of the Fourier method with a more standard basis set expansion provides a useful tool for multi-dimensional calculations. The two test cases described have been shown to produce results which are not at odds with those reported in the literature. Thus, there can be some confidence in the accuracy of the calculations done in this work.

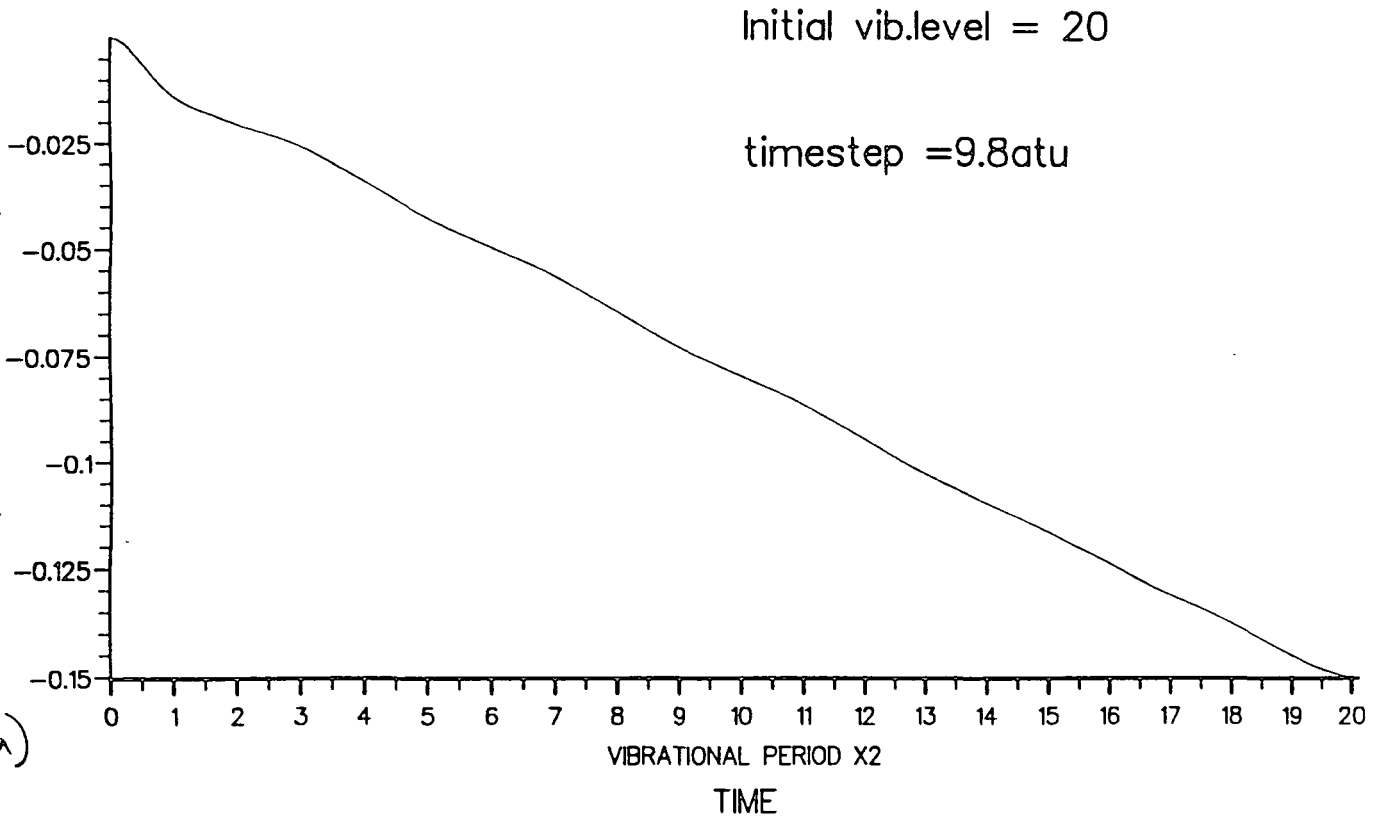

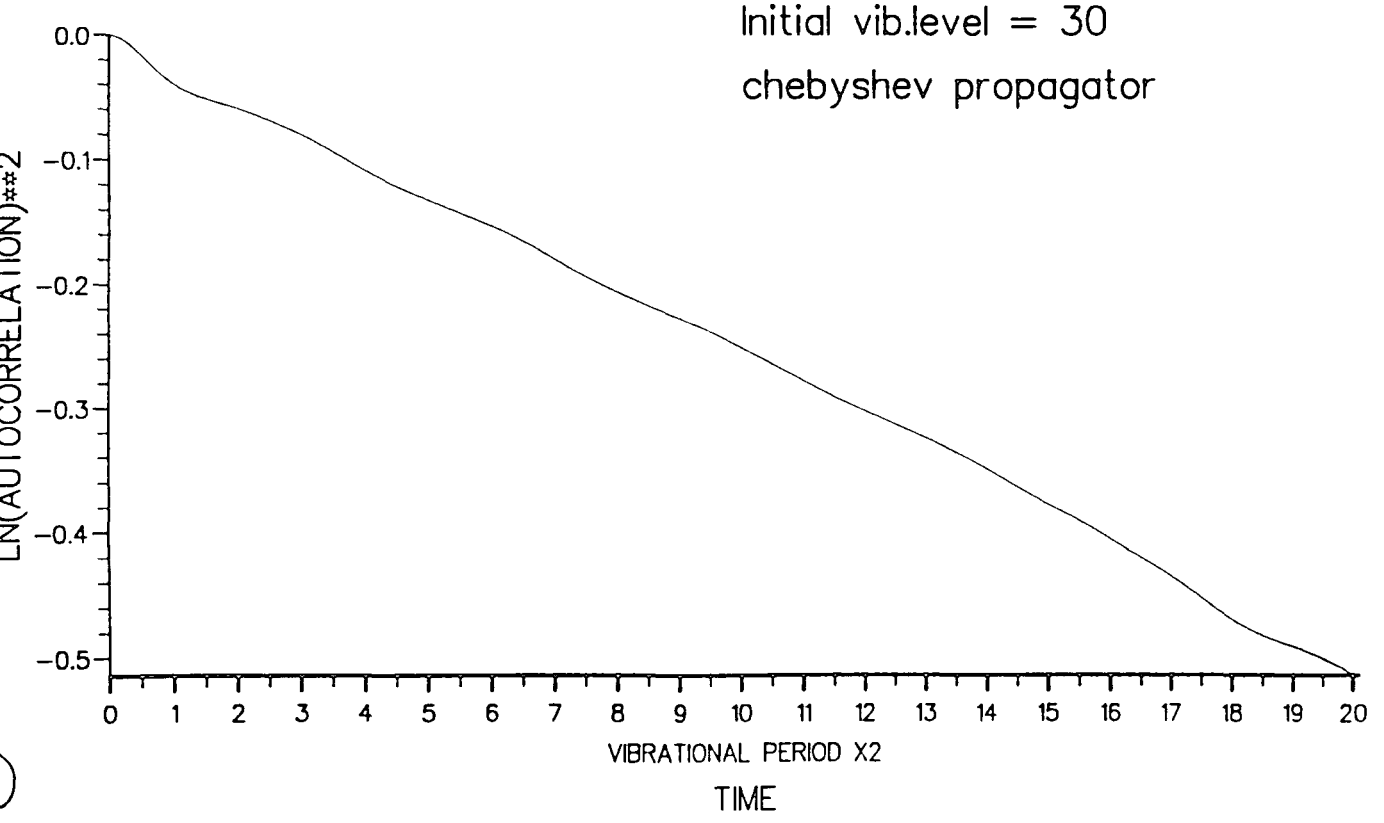

Fig. 18. a). $\ln(A_c)$ against time, for the dissociation of HeI_2 $v = 20$. b). $\ln(A_c)$ against time, for the dissociation of HeI_2 $v = 30$.

5: The Sodium Trimer

5.1 Introduction

The equilibrium geometry of the sodium trimer is not, as might at first be thought, an equilateral triangle. In the ground electronic state, as well as in some of the excited electronic states, there is an unpaired electron in a degenerate electronic orbital. This leads to a Jahn-Teller (or pseudo-Jahn-Teller) distortion away from the equilateral geometry towards an isosceles triangle geometry. In many of the electronic states there is only a small barrier between the various acute and obtuse angled isosceles triangle geometries, and the molecule will change from one geometry to another with relative ease. This is sometimes called pseudorotation.

The spectroscopy of Na_3 has received considerable attention over the past few years, both theoretically and experimentally. There are two main reasons for this interest. First, a study of small metal clusters is important because a knowledge of their basic properties, e.g. geometry, bond strength and reactivity, is an aid to understanding the nucleation and growth of small metal particles and eventually the build-up of the metallic state. Secondly, their optical, chemical and catalytic properties can be utilised in a variety of ways.

The small number of vibrational modes makes the analysis of the nuclear dynamics interesting on theoretical grounds because studies can be detailed without becoming too cumbersome. In particular, there has been great interest in the sodium trimer because of the ability to study, in some detail, the changes in its structure and dynamics due to the approach or intersection of several Born-Oppenheimer potential surfaces. There is a growing interest in this field, particularly with respect to the Jahn-Teller effect [97] and Berry's geometrical phase [98] in molecular systems. A recent review has summarised the theory related to the geometric phase, in a suitable form for molecular systems, and suggested possible consequences which could be compared to experiments [99]. Recently, the results of several spectroscopic experiments have been analysed using the Jahn-Teller effect, e.g. the resonant two-photon ionisation spectrum of triptycene [100] and the stimulated emission pumping spectrum of the methoxy radical [101].

Time-dependent experiments and calculations have been carried out on the Na_2 system [102] [103]. These demonstrated the usefulness of the time-dependent approach in understanding vibrational wavepacket motion and also helped to identify the various ionisation pathways present in the system. The present work extends these studies to the sodium trimer. The use of time-dependent methods to study the sodium trimer, both ex-

perimentally and theoretically, is particularly interesting since it gives a direct insight into multi-dimensional wavepacket motion on a potential energy surface and leads to a greater understanding of the dynamical aspects of molecular multiphoton ionisation.

5.1. 1 Background

The spectroscopy of the sodium trimer has now been the subject of several investigations in which, with the help of molecular beams and lasers, individual vibronic levels have been resolved and analysed. Experiments have been carried out to investigate the electronically excited states as well as the ground state.

The techniques

A variety of spectroscopic techniques is available to study small metal clusters, including: two-photon ionisation; ion-depletion experiments; and stimulated emission pumping spectroscopy (S.E.P.). The analysis of hot bands in the results of the two-photon ionisation experiments can lead to information about the ground state.

In both the two-photon and the ion-depletion experiments the Na_3 molecules, which are produced in a molecular beam, are excited electronically with a tunable laser ω_1. In the resonant two-photon ionisation scheme the excited molecules are ionised with a second laser ω_2. The photoions formed are detected with a quadrupole mass spectrometer. In the depletion spectroscopy experiment, which is used for probing the Na_3 dissociative states, an ultraviolet laser ω_3 directly ionises Na_3 molecules in the ground state and, by detecting the photoions, monitors the remaining population in the molecular beam. In this experiment whenever the laser ω_1 is on resonance with an excited state the population of Na_3 molecules in the molecular beam decreases. Thus, there are fewer molecules which can be ionised by the ultraviolet laser ω_3, and so there is a depletion in the photoion signal. Hence spectral resonances are recorded as depletion in the signal. The lasers ω_1 and ω_3 are applied simultaneously.

S.E.P. is also a two-photon excitation process [104]. The first photon excites the molecule to an intermediate level of an electronically excited state, whose population is monitored in some way, e.g. by detecting undispersed side fluorescence. The second photon is then used to stimulate emission from the intermediate level. If there is a decrease in the population of the intermediate level then the second photon is on resonance. Thus the energy levels to which the molecule is transferred during the stimulated emission can be investigated by varying the frequency of the second photon. The two photons can be applied simultaneously or sequentially. The S.E.P. experiment on Na_3 [105] [106] uses the ion-depletion technique to monitor the population of the intermediate level. The Na_3 molecules, produced in a molecular-beam apparatus, are excited to an intermediate level of the C state by

a first laser ω_1. A second laser ω_2 is then used to induce two competitive processes in the excited trimers: (1) direct photoionisation and (2) stimulated emission down to vibronic ground-state levels. The Na_3^+ ion signal is detected using a quadrupole mass spectrometer, as a function of ω_2. That is, the population of the intermediate level, which is proportional to the ion signal, is measured as a function of ω_2. At resonance the second process is much more likely than the first, by a factor of 10^2–10^3, and so a dip will occur in the ion signal for each transition to a ground-state level. The C state is used as the intermediate state in this experiment because the vibronic levels of this state have been extensively studied, and an assignment of them exists, so that it is possible to identify the particular intermediate level used.

The experiments

The excitation spectrum of Na_3 has been systematically investigated from 700 to 330 nm, both by two-photon ionisation (T.P.I.) experiments and by depletion experiments [107][108].

Four band systems are observed: A, B, C and D. The B state, which is bound, is of interest here (see figure 43). Among the most important characteristics of the richly banded system are: first, a long progression composed of nearly equally spaced bands ($\omega \approx 128$ cm^{-1}) appears to be split into doublets; secondly, a series of closely spaced bands fanning out from the doublet and increasing steadily in breadth accompanies each member of the main progression; thirdly, a much weaker pattern of levels accounting for all remaining bands fits to a harmonics series with $\omega \approx 137$ cm^{-1}. This spectrum has been explained in terms of the pseudorotational motion of the sodium trimer.

The vibronic structure of the Na_3 ground state has been investigated both by stimulated emission pumping spectroscopy and by the analysis of hot bands in the two-photon ionisation spectra.

The analysis of the hot bands is a straightforward extension to the two-photon ionisation experiment on the excited states [109]. The B system exhibits a clear hot-band structure. The hot band structure can be interpreted to give X state vibrational frequencies, which are for the symmetric stretch 139 cm^{-1}, and for the bend/asymmetric stretch 50 cm^{-1} and 87 cm^{-1}. Similar results are obtained for the other states.

In the S.E.P. experiment numerous resonances are observed in the spectrum in the 150–1000 cm^{-1} range, which indicates that the molecule is particularly deformable. A strong and simple pattern found in the low-resolution spectrum can again be interpreted by the three zeroth-order normal frequencies (for the symmetric stretch 139 cm^{-1}, and for the bend/asymmetric stretch 49 cm^{-1} and 87 cm^{-1}).

Time-resolved experiments

The aim of the present work is to reproduce the results of time-resolved femtosecond pump-probe experiments on the Na_3 system, being carried out in Freiburg, as well as the results of similar experiments being carried out in Berlin using picosecond lasers. It is hoped that by doing so a full explanation, and thus a greater understanding, of the experimental results will be obtained. It is also hoped that these calculations will give an insight into the dynamics of systems in non-stationary states.

In the femtosecond experiment [110] [111] the Na_3 is prepared in its ground electronic state in a supersonic beam. The same laser is used for both the pump and the probe, which has a central frequency, $\omega_{central}$, equal to 620 nm (16129 cm^{-1}). The time profile of the pulse is roughly Gaussian with a temporal full-width of approximately 70 fs. The spectral width of the laser pulse has been measured (figure 19); it is not the same as the value implied by its temporal width. The molecules in the beam are excited with the femtosecond laser pulse (the pump) to an electronically excited state, the B state, of Na_3. The pump laser has only sufficient energy to populate the lowest 250 cm^{-1} of the B state. After a given interval of time the second femtosecond laser pulse (the probe) is used to ionise the Na_3. There is only just enough energy in the probe pulse to ionise the Na_3 to Na_3^+. The ions that are produced are then detected. This is done using time-of-flight spectroscopy, which determines the masses and released kinetic energy of the ionic fragments, as well as the energy distribution of the ejected electrons. The experiment is repeated for many different pump-probe delay times, i.e. the interval of time between the application of the pump and probe laser pulses, for up to a maximum of approximately 12 ps. This variation in the pump-probe delay time gives rise to a varying Na_3^+ signal. The results show an ion signal that takes a few femtoseconds to appear and then oscillates, though not back to zero, with a principal period of 320 fs, corresponding to a wavenumber of 105 cm^{-1}. The signal decays exponentially with a lifetime of approximately 2 ps. The Fourier transform of the ion signal shows peaks at 12(m), 19(m), 34(w), 50(m), 73(m), 105(vs), 90(s), 123(w) and 141.5(w) cm^{-1} and higher frequencies (w = weak, m = medium, s = strong, vs = very strong).

At the same time the zero kinetic energy electrons which are ejected on ionisation are detected. The time-dependent signal is similar to that of the Na_3^+, and the same frequencies are obtained in the Fourier transform.

The pump laser pulse produces a wavepacket on the B state, which moves about the potential energy surface. When the probe laser pulse is applied, the position of the wavepacket on the B state will vary, i.e. the molecule will be in different molecular configurations, depending on the pump-probe delay time. The probability of the probe laser ionising the Na_3 depends on the position of the wavepacket on the potential surface. Thus, the oscillations in

the Na_3^+ signal are due to the motion of the time-dependent wavefunction on the potential surfaces of the B and X electronic states of Na_3. The X state frequencies occur because the pump laser can produce a wavepacket on the ground state by a 2-photon excitation via the B state, and the probe laser can ionise it by another 2-photon process. The contribution of the X state frequencies to the total ion signal becomes less significant at lower powers. This in principle allows the frequencies to be assigned to the two different states, though the procedure is experimentally difficult.

The frequencies have tentatively been assigned as follows [111]: 12, 19 cm^{-1} are pseudorotation frequencies on the B state; 50 cm^{-1}, an asymmetric stretch on the X state; 73 cm^{-1}, a bending frequency on the B state; 90 cm^{-1}, a bending frequency on the X state; 105 cm^{-1}, a symmetric stretch on the B state; 141.5 cm^{-1}, a symmetric stretch on the X state.

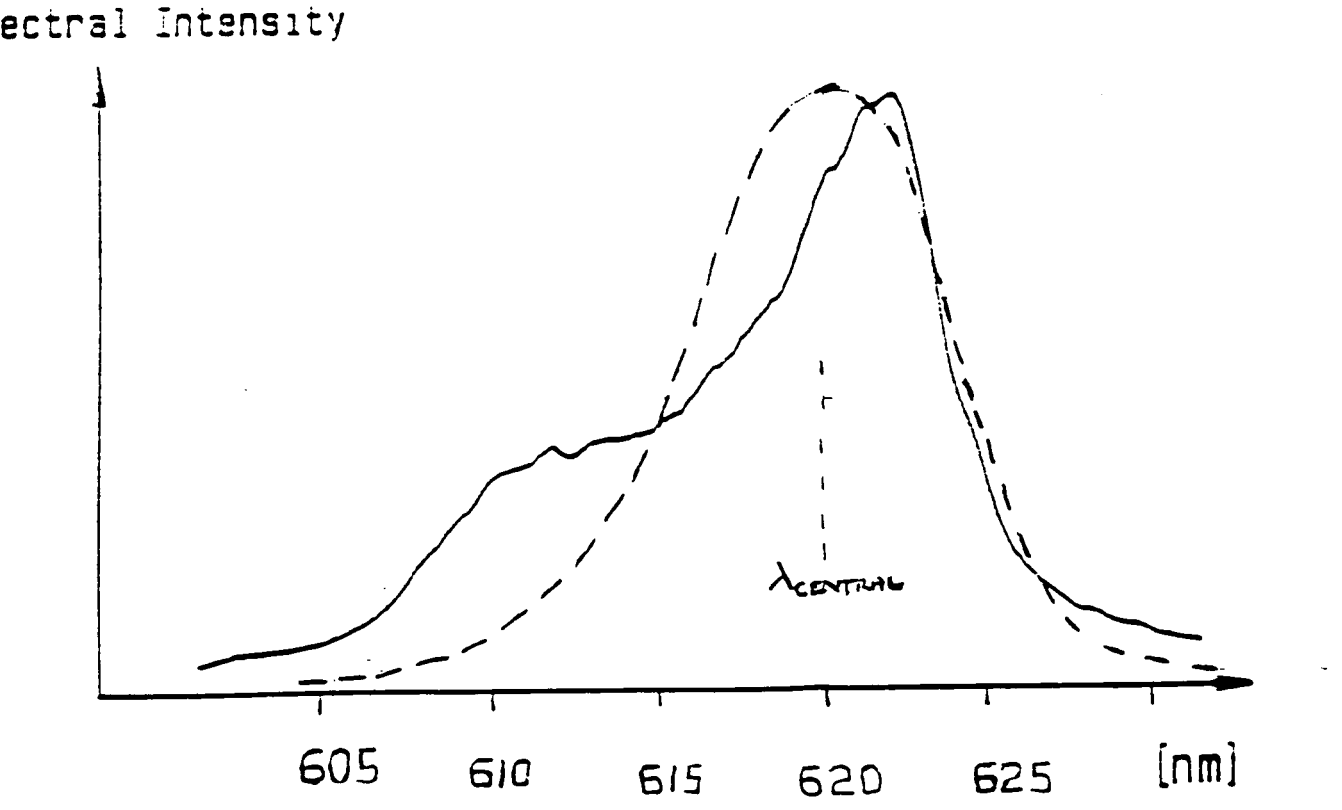

Fig. 19. The spectral intensity of the laser pulse in the femtosecond experiment. The full line is the experimental measurement, and the dashed line shows the spectral intensity expected from Heisenberg's uncertainty principle for a laser pulse with a 70 fs temporal width.

Transient two-photon ionisation experiments are also being carried out on the sodium trimer, using picosecond pump-probe techniques followed by mass-selective detection [112]

[113] [114] [115]. Again, the same laser is used for both the pump and the probe, with ω_{central} equal to 619.7 nm (16136 cm^{-1}). The time profile of the pulse is roughly Gaussian with a temporal full-width of approximately 1.3 ps. The spectral width of the laser pulse has been measured and is found to have a value double that implied by its temporal width. When the first photon is resonant with some vibrational level of the B state, the time-dependence of the Na_3^+ signal shows a distinct beat structure, with a 3 ps period of oscillation, corresponding to a wavenumber of 11 cm^{-1}; the signal decays exponentially, with a decay time of about 6 ps. This experiment has been repeated with ω_{central} equal to 617 nm (16207 cm^{-1}), 620 nm (16129 cm^{-1}) and 625 nm (16000 cm^{-1}), as well as other frequencies; the results are reported to be essentially the same. For non-resonant excitation photons no oscillation is observed.

5.2 The Coordinates

The complete nuclear permutation inversion group of the sodium trimer is $D_{3h}(M)$. It is necessary to use the complete nuclear permutation inversion group due to the 'floppy' nature of the sodium trimer, which ensures that all nuclear permutations, P, and permutation-inversions, P^*, are feasible [116]. $D_{3h}(M)$ is isomorphic to the D_{3h} point symmetry group.

It is a straightforward matter to find the normal mode vibrations of this molecule using group theory. They are found to belong to the irreducible representations a_1' and e' of the D_{3h} point symmetry group, and can be described as:

$$Q_x = \frac{1}{\sqrt{3}}\left[-x_1 + \left(\frac{1}{2}x_2 + \frac{\sqrt{3}}{2}y_2\right) + \left(\frac{1}{2}x_3 - \frac{\sqrt{3}}{2}y_3\right)\right], \tag{130}$$

where Q_x is the bending vibration and x_i, y_i are the Cartesian coordinates of each atom i;

$$Q_y = \frac{1}{\sqrt{3}}\left[y_1 + \left(\frac{\sqrt{3}}{2}x_2 - \frac{1}{2}y_2\right) + \left(-\frac{\sqrt{3}}{2}x_3 - \frac{1}{2}y_3\right)\right], \tag{131}$$

where Q_y is the asymmetric stretch;

$$Q_s = \frac{1}{\sqrt{3}}\left[-x_1 + \left(\frac{1}{2}x_2 - \frac{\sqrt{3}}{2}y_2\right) + \left(\frac{1}{2}x_3 + \frac{\sqrt{3}}{2}y_3\right)\right], \tag{132}$$

where Q_s is the symmetric stretch. Q_x and Q_y are the two components of the normal e'-type displacements. Q_s is obviously the normal a_1'-type displacement, but will not be considered at present, since the totally symmetric displacement, while affecting the potential, does not change its symmetry [117]. The definitions of Q_x and Q_y vary throughout the literature. This is evident in many ways. First, the symbols Q_x and Q_y can be reversed, so that Q_y represents the bend and Q_x represents the stretch, and secondly, Q_x as defined here can be called an asymmetric stretch, and Q_y a bend. In particular the assignment of frequencies as bends or asymmetric stretches must be considered carefully to ensure the correct mode, i.e. Q_x or Q_y, is chosen.

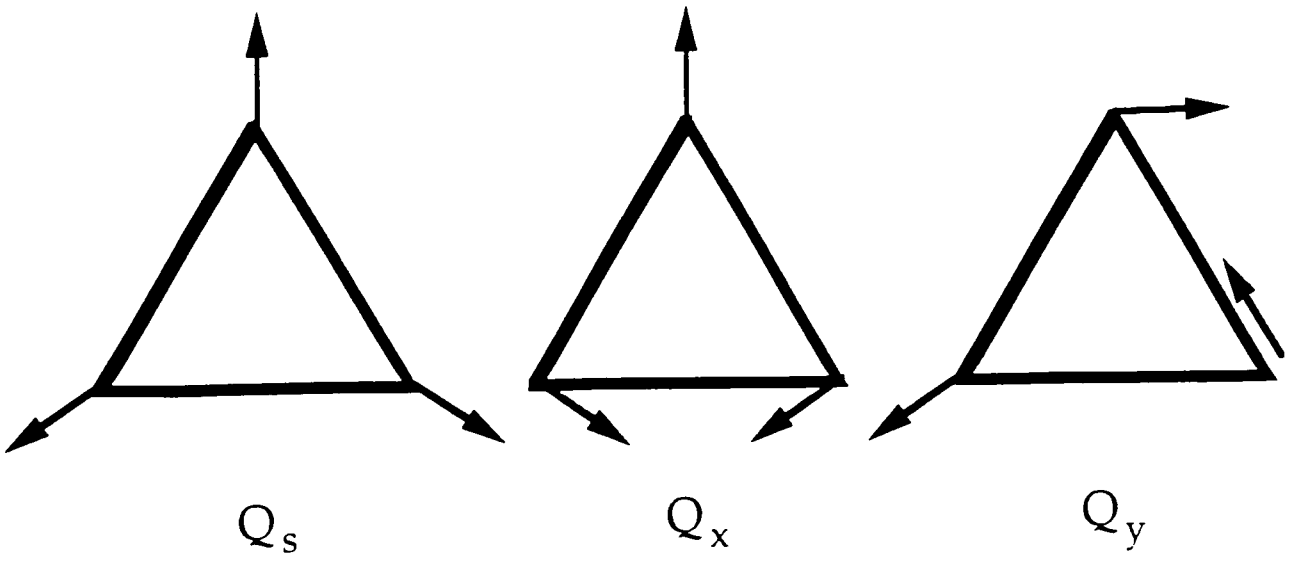

Fig. 20. The normal mode vibrations of the sodium trimer.

Consider now a Cartesian space in Q_x and Q_y. At the origin of this space the sodium trimer has an equilateral geometry. For a displacement in the positive Q_x direction the molecule will have an acute isosceles triangle geometry, whilst for a displacement in the negative Q_x direction the molecule will have an obtuse isosceles triangle geometry. At other positions around the origin the molecule will be either an obtuse or acute isosceles triangle. The molecule can change from one obtuse isosceles triangle to another without going through the equilateral geometry, but through an acute isosceles geometry. This change in configuration looks at first to be a rotation of the molecule and is sometimes called a *pseudorotation.*

The wavepacket calculations are initially carried out in two dimensions, which correspond to Q_x and Q_y. Q_x and Q_y can be expressed in terms of r and ϕ, where

$$r^2 = (Q_x^2 + Q_y^2), \qquad \tan\phi = Q_y/Q_x. \tag{133}$$

The angle ϕ is often described as the pseudorotation coordinate. This is because as the origin of this space is circled following ϕ, the molecule undergoes the pseudorotational motion. The calculation is performed using r and ϕ.

Using these coordinates, i.e. polar coordinates, and introducing a reduced wavefunction such that:

$$\Psi(r,\phi) = \frac{\Psi_m(r,\phi)}{\sqrt{r}}, \tag{134}$$

the kinetic energy operator is:

$$\hat{T} = \frac{-\hbar^2}{2m}\left[\frac{1}{4r^2} + \frac{d^2}{dr^2} + \frac{1}{r^2}\frac{d^2}{d\phi^2}\right]. \tag{135}$$

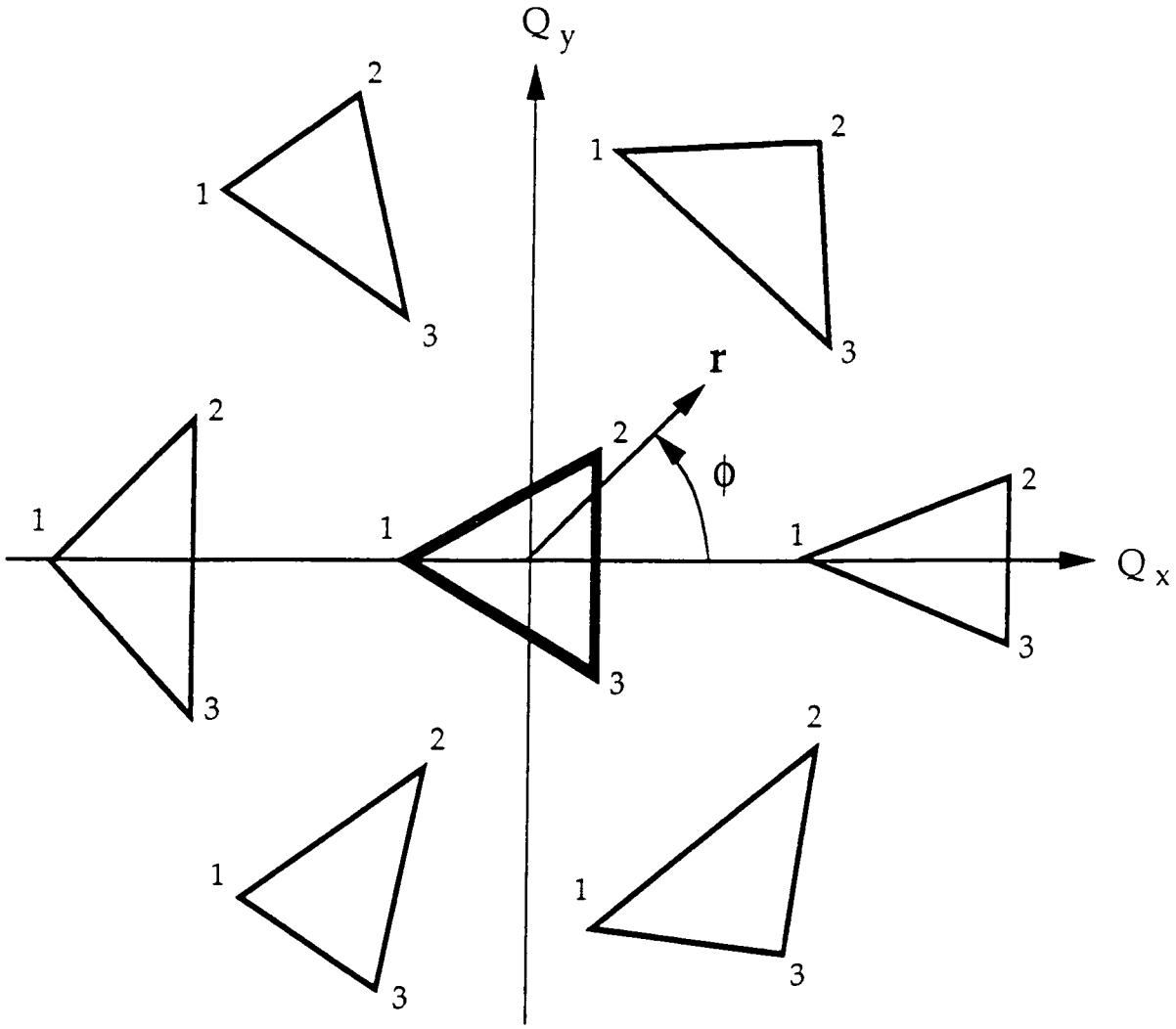

Fig. 21. The pseudorotation of the sodium trimer.

5.3 Potentials

The theory used to describe the effect of Jahn-Teller distortions on the potential energy surface of the ground state, and the excited states, of Na_3 has been discussed at length in the literature. However, a brief summary is necessary here in order to establish a consistent notation for both the ground state and the electronically excited states. The notation varies in the literature both in the symbols given to the various vibronic coupling constants and in the use of various definitions of the dimensionless constants that are extensively used as alternatives to the vibronic coupling constants. In the following, dimensionless constants will not be used and the connection between the constants described here and the dimensionless alternatives used in some of the literature will be discussed in Appendix C. The adiabatic theorem, the various coupling constants and the derivation of an adiabatic potential are discussed in Appendix B.

5.3. 1 The Ground State

This state can be understood to be the result of $E \otimes e$ mixing of the components of a degenerate electronic state. That is the components of the electronic state of symmetry E are mixed by a vibration of symmetry e.

Consider an E' electronic state in a molecule belonging to the D_{3h} symmetry group, e.g. the ground state of Na_3.

The two electronic wavefunctions of the E' term, at the equilateral geometry, are denoted $\psi_x^{E'}$ and $\psi_y^{E'}$; these are not functions of the nuclear coordinates, Q, but only of the electronic coordinates, q_e. The potential, $V(q_e, Q)$, which describes the interaction between the electrons and the nuclei, as well as the internuclear repulsion, is then expanded using a Taylor expansion about the equilateral geometry. Complex combinations of the normal modes (given above) and degenerate electronic components are now used such that $Q^+ = Q_x + iQ_y = re^{i\phi}$, $Q^- = Q_x - iQ_y = re^{-i\phi}$, $\psi^+ = \psi_x^{E'} + i\psi_y^{E'}$, and $\psi^- = \psi_x^{E'} - i\psi_y^{E'}$. Then the following linear and quadratic vibronic coupling constants, which are matrix elements of the coefficients in the potential expansion, can be defined:

$$F_E = \left\langle \psi^+ \left| \left(\frac{\partial V}{\partial Q^-} \right)_0 \right| \psi^- \right\rangle, \qquad G_E = \left\langle \psi^+ \left| \left(\frac{\partial^2 V}{\partial Q^+ \partial Q^+} \right)_0 \right| \psi^- \right\rangle. \tag{136}$$

Also, K_E, a force constant, can be defined:

$$K_E = \int \psi^+ \left(\frac{\partial^2 V}{\partial Q^+ \partial Q^-} \right) \psi^+ \, d^3r. \tag{137}$$

The secular determinant, using a basis of the purely electronic wavefunctions, ψ^+ and ψ^-, is then (as a function of r and ϕ):

$$\begin{vmatrix} \frac{1}{2}K_E r^2 - \epsilon & F_E r e^{i\phi} + G_E r^2 e^{-2i\phi}/2 \\ F_E r e^{-i\phi} + G_E r^2 e^{2i\phi}/2 & \frac{1}{2}K_E r^2 - \epsilon \end{vmatrix} = 0, \tag{138}$$

thus the adiabatic potential is:

$$\epsilon_\pm(r, \phi) = \frac{1}{2}K_E r^2 \pm r \left[F_E^2 + F_E G_E r \cos(3\phi) + \left(\frac{G_E}{2} \right)^2 r^2 \right]^{1/2}, \tag{139}$$

The lower surface is often described as a warped 'Mexican hat'; along the bottom of the trough of the 'Mexican hat' three wells occur, alternating regularly with three humps. The extremal points of the surface (r_0, ϕ_0) are:

$$r_0 = \frac{\pm F_E}{K_E \mp (-1)^n G_E}, \qquad \phi_0 = \frac{n\pi}{3}, \quad n = 0, 1, \ldots, 5, \tag{140}$$

the upper and lower signs corresponding to cases $F_E > 0$ and $F_E < 0$ respectively. If $(F_E \times G_E) > 0$ then the points at which $n = 1, 3, 5$ are saddle points and the points at

which $n = 0, 2, 4$ are minima, whereas for $(F_E \times G_E) < 0$ these two types of extremal points are interchanged. The depth of the trough, relative to the point where the two electronic components are degenerate at $r = 0$, i.e. the Jahn-Teller stabilisation energy, is given by:

$$E_s = \frac{F_E^2}{2(K_E - |G_E|)} \tag{141}$$

and the (minimum) barrier height $E_{\rm loc}$ between the minima is:

$$E_{\rm loc} = \frac{2E_s|G_E|}{(K_E + |G_E|)} = \frac{F_E^2|G_E|}{(K_E^2 - |G_E|^2)}. \tag{142}$$

This barrier height $E_{\rm loc}$ is often described as the barrier to pseudorotation.

The two wavefunctions, $\psi'_{\pm}$, which are the eigenvectors of the secular equations, are:

$$\psi'_- = \frac{1}{\sqrt{2}}(e^{i(\Omega/2)}\psi^+ - e^{i(-\Omega/2)}\psi^-), \tag{143}$$

$$\psi'_+ = \frac{1}{\sqrt{2}}(e^{i(\Omega/2)}\psi^+ + e^{i(-\Omega/2)}\psi^-), \tag{144}$$

where

$$\tan\Omega = \frac{F_E \sin\phi - |G_E| r \sin(2\phi)/2}{F_E \cos\phi + |G_E| r \cos(2\phi)/2}. \tag{145}$$

An interesting point to notice in this equation is that Ω acts qualitatively like ϕ, when $F_E > |G_E|r$, but acts qualitatively like -2ϕ when $F_E < |G_E|r$. Thus, for the portion of space given by $r < F_E/|G_E|$, the electronic wavefunction has to do two circuits of parameter space (i.e. $\phi = 0 \rightarrow 4\pi$) before it returns to its initial value, while if just one circuit is done the electronic wavefunction will change its sign. In order then that the total wavefunction be single valued on one circuit of parameter space, the nuclear wavefunction must also change its sign on doing a circuit of parameter space. This will give rise to fractional quantisation of the quantum numbers associated with the nuclear motion. This is sometimes referred to as the adiabatic sign-change theorem. This is a special case of Berry's geometrical phase which has been discussed extensively in connection with $E \otimes e$ Jahn-Teller systems [118], and has been used to explain (though probably mistakenly, see below) the spectrum of the B state of the sodium trimer [108].

Generalised valence bond and configuration interaction calculations have been done that characterise the ground state (and the excited electronic states) of Na_3 [119]. For the ground state, the stabilisation energy is given as 669 cm^{-1}, the localisation energy is 131 cm^{-1} and the dimensionless coupling constants corresponding to G_E and F_E (g and K in the notation of ref. 119) are -0.108 and 3.72 respectively. The symmetric stretch frequency is 135 cm^{-1} and ω_0 is 86 cm^{-1}, where ω_0 is defined to be the vibrational frequency for the motion along the radial displacement coordinate. The minimum in the potential in the

radial direction, r_0, is at -0.59 Å (i.e. it is an obtuse isosceles triangle) and the equilibrium value of the symmetric stretch displacement, Q_{s_0}, is 3.63 Å.

However, the fit to the absorption spectrum, to obtain the correct line intensities, yields different parameters for the ground-state surface to those given above [120]. The dimensionless coupling constants corresponding to G_E and F_E are -0.076 and 5.456 respectively, and ω_0 is 87 cm^{-1}. This corresponds to a stabilisation energy of approximately 1400 cm^{-1} and a localisation energy of approximately 199 cm^{-1}. The value of r_0 is approximately -0.74 Å (i.e. it is an obtuse isosceles triangle). This is the potential surface used here. The value of Q_{s_0} is taken to be 3.63 Å and the symmetric stretch frequency is taken to be 135 cm^{-1}, using the values from the above theoretical potential.

An *ab initio* configuration-interaction study has been done on the potential energy surface of the ground state of Na_3 [121]. The most striking feature of the surface is its extreme flatness. The molecule can pseudorotate from the obtuse-triangle minimum to the saddle point with an energy expenditure of 2.1 $kJmol^{-1}$ (175.4 cm^{-1}); this is the localisation energy. The transformation from obtuse to acute via the equilateral form requires an activation energy of only 6.7 $kJmol^{-1}$ (559.7 cm^{-1}); this is the Jahn-Teller stabilisation energy. Even substantially larger excursions are relatively effortless. A linear symmetric conformation lies only 12.5 $kJmol^{-1}$ (1044.2 cm^{-1}) above the minimum. The normal mode frequencies calculated in the *ab initio* configuration-interaction study are: symmetric stretch 147 cm^{-1}; bending 84 cm^{-1}; asymmetric stretch 89 cm^{-1}. The value of Q_{s_0} is given as 3.5 Å. An analytic representation of this potential has been presented [122].

Despite some differences between the potential obtained from the fit to the experimental spectrum and those calculated theoretically, they all have the same general features, i.e. very flat with a conical intersection at the equilateral geometry. As well as this qualitative agreement, there is also some quantitative agreement, e.g. the frequency for the radial motion (or bending frequency at small distortions) compares well in all the potentials. The *ab-initio* potential reproduces the barrier to pseudorotation quite well (175.4 cm^{-1} compared to the experimental value of 199 cm^{-1}), though the potential obtained from the generalised valence bond calculations underestimates the value substantially (131 cm^{-1}). Both the theoretical potentials underestimate the Jahn-Teller stabilisation energy. The values of Q_{s_0} and of the symmetric stretch frequency given by the theoretical potentials agree quite well, so that it appears to be reasonable to use the values obtained from the generalised valence bond calculations in the potential used here.

The eigenstates and eigenvalues

In order to understand the dynamics of a system it is often helpful to have some

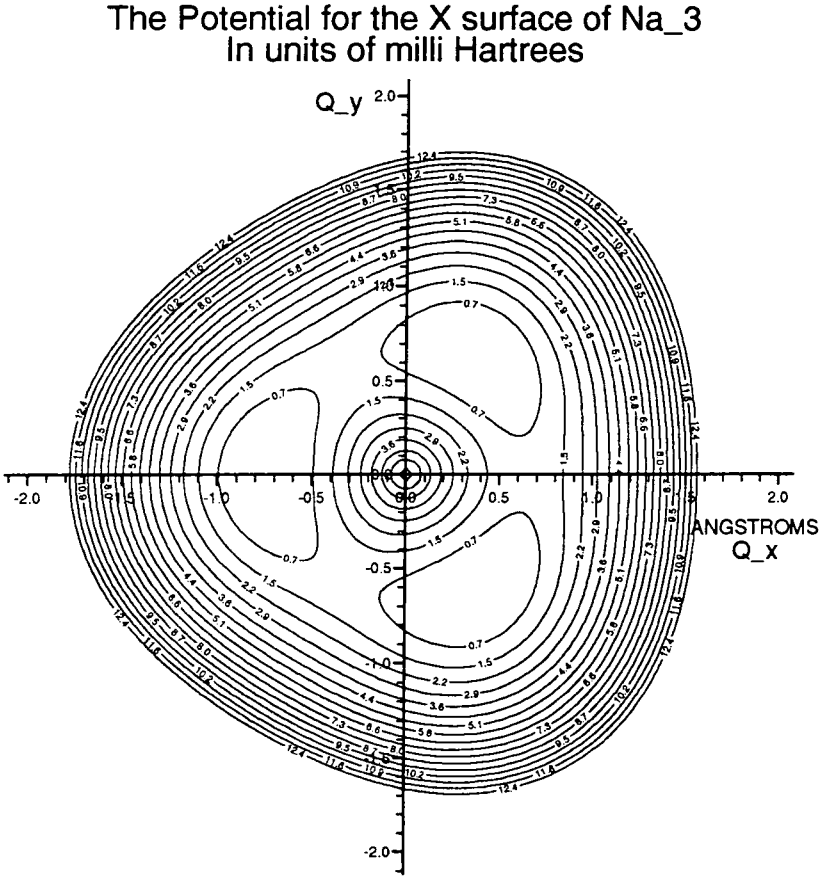

Fig. 22. Contour diagram of the potential of the ground state used in this work (1 mE_h $\approx$ 219 cm^{-1}).

knowledge of the eigenstates and corresponding eigenvalues.

Consider first the linear Jahn-Teller effect, where the quadratic coupling constant G_E is zero, and there is no barrier to pseudorotation. The potential for the lower surface will be of the form:

$$V(r) = \frac{1}{2}K_E r^2 - rF_E, \tag{146}$$

which can be expressed as

$$V(r) = \frac{1}{2}K_E(r - r_0)^2 - E_s, \tag{147}$$

where r_0 is equal to F_E/K_E and E_s is equal to $F_E^2/2K_E$. This potential, which is harmonic about r_0, is radially symmetrical and obviously is not dependent on ϕ.

Thus, the motion on the potential can be described by free 'rotations' along the trough together with radial vibrations to and fro across the trough [123]. The eigenfunctions can be approximated as a product of angular motion and radial motion:

$$\Psi_{u,j} = \frac{\exp[ij\phi]N_u H_u[\alpha(r - r_0)]\exp[-\alpha(r - r_0)^2]}{\sqrt{2\pi r}}, \tag{148}$$

where j is a 'pseudorotational' quantum number for the angular motion and u is a vibrational quantum number for radial motion. The constant α is equal to $mK_E/\hbar^2$ and $H_u[\alpha(r - r_0)]$ is a Hermite polynomial of order u, with normalisation constant N_u. The quantum number j will be half integral due to the adiabatic phase change explained above. This approximate description of the eigenfunctions is valid at low energies when the molecule is assumed to have a constant moment of inertia, i.e. the rotations are at r fixed at r_0.

Also, the energy levels can be described approximately by these two quantum numbers u and j:

$$E_{u,j} = (u + \tfrac{1}{2})\omega_E^2 + Aj^2, \tag{149}$$

where A is a pseudorotational constant, which can be given by:

$$A = \frac{\hbar^2}{2mr_0^2} \qquad \text{or} \qquad A = \frac{(\hbar\omega_E)^2}{4E_s}, \tag{150}$$

where ω_E is the vibrational frequency of the degenerate modes, which is related to K_E, and m is the reduced mass of the modes (in this case just the mass of a sodium atom).

This description of the energy levels is for G_E equal to zero. For small G_E it will continue to be a good description, but as G_E gets larger and the wells in the 'trough' become deeper, it will no longer be even approximately correct. The quadratic coupling constant G_E couples together the radial motion and the angular motion through terms in the potential. This means that the motion in the radial direction will depend on the angular motion. The extent to which this occurs can be measured by the circularity of the potential. The circularity of the potential describes how much the value of r, along the minimum energy path around the 'trough' of the P.E.S., varies with ϕ. For the functional form of the potential described here, this will depend on the value of the quadratic coupling constant, which also determines the barrier to pseudorotation. A fundamental problem with the functional form used for the potential here may be the linking together of the circularity and the barrier to pseudorotation.

5.3. 2 The B Excited State

The generalised valence bond and configuration interaction calculations that have been done on the excited electronic states of Na_3 indicate that the B state involves a complicated mixing between an electronic state with E' symmetry and an A_1' state, in which coupling between the A_1' and the E' state dominates the usual coupling between E' components [119]. This has been supported both by an analysis of the vibrational spectrum [120] and by recent rotationally resolved experiments [124] [125].

Consider an E' electronic state, with corresponding wavefunctions at the equilateral geometry, $\psi_x^{E'}$ and $\psi_y^{E'}$, at energy $\epsilon_{E'}$, close in energy to a A_1' electronic state with corresponding wavefunction at the equilateral geometry, $\psi^{A_1'}$, at energy $\epsilon_{A_1'}$, in a molecule belonging to D_{3h} symmetry group, e.g. the B state of Na_3 [119][120]. Again these electronic wavefunctions are functions only of the electronic coordinates. As described above it is a straightforward matter to find the normal mode vibrations of this molecule using group theory; they are found to belong to the irreducible representations a_1' and e'. Only the e' vibrations will be considered at present since the a_1' vibration does not change the symmetry of the adiabatic potential. The secular determinant that must be solved, again using complex combinations of the normal modes and degenerate electronic components such that $Q^+ = Q_x + iQ_y = re^{i\phi}$, $Q^- = Q_x - iQ_y = re^{-i\phi}$, $\psi^+ = \psi_x^{E'} + i\psi_y^{E'}$, and $\psi^- = \psi_x^{E'} - i\psi_y^{E'}$, is then:

$$\begin{vmatrix} \frac{1}{2}K_E r^2 + \epsilon_{E'} - \epsilon & F_E r e^{i\phi} + (G_E/2) r^2 e^{-2i\phi} & P r e^{-i\phi} + (f/2) r^2 e^{2i\phi} \\ F_E r e^{-i\phi} + (G_E/2) r^2 e^{2i\phi} & \frac{1}{2}K_E r^2 + \epsilon_{E'} - \epsilon & P r e^{i\phi} + (f/2) r^2 e^{-2i\phi} \\ P r e^{i\phi} + (f/2) r^2 e^{-2i\phi} & P r e^{-i\phi} + (f/2) r^2 e^{2i\phi} & \frac{1}{2}K_A r^2 + \epsilon_{A_1'} - \epsilon \end{vmatrix} = 0, \quad (151)$$

where F_E and G_E are the linear and quadratic vibronic coupling constants within the E state, and P and f are the linear and quadratic vibronic coupling constants between the A_1' and E' state. These coupling constants are again the matrix elements of the coefficients in the potential expansion.

A number of approximations are now made in order to obtain a reasonably simple solution [119]. These are, first, that F_E and G_E are set equal to zero, implying that there is no interaction within the E state; secondly, that the force constants in the two states are the same, i.e. $K = K_E = K_A$; and finally, that $|Pr/K| \approx r^2 \gg |\epsilon_{E'} - \epsilon_{A_1'}|$, which is the case for large distortions. The adiabatic potential obtained is:

$$\epsilon_0 = \frac{Kr^2}{2} \quad (152)$$

$$\epsilon_\pm = \frac{Kr^2}{2} \pm r\left[2P^2 + 2Pfr\cos(3\phi) + \left(\frac{fr}{\sqrt{2}}\right)^2\right]^{1/2}. \quad (153)$$

The lowest surface ϵ_- has three-fold symmetry using these approximations, with equivalent minima ($-$ sign) and saddle points ($+$ sign) defined by:

$$-\cos(3\phi_0) = \pm 1, \qquad r_0 = \sqrt{2}\,P/(K \pm \sqrt{2}\,|f|), \quad (154)$$

with

$$E_s = \frac{P^2}{(K - \sqrt{2}\,|f|)}, \qquad E_{\rm loc} = \frac{2\sqrt{2}\,|f|P^2}{(K^2 - 2f^2)}, \quad (155)$$

where E_s is measured from $\epsilon_{E'}$. An interesting point to notice here is the similarity in the expressions obtained above for two-state and three-state interactions, equations (139) and (153); with a change in definition $\sqrt{2}\,f = G_E$ and $\sqrt{2}\,P = F_E$ the expressions become identical.

The B state corresponds to the lowest of these three surfaces, i.e. ϵ_-. The eigenstates of this potential can be approximated in a similar way to that described for the X state. The energy levels of this potential can also be expressed in terms of two quantum numbers, u and j, using equation (149), provided that the quadratic coupling constant f is very small. However, in this case there is *not* a conical intersection at the origin so that the quantum number j is integral. Thus the assignment of the vibrational spectrum using half-integral j is not correct [108].

From the above mentioned generalised valence bond calculations, the stabilisation energy of the B state is given as 1073 cm^{-1}, the localisation energy is 72 cm^{-1} and the dimensionless coupling constants corresponding to f and P are $-0.035/\sqrt{2}$ and $4.90/\sqrt{2}$ respectively. The symmetric stretch frequency is 110 cm^{-1} and ω_0 is 86 cm^{-1}. The value of r_0 is -0.66 Å (i.e. it is an obtuse isosceles triangle) and Q_{s_0} is 3.99 Å.

However, the fit to the absorption spectrum again yields different parameters for this surface [120]. For this state the parameters are in fact quite different from those obtained from the generalised valence bond calculations, giving different values for the radial frequency and the barrier to pseudorotation. The dimensionless coupling constants corresponding to f and P are $-0.0063/\sqrt{2}$ and $4.34/\sqrt{2}$ respectively, and ω_0 is 127 cm^{-1}. This corresponds to a stabilisation energy of 1196 cm^{-1} and a localisation energy of 15 cm^{-1}. The value of r_0 is approximately -0.48 Å (i.e. it is an obtuse isosceles triangle). This is the potential surface that is used here. The value of Q_{s_0} is taken to be 3.7 Å, because there is relatively little excitation seen in this coordinate in the static spectroscopy, so that the equilibrium value of this coordinate must be similar to that of the ground state (3.63 Å) . The symmetric stretch frequency is taken to be 110 cm^{-1}, using the value from the generalised valence bond calculations, since it appears to compare well with the value obtained from the femtosecond experiments.

The B state has been found from the experimental excitation spectrum to be 625 nm (16000 cm^{-1}) above the ground state, i.e. in T.P.I. experiments the origin of the $0-0$ band for the B state is at 625 nm.

5.3. 3 The Cation—Na_3^+

The ground state of Na_3^+ is not subject to Jahn-Teller distortions, because Na_3^+ has a doubly occupied fully bonding orbital ($1a_1'$), whereas the neutral species has an additional

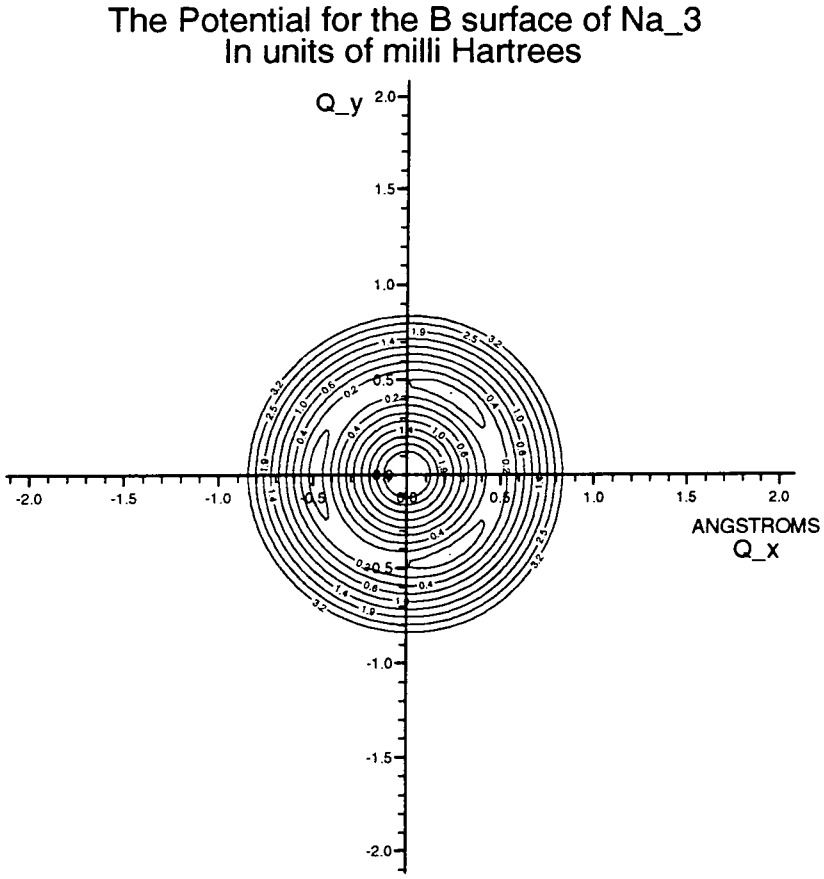

Fig. 23. Contour diagram of the potential of the B excited state used in this work (1 mE_h $\approx$ 219 cm^{-1}).

singly occupied antibonding orbital ($1e'$); this also means that the bond energy of the cation is expected to be greater than that of the neutral trimer [126]. It has been suggested that the surface is very similar to that of the neutral species, apart from effects due to the conical intersection, i.e. it is very flat [127] [128]. An *ab-initio* potential surface for Na_3^+ has been calculated and presented in an analytical form [129]. On fitting to the anharmonic spectrum the normal frequencies were calculated to be: symmetric stretch $\nu_1 = 142$ cm^{-1}; and doubly degenerate bend $\nu_2 = 101$ cm^{-1}. The value of Q_{s_0} is calculated to be 3.443 Å.

The ionisation energy of Na_3, found from experiments, is approximately 4 eV (32261 cm^{-1}) [130].

5.4 The Wavefunctions

The ground-state vibrational wavefunction of Na_3, which is used as the initial state in the wavepacket calculation, and the ground-state wavefunction of Na_3^+, which is used in calculating the ion signal (see later), are calculated from their potentials [120] [129] using Tennyson's variational method [131]. The program TRIATOM [132] [133] is used with

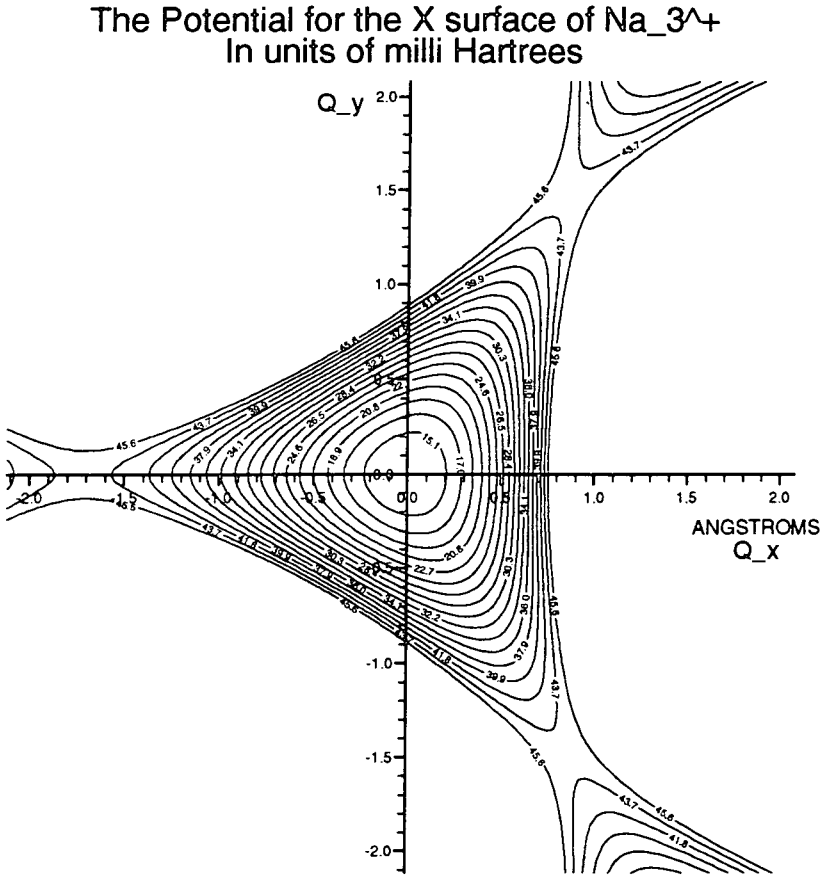

Fig. 24. Contour diagram of the *ab-initio* potential of the ground state of the ion (1 mE_h $\approx 219\ \mathrm{cm}^{-1}$).

Jacobi, or scattering, coordinates for both systems.

The wavefunctions are expressed as products of Legendre polynomials, $\Theta_j(\theta)$, (for $J_{\mathrm{tot}} = 0$), and Morse oscillator-like functions, $H_n(r)$:

$$\Psi_l(r_1, r_2, \phi) = \sum_{jmn} d^l_{jmn} \Theta_j(\theta) r_1^{-1} H_n(r_1) r_2^{-1} H_m(r_2), \tag{156}$$

where H_m and H_n are given by:

$$H_n(r) = \beta^{1/2} N_{n\alpha} \exp(-\frac{1}{2}y) y^{(\alpha+1)/2} L^\alpha_n(y), \tag{157}$$

with

$$y = A\exp[-\beta(r-r_e)], \quad \text{where} \quad A = \frac{4D_e}{\omega_e}, \qquad \beta = \omega_e \left(\frac{\mu}{2D_e}\right)^{1/2}, \quad \text{and} \quad \alpha = \text{integer}(A). \tag{158}$$

The parameters μ, r_e, ω_e and D_e can be associated with the reduced mass, the equilibrium bond length, the energy of the fundamental vibration and the dissociation energy of the bond. These parameters are optimised by minimising the energy of the ground state, using

a basis set which is a subset of the full set used for the calculation of the wavefunction. The values used in the present work are listed in table 4. L_n^α is an associated Laguerre polynomial, with a normalisation constant $N_{n\alpha}$. In the systems under consideration, because of the parameters used, the values of α are very large, making normalisation of these functions computationally intricate.

Table 4. Optimised parameters for Na_3 and Na_3^+ basis sets.

coordinate	μ/a.m.u.	r_e/a_0	D_e/E_h	ω_e/E_h
Na_3, r_1	22.98977	8.277	0.016081	0.0005566
Na_3, r_2	22.98977	4.723	0.017705	0.0007180
Na_3^+, r_1	22.98977	6.487	0.050770	0.0005214
Na_3^+, r_2	22.98977	5.661	0.086270	0.0005081

The coefficients, d^l_{jmn}, are found using TRIATOM and then used in equation (156) to determine the appropriate wavefunction.

The wavefunctions in both cases are found to be approximately Gaussian, centered at the equilibrium geometry of the molecule. Thus, the wavefunction of the X state of Na_3 was found to be approximately Gaussian at ($Q_x = -0.74$ Å,$Q_y = 0.0$) with an energy of 136.6 cm^{-1} above the bottom of the 'trough'. The wavefunction of the X state of Na_3^+ was found to be approximately Gaussian at ($Q_x = 0.0, Q_y = 0.0$) with an energy of 150.4 cm^{-1} above the bottom of the well.

5.5 The Simulation of the Experiments

As stated previously, the time-dependent or wavepacket method is used to model the time-dependent experiments on the sodium trimer. This method can be divided into three distinct parts. First, the initial state must be defined. Secondly, the wavepacket must be propagated. Thirdly, the observables must be extracted.

5.5. 1 The Preparation of the Initial State

Before the pump laser is turned on the Na_3 is in its ground vibrational state in its ground electronic state. When the pump laser is turned on the Na_3 is promoted to various vibrational states in its B electronic state. Thus, the pump laser prepares the initial wavepacket on the B state which is to be propagated in time and then probed by a second laser pulse.

Therefore, what is required is to model the effect of the pump laser and so the creation of the initial wavepacket on the B state from an initial wavepacket on the X state. To

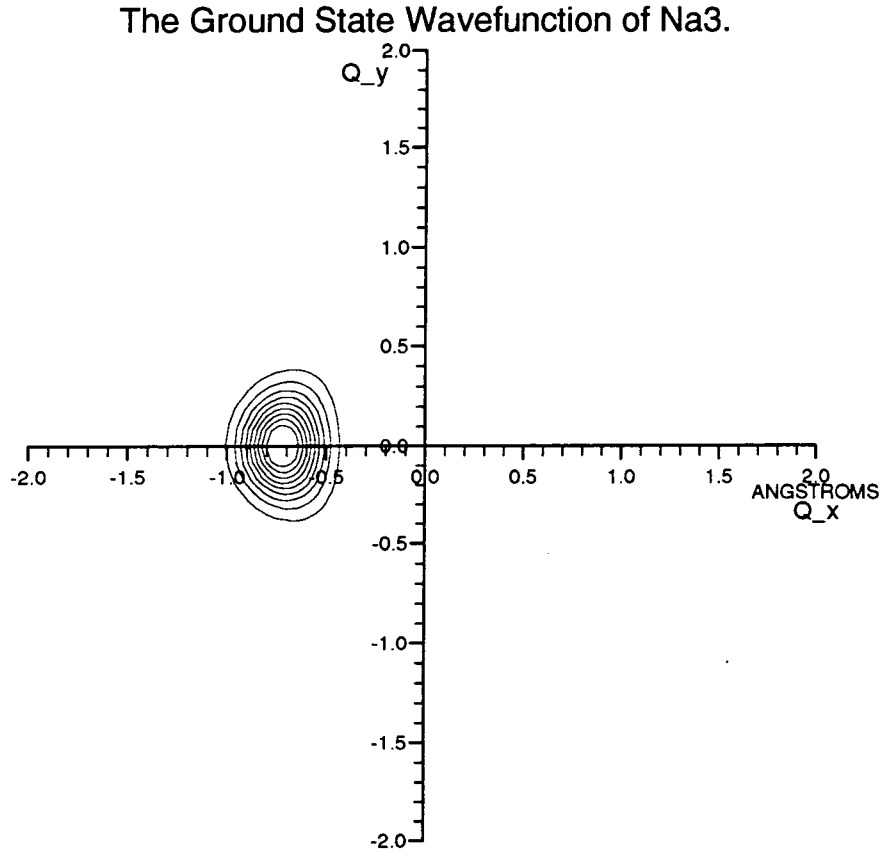

Fig. 25. Contour diagram of the ground-state wavefunction of Na_3.

describe the short pulse excitation process, i.e. the effect of the laser pulse, time-dependent first-order perturbation theory is used [134]. The wavefunction can be written as:

$$\Psi_B(t) = i \int_0^t U_B(t-t')[\mu_{BX} E(t')] U_X(t') \Psi_X(0)\, dt', \tag{159}$$

where $\Psi_X(0)$ is the initial wavefunction on the X state, U_B and U_X are the time evolution operators used to propagate the wavefunctions in time on the appropriate surfaces. Here, $U_X(t')$ is simply $e^{-iE_X t'}$, where E_X is the energy of the ground vibronic state of the X state beneath the ground vibronic state of the B state (-16000 cm^{-1}), since $\Psi_X(0)$ is stationary, i.e. is an eigenfunction of the ground-state Hamiltonian. The transition dipole function, μ_{BX}, is approximated to a constant in the present work. The electric field due to the laser is of the form:

$$E(t) = E_0 f(t) e^{-i\omega t}, \tag{160}$$

where E_0 is the electric field vector and $f(t)$ describes the temporal shape of the laser pulse, which has a Gaussian profile in this case, and ω is the central frequency of the pulse.

In physical terms this can be considered in the following way. The laser pulse, although short, is not a δ function of time. (If the laser pulse were a δ function the wavepacket on the

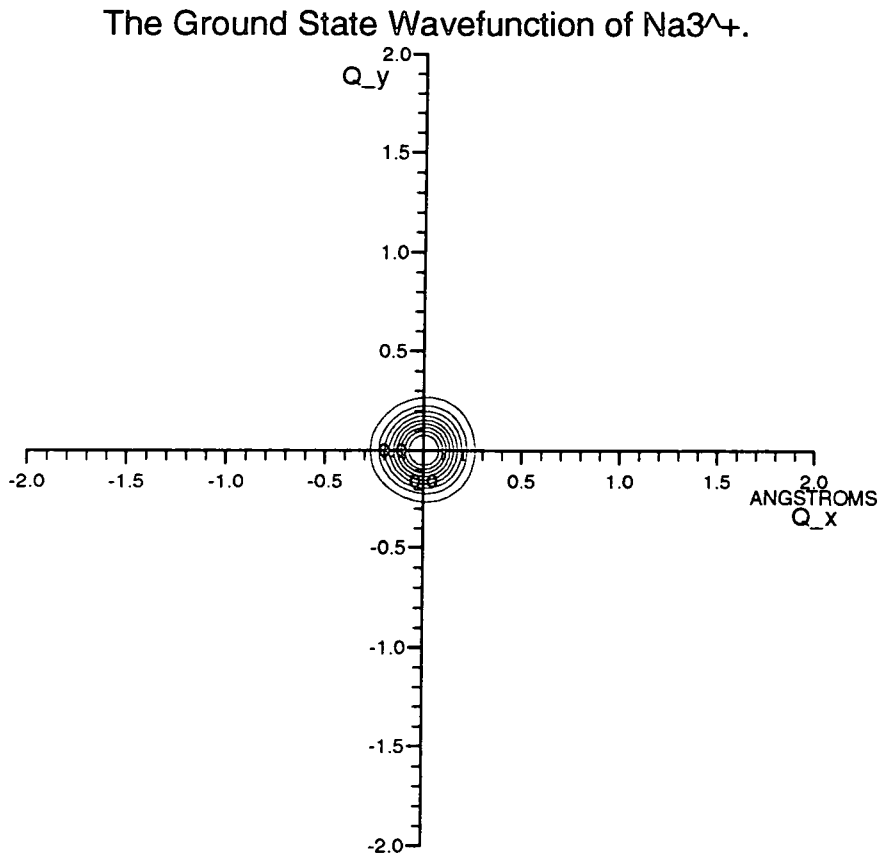

Fig. 26. Contour diagram of the ground-state wavefunction of Na_3^+.

ground state would be moved vertically up onto the upper state since the complete certainty in the time of the pulse would lead to complete uncertainty in its energy, hence it would be equivalent to 'white light'.) Thus, the initial wavefunction will not be promoted to the excited state instantaneously. The part of the wavefunction which has not been promoted will evolve on its own surface (for a time equal to t'), until the time when it is promoted (at time equal to t'), after which it will evolve on the excited state potential surface (for a time equal to $t - t'$). What this means in terms of the actual wavepacket generated on the excited electronic state has been considered in detail in a series of papers by Williams and Imre [135] [136] [137]. They showed that each of the parts of the wavepacket promoted onto the excited state has a particular phase. Once on the excited state its phase will begin to vary depending on the energy which the wavepacket was given by the laser pulse (how much it is detuned from the zero of energy on the potential energy of the excited state) and the Hamiltonian of the state. Parts of the wavepacket which arrive subsequently will interfere with the wavepacket already on the excited state either constructively or destructively depending on how much the phase of the wavepacket on the excited state has changed from when 'it arrived'. Williams and Imre showed that for certain laser pulses

the norm on the excited could initially increase, but then show a decrease, in the case of destructive interference occurring on the excited state.

The calculation is carried out by discretising the time integral and then relating the wavefunction at time $t + \Delta t$ to the wavefunction at t to give:

$$\Psi_B(t + \Delta t) = U_B(\Delta t)\Psi_B(t) + i\Delta t f(t + \Delta t)e^{-i(\omega + E_X)(t+\Delta t)}\Psi_X(0), \qquad (161)$$

where t is measured from the beginning of the pump laser pulse. The Δt in equation (161) must be chosen to be small enough for the excitation process to be properly described. The calculations were repeated at shorter timesteps in order to check that the calculations were converged with respect to this Δt.

5.5. 2 Propagation of the Wavepacket

The time-dependent Schrödinger equation is used to propagate the wavefunction in time. There are several methods for propagating the initial wavefunction, which have been discussed previously. Here a global propagator carries out the propagation. This type of propagator uses a polynomial expansion of $U(t)$, where the form of this operator is given by:

$$\Psi(t) = U(t)\Psi(0) = \exp\left[\frac{-i}{\hbar}H\,dt\right]\Psi(0). \qquad (162)$$

Thus an expansion of the type:

$$U(t) \approx \sum_{k=0}^{N} p_k P_k(-iH\Delta t/\hbar), \qquad (163)$$

is used, where P_k are complex Chebyshev polynomials.

The potential used for the calculation (i.e. V) is that for the B excited state. The zero of energy is taken to be at the bottom of the 'trough', plus a constant which corresponded to an approximate zero point energy of the surface. This zero point energy is approximated using:

$$E_{ZP} = \frac{\omega_0}{2} + \frac{\omega_\phi}{2}.$$

Thus the zero of energy is the stabilisation energy, E_s, less the approximate zero point energy, E_{ZP}, beneath the energy of the equilateral geometry.

5.5. 3 Extracting the Observables

The Na_3^+ signal

The quantity that is measured in the experiments is the Na_3^+ signal. The Na_3^+ is created by the probe laser promoting the wavepacket on the B state to the ground electronic state of the ion.

Therefore, what is required is to model the effect of the probe laser and so the creation of a wavepacket on the ground ionic electronic state from the time-evolving wavepacket on the B state. The effect of the probe laser is modelled in a similar way to the effect of the pump laser. There is an added complication in this case, since the state formed is ionic [138]. The electron, which is ejected on formation of the Na_3^+, can have a range of energies and a calculation must in principle be done corresponding to each of these energies. However, in the present work it is assumed that the kinetic energy of the departing electron is approximately zero. This can be done because the zero kinetic energy signal of the electron is very similar to that of the Na_3^+ signal [111]. Thus the wavefunction on the potential energy surface of the ground state of the cation can be calculated, using the wavefunction on the B state, to be:

$$\begin{aligned}\Psi_{X^+}(t_D, t_2 + \Delta t) =& U_{X^+}(\Delta t)\Psi_{X^+}(t_D, t_2) \\ &+ i\Delta t f(t_2 + \Delta t)e^{-i\omega(t_2+\Delta t)}U_B(t_D + t_2 + \Delta t)\Psi_B(t_D = 0).\end{aligned} \tag{164}$$

t_D is the time delay between the pump and probe lasers, i.e. the time between the centre of the pump and probe laser pulses. t_2 is a measure of the time for which the probe laser has been on, i.e. a measure of the time for which the probe laser has created probability density on the X state of the ion, and is varied between $-t_{\text{mid}}$ and t_{mid}. The probe and the pump laser pulses are each assumed to be centred at a time of t_{mid} from the time when they are switched on. Thus, the calculation is done until the probe laser has died off to zero, at a time $t_2 = t_{\text{mid}}$, i.e. until the norm of the wavefunction on the X state of the ion becomes constant. The pump and probe laser are taken not to overlap temporally in this calculation, so that for values of t_D of less than $2 \times t_{\text{mid}}$ no calculation is done.

Again the transition dipole function for ionisation, μ_{X^+B}, is taken to be constant. Also $f(t)$ is again taken to have a Gaussian profile.

The Na_3^+ signal is taken to be the norm of the wavefunction on the X state of the ion, i.e.

$$S(t_D) = \langle \Psi_{X^+}(t_D, t_{\text{mid}}) | \Psi_{X^+}(t_D, t_{\text{mid}}) \rangle. \tag{165}$$

Values of $S(t_D)$ are not obtained for t_D less than $2 \times t_{\text{mid}}$, because of the requirement that the pump and probe laser pulses do not overlap. This function is Fourier transformed to give a spectrum which contains frequencies characteristic of the motion on the B state potential energy surface:

$$S(\omega) = \int_{-\infty}^{\infty} S(t_D)e^{2\pi i\omega t_D}\, dt = 2\Re \int_0^{\infty} S(t_D)e^{2\pi i\omega t_D}\, dt. \tag{166}$$

The last equality arises because the frequency spectrum is always real. The magnitude of this function is used to represent the power density spectrum.

An approximate method

To treat the probe laser exactly is computationally expensive, and can only be done for the femtosecond experiment. Therefore an attempt is made to approximate the observable, the Na_3^+ signal. An assumption is made that the only state of the ion which is populated by the probe laser pulse is the ground vibrational state. The justification of this assumption, for the femtosecond experiment, is that the energy available in the probe laser is restricted, so that only the ground state can be reached energetically. Thus the Na_3^+ signal is thought of as the time-dependent square modulus of the overlap of the wavepacket with the wavefunction of the ground state of Na_3^+.

The square modulus of the overlap function, $A(t_D)$, is given by:

$$A(t_D) = \left| \int \int \Psi_{(X_0^+)}(0)^* \Psi_B(t_D)\, dQ_x dQ_y \right|^2 , \tag{167}$$

where $\Psi_{(X_0^+)}$ is the ground-state wavefunction of the ionised state, and the delay time, t_D, is the time measured from the centre of the pump laser pulse. (Both the wavefunctions depend on the two coordinates.) Another assumption made is that $\Psi_{(X_0^+)}$ can be considered to be essentially independent of time, i.e. at the same energy as the zero of the calculation, which implies that the ionisation potential of the B state is equal to the central frequency of the laser pulse. The Fourier transform of this overlap function (over a time from the end of the pump laser pulse to the end of the propagation) is used to give the power density spectrum.

In the picosecond experiments where laser pulses with various different central frequencies are used it may be appropriate to overlap the wavepacket on the B state with different vibrational eigenfunctions of the ionic state. For these experiments, *if* the zero kinetic energy signal of the electron can also be assumed to be similar to the ion signal, the approximation can be expected to work particularly well. (There is no experimental evidence to support this at present.) This is because the laser pulse has a very narrow energy spread and because vibrational levels in the ionic state are widely spaced. This implies that, if the departing electron has negligible kinetic energy, only one vibrational state of the ion will be populated.

It is interesting to compare these results, i.e. those obtained using the overlap function and giving an approximate ion signal, to those which are obtained by the previous method, which treats explicitly the effect of the probe laser. Thus, for the femtosecond experiment the quality of this approximation can be judged, and a decision made on whether the approximation should be used with the picosecond experiments. The use of the modulus of the autocorrelation function has also been suggested as an approximate ion signal [115]. This was suggested because for the picosecond experiments the largest signal is obtained

at zero time delay, implying that the best conditions for ionisation were described by the initial wavefunction. However, this proposition seems physically unreasonable.

Other observables

Besides the experimental signal and the pictures of the wavefunction at each timestep, some observables were calculated, in order to gain a better understanding of the chemical dynamics of this system. In particular the study of these can help to elucidate the coupling between the radial and angular motion.

The norm and energy were calculated:

$$\text{norm}(t) = \int \Psi_B(t)^* \Psi_B(t)\, d\tau, \tag{168}$$

where t is measured from the beginning of the pump laser pulse, and

$$E_T(t) = \frac{\int \Psi_B(t)^* H \Psi_B(t)\, d\tau}{\int \Psi_B(t)^* \Psi_B(t)\, d\tau}. \tag{169}$$

It was particularly interesting to note how the norm varied whilst the pump laser was still 'on'. The normalisation is required since the norm of the B state changes whilst the pump laser pulse is still on.

An attempt was made to calculate the energy in each mode, that is the energy in the radial mode and the energy in the angular mode, so that the transfer of energy between modes could be followed. This was done by splitting the Hamiltonian into radial-like and angular-like parts. This was not entirely straightforward since the potential is a complicated mixture of both coordinates. The Hamiltonian for the radial motion was approximated as:

$$\begin{aligned} H_r =& \frac{-\hbar^2}{2m}\left[\frac{1}{4r^2} + \frac{d^2}{dr^2}\right] \\ &+ \left[\frac{r^2 K}{2} - P' r + \frac{1}{2} f' r^2 - \frac{1}{2}\frac{f'^2 r^3}{P'} + \frac{1}{8}\frac{f'^4 r^5}{P'^3} - \frac{2}{8}\frac{f'^3 r^4}{P'^2}\right], \end{aligned} \tag{170}$$

where $P' = \sqrt{2}\,P$ and $f' = \sqrt{2}\,f$, and the Hamiltonian for the angular motion was approximated as:

$$\begin{aligned} H_\phi =& \frac{-\hbar^2}{2m}\left[\frac{1}{r^2}\frac{d^2}{d\phi^2}\right] \\ &+ \left[-f' r^2 \cos^2\left(\frac{3\phi}{2}\right) + \frac{1}{8}\frac{f'^2 r^3}{P'}\cos^2(3\phi) + \frac{2}{8}\frac{f'^3 r^4}{P'^2} 2\cos\left(\frac{3\phi}{2}\right)\right]. \end{aligned} \tag{171}$$

The average values of r and $\cos\phi$ were also calculated:

$$\langle r(t)\rangle = \frac{\int \Psi_B(t)^* r \Psi_B(t)\, d\tau}{\int \Psi_B(t)^* \Psi_B(t)\, d\tau}, \tag{172}$$

and

$$\langle \cos\phi(t) \rangle = \frac{\int \Psi_B(t)^* \cos\phi \Psi_B(t)\, d\tau}{\int \Psi_B(t)^* \Psi_B(t)\, d\tau}. \tag{173}$$

The autocorrelation function

In Chapter 2 it was shown how the autocorrelation function could be used to obtain information about the eigenvalues of a system. In the present work, the overlap between the wavefunction created on the B state at the end of the pump laser pulse, and propagating wavefunction was calculated:

$$C(t) = \langle \Psi_B(2 \times t_{\text{mid}}) | \Psi_B(t) \rangle \tag{174}$$

The Fourier transform of the autocorrelation function (over a time from the end of the pump laser pulse to the end of the propagation) contains information on the energies of the eigenstates of the surface that are present in the wavepacket. In the case of the femtosecond experiment, the pulse laser has a wide energy range, so that the wavepacket produced will be made up of many different eigenstates. Thus the frequency spectrum produced by the femtosecond calculation is nearly equivalent to the spectrum obtained from the time-independent experiments on the B state of the sodium trimer. The energy levels should be identical, but the relative magnitudes of the peaks will differ. If a laser pulse equivalent to 'white light' is used the spectrum obtained would correspond exactly to the absorption spectrum. In the case of the picosecond experiment, the pulse laser has a narrow energy range, so that the wavepacket produced will be made up of very few eigenstates. The frequency spectrum obtained from these calculations will be less useful to compare to the time-independent experiments, but will give information about the eigenstates that are present in the wavepacket.

As mentioned above, that it has been suggested [115] that the 'autocorrelation function' be used to model the ion signal. This was because in the picosecond experiments the largest ion signal was found for zero delay time, i.e. the wavefunction at zero time delay described the best conditions for ionisation. Thus, the suggestion is that the ion signal be modelled by the function formed by the overlap of the wavefunction at zero delay time, i.e. at a time corresponding to the middle of the pump laser pulse, and the propagating wavefunction. Here, this is not the true autocorrelation function; it is just another overlap function, which will be called the zero time delay overlap function:

$$C_F(t_D) = \frac{\langle \Psi_B(t_D = 0) | \Psi_B(t_D) \rangle}{\sqrt{\langle \Psi_B(t_D) | \Psi_B(t_D) \rangle}}. \tag{175}$$

Thus it has been suggested that the modulus of this function could be used to model the ion signal.

5.6 The Results

Calculations were done to simulate both the femtosecond and the picosecond time-dependent experiments. That is the calculations were done several times: once for a laser pulse of width 70 fs (F.W.H.M.), centred at a time of 120 fs, with central frequency, ω, of 16129 cm^{-1}; once for a laser pulse of width 1.3 ps (F.W.H.M.), centred at a time of 2.4 ps, with central frequency of 16136 cm^{-1}, and then again with the same pulse width but with central frequencies of 16207 cm^{-1}, 16129 cm^{-1} and 16000 cm^{-1}; the calculations were also done assuming a laser pulse of 'white light', i.e. the initial wavefunction was moved vertically from the X state to the B state.

5.6. 1 The Initial Wavefunction

Several graphics programs have been written, utilising the Uniras and graPHIGS graphics subroutine libraries, to visualise the motion of the wavepackets in the (r, ϕ) plane. The formation of the initial wavefunction on the B state from the wavefunction on the X state was followed by taking 'snapshots' of the wavefunction at intervals in time, while the pump laser pulse was 'on'.

The simulations of the two time-resolved experiments, i.e. the femtosecond and the picosecond, produce very different initial wavefunctions. For both simulations at the beginning of the pump laser pulse the wavepacket produced is very similar to the ground-state wavefunction on the X state. Initially, the molecule 'thinks' that the laser pulse is 'white light', i.e. the wavefunction on the ground state is moved vertically to the B state. However, as the laser pulse stays on, the wavepacket produced begins to show the characteristics of the frequency of the laser pulse, the true width of the laser pulse and the potential energy surface on which the wavepacket is evolving. This comes about as the different parts of the wavepacket, which 'arrived' at different times, interfere with each other to produce the 'final' wavepacket.

The pictures that demonstrate these results for the femtosecond experiment are shown in figure 27. The time in this figure is measured from the beginning of the pump laser pulse.

In the femtosecond experiment, there is a fairly large energy spread in the laser pulse, approximately 300 cm^{-1}, so that the wavepacket produced is a superposition of very many different eigenfunctions of the B state. Thus, the wavepacket produced in the simulation is expected to be in some ways similar to the wavepacket produced by vertical excitation. This means that the wavepacket will be radially excited as the positions of r_0 are different on the X and B surfaces (by approximately 0.27 Å). As suggested above, at the beginning of the pump laser pulse the wavepacket on the B state is very similar to the ground-state

Table 5. Eigenfunctions present on the B surface in the picosecond experiment.

Laser Wavelength	Eigenfunctions Present
625 nm	$u = 0, j = 0, 1, 2$
620 nm	$u = 1, j = 0, 1, 2$
619.7 nm	$u = 1, j = 0, 1, 2$
617 nm	$u = 1, j = 4, 5 \quad u = 0, j = 8$

wavefunction on the X state. However, it can be seen that by the middle of the laser pulse the wavepacket has moved substantially towards the equilibrium value of r, i.e. the r_0 for the B surface. By the end of the pulse the wavepacket has moved away from its equilibrium radial value towards the equilateral geometry. In doing so it has 'hit' the curved potential wall near the origin of the coordinate space and has spread out angularly, as well as moving towards slightly larger values of r.

The pictures that demonstrate these results for the simulation of the picosecond experiments at different laser frequencies are shown in figures 28 → 31.

In the picosecond experiment there is very little energy spread around the central frequency of the pulse, approximately 15 cm^{-1}. Thus it is expected that in this case the wavefunction produced in the simulation will almost be an eigenstate of the B state. As in the simulation of the femtosecond experiment the wavepacket produced initially is very similar to the ground-state wavefunction, i.e. there is a great deal of radial excitation. However, due to the very limited spread of frequency in the laser pulse, by the time the laser pulse has stopped there are a few eigenfunctions present, now with very little radial excitation. These eigenfunctions can be identified easily, both by their angular form and by a knowledge of the energy levels around the excitation frequency of the laser pulse [120]. The eigenfunctions present on the B surface in the simulation of each picosecond experiment are listed in table 5.

5.6. 2 The Propagating Wavefunction

In the simulation of the femtosecond experiment, after the wavepacket has been created by the pump laser pulse, it starts to vibrate along the radial direction. This is expected since the equilibrium position in the radial direction on the B state differs from that on the X state. After a very short time (less than a hundred femtoseconds) the wavepacket starts to spread out. Then motion on the surface appears to become largely disorderly, with the wavefunction spreading out over the whole of the angular space, whilst still vibrating backwards and forwards across the 'trough'.

In the picosecond experiment, after the wavepacket has been created by the pump laser pulse, it moves very little. This is not unexpected since it has already been stated that the wavefunction produced is almost an eigenstate. However, it is not completely stationary and the motion appears to be the result of the beating of two or three eigenstates. This beating shows itself as a slow movement of the maximum of the wavefunction from one side of the potential energy surface to the other, i.e. the wavefunction moves around the 'trough'.

5.6. 3 The Observables

5.6. 4 The Femtosecond Experiment

The other observables

The results of the calculation of the various observables are shown in figures 32. The norm of the wavefunction rises very rapidly during the pump laser pulse, and subsequently stays constant. The energy decreases during the pump laser pulse as the high energy components, present initially, interfere destructively and so disappear; after the pulse stops the energy stays constant. The energy in the radial mode decreases rapidly during the pulse, for the same reasons that the total energy decreases, i.e. the very highly excited components in the radial direction have died out.

After the laser pulse has stopped there is a strong oscillation in the radial and angular energy (it is a little difficult to see the radial energy oscillation due to the scale, which includes the large variation while the laser pulse was on); by the time this oscillation has damped down energy has been transferred between the radial mode and the angular mode. Over the same time the amplitude of the radial motion is strongly damped and the average value of $\cos\phi$ has approached zero, showing that the wavefunction has spread out.

At first this large oscillation in the energies of the radial and angular modes seems a little surprising, as does the damping of the motion in the radial direction. However, the initial wavefunction is not separable, i.e. it cannot be written as a product of the functions in the radial mode and the functions in the angular mode. Therefore, even if there is no potential coupling (i.e. if the quadratic coupling constant is set to zero), the motion of the wavepacket on the potential surface is not separable, so that there is a flow of energy between the two modes. Also, the wavepacket produced initially on the B state is displaced a certain amount from the equilibrium position in the radial direction. This displacement will not, however, be the amplitude of the radial motion on the B surface. The wavepacket which is promoted from the X state has a width associated with that surface. However, once on the B state the characteristics of the wavepacket, i.e. its width and amplitude, will

change until they 'fit' the potential on the B state.

After this initial period the oscillation in the energy in the two modes becomes less pronounced; the average value of r oscillates about its equilibrium value, in a way indicative of wavepacket motion, and is only slightly damped; the average value of $\cos\phi$ oscillates around an average value of zero, with a changing period of oscillation, implying that the motion on the surface is disorderly.

A short investigation into the initial strong damping of the radial motion

Figures 33 $\rightarrow$ 35 show how the observables change, from a time after the laser pulse has finished, for the simulation of the femtosecond experiment, for the vertical excitation of the laser pulse from the X state to the B state, and lastly for the simulation of an altered femtosecond experiment with the temporal width of the laser pulse set to approximately 41 fs (all with the quadratic coupling constant set to zero).

For all three figures it can be seen that initially the wavepacket has a large displacement from the equilibrium in the radial direction. However, the wavepacket quickly changes, with the amplitude of the motion in the radial direction decreasing with each oscillation in the wavepacket. During this period there is also a large oscillation in the energies in the radial and angular modes. Eventually the wavepacket appears to reach an equilibrium situation, after which the amplitude of the motion in the radial direction remains fairly constant.

The wavepackets created on the B state with the three different laser pulses, described above, differ from each other. The higher the energy of the laser pulse, or spectral width of the laser pulse, the more high states there are in the wavepacket, and the larger the initial displacement from the equilibrium position in the radial direction. However despite this, after this initial period when the wavepacket motion in the radial direction is damped, the amplitude of the oscillation in the radial direction does not give an indication of the energy in the radial mode. For example, in the case of the vertical excitation the eventual amplitude of the radial motion is low, although there is a greater energy in the radial mode compared to the other two cases.

Now consider the effect of the potential coupling on this initial damping of the radial motion. Figures 36 and 37 show how the various observables change, from a time after the laser pulse has finished, for the femtosecond experiment with the dimensionless quadratic coupling constant set to $-0.0063/\sqrt{2}$ (as used usually) and $-0.01/\sqrt{2}$. Figure 33 shows the same information for the coupling constant set to zero.

It is interesting to note that increasing the magnitude of the quadratic coupling constant, which increases the barrier to angular motion, decreases the initial damping in the radial motion. The larger the magnitude of the quadratic coupling constant the larger the

amplitude of the motion in the radial motion after the fast initial damping.

For larger times the increase in the magnitude of the quadratic coupling constant gives rise to an increased oscillation in the energies in the radial and angular modes. The amplitude of the motion in the radial direction is steadily damped (though not to the same extent as during the initial damping of the radial motion), the more so the larger the magnitude of the quadratic coupling constant.

The Na_3^+ signal

The Na_3^+ signals calculated using both the exact and the approximate methods are shown in figures 38 and 39 for the femtosecond experiment, together with their Fourier transforms. Figure 40 shows the Fourier transform of the exact signal, the approximate signal and the modulus of the zero time delay overlap function. Both the ion signals have large peaks at 127 cm^{-1}. There appear to be few other frequencies present in any of the spectra. The agreement between the exact method of calculating the ion signal and the approximate method appears to be good. The zero time delay overlap function shows more structure than the other signals.

The large peak in the spectrum at 127 cm^{-1} is expected. The cation has an equilateral geometry, thus in order to be ionised the Na_3 must move towards the equilateral geometry. Therefore the frequency which corresponds to the motion to and fro across the 'trough', towards and away from the equilateral geometry, i.e. the radial frequency, is strongly represented in the ion signal. Given that the ground vibrational state of the ion is approximately a Gaussian centred at the origin it expected that the overlap will be largest when the wavepacket moves in towards the equilateral geometry. The average value of r shows a strong relation to the calculated ion signal. When the value of r is at its minimum, the ion signal is at its maximum and vice versa. That few other frequencies are present with any significant magnitude is not entirely unexpected. The time dependence of the total ion signal in pump-probe experiments has been investigated by Engel for a generalised system [138], and it was stated that the ion signal may not necessarily yield much information about the molecular dynamics within an intermediate electronic state. In the simulation of the femtosecond experiment done here, the energy restriction in the probe laser ensured that some information, e.g. regarding the radial frequency, was obtained. However the energy spread associated with the laser pulse meant that the smaller frequencies, i.e. those corresponding to the pseudorotational motion, were not present in the ion signal.

The autocorrelation function

The autocorrelation function calculated for the femtosecond experiment is shown in figure 41 together with its Fourier transform. The energy levels correspond well with the

static spectroscopy.

The autocorrelation function, calculated for the vertical excitation of the wavepacket from the X state to the B state, and its Fourier transform are shown in figure 42. Figure 43 shows the experimental spectrum together with the Fourier transform of the autocorrelation function for vertical excitation. The energy levels of course again correspond well with the static spectroscopy, but in this case the intensities also show a fair correspondence with the experimental results. The potential used for the propagation, i.e. the B state, was obtained from a fit to the energy levels observed in the static spectroscopy [120]. Also, the potential used to describe the X state, and so consequently the ground-state wavefunction of the X state, was obtained from a fit to the intensities of the energy levels in the static spectroscopy [120]. Hence the good agreement of both the energy levels and the intensities is to be expected.

5.6. 5 The Picosecond Experiments

The other observables

The results of the calculation of the various observables are shown in figures 44 $\rightarrow$ 47. The results for the three lowest excitation frequencies are similar. The norm rises gradually to a constant value over the time of the pump laser pulse. The energy rises rapidly initially, as the wavepacket produced on the B surface 'thinks' that it is being vertically excited from the ground state. However, the destructive interference between the high energy parts of the wavepacket soon reduce the energy, which then remains constant. The energy in the radial and angular modes shows a similar reduction. After the laser pulse has finished there is a small oscillation in the angular energy, but the corresponding oscillation in the radial mode is too small to see. The average value of r shows a decrease while the laser pulse is still 'on' but then remains nearly constant, showing a very small oscillation. The average value of $\cos\phi$ oscillates slowly throughout the propagation; this oscillation appears to correlate with the small oscillation in r. This gradual variation in the value of ϕ was noticed whilst discussing the propagating wavefunction and the slow movement of the wavefunction around the 'trough'. It can be seen that there is a small coupling between the radial and angular modes in these experiments.

The results for the calculation at 16207 cm^{-1} show an interesting difference. The norm increases initially but some time after the middle of the pulse it decreases. The energy of the laser pulse above the zero-point energy of the B surface is large. This means that the phase of the 'wavepackets arriving' on the surface are changing rapidly with respect to those which are already on the surface. The different 'sets of wavepackets' will interfere with each other, and in this case because their phases are so different the interference will

be destructive so that the norm of the wavefunction on the surface will decrease. The variation in the observables after the laser pulse has finished is then similar to the other picosecond experiments.

A short investigation into the radial and angular coupling

If the quadratic coupling is set to zero, the coupling between the radial and angular modes should disappear. This is the case for the picosecond experiments since the initial wavefunction is approximately separable, as only one vibrational state in the radial mode is excited (with the exception of the 16207 cm^{-1} picosecond experiment). Figures 48 $\rightarrow$ 50 show the change in the observables, from a time after the laser pulse has finished, for the 16136 cm^{-1} picosecond experiment, with the dimensionless quadratic coupling constant set to 0.0, $-0.0063/\sqrt{2}$ and $-0.01/\sqrt{2}$. (The variation in the quadratic coupling constant will affect the energy levels slightly and the wavepacket produced will be a little different. This makes it difficult to separate out completely the various different factors which alter the observables as the wavepacket propagates in time.)

Figure 48 shows that the coupling between the two modes does indeed disappear when the potential coupling in the Hamiltonian is removed, though the average value of $\cos\phi$ still oscillates, with a large amplitude, as the angular modes present beat together. For non-zero values of the quadratic coupling constant the energy in the radial and angular modes oscillate. The average values of r and $\cos\phi$ also oscillate.

An increased value of the magnitude of the quadratic coupling constant increases the amplitude of the oscillations in the energies of the radial and angular modes. It does not increase the amplitude of the oscillation in r, but this may be because the wavepacket formed is different.

The Na_3^+ signal

The Na_3^+ signal is only calculated using the approximate method for the picosecond experiment, due to difficulties involved in the computation of the exact Na_3^+ signal; these difficulties were mainly to do with limitations of computer time and memory. These results are shown in figures 51 $\rightarrow$ 54.

For the simulation of all the picosecond experiments the overlap with the first excited vibrational state of the bend was used. At least for the simulation at 16000 cm^{-1}, if not for those at the higher frequencies, it would be expected that the overlap with the ground vibrational state would be appropriate (on energetic grounds) to model the ion signal. However, it was found that the overlap with the ground vibrational state showed little, if any, structure.

For the picosecond experiments the oscillation in the ion signal arises from the beating

together of the various pseudorotational modes. This beating gives rise to a time-dependent wavefunction which moves in an angular manner on the P.E.S., so that the wavefunction moves around the 'trough' of the potential. As the wavepacket moves around the trough, i.e. as the average value of $\cos\phi$ varies, it will also move slightly into and away from the equilateral geometry, i.e. the average value of r will vary, depending on the circularity of the potential which is measure of the extent of the potential coupling.

The B state potential used here is almost perfectly circular, i.e. the value of r around the trough is almost constant. This is a consequence of the fact that the barrier to pseudorotation is thought to be low. Given that the potential is almost circular, the wavepacket as it moves around the trough will have an almost constant value of r, so that the overlap of this wavepacket with the ground vibrational state of the ion, which depends largely on the variation in the radial displacement, will be almost constant. Thus, in order to compensate for the potential, which is thought to be 'too' circular, the overlap is formed with the first excited vibrational state of the bend, which is not angularly symmetrical as is the ground vibrational state.

The results for the lowest frequency (16000 cm^{-1}) show an oscillation with a period of approximately 2.6 ps. The results for the calculations at 16129 cm^{-1} and 16136 cm^{-1} show an oscillation with a period of approximately 2.1 ps. The ion signal for these simulations grows steadily from zero delay time, and then oscillates without any decay. These signals arise from the beating together of the $j = 0, 1$, and 2 pseudorotational levels. These energy levels will give beat frequencies of approximately: 3.5 cm^{-1}, corresponding to a period of 9.5 ps; 12.6 cm^{-1}, corresponding to a period of 2.6 ps; and lastly, 16.1 cm^{-1}, corresponding to a period of 2.1 ps. The second of these frequencies appears to be dominant in the results for the calculation at 16000 cm^{-1}, whilst the last of these beat frequencies appears to be dominant in the signal for the calculations at 16129 cm^{-1} and 16136 cm^{-1}. The results for the calculation at 16207 cm^{-1} show a small oscillation with a period of approximately 1.0 ps. The ion signal at this frequency is largest soon after zero delay time, but after the initial decay the signal does not steadily decrease. This signal arises from the beating together of the $u = 1, j = 4, 5$ and $u = 0, j = 8$ pseudorotational levels. The $u = 1, j = 5$ and the $u = 1, j = 4$ levels differ in energy by approximately 32 cm^{-1}, which corresponds to a period of 1.0 ps. The $u = 0, j = 8$ level is approximately 8 cm^{-1} above the $u = 1, j = 4$ level; this frequency corresponds to a period of 4.1 ps. This period is not seen in the overlap function.

The autocorrelation function and the zero time delay overlap function

Figures 55 $\rightarrow$ 58 show the zero time delay overlap function and the Fourier transform of the autocorrelation function for the picosecond calculations. The modulus of the zero

time delay overlap function shows all the beating frequencies described above, though as for the overlap function some frequencies are dominant. The value of the function is largest soon after zero delay time, but shows no steady decay at greater times.

The Fourier transform of the autocorrelation function confirms that the energy levels that were identified in the initial wavefunction are in fact those present in the propagating wavefunction.

5.7 Conclusions

The static spectroscopy was successfully modelled using the potential of the B state and initial wavefunction of the X state. Thus, there can be a certain amount of confidence in these.

The initial wavepacket created by the femtosecond laser pulse is made up of many states, which are excited both in the radial mode and in the angular mode. This wavepacket has a large amplitude motion in the radial direction. The angular motion appears to be mostly disorderly. The oscillation of the wavepacket in the radial direction gives rise to an ion signal which oscillates with the frequency of the radial motion.

The initial wavepacket created by the picosecond laser pulse is made up of very few states, which are excited in the angular mode, but are in one particular radial state. The angular states present interfere with each other to produce a wavefunction which moves angularly. The small coupling of the angular and radial modes, through the quadratic coupling constant, means that as the wavepacket moves angularly it moves radially as well. This small radial motion gives rise to an ion signal which oscillates with the beat frequencies of the angular modes.

The approximate method of calculating the ion signal for the femtosecond simulations appears to give satisfactory agreement with the exact method of calculation. This means that for the picosecond experiments the calculation of the ion signal can be carried out using this approximation. However, it may be more appropriate for a variety of reasons to use vibrational states, other than the ground state, to form the overlap function. In fact, for the picosecond experiments the modulus of the zero time delay overlap function shows slightly better agreement with the experiment than the square modulus of the overlap function. A useful implication of the success of the approximate method is that the calculations can be extended to three dimensions, i.e. including the symmetric stretch. In the three dimensional calculations, it would not be possible to calculate the exact ion signal with the present computational resources, so that it is necessary to have some approximate method to calculate the ion signal.

The calculation using the femtosecond laser pulse shows poor agreement with the ex-

perimental results. The experimental spectrum shows a small peak at 123 cm^{-1} which possibly corresponds with the radial frequency of 127 cm^{-1}. Superficially, the poor agreement can be attributed to the dominance of the results by the symmetric stretch frequency. However, the static spectroscopy appears to show very little, if any, excitation in the symmetric stretch frequency. This makes the results of the femtosecond experiment rather difficult to understand.

The picosecond experiments at 625, 620, and 619.7 nm show some agreement with the experimental results. The oscillations though are not with a time period of 3 ps but of approximately 2 ps. The results at 617 nm show less similarity to the reported experimental results. The ion signal oscillates with a long time period of approximately 4 ps, which can be compared to the experimental value of 3 ps, but there is also a short time period in the oscillation of approximately 1 ps, which has no corresponding value in the experimental ion signal. However, it is possible that on a better potential surface the energy gap between the $u = 0, j = 8$ and the $u = 1, j = 4$ levels could widen slightly so that the beating between these two levels could yield the required frequency. The $u = 0, j = 8$ level is not resolved in the static spectroscopy, so it is not possible to gain information about its true energy from the stationary spectrum.

It is not expected that the calculation in three dimensions will greatly alter the results of the picosecond calculations at 625 nm; however with a symmetric stretch frequency of 110 cm^{-1}, extra energy levels in the regions excited by the laser pulses at 620, 619.7 and 617 nm may effect the results of the calculations.

The Creation of a wavepacket on the B state fs expt.

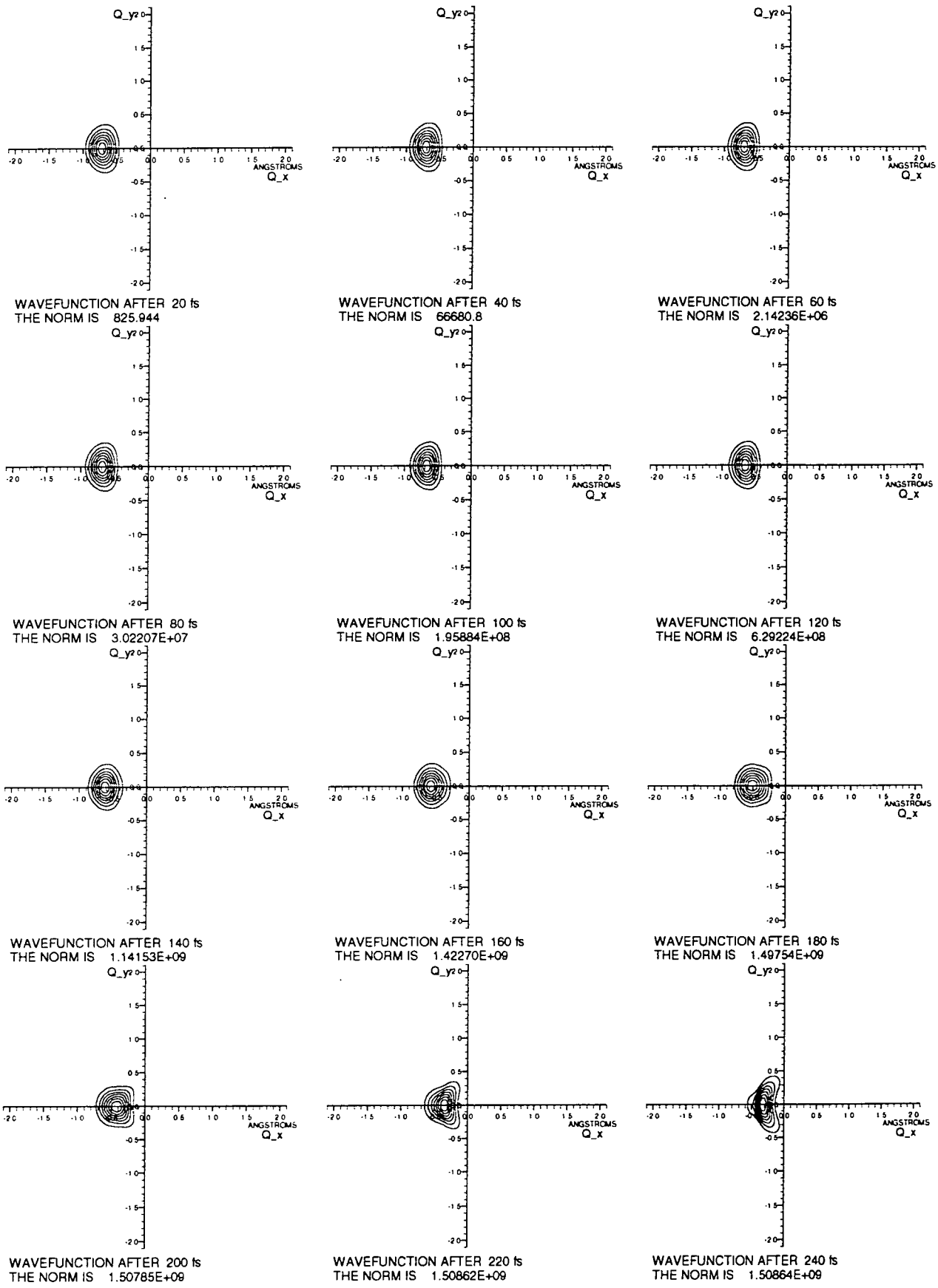

Fig. 27. 'Snapshots' of the wavefunction evolving in time during the femtosecond experiment.

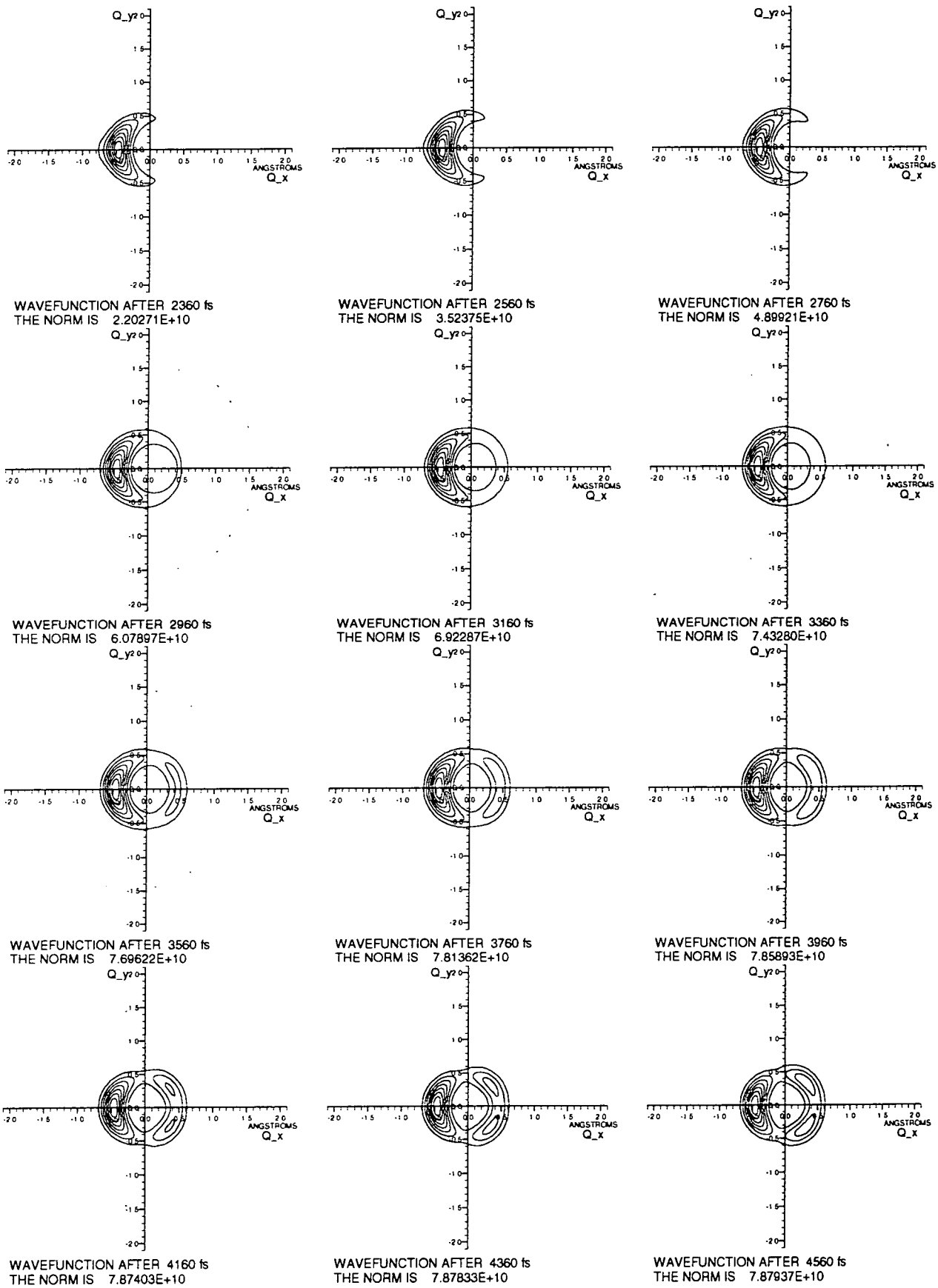

Fig. 28. 'Snapshots' of the wavefunction evolving in time during the 16000 cm^{-1} picosecond experiment.

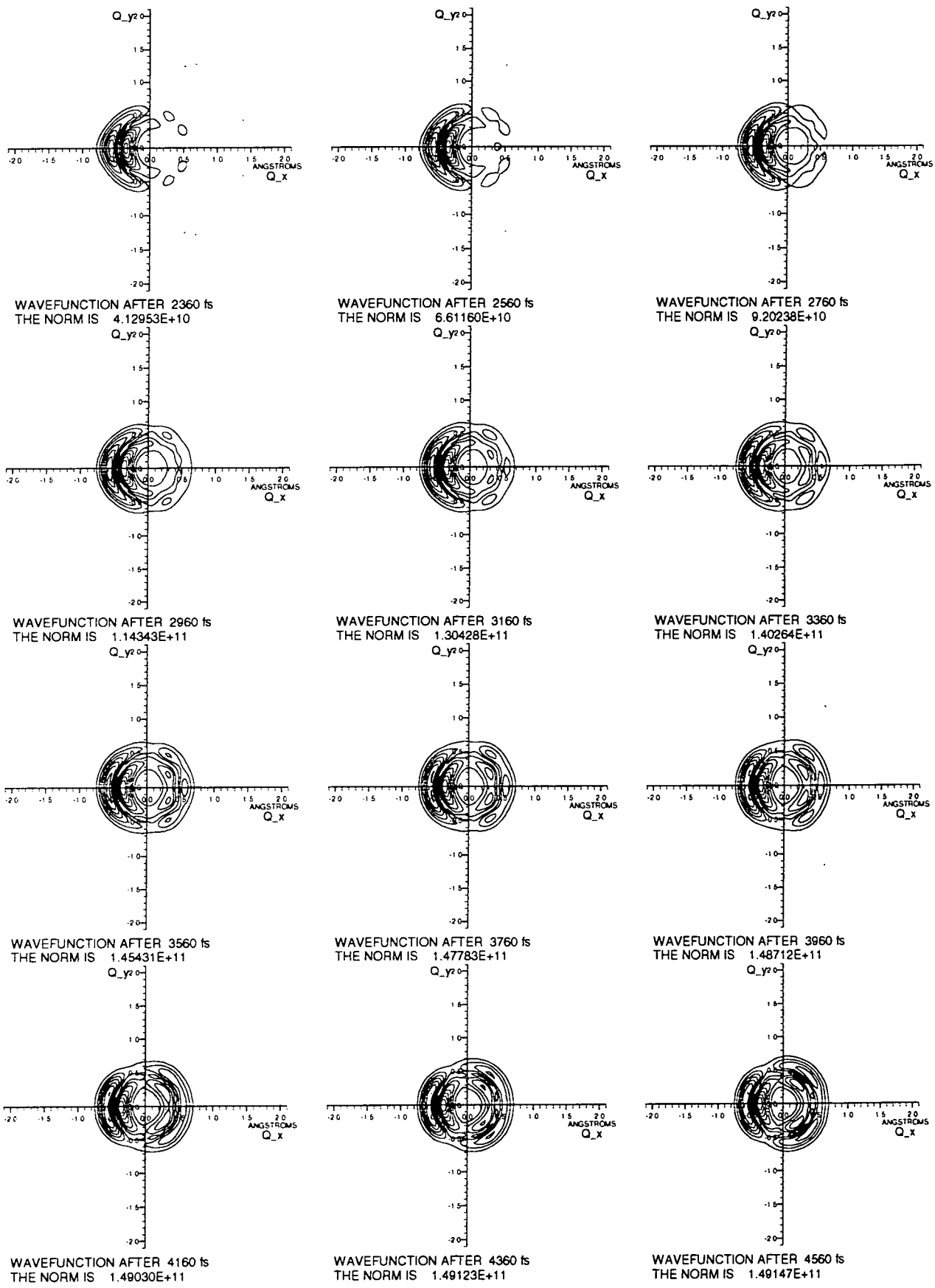

Fig. 29. 'Snapshots' of the wavefunction evolving in time during the 16129 cm^{-1} picosecond experiment.

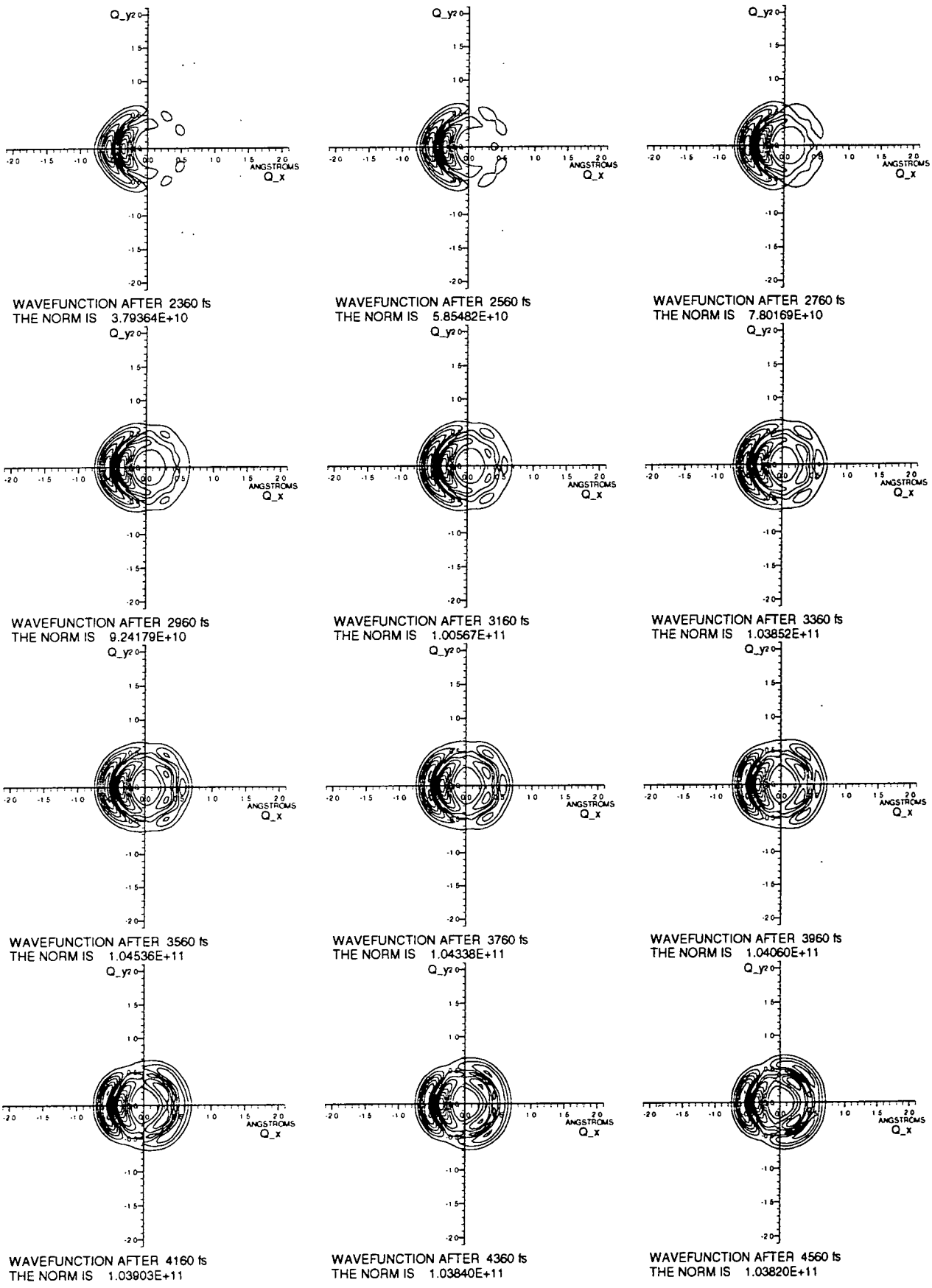

Fig. 30. 'Snapshots' of the wavefunction evolving in time during the 16136 cm^{-1} picosecond experiment.

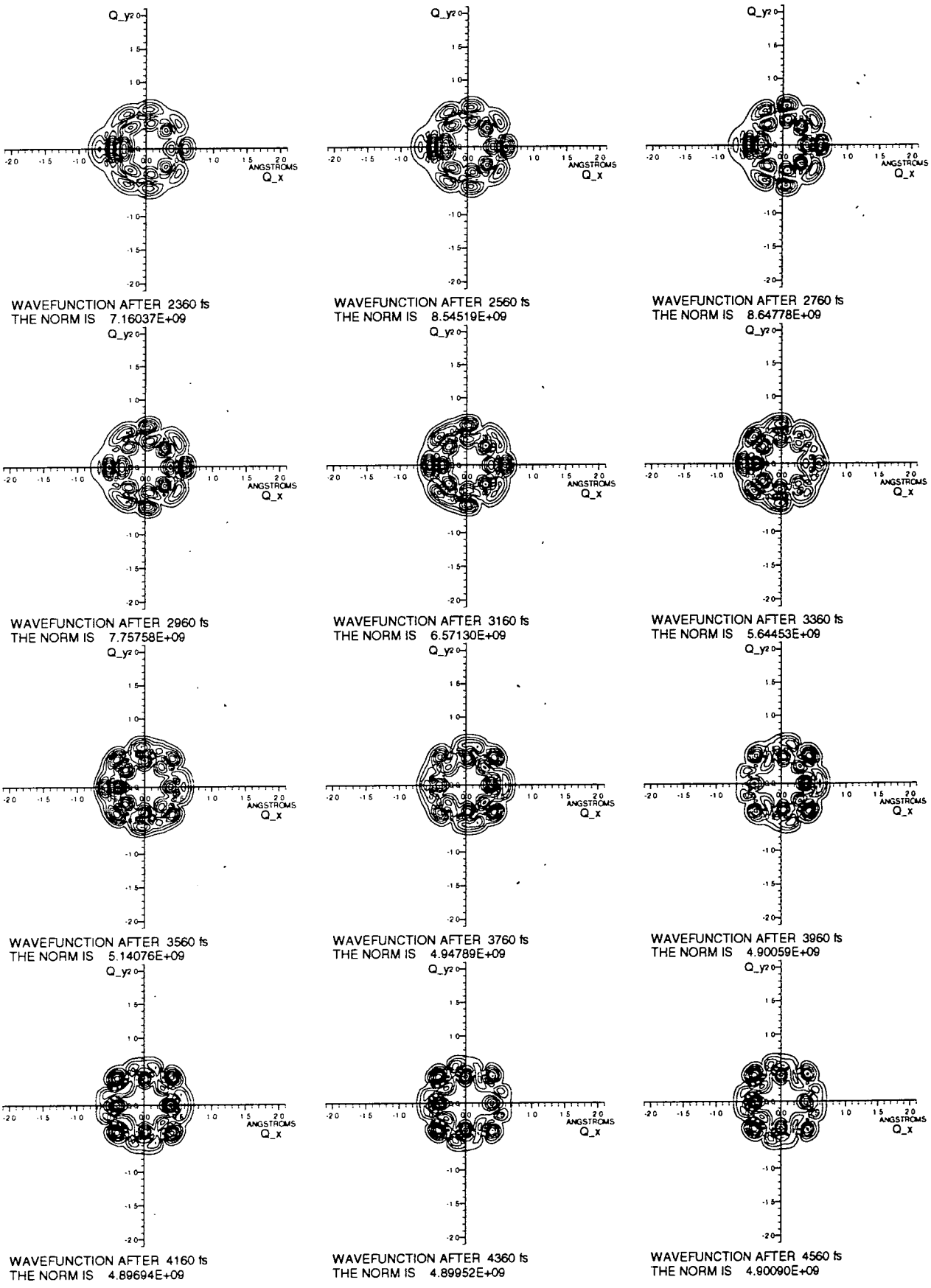

Fig. 31. 'Snapshots' of the wavefunction evolving in time during the 16207 cm^{-1} picosecond experiment.

Results for fs expt.

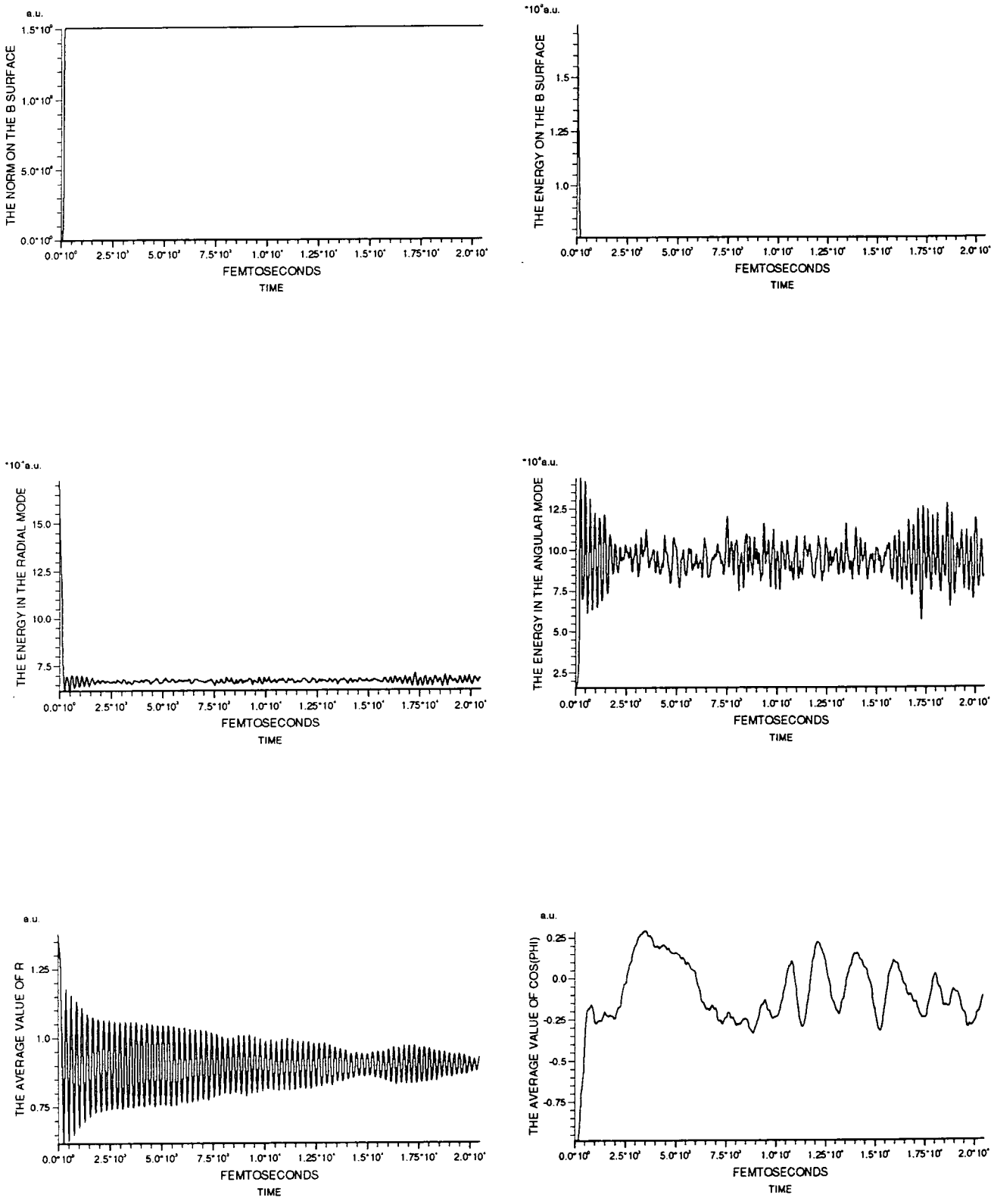

Fig. 32. Graphs showing the variation of the observables over the entire propagation time for the femtosecond experiment.

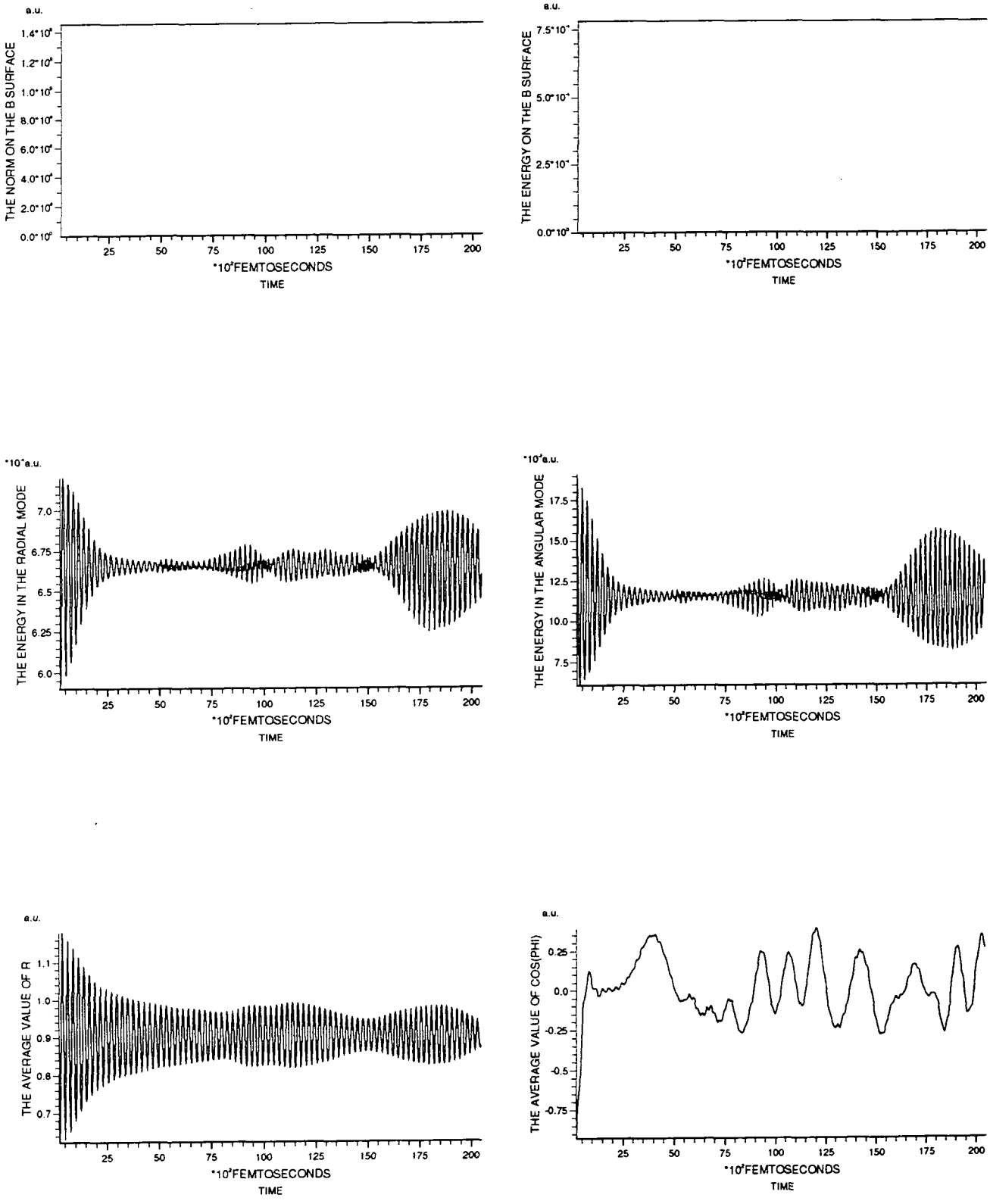

Fig. 33. Graphs showing the variation of the observables over the time after the pump laser pulse has finished for the fs expt., with the quadratic coupling constant set to zero.

Results for vertical excitation, f=0.0.

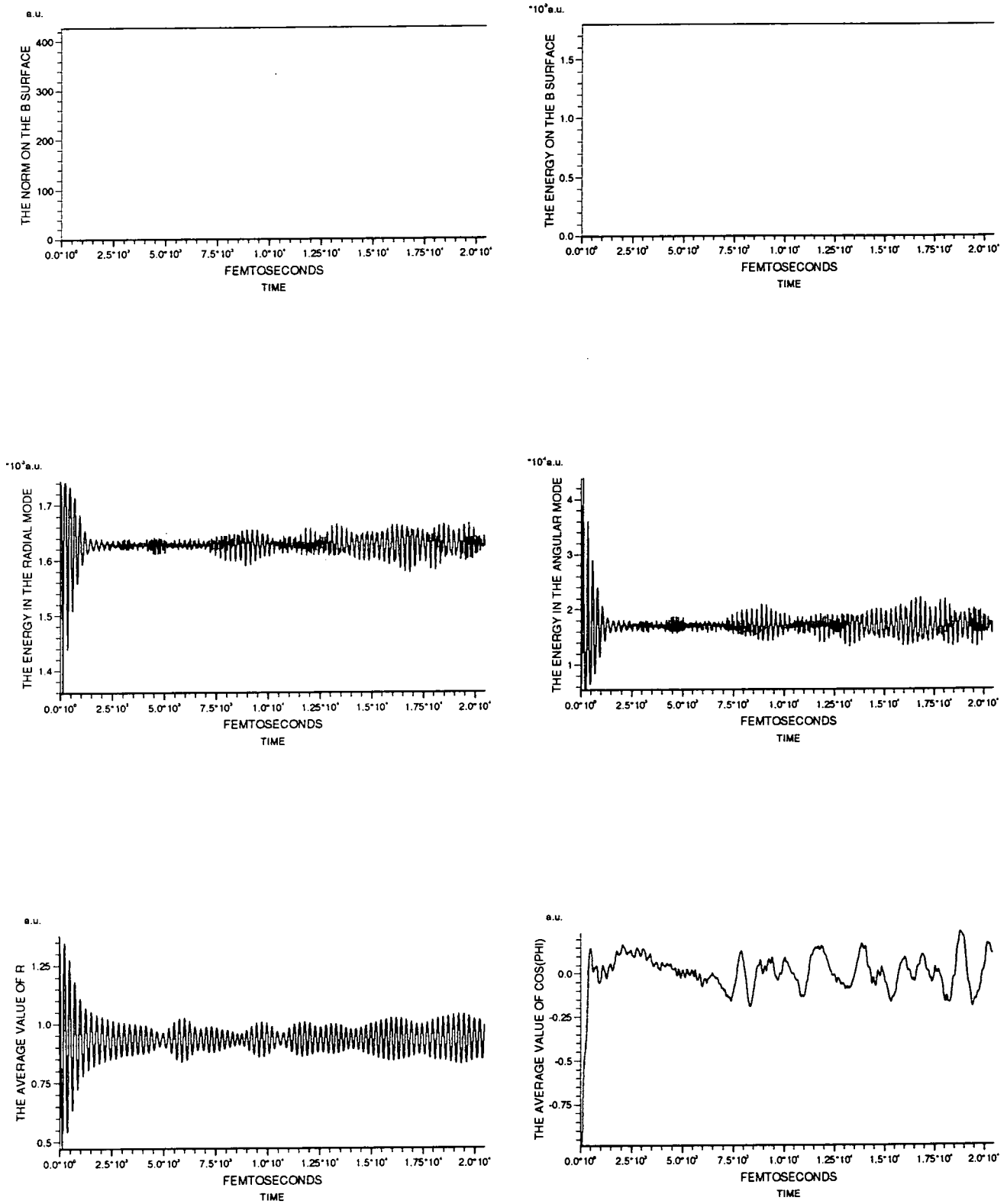

Fig. 34. Graphs showing the variation of the observables over the propagation time for the vertical excitation, with the quadratic coupling constant set to zero.

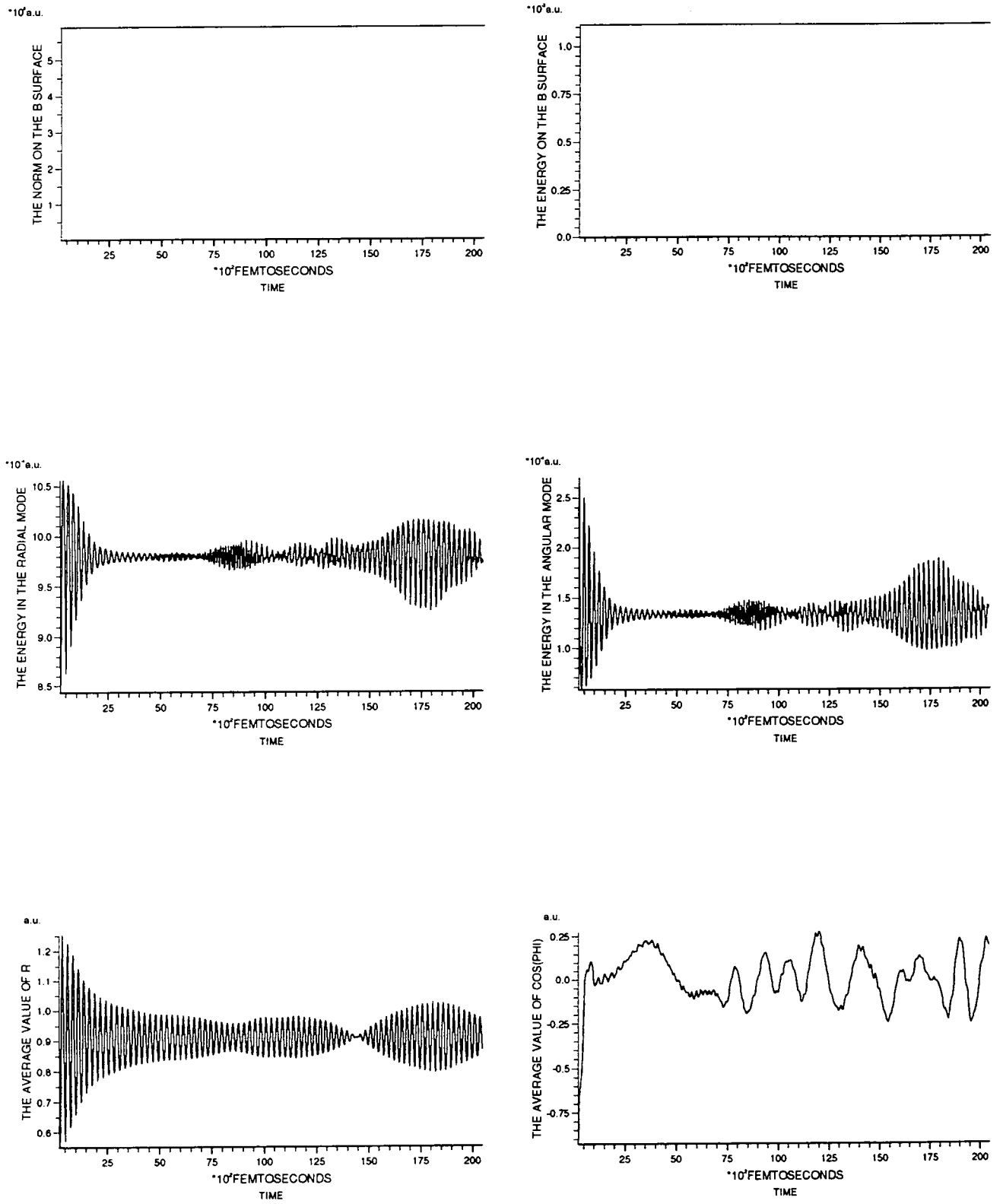

Fig. 35. Graphs showing the variation of the observables over the time after the pump laser pulse has finished for the **altered** fs expt., with f set to zero.

Results for fs expt.

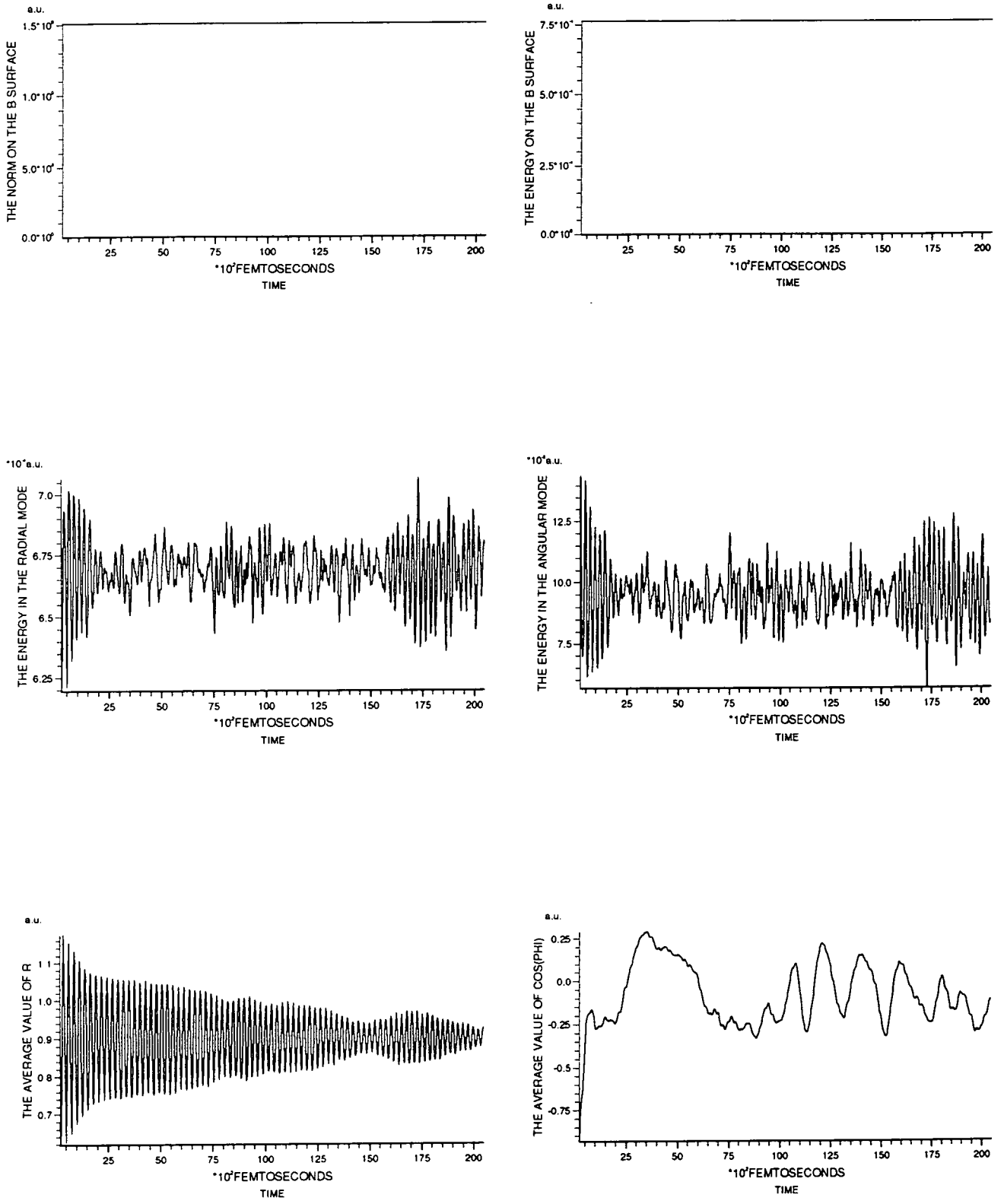

Fig. 36. Graphs showing the variation of the observables over the time after the pump laser pulse has finished for the fs expt., with f set to $-0.0063/\sqrt{2}$.

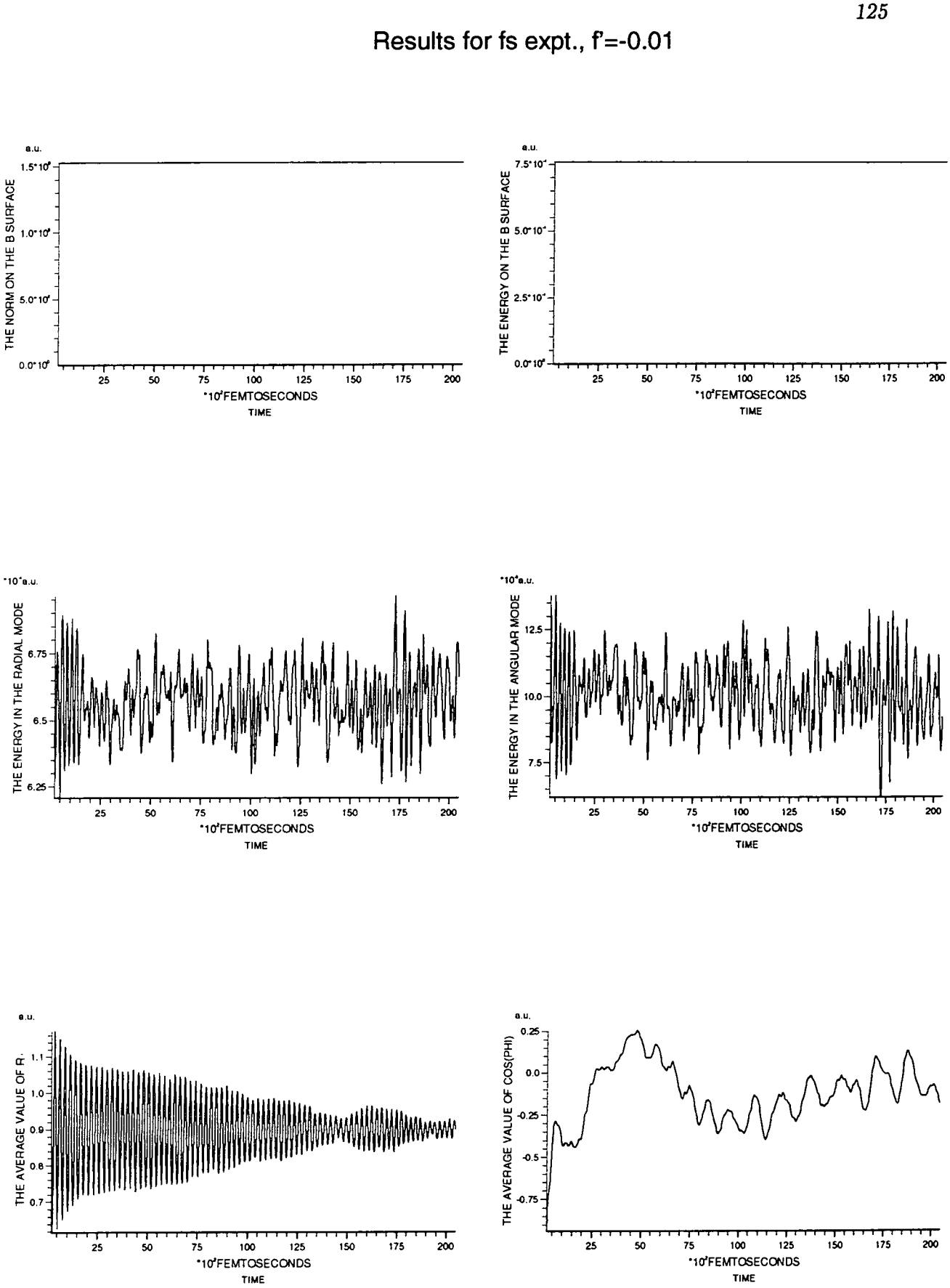

Fig. 37. Graphs showing the variation of the observables over the time after the laser pulse has finished for the fs expt., with f set to $-0.01/\sqrt{2}$.

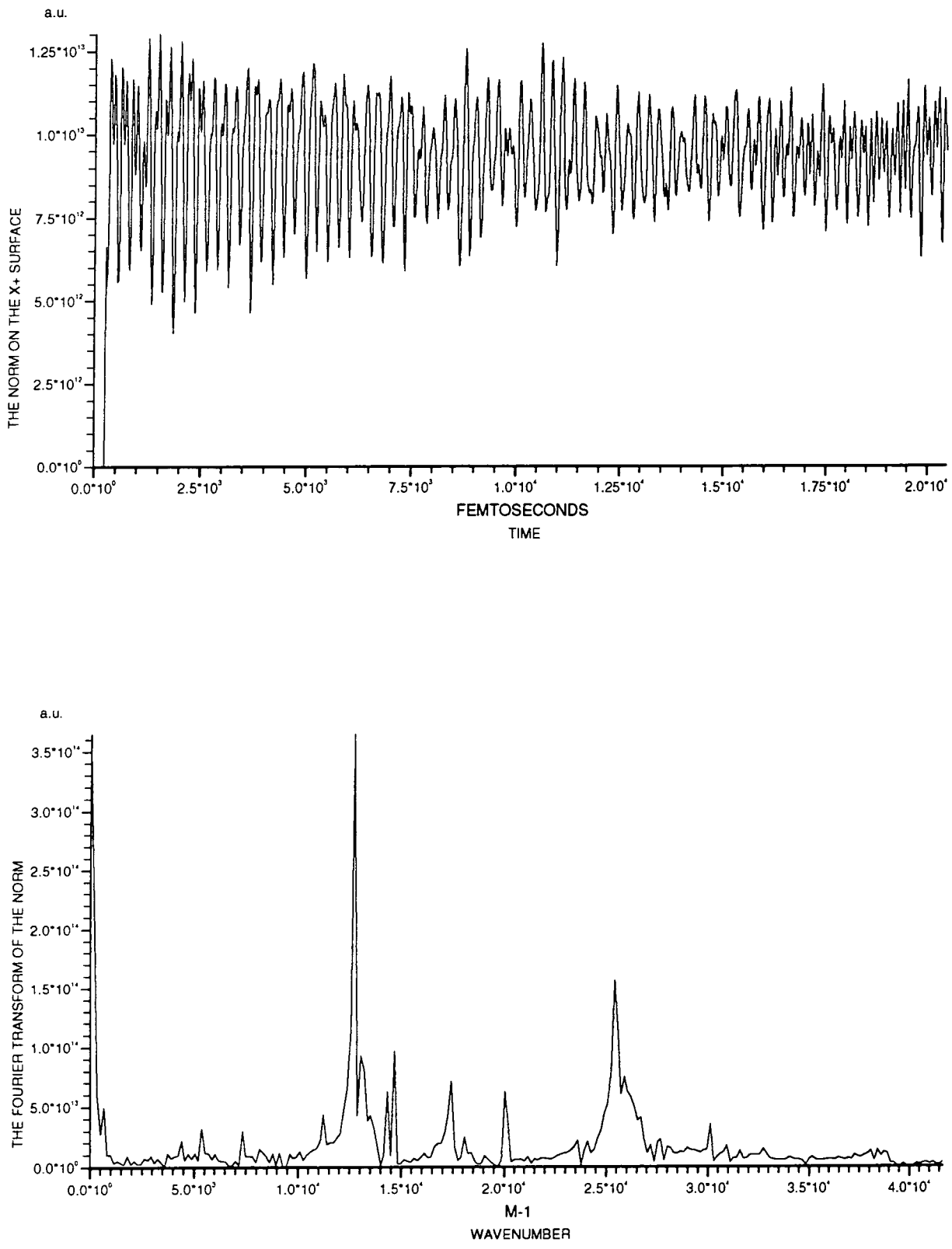

Fig. 38. Graphs showing the Na_3^+ signal as a function of delay time and its Fourier transform for the femtosecond experiment.

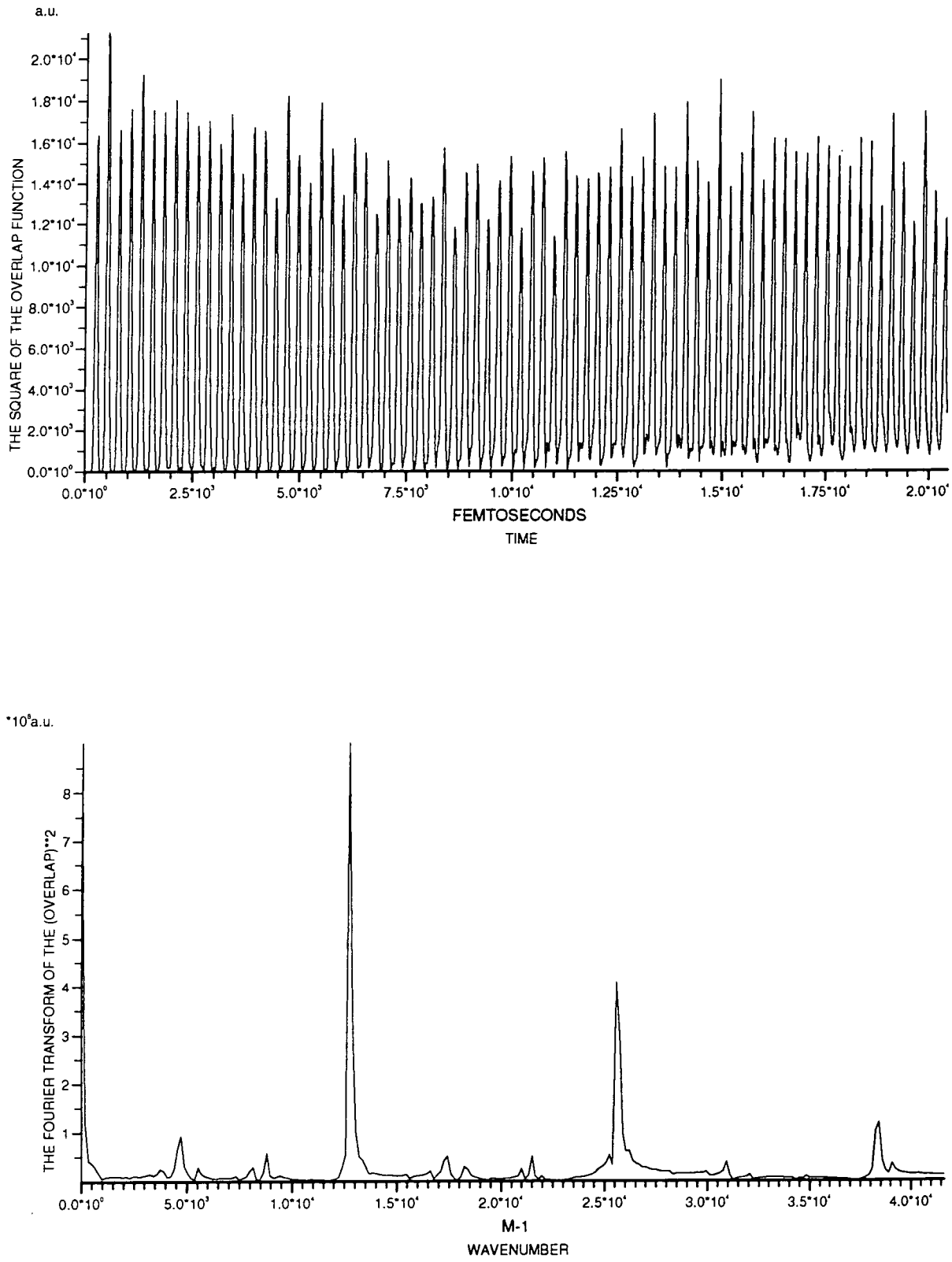

Fig. 39. Graphs showing the *approximate* Na_3^+ signal as a function of t_D and its Fourier transform for the femtosecond experiment.

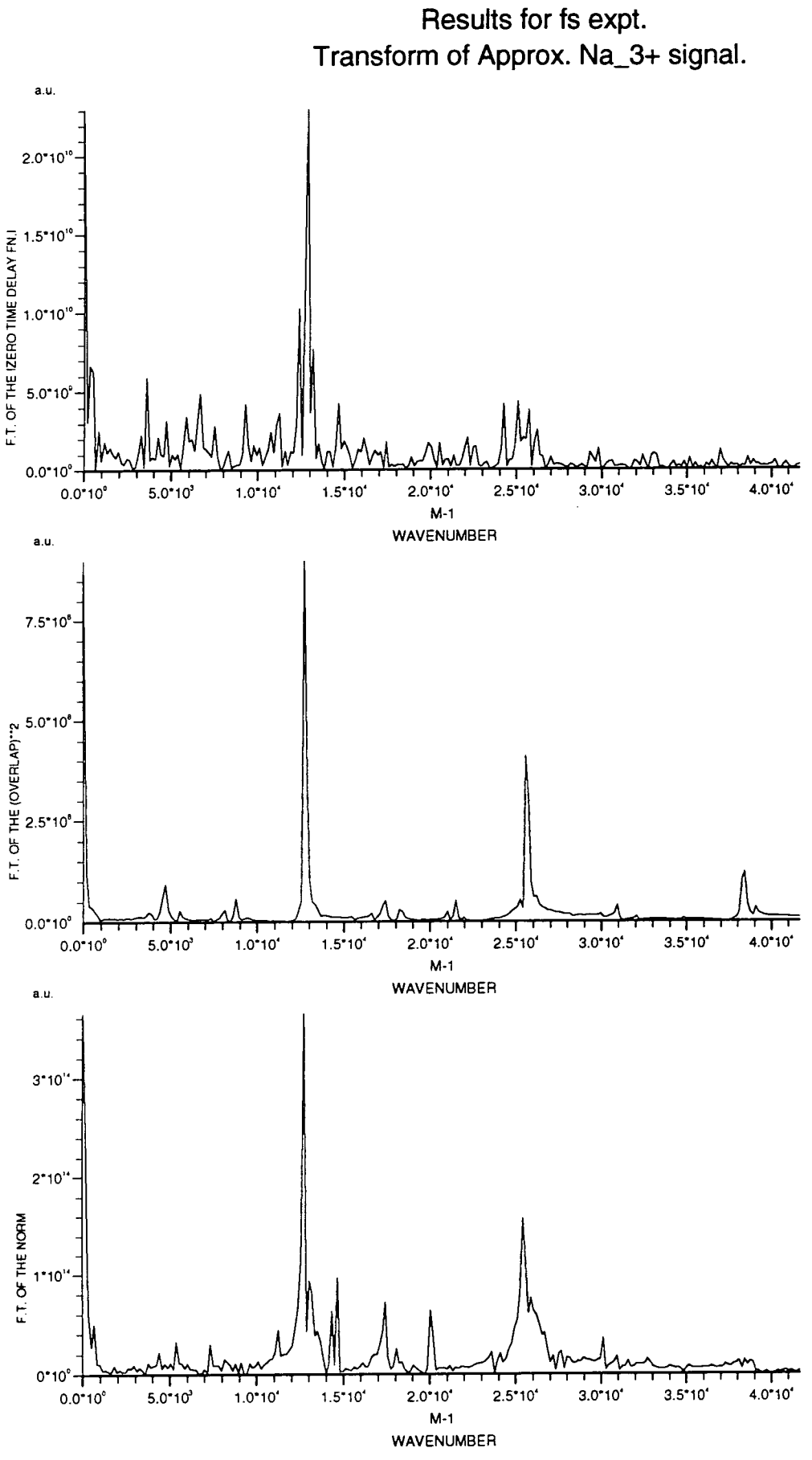

Fig. 40. Graphs showing the Fourier transform of the exact and approximate Na_3^+ signal and the modulus of the zero time delay overlap fn. for the fs expt.

Results for fs expt.
Transform of Autocorrelation function, showing energy levels.

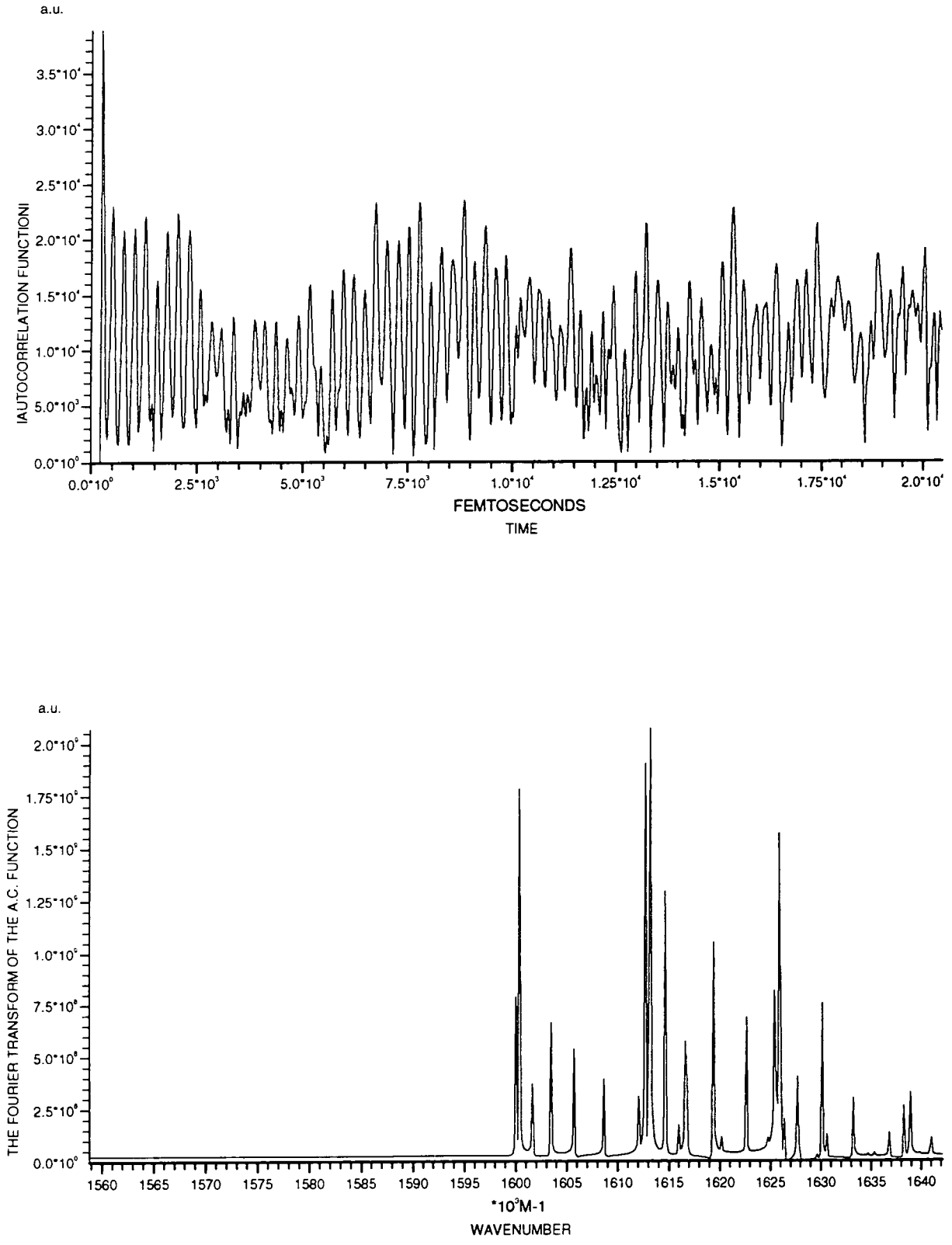

Fig. 41. Graphs showing the autocorrelation function and its Fourier transform for the femtosecond experiment.

Results for vertical excitation.
Transform of Autocorrelation function, showing energy levels.

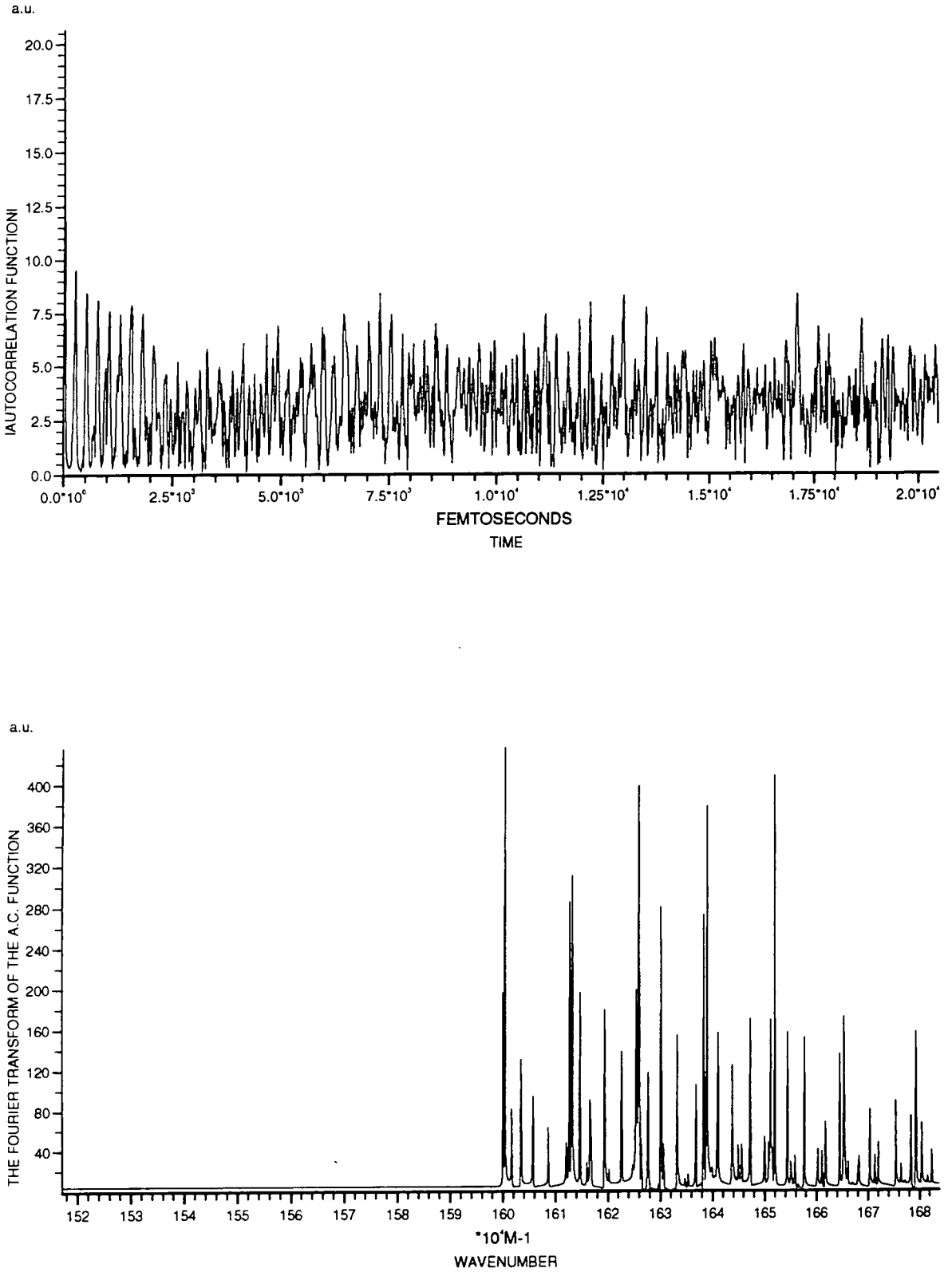

Fig. 42. Graphs showing the autocorrelation function and its Fourier transform for vertical excitation.

Results for vertical excitation.
Transform of Autocorrelation function, showing energy levels.

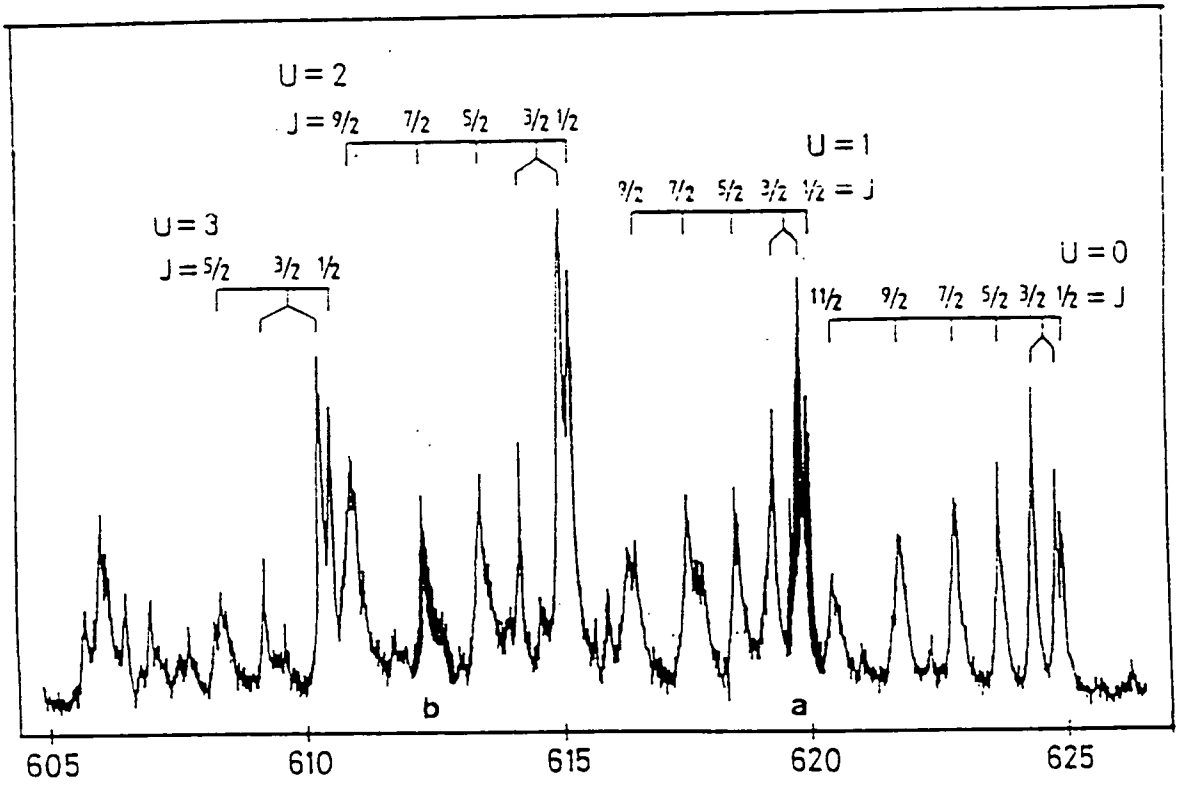

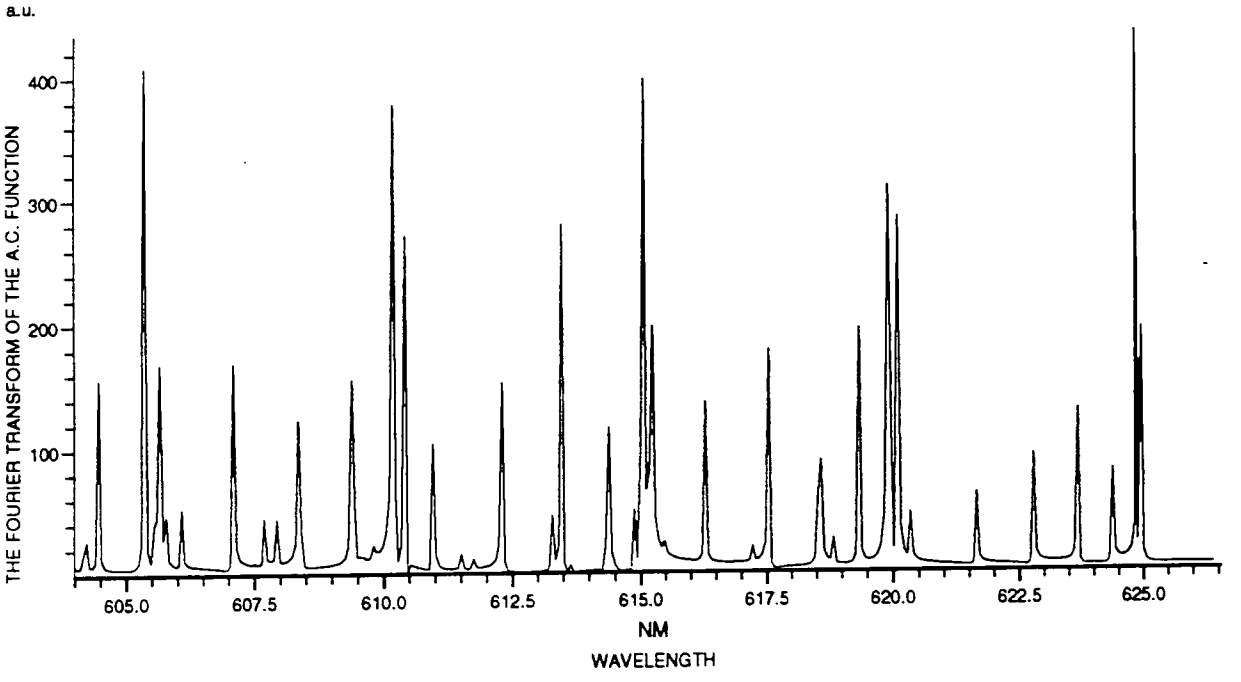

Fig. 43. Graphs showing the experimental spectrum and the Fourier transform of the autocorrelation function for vertical excitation.

Results for 16000 cm-1 ps expt.

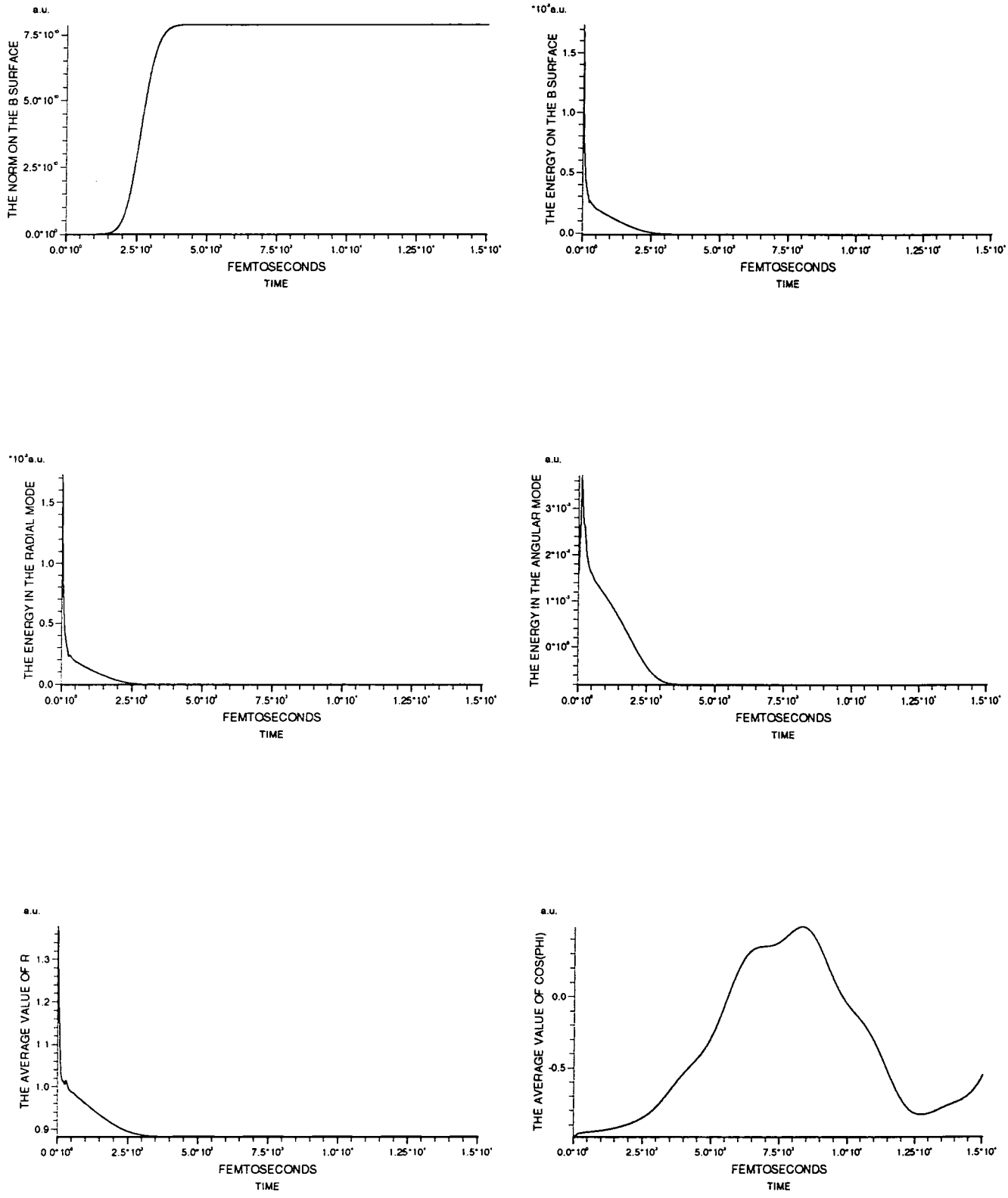

Fig. 44. Graphs showing the variation of the observables over the entire propagation time for the 16000 cm^{-1} picosecond experiment.

Results for 16129 cm-1 ps expt.

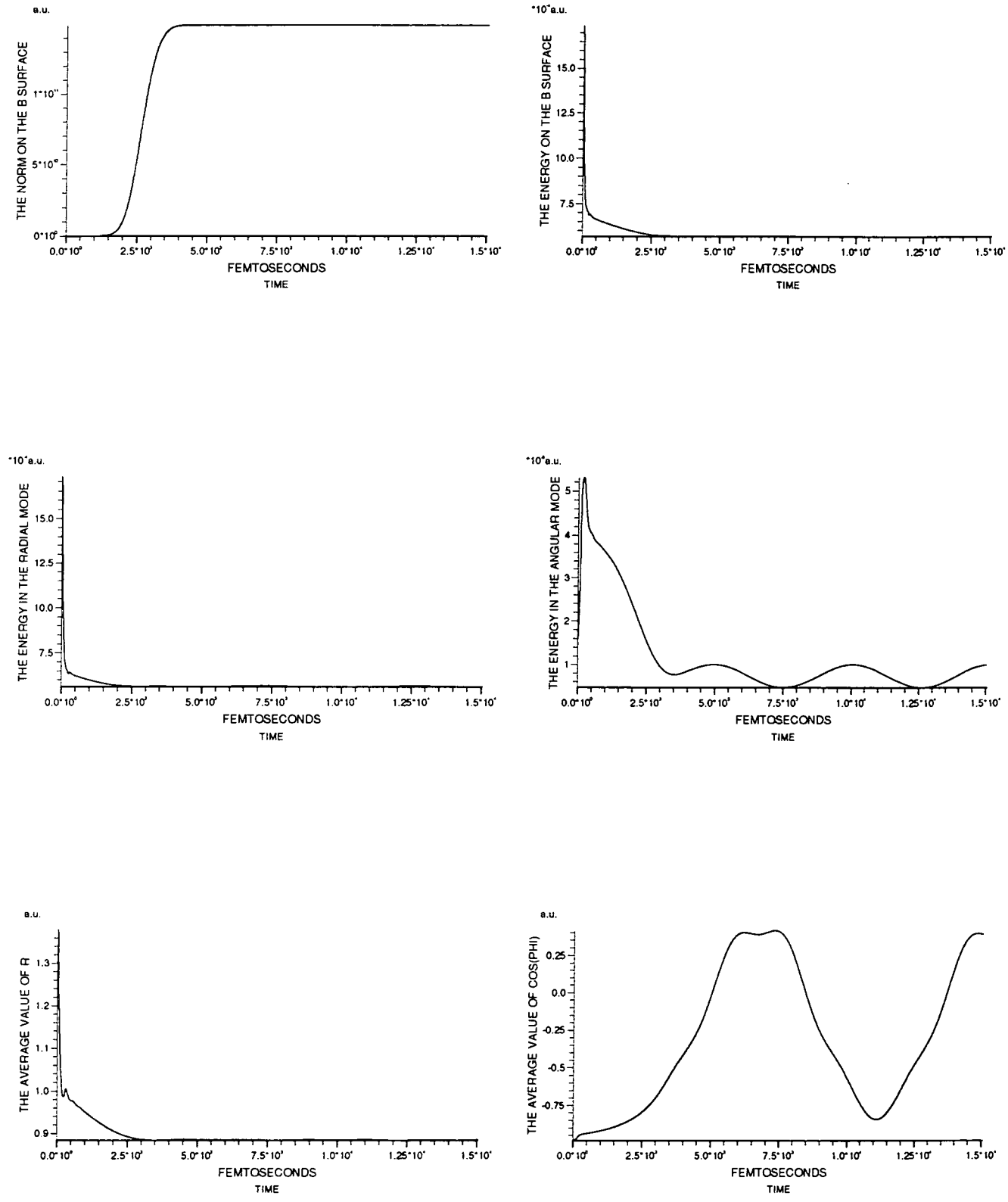

Fig. 45. Graphs showing the variation of the observables over the entire propagation time for the 16129 cm^{-1} picosecond experiment.

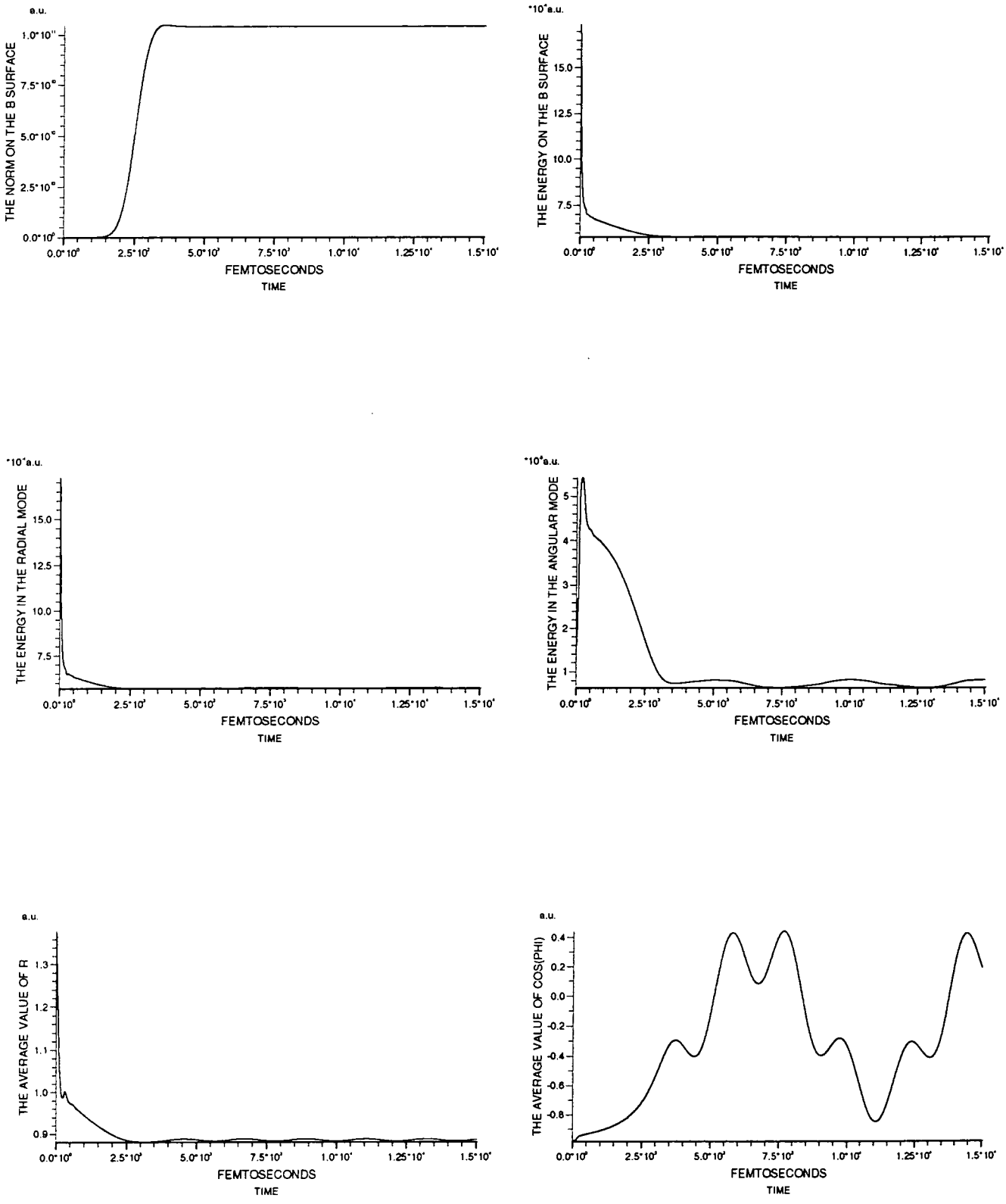

Fig. 46. Graphs showing the variation of the observables over the entire propagation time for the 16136 cm^{-1} picosecond experiment.

Results for 16207 cm-1 ps expt.

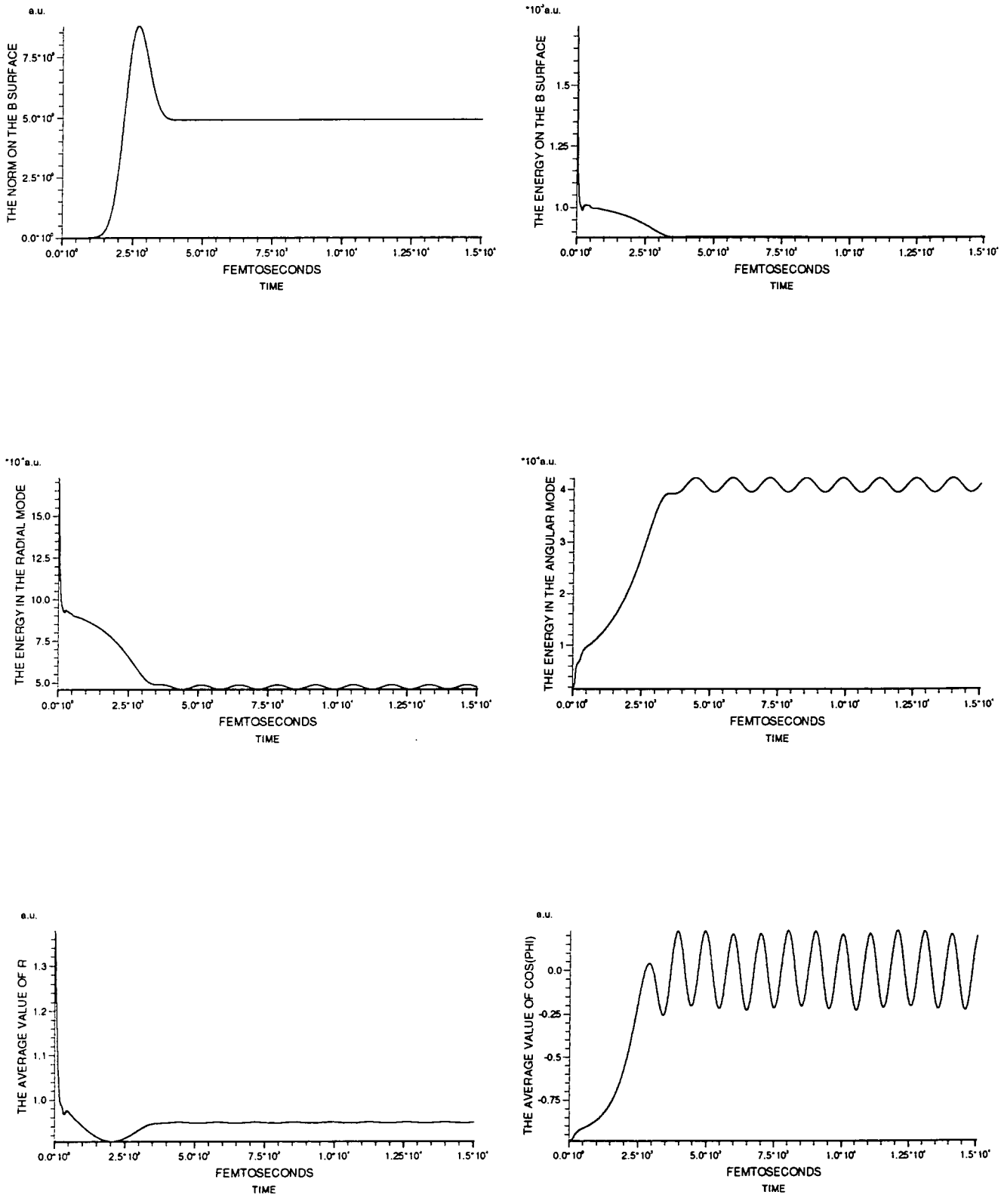

Fig. 47. Graphs showing the variation of the observables over the entire propagation time for the 16207 cm^{-1} picosecond experiment.

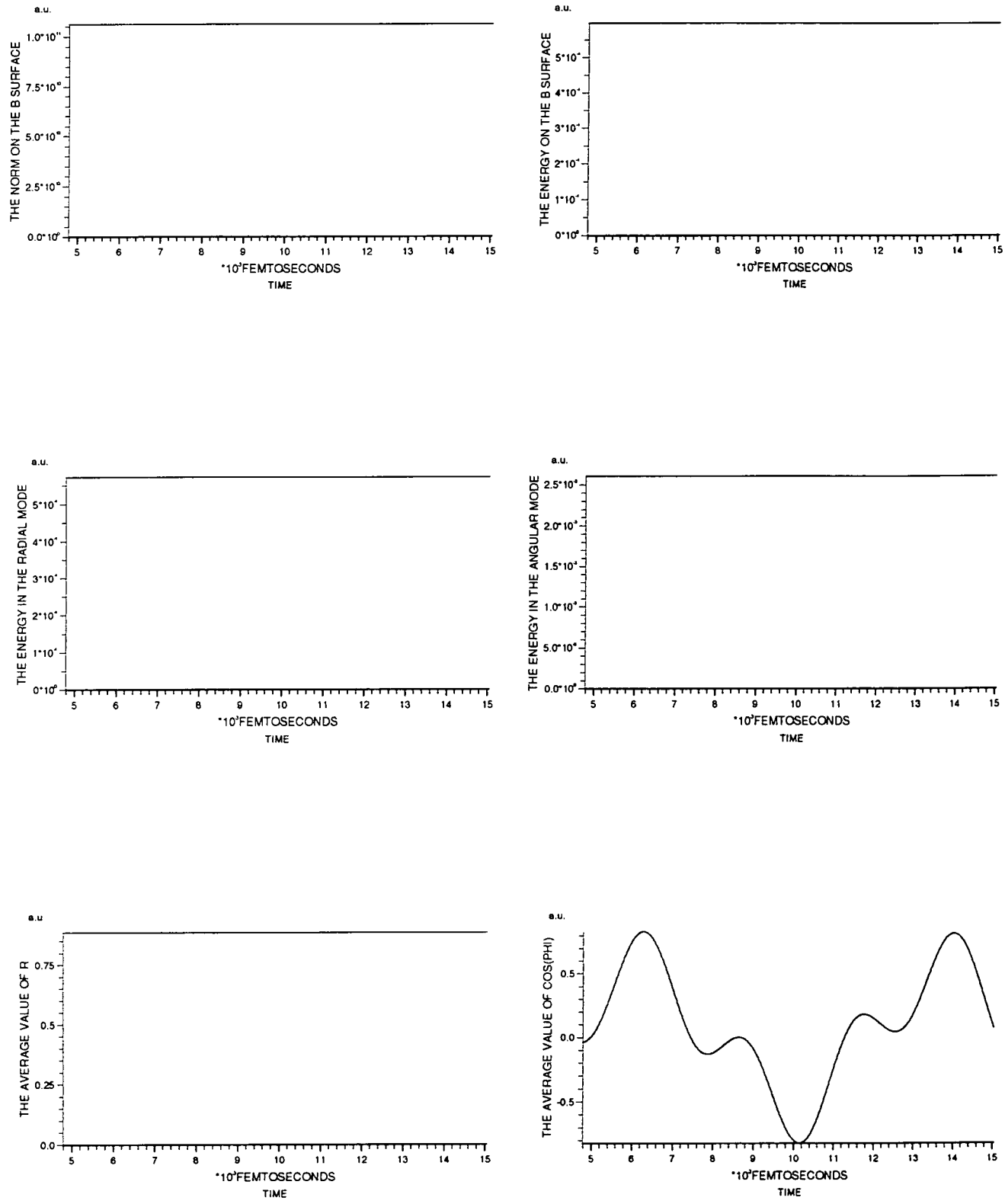

Fig. 48. Graphs showing the variation of the observables over the time after the laser has finished for the 16136 cm^{-1} ps expt., with f set to zero.

Results for 16136 cm-1 ps expt.

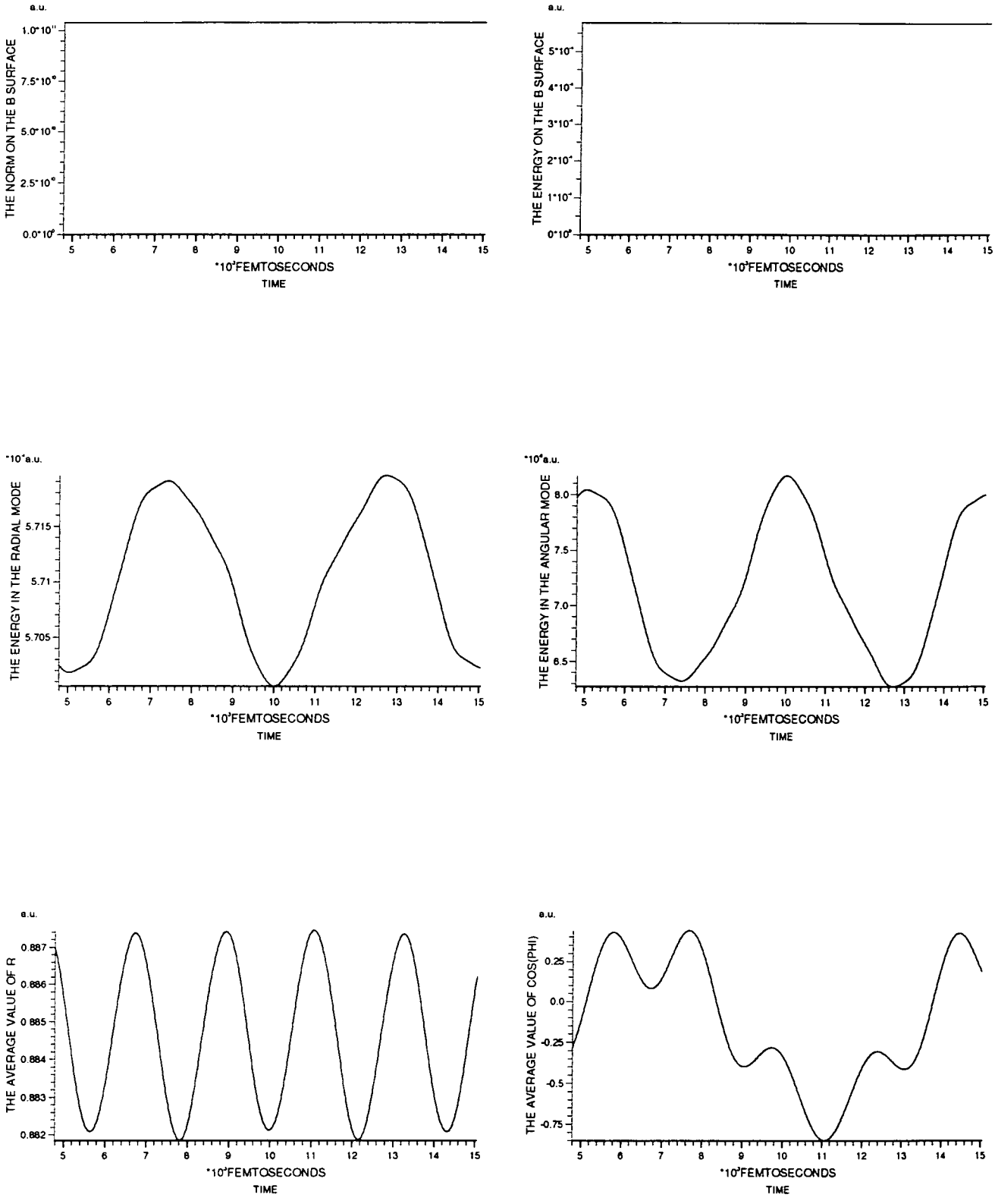

Fig. 49. Graphs showing the variation of the observables over the time after the laser has finished for the 16136 cm^{-1} picosecond experiment.

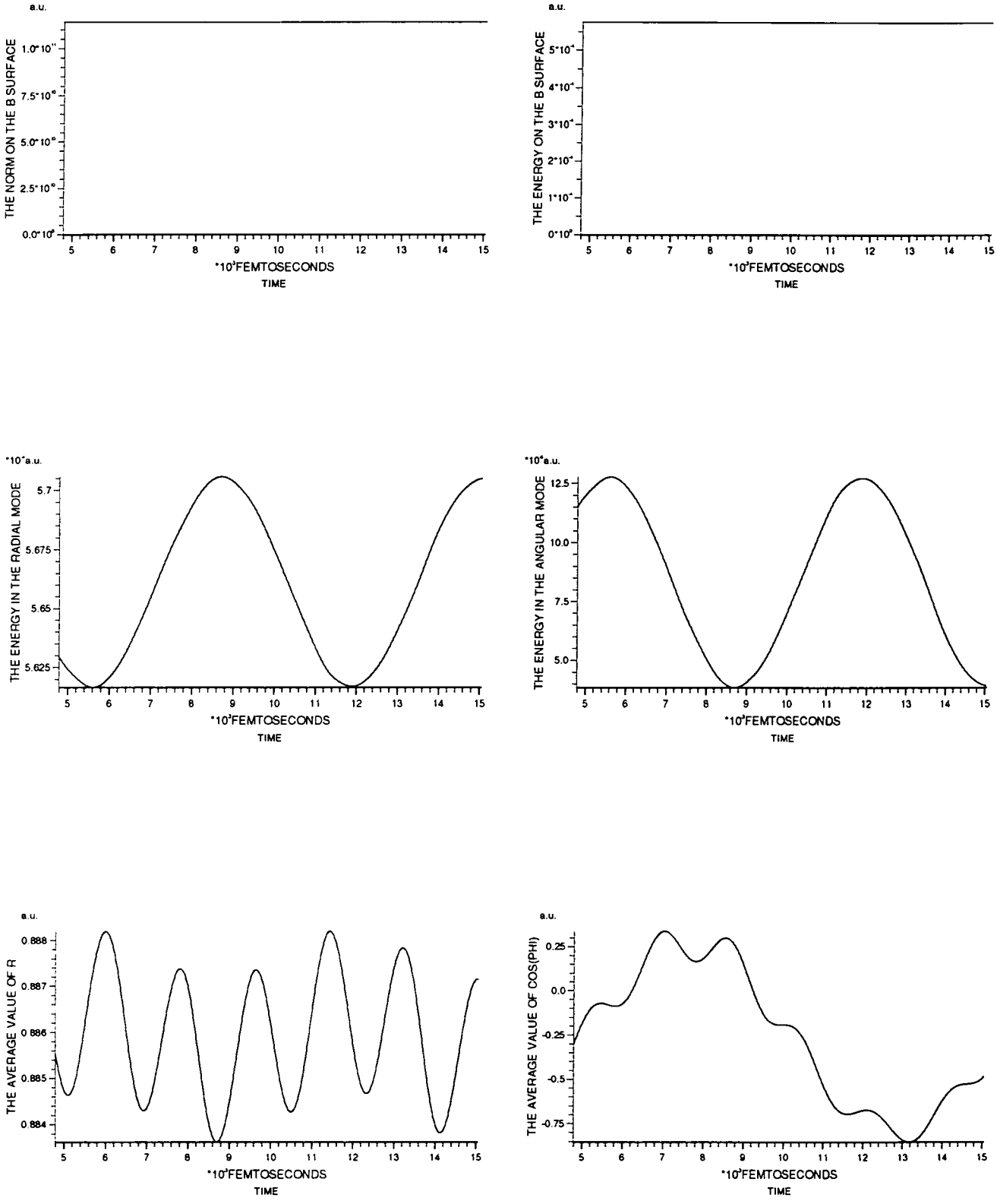

Fig. 50. Graphs showing the variation of the observables over the time after the laser has finished for the 16136 cm^{-1} ps expt., with f set to $0.01/\sqrt{2}$.

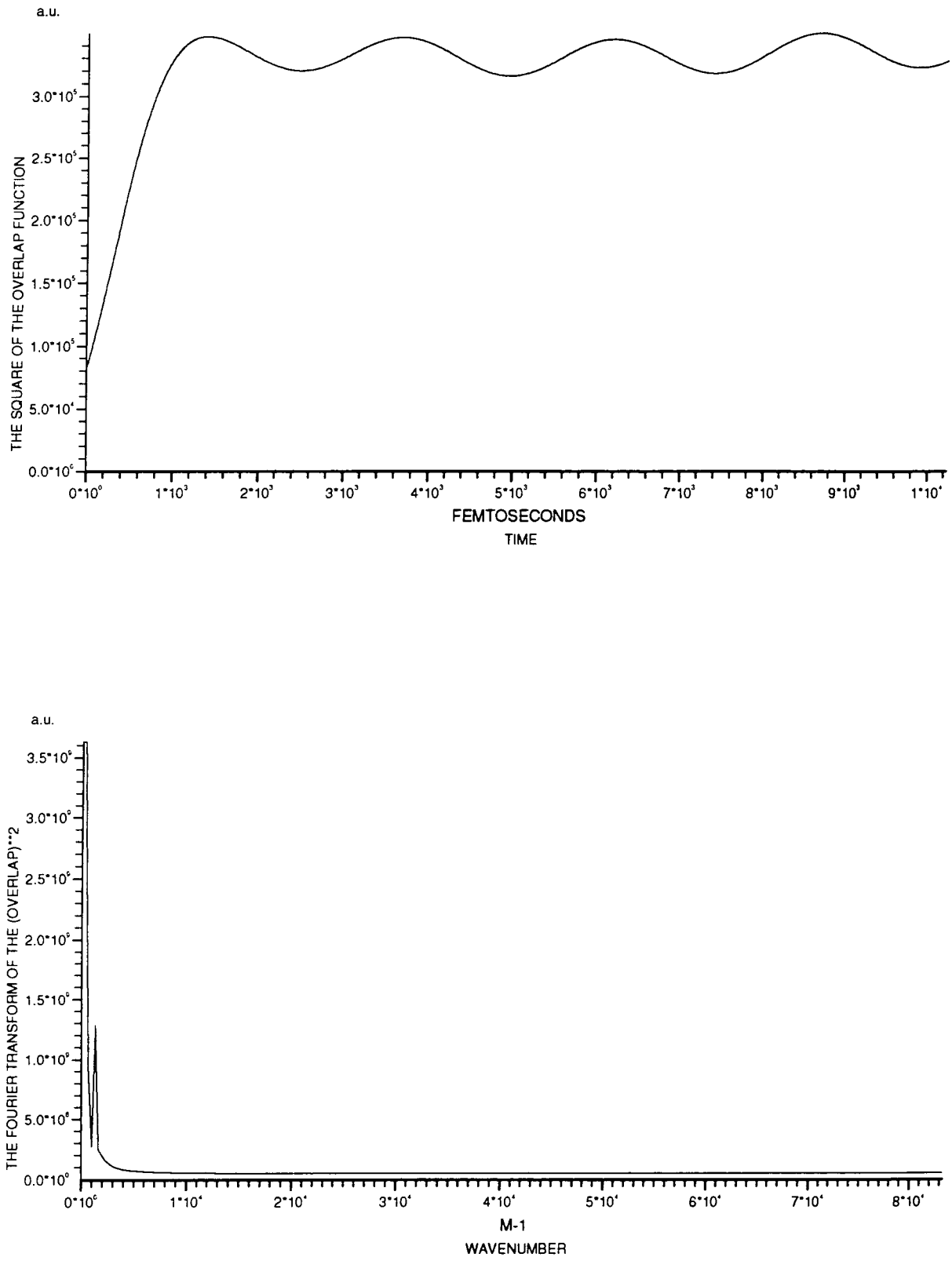

Fig. 51. Graphs showing the *approximate* Na_3^+ signal as a function of t_D and its Fourier transform for the 16000 cm^{-1} picosecond experiment.

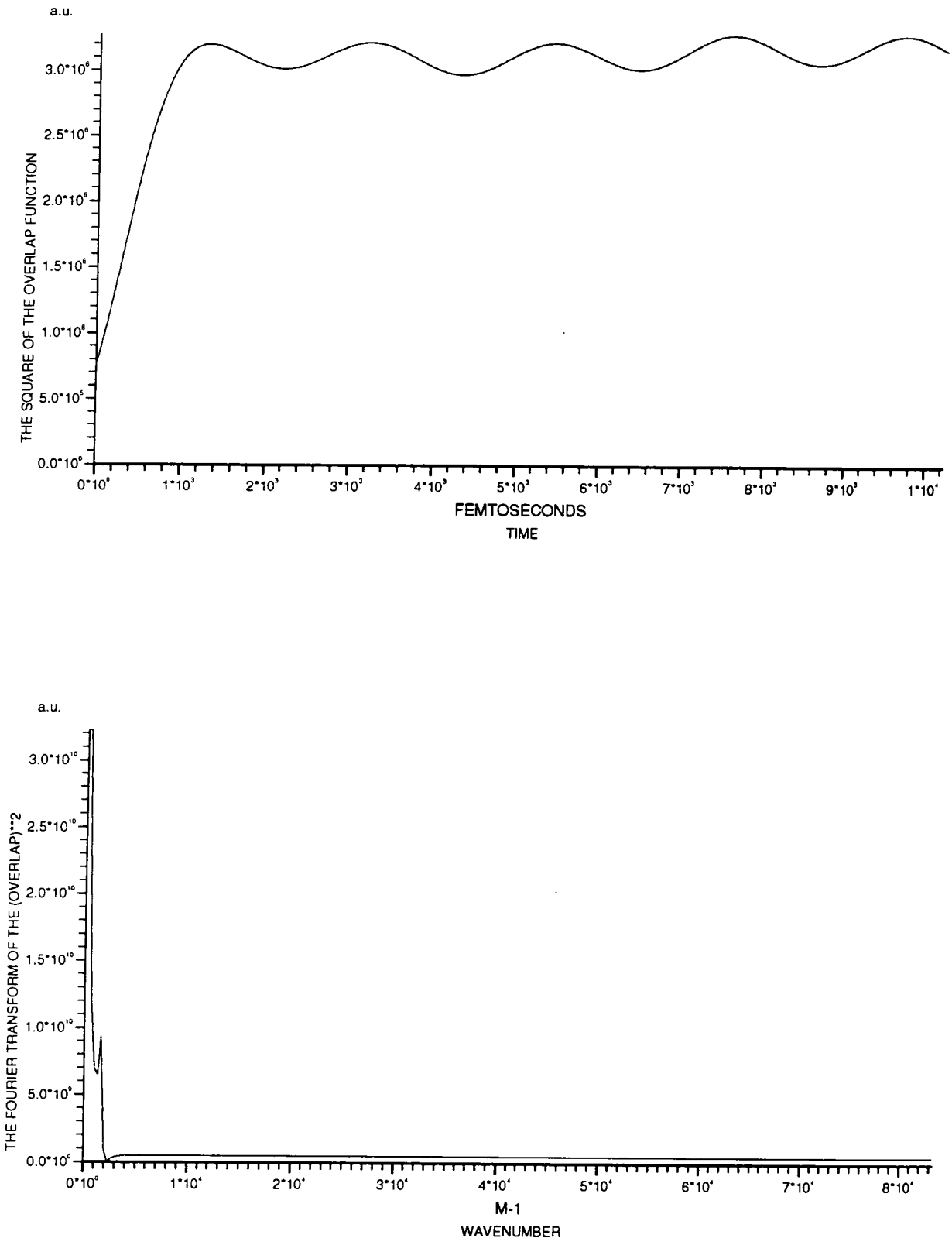

Fig. 52. Graphs showing the *approximate* Na_3^+ signal as a function of t_D and its Fourier transform for the 16129 cm^{-1} picosecond experiment.

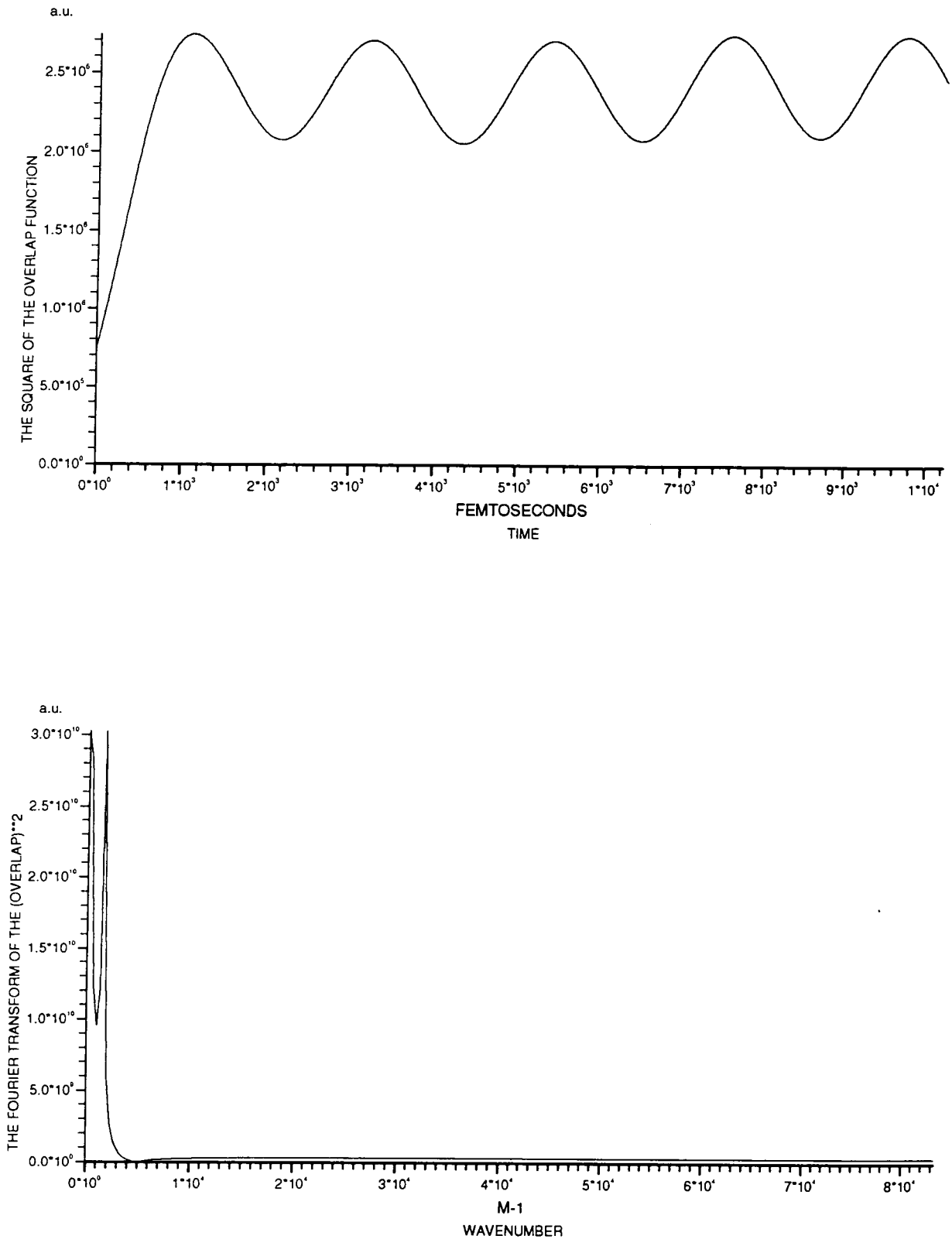

Fig. 53. Graphs showing the *approximate* Na_3^+ signal as a function of t_D and its Fourier transform for the 16136 cm^{-1} picosecond experiment.

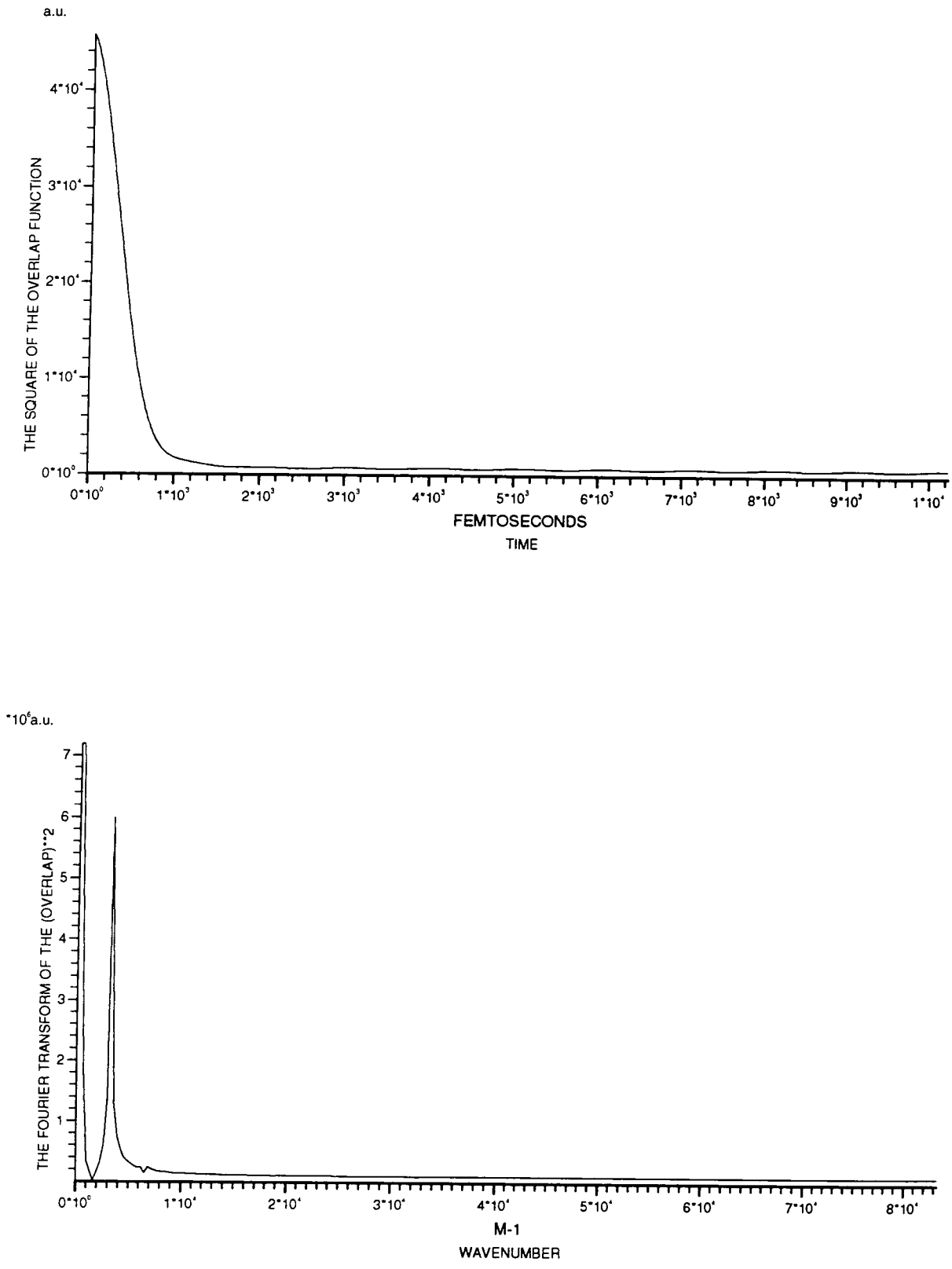

Fig. 54. Graphs showing the *approximate* Na_3^+ signal as a function of t_D and its Fourier transform for the 16207 cm^{-1} picosecond experiment.

Results for 16000 cm-1 ps expt.
Transform of Autocorrelation function, showing energy levels.

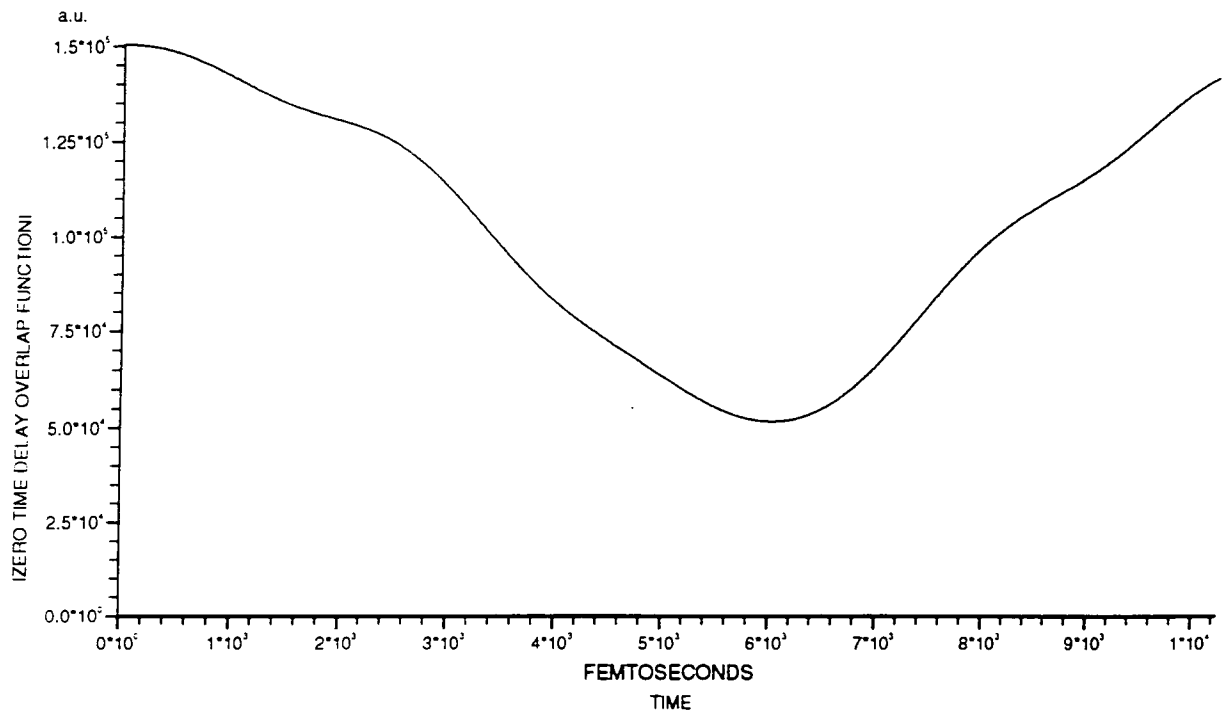

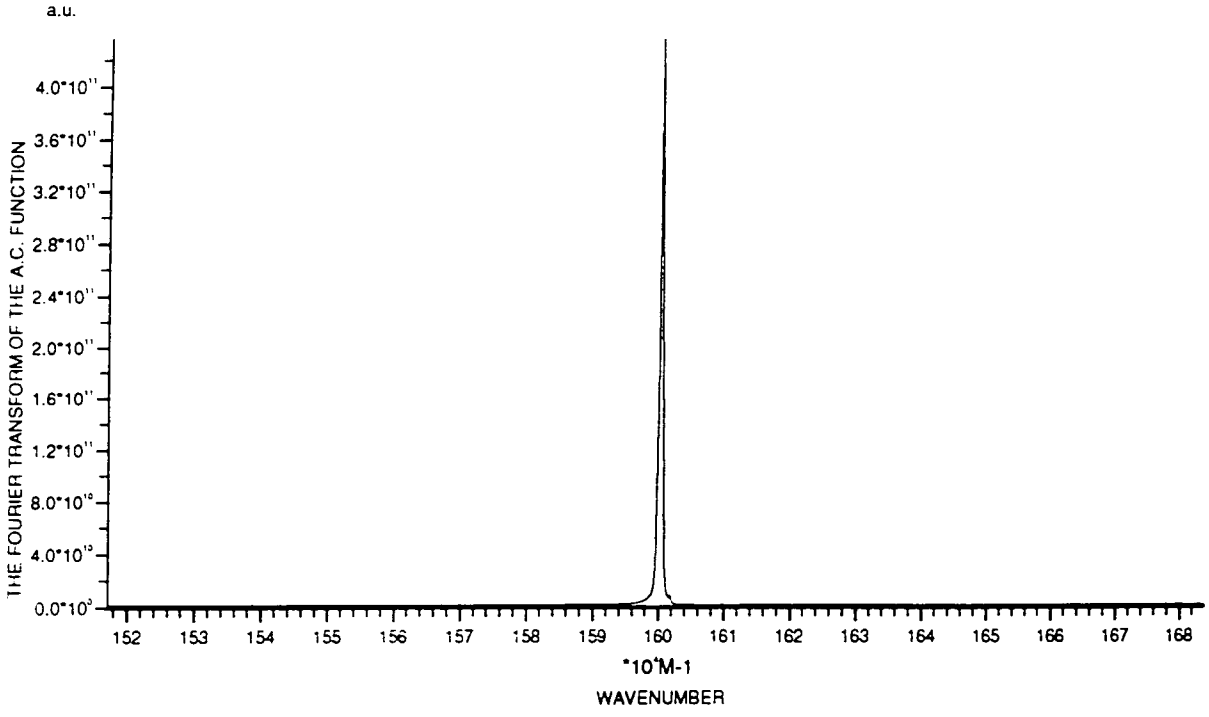

Fig. 55. Graphs showing the zero time delay overlap fn. over t_D and the Fourier transform of the autocorrelation fn. for the 16000 cm^{-1} ps expt.

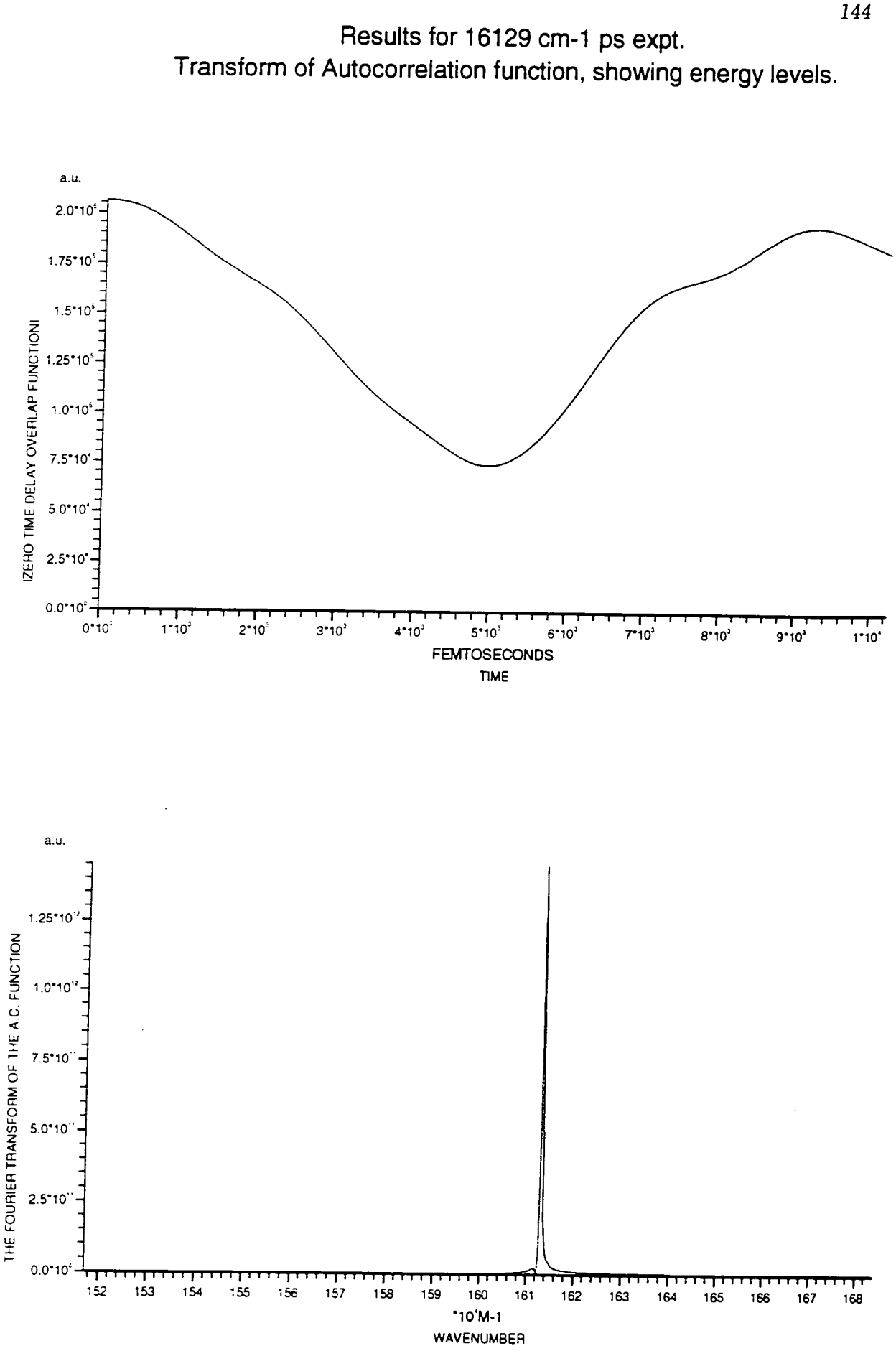

Fig. 56. Graphs showing the zero time delay overlap fn. over t_D and the Fourier transform of the autocorrelation fn. for the 16129 cm^{-1} ps expt.

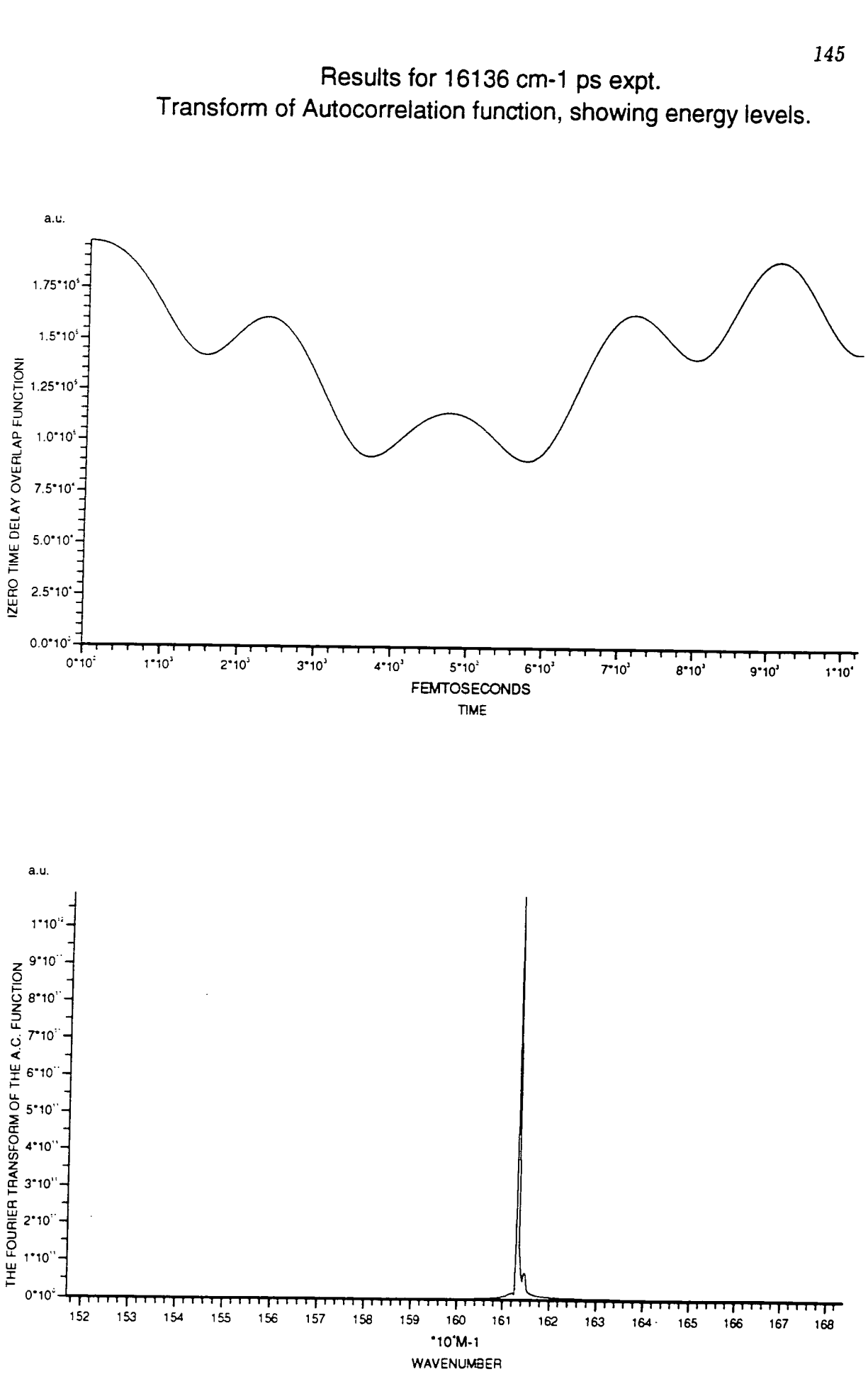

Fig. 57. Graphs showing the zero time delay overlap fn. over t_D and the Fourier transform of the autocorrelation fn. for the 16136 cm^{-1} ps expt.

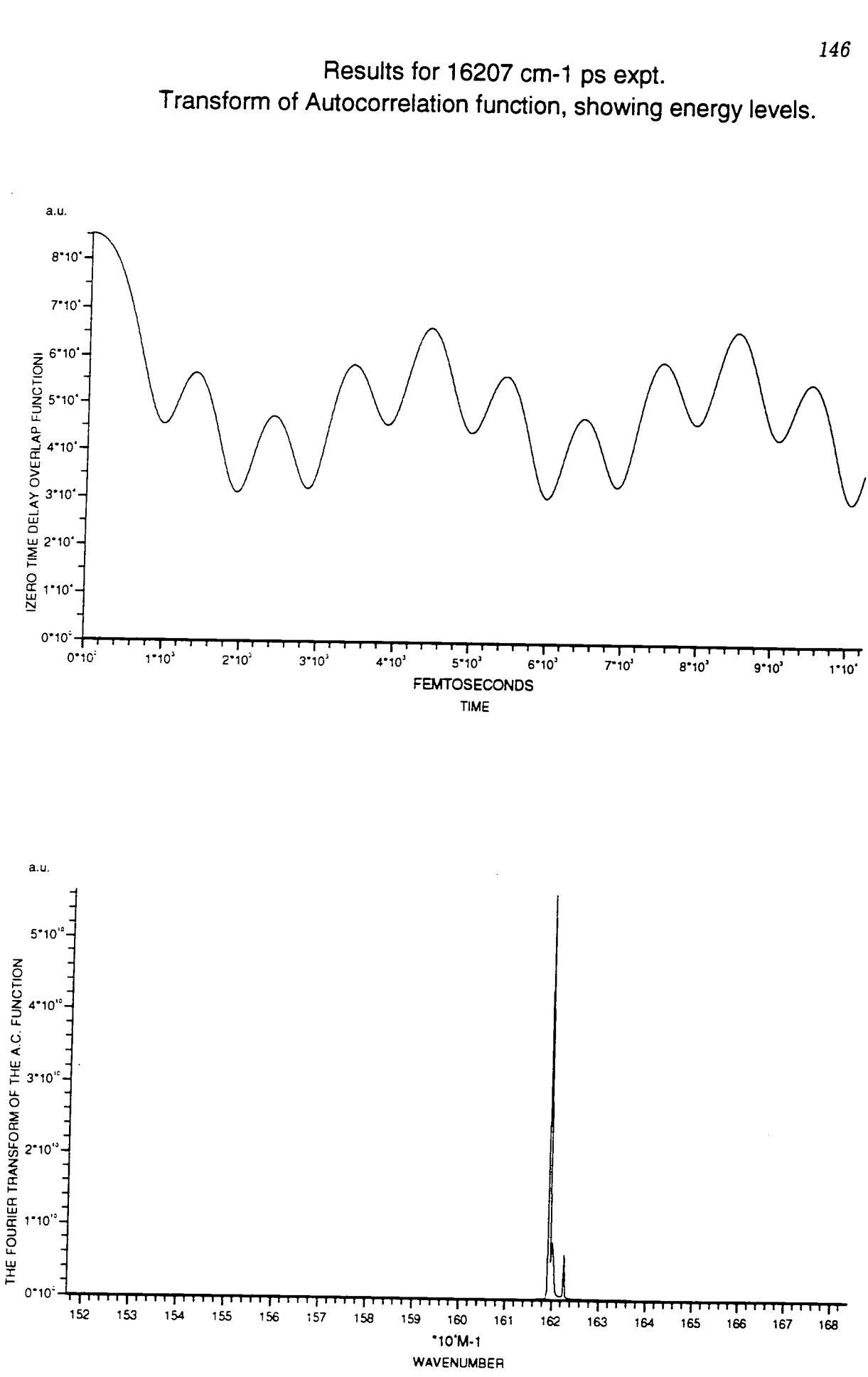

Fig. 58. Graphs showing the zero time delay overlap fn. over t_D and the Fourier transform of the autocorrelation fn. for the 16207 cm^{-1} ps expt.

6: Three Dimensions

The previous chapter is concerned with two-dimensional calculations on the sodium trimer, i.e. the effect of the symmetric stretch has not been taken into account. This mode is usually considered to be less important because it is of a_1' symmetry, so that distortion in this coordinate does not change the symmetry of the potential. However, there is evidence that the coupling between the symmetric stretch and the other two vibrational modes may be significant [117][119].

The question of interest for the femtosecond experiments, which calculations in three dimensions can address, is concerned with the very strong intensity of the symmetric stretch frequency compared to the pseudorotational-radial frequency in the experimental spectrum of the ion signal. The dominance of the results by this frequency implies that the molecule is highly excited in the symmetric stretch coordinate. This means that there is a wavepacket on the B state which moves towards and away from the equilibrium geometry of the symmetric stretch coordinate for the ion ($Q_{s_0} = 3.443$ Å), with a high amplitude motion. However, the static spectroscopy shows little, if any, excitation in the symmetric stretch coordinate. This implies that the wavepacket produced on the three dimensional B state surface would not be highly excited in the symmetric stretch coordinate, and that the ion signal would not be dominated by the symmetric stretch frequency. In the last chapter it was seen that the wavepacket produced on the B state surface was highly excited in the radial direction, i.e. it moved backwards and forwards across the 'trough' with a high amplitude motion. Thus, it would be expected that the ion signal would reflect this strongly varying radial displacement, i.e. the results would be dominated by the radial frequency.

For the picosecond experiments the questions of interest are: first, whether the extra energy levels due to the symmetric stretch frequency will be populated to any extent and so affect the beating frequencies seen in the ion signal; and secondly, whether a coupling of the (Q_x, Q_y) and the Q_s vibrational modes can explain the rapid decay in the ion signal.

The Hamiltonian in three dimensions is:

$$H = \frac{-\hbar^2}{2m}\left[\frac{1}{4r^2} + \frac{d^2}{dr^2} + \frac{1}{r^2}\frac{d^2}{d\phi^2}\right] + \frac{-\hbar^2}{2m}\frac{d^2}{dQ_s^2} + V(r, \phi, Q_s). \qquad (176)$$

In the following, when the radial direction is mentioned, this refers to the radial mode in the pseudorotational space and does not refer to the symmetric stretch mode.

6.1 The Potential—$V(r, \phi, Q_s)$

The three-dimensional potential is divided into two terms:

$$V(r, \phi, Q_s) = V_{Q_s}(Q_s) + V_C(r, \phi, Q_s). \tag{177}$$

The first term $V_{Q_s}(Q_s)$ only depends on the Q_s coordinate, and the second term $V_C(r, \phi, Q_s)$ couples together all three coordinates. An harmonic potential is used for $V_{Q_s}(Q_s)$:

$$V_{Q_s}(Q_s) = \frac{K_{Q_S} \Delta Q_s^2}{2}, \tag{178}$$

where ΔQ_s is the distortion in the symmetric stretch coordinate away from its equilibrium position (when there is no coupling), Q_{s_0}. The force constant, K_{Q_S}, is derived from the symmetric stretch frequency, ω_{Q_s}:

$$K_{Q_s} = (2\pi)^2 \omega_{Q_S}^2 m, \tag{179}$$

(the reduced mass of the mode is in this case the mass of a sodium atom).

Now the potential which couples all three vibrational coordinates, $V_C(r, \phi, Q_s)$, must be introduced. A form for this potential has been suggested by Meiswinkel and Köppel [117]; this potential takes into account the influence of the totally symmetric mode on the $E \otimes e$ Jahn-Teller effect. Here, an implicit extension of this potential is used, to describe the influence of the totally symmetric mode on the pseudo-Jahn-Teller effect, (as for the B state of the sodium trimer, described previously). The potential can be expressed in the following form:

$$V_{\pm}(r, \phi, Q_s) = \frac{Kr^2}{2} \pm r \left[2(P + b\Delta Q_s)^2 + 2f(P + b\Delta Q_s) r \cos(3\phi) + \left(\frac{fr}{\sqrt{2}} \right)^2 \right]^{1/2}, \tag{180}$$

where P, K and f have been defined previously (in Chapter 5) and b represents the bilinear coupling constant involving both vibrational modes (e' and a_1'). $V_C(r, \phi, Q_s)$ is taken to be $V_-(r, \phi, Q_s)$. Comparing this potential to that defined previously, equation (153), it can be seen to be analogous except that the linear coupling constant P is replaced by the term $P + b\Delta Q_s$. It is assumed that the bilinear coupling constant is of comparable magnitude to the normal quadratic coupling constant [117].

The positions of the minima and saddle points depend on the signs of the coupling constants in a similar way to that described in the last chapter; thus, the surface is characterised by the following extremal points $(r_0, \phi_0, \Delta Q_{s_{s,0}})$:

$$-\cos(3\phi_0) = \pm 1, \qquad r_0 = \frac{\sqrt{2}\, P}{(K - 2(b^2/K_{Q_s}) \pm \sqrt{2}\,|f|)}, \tag{181}$$

and

$$\Delta Q_{s_s,0} = \frac{2P(b/K_{Q_s})}{(K - 2(b^2/K_{Q_s}) \pm \sqrt{2}|f|)}, \tag{182}$$

where $\Delta Q_{s_s,0}$ is the amount by which the position of the minimum and saddle points in the symmetric stretch coordinate are shifted from the equilibrium position when there is no coupling (Q_{s_0}). The Jahn-Teller stabilisation energy and the localisation energy are given by:

$$E_s = \frac{P^2}{(K - 2(b^2/K_{Q_s}) - \sqrt{2}\,|f|)}, \qquad E_{\rm loc} = \frac{2\sqrt{2}\,|f|P^2}{[(K - 2(b^2/K_{Q_s}))^2 - 2f^2]}. \tag{183}$$

6.2 The Simulation of the Experiment in Three Dimensions

The inclusion of the third dimension, i.e. the symmetric stretch, can be achieved by the use of the coupled channel method, which was discussed in Chapter 4, or by a simple extension of the methods used in the two-dimensional case. In either case the simulation of the experiments was carried out in the same way, i.e. the pump laser produces the initial wavepacket on the B state, this is propagated in time, and then the observables are extracted from the time-dependent wavefunction.

The simulation of the experiment using the full three dimensional calculations, i.e. rather than using the coupled channel method, was achieved by taking advantage of the implicit parallelism in the problem. This was described earlier (in Chapter 2) w.r.t. the multi-dimensional Fourier transforms, and the fact that these transforms can be calculated in several independent stages.

6.2. 1 Coupled Channel Method

This method involves an expansion of the wavefunction in a suitable basis set, and is essentially exact provided sufficient basis functions are used. The wavefunction is then substituted into the T.D.S.E. to produce a set of coupled differential equations.

In this case the wavefunction is expanded in a basis set as follows:

$$\Psi_B(t) = \sum_{v'} \psi_{(B,v')}(r,\phi,t)\chi_{v'}(Q_s), \tag{184}$$

where the functions $\chi(Q_s)$ represent the Q_s vibrational states, and are solutions of:

$$\left(\frac{-\hbar^2}{2m}\frac{d^2}{dQ_s^2} + V_{Q_s}(Q_s)\right)\chi_v(Q_s) = E_v\chi_v(Q_s). \tag{185}$$

As stated above a harmonic potential is used for $V_{Q_s}(Q_s)$ so that E_v is equal to $\hbar\omega_{Q_s}v$, and $\chi_v(Q_s)$ are harmonic oscillator functions. As for the two-dimensional calculations, the

zero-point energy is subtracted from the potential, thus the value of E_v does not include a $\hbar\omega_{Q_s}/2$ term.

Inserting $\hat{H}$ and Ψ_B into the T.D.S.E., left-multiplying both sides by $\chi^*_{v''}$ and integrating over Q_s gives:

$$i\frac{\partial\psi_{(B,v'')}(r,\phi,t)}{\partial t} = \frac{-\hbar^2}{2m}\left[\frac{1}{4r^2}+\frac{d^2}{dr^2}+\frac{1}{r^2}\frac{d^2}{d\phi^2}\right]\psi_{(B,v'')}(r,\phi,t) + E_{v''}\psi_{(B,v'')}(r,\phi,t) + \sum_{v'}\langle v''|V(r,\phi,Q_s)|v'\rangle\psi_{(B,v')}(r,\phi,t). \tag{186}$$

The only difference between this equation and those propagated previously is the potential, which requires a sum over matrix elements $\langle v''|V(r,\phi,Q_s)|v'\rangle$ for each channel. Once these matrix elements are calculated, the same method as described in Chapter 5 can be used to propagate the wavefunction in time.

6.2. 2 The Initial Wavefunction for the Coupled Channel Method

The full three dimensional initial packet on the ground state can be expanded in the basis given above; the coefficients will be the initial packets in each channel:

$$\Psi_X(r,\phi,Q_s) = \sum_v \Psi_{(X,v)}(r,\phi)\chi_v(Q_s). \tag{187}$$

Thus, the full three dimensional packet on the ground state, $\Psi_X(r,\phi,Q_s)$, obtained from TRIATOM, as was described in Chapter 5, is projected onto the basis functions to produce the initial packet in each channel:

$$\Psi_{(X,v)}(r,\phi) = \langle v|\Psi_X(r,\phi,Q_s)\rangle. \tag{188}$$

The pump laser is treated as before, using first-order time-dependent perturbation theory, so that $\Psi_B(t)$ is produced from the initial packet on the ground state. However, in this case the pump laser is exciting the initial packet to several different 'channels', each with energy E_v, and a different wavepacket is formed in each 'channel'.

6.2. 3 The Observables

The Na_3^+ signal

The calculation of the Na_3^+ signal was not done by explicit inclusion of the probe laser. This is because the full treatment of the probe laser would have been extremely computationally intensive. Thus the Na_3^+ signal was calculated in the approximate way described in the previous chapter, i.e. using the square modulus of the overlap of the time-dependent wavefunction with the ground-state wavefunction of the ion. For the picosecond experiments the Na_3^+ signal was calculated using the overlap of the time-dependent wavefunction

with another wavefunction of the ion, i.e. the wavefunction for first excited vibrational state of the bend. The reasons for this were discussed in Chapter 5. The zero time delay overlap function was also used to model the ion signal.

Other observables

The norm and energy were calculated. The energy in each mode was calculated approximately. The Hamiltonian used for the radial motion was:

$$H_r = \frac{-\hbar^2}{2m}\left[\frac{1}{4r^2} + \frac{d^2}{dr^2}\right] + \left[\frac{r^2K}{2} - P'r + \frac{1}{2}f'r^2 - \frac{1}{2}\frac{f'^2r^3}{(P' + b'\Delta Q_s)} + \frac{1}{8}\frac{f'^4r^5}{(P' + b'\Delta Q_s)^3} - \frac{2}{8}\frac{f'^3r^4}{(P' + b'\Delta Q_s)^2}\right] \tag{189}$$

where $P' = \sqrt{2}\,P$, $f' = \sqrt{2}\,f$ and $b' = \sqrt{2}b$. The Hamiltonian for the angular motion was approximated as:

$$H_\phi = \frac{-\hbar^2}{2m}\left[\frac{1}{r^2}\frac{d^2}{d\phi^2}\right] + \left[-f'r^2\cos^2\left(\frac{3\phi}{2}\right) + \frac{1}{8}\frac{f'^2r^3}{(P' + b'\Delta Q_s)}\cos^2(3\phi) + \frac{2}{8}\frac{f'^3r^4}{(P' + b'\Delta Q_s)^2}(2\cos\left(\frac{3\phi}{2}\right))\right]. \tag{190}$$

These are very similar to those used in the last chapter, equations (170) and (171), except that P' is now replaced by $(P' + b'\Delta Q_s)$ (apart from the second term in the potential part of H_r). The Hamiltonian used to describe the motion in the Q_s coordinate is:

$$H_{Q_s} = \frac{-\hbar^2}{2m}\left[\frac{d^2}{dQ_s^2}\right] + \left[\frac{\Delta Q_s^2 K_{Q_s}}{2} - b'\Delta Q_s\right]. \tag{191}$$

The average values of r, ϕ and ΔQ_s were also calculated, as well as the autocorrelation function and the zero time delay overlap function.

6.3 The Calculations

As in the last chapter, the calculations were done to simulate both the femtosecond and the picosecond experiments, so that the calculations were done several times with different parameters for the laser pulses, which were given in the last chapter. The calculations were also done assuming the laser pulse was 'white light'.

6.3. 1 The Femtosecond Experiment

In order to try to resolve the apparent paradox concerning the intensity of the symmetric stretch frequency in the results of the femtosecond experiments, various parameters of the three-dimensional potential of the B state, and of the femtosecond laser pulse, were altered

to investigate their effect on the time-dependence of the ion signal. The calculations at the various different parameters were also carried out with a 'white light' laser pulse in order to investigate their effect on the static spectroscopy. The parameters which were varied were:

1. The position of the minimum in the symmetric stretch coordinate, Q_{s_0} (with the bilinear coupling constant b set to zero). It is expected that if the value of Q_{s_0} differed greatly between the X and B states, there would be a great deal of excitation in the Q_s mode, and the wavepacket would oscillate along this coordinate giving rise to an ion signal dominated by this frequency. However, it is also expected that if the value of Q_{s_0} differed greatly between the X and B states, the static spectroscopy would show many lines corresponding to the symmetric stretch mode. The calculations were carried out for values of Q_{s_0} of 3.7 Å, 3.8 Å and 3.9 Å. These calculations were done simply to confirm the apparent contradiction between the results of the femtosecond experiments and the static spectroscopy.

2. The value of the bilinear coupling constant b. The calculation was done using a dimensionless bilinear coupling constant, corresponding to b, equal to $0.012/\sqrt{2}, 0.048/\sqrt{2}$, $0.086/\sqrt{2}, 0.1/\sqrt{2}$ and $1.5/\sqrt{2}$. The value of Q_{s_0}, the equilibrium position of the symmetric stretch coordinate when there is no coupling, was set to 3.7 Å. Again the effects on the time-dependence of the ion signal and the static spectroscopy were monitored.

3. The temporal width of the femtosecond laser pulse (with Q_{s_0} set to 3.7 Å, and b set to zero). The spectral width of the laser pulse is not particularly well described using a laser pulse with a temporal width of 70 fs. This is because, as was seen in the last chapter, the spectral width of the laser pulse is not completely determined by its temporal width (see figure 19). Thus, in order to model the spectral width of the laser pulse, the temporal width was decreased to approximately 41 fs. A laser pulse with this temporal width has a spectral width of approximately 500 cm^{-1}. It was seen in the last chapter that the narrower the pump laser pulse that was used, the stronger the initial damping of the amplitude of the radial motion. Obviously, if the radial motion is initially strongly damped then the ion signal will show less dependence on the radial frequency and the symmetric stretch frequency will appear stronger.

6.3. 2 The Picosecond Experiments

For the picosecond experiments, the calculations were carried out initially for b equal to zero (with Q_{s_0} set to 3.7 Å), to investigate the effect of the introduction of extra energy levels, and then with different values of b, to investigate the effect of the coupling between the symmetric stretch mode and the other two modes. The calculation was done using

a dimensionless bilinear coupling constant, corresponding to b, equal to $0.012/\sqrt{2}$ and $0.048/\sqrt{2}$.

6.4 The Results

6.4. 1 The Femtosecond Experiment

The effect of the variation of Q_{s_0}

As expected an increase in Q_{s_0} away from the value on the X surface (3.63 Å), produced much larger oscillations in Q_s. This can be seen in figures 59 and 60, which show the calculated observables over the propagation time for Q_{s_0} equal to 3.7 Å and 3.9 Å. It can also be seen from these figures that the zero coupling between the symmetric stretch and the other modes gives rise to a motion which is completely separable, i.e. there is no change in the energy in the Q_s mode, and the observables for the radial and angular modes are similar to those for the two-dimensional calculation. Figures 61 and 62 show the ion signal and its Fourier transform for the different values of Q_{s_0}. It can be seen that as Q_{s_0} increases, the intensity of the peak in the Fourier transform at 110 cm^{-1}, which corresponds to the symmetric stretch frequency, increases compared to the intensity of the peak at 127 cm^{-1}, which corresponds to the radial frequency. Other frequencies observed in the spectra, with varying intensities, are: 17 cm^{-1}, which corresponds to a beating frequency between the radial motion (127 cm^{-1}) and the symmetric stretch (110 cm^{-1}); 34 cm^{-1}, which corresponds to a beating frequency between the first overtone of the radial frequency (254 cm^{-1}) and the first overtone of the symmetric stretch (220 cm^{-1}); 93 cm^{-1}, which corresponds to a beating frequency between the radial motion (127 cm^{-1}) and the first overtone of the symmetric stretch frequency (220 cm^{-1}); 144 cm^{-1}, which corresponds to a beating frequency between the first overtone of the radial frequency (254 cm^{-1}) and the symmetric frequency (110 cm^{-1}); 220 cm^{-1}, which corresponds to the first overtone of the symmetric stretch; and 254 cm^{-1}, which corresponds to the first overtone of the radial frequency.

The experimental spectrum, of the Fourier transform of the ion signal, shows frequencies at 12(m), 19(m), 34(w), 50(m), 73(m), 105(vs), 90(s), 123(w) and 141.5(w). It seems then that increasing Q_{s_0} produces an ion signal which shows a fair correspondence the experimental results.

However, the results of the calculations for the vertical excitation of the laser pulse (figures 63 and 64), i.e. those which correspond with the static spectroscopy, show that as Q_{s_0} increases, the intensity of the peaks in the energy spectrum which correspond to the symmetric stretch frequency also increase (note that the resolution of these spectra

are lower than for the two-dimensional case since the propagation was done for half the length of time). This does not correspond well with the results obtained for the static spectroscopy, which show little, if any, excitation in the symmetric stretch.

Thus, it appears that the value of Q_{s_0} for the B state must indeed be similar to that for the X state. Therefore, other parameters must be investigated if an ion signal, which corresponds well with the experimental one, is to be obtained.

The effect of the variation of b

Figures 65 and 66 show the observables calculated over the propagation time, for two values of b ($0.012/\sqrt{2}$ and $0.086/\sqrt{2}$). It can be seen that increasing b shifts the position of the equilibrium position on the B surface, away from Q_{s_0}, by an amount ΔQ_{s_0} (see equation (182)), which increases as b increases. This shift in the minimum on the surface gives rise to a motion in the symmetric stretch with a different amplitude than for the $b = 0.0$ case. As well as this shift in the equilibrium and change in the amplitude of the motion, the oscillation in Q_s can now be seen to depend not only on the symmetric stretch frequency, but also on the radial frequency. The reason for this is, of course, that the eigenstates of the potential are no longer separable into those depending on Q_s only, and those depending on r and ϕ only. Thus the vibrational modes in Q_s will now be weakly dependent on r and ϕ. Also the vibrational modes in r (which are also weakly depend on ϕ) will now be weakly dependent on Q_s. This can be seen from the figures: the motion in r is now also dependent on the symmetric stretch frequency. As well as the effect on the oscillation in each mode, it can be seen that energy is exchanged between these modes. Thus energy is transferred from the radial mode, which was initially highly excited, to the symmetric stretch mode, which initially has only a small amount of excitation.

The question then is how this coupling effects the ion signal. Figures 67 and 68 show the ion signal and its Fourier transform for the two values of b. It can be seen that as b is increased the relative intensity of the symmetric stretch frequency increases a little, but also that the spectrum becomes much more 'irregular', i.e. there are very many peaks in the spectrum. Since the increase in b changes the oscillation in Q_s and also makes the motion in r depend on this frequency, the increase in the intensity of the symmetric stretch frequency is not unexpected. However, the motion on the surface is much more complicated giving rise to a signal with many different frequency components.

Figures 69 and 70 show the corresponding results for the vertical excitation, i.e. the static spectroscopy, for the two values of b. The lines in the spectra are expected to become broader as b increases, because the energies of the various zeroth-order eigenstates (i.e. those corresponding to the completely uncoupled potential) will be broadened, as the states mix

together. (The experimental spectrum does show some width to each peak, but this is mostly likely explained by the lack of rotational resolution.) However, there is not much evidence for this broadening in the spectra of the simulated static spectroscopy, though the energy levels corresponding to the excited symmetric stretch states seem to be less distinct.

Thus, although increasing b does in some way increase the correspondence of the ion signal to the experimental one, the other factor associated with this increase is not totally acceptable, i.e. the irregularity in the spectrum of the ion signal.

The effect of the variation of the temporal width

Figure 71 shows the observables calculated over the propagation time (for the femtosecond experiment with the narrower laser pulse); compared to figure 59 (for the femtosecond experiment) the amplitude of the radial motion can be seen to be smaller. Also the amplitude of the motion in the symmetric stretch is slightly larger. Figure 72 shows the approximate ion signal (for the femtosecond experiment with the narrower laser pulse). Compared to figure 61 (for the femtosecond experiment) the symmetric stretch frequency has increased its intensity relative to the radial frequency. Thus, an explanation for the poor agreement of the calculations done here with the experimental results could be the inadequate modelling of the pump laser pulse by a single Gaussian whose spectral width is determined only by its temporal width.

Correlation with the results of Gerber's experiments

The Freiburg experiments produced a time-dependent Na_3^+ signal, together with the Fourier transform of this, which gave a spectrum containing frequencies characteristic of motion on the B surface. As stated previously, the spectrum contains many frequencies including the symmetric stretch frequency (105 cm^{-1}) and the radial frequency (123 cm^{-1}). The intensity of the symmetric stretch frequency is much stronger than that of the radial frequency.

The results obtained here also show a symmetric stretch frequency (110 cm^{-1}) and a radial frequency (127 cm^{-1}). The frequencies appear to agree well. The other frequencies in the experimental spectrum may arise from the beating together of these two frequencies and their overtones. However, in order that the results obtained for the static spectroscopy continued to agree well with the experimental results, parameters for the potential were used that gave the intensity of the symmetric stretch frequency to be much less than the radial frequency. In order to obtain a better agreement with the experimental results, it was necessary to use a laser pulse which had a larger spectral width than that implied by the experimental temporal width.

Even at best, the correlation with the experimental results cannot be expected to

be very good because there have been many approximations involved in obtaining the calculated results. Some of these are:

1. The quality of the potential surfaces used, particularly the approximate treatment of the coupling of the (Q_x, Q_y) and the Q_s vibrational modes.
2. The approximate method by which the Na_3^+ signal for the three-dimensional calculations was obtained. Uncertainty concerning the ionisation potential of the sodium trimer makes the assessment of the reliability of this assumption difficult.
3. The modelling of the laser pulse by one pulse with a Gaussian time profile, whose spectral width is determined by its temporal width.
4. The neglect of the coupling between the B and X states. The X state should be included in the time-dependent part of the calculation because the pump can produce a wavepacket in the X state by two-photon excitation via the B state, and the probe can ionise it via another two-photon process.

6.4. 2 The Picosecond Experiments

The effect on the beating frequencies

The Fourier transform of the autocorrelation function for all the picosecond experiments showed that the same energy levels were populated as in the two-dimensional calculations, with small differences in the relative intensities. The ion signals (approximated using both the overlap function and the zero time delay overlap function) obtained for the picosecond experiments showed no difference to those obtained in the two-dimensional calculations, except that the ion signal for the 16207 cm^{-1} picosecond experiment had a larger amplitude of oscillation. Therefore, the extra energy levels (corresponding to the symmetric stretch mode) are not populated and consequently there is no effect on the beating frequencies seen in the ion signal. For the 16000, 16129 and 16136 cm^{-1} experiments this is possibly because the spectral width of the laser pulse is not great enough to excite the lowest excited symmetric stretch level at 16110 cm^{-1}. For the 16207 cm^{-1} picosecond experiment, it seems likely that the laser pulse would be able to excite the energy level at 16220 cm^{-1} (the second excited state of the symmetric stretch). However, this is very close in energy to the $u = 1, j = 5$ energy level so that the beat frequencies would change little, making the effect of this excitation difficult to see, unless the excitation was very large, which is unlikely since it has already been noted that the equilibrium position of the symmetric stretch mode on the B surface is very similar to that on the X surface.

The effect of the variation of b

Figure 73 shows the variation in the observables calculated over the propagation time

for the 16207 cm^{-1} picosecond experiment. It can be seen that the radial and angular modes have been coupled to the symmetric stretch mode. There is now a small amplitude motion in the symmetric stretch, and there is a flow of energy between all three modes. Figure 74 shows the ion signals obtained for the simulation of the 16207 cm^{-1} picosecond experiments for b set to $0.048/\sqrt{2}$. The ion signal now contains a faster oscillation corresponding to the symmetric stretch frequency. The picosecond experiments at other frequencies showed similar behaviour.

The introduction of the coupling between the symmetric stretch and the other two modes did not produce a decaying ion signal for any of the picosecond experiments.

Correlation with the results of Wõste's experiments

The inclusion of the symmetric stretch frequency has not improved the correlation of the calculated results to the experimental results. As was discussed at the end of Chapter 5, the picosecond experiments at 625, 620, and 619.7 nm show some agreement with the experimental results. The oscillations though are not with a time period of 3 ps but of $\approx$ 2 ps. The results at 617 nm show less similarity to the experimental results. The ion signal oscillates with a long time period of approximately 4 ps, which can be compared to the experimental value of 3 ps, but there is also a short time period in the oscillation of approximately 1 ps, which has no corresponding value in the experimental ion signal. None of the ion signals obtained for the picosecond experiments show the fast decay that is found in the experimental results.

As for the femtosecond experiments, it is not expected that the correlation between the results obtained here and the experimental results will be very good. Some of the reasons for this poor comparison are the same as for the femtosecond experiment. However, there are some other reasons in the case of the picosecond experiments:

1. The quality of the potential surfaces used. In particular the linking together of the barrier to pseudorotation and the circularity of the potential, through the quadratic coupling constant, ensuring that, because the barrier to pseudorotation is thought to be small, the potential is almost circular.
2. Uncertainity over the spectral width of the laser pulse. The laser pulse is said to have a spectral width double that implied by its temporal width. It is thought that this may be due to imperfect mode locking in the dye laser. This may affect the particular levels excited by the laser pulse, and so the frequency with which they beat together.
3. The accuracy with which the excitation energy between the X state and the B state is known, which due to the narrow spectral width of the laser pulse becomes very important. If the B state is placed at an energy which is slightly incorrect this may

cause the laser pulse to be off resonance, which will clearly have a large effect on the results. There is only a small uncertainty in this excitation energy: a value of 16000 cm^{-1} is used here, whilst the most reliable experiments report a value of 15996 cm^{-1} [108]. It is possible that this 4 cm^{-1} difference may be significant for a laser pulse with a spectral width of 15 cm^{-1}, as used for the picosecond experiments.

6.5 Conclusions

The initial wavepacket that is created by the femtosecond laser pulse is, as in the two-dimensional calculations, made up of many states, which are excited in the radial, angular and symmetric stretch modes. This wavepacket has a large amplitude motion in the radial direction, and a small amplitude motion in the symmetric stretch coordinate. However, this is at odds with the experimental femtosecond results which imply that the wavepacket has a small amplitude motion in the radial direction and a large amplitude motion in the symmetric stretch. In order to create a similar wavepacket in the simulation of the experiment, a better model of the laser pulse will have to be developed, which allows the spectral width of the pulse to be determined independently of its temporal width.

The picosecond experiments can be simulated in two dimensions. The inclusion of the extra dimension adds no extra insight into the results of these experiments. As in the two-dimensional calculations, the oscillating ion signal arises because of the beating together of various pseudorotational modes. In order to gain more than the qualitative idea of the experiments given here, it will be necessary to obtain a potential which correctly describes both the energy levels of the pseudorotational modes and the coupling between the radial and angular modes.

Results for fs expt. Q_s0=3.7A, b=0.0

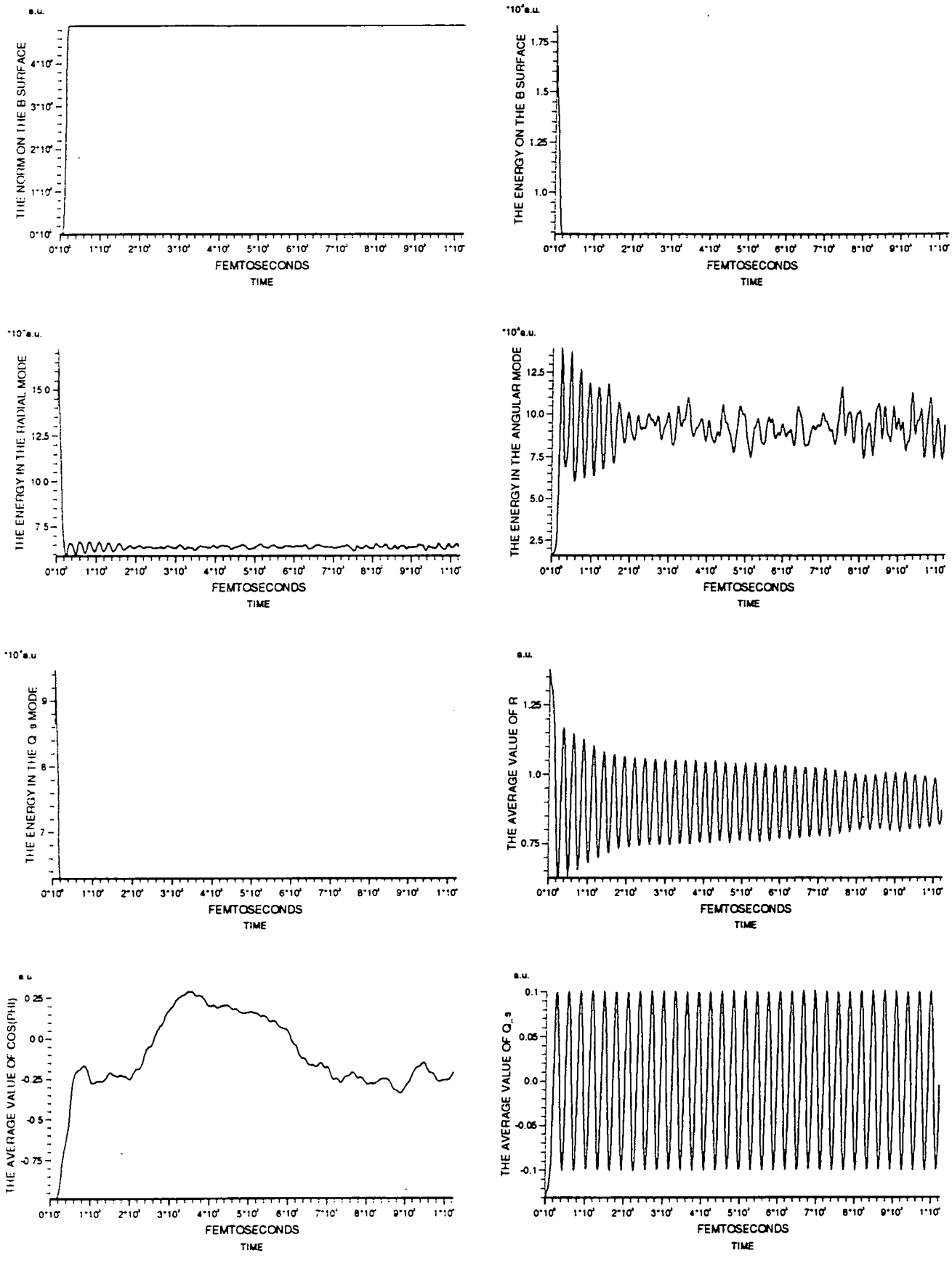

Fig. 59. Graphs showing the variation of the observables over the entire propagation time for the femtosecond experiment, with $b = 0.0, Q_{s_0} = 3.7$ Å.

Results for fs expt. Q_s0=3.9A, b=0.0

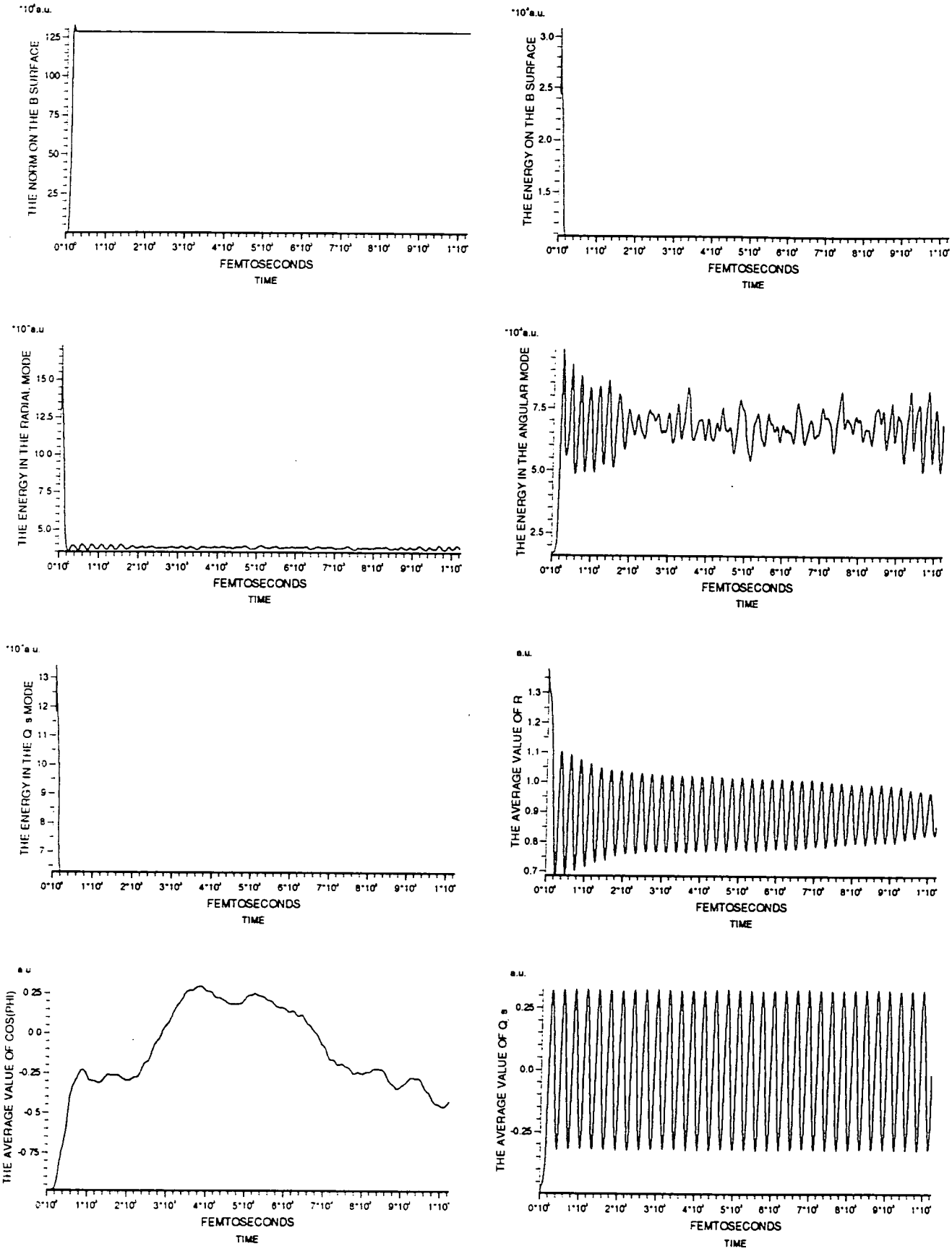

Fig. 60. Graphs showing the variation of the observables over the entire propagation time for the femtosecond experiment, with $b = 0.0, Q_{s_0} = 3.9$ Å.

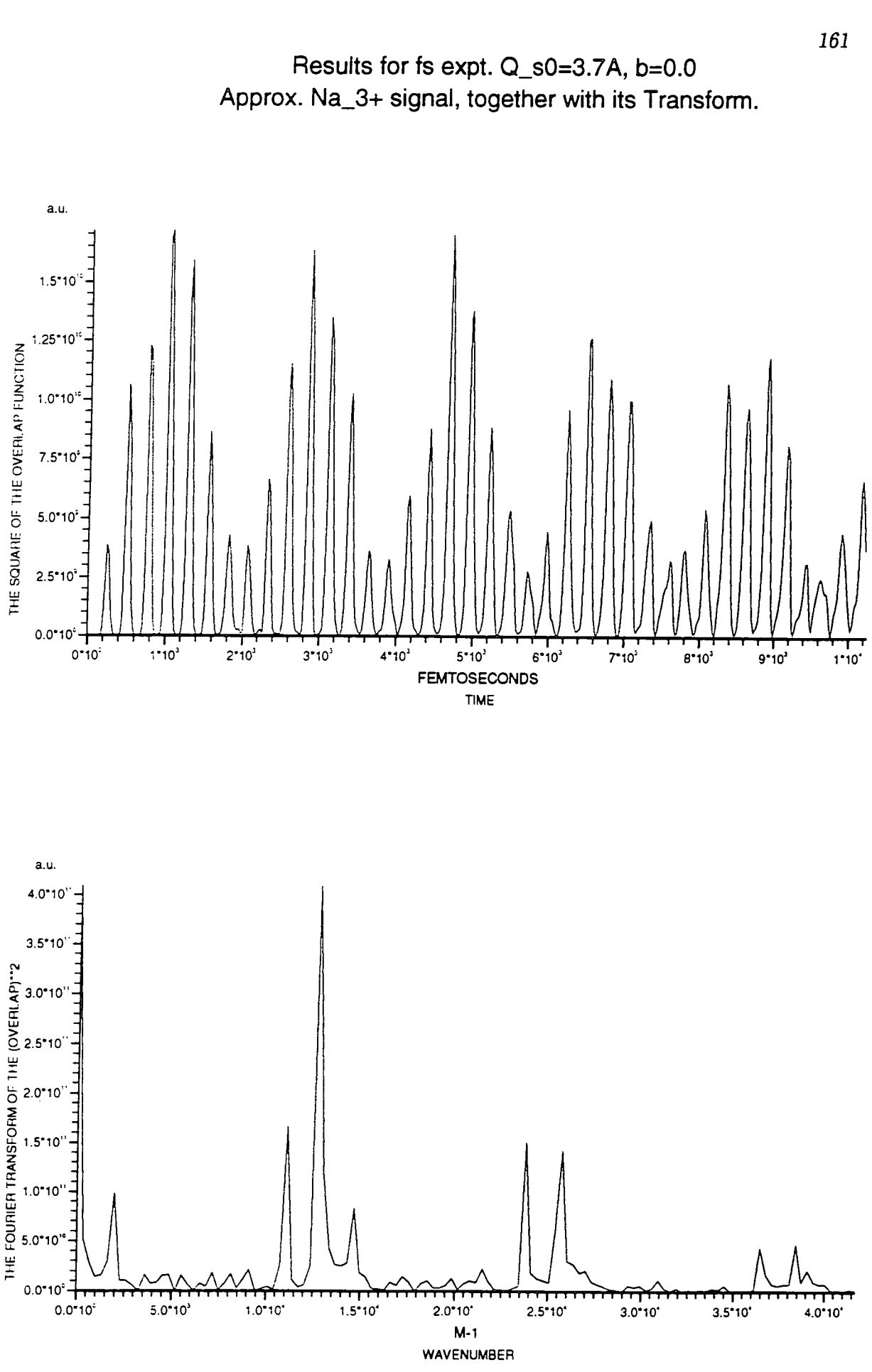

Fig. 61. Graphs showing the *approximate* Na_3^+ signal and its Fourier transform for the femtosecond experiment, with $b = 0.0, Q_{s_0} = 3.7$ Å.

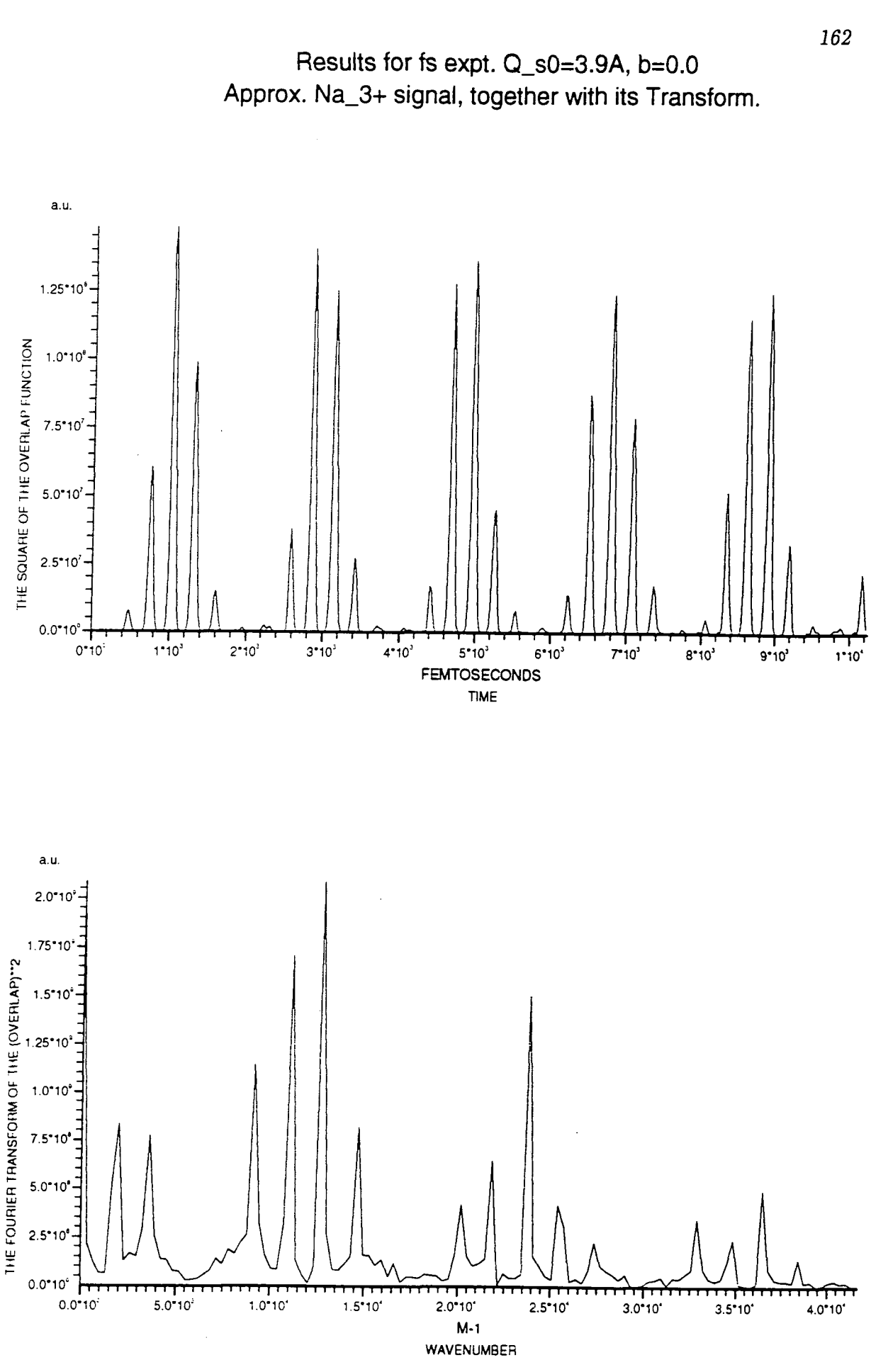

Fig. 62. Graphs showing the *approximate* Na_3^+ signal and its Fourier transform for the femtosecond experiment, with $b = 0.0, Q_{s_0} = 3.9$ Å.

Results for vertical excitation Q_s0=3.7A, b=0.0.
Transform of Autocorrelation function, showing energy levels.

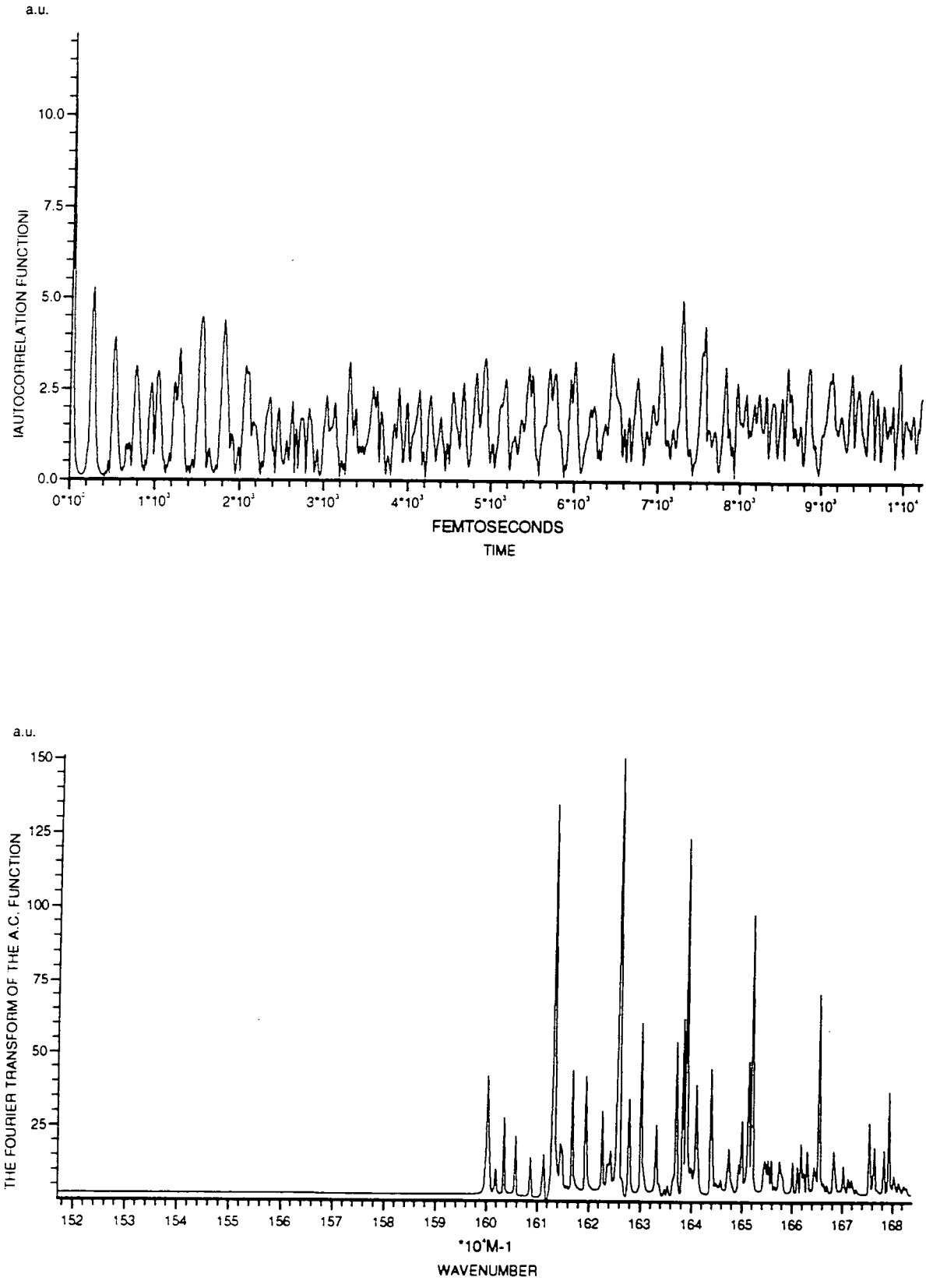

Fig. 63. Graphs showing the autocorrelation function and its Fourier transform for vertical excitation, with $b = 0.0, Q_{s_0} = 3.7$ Å.

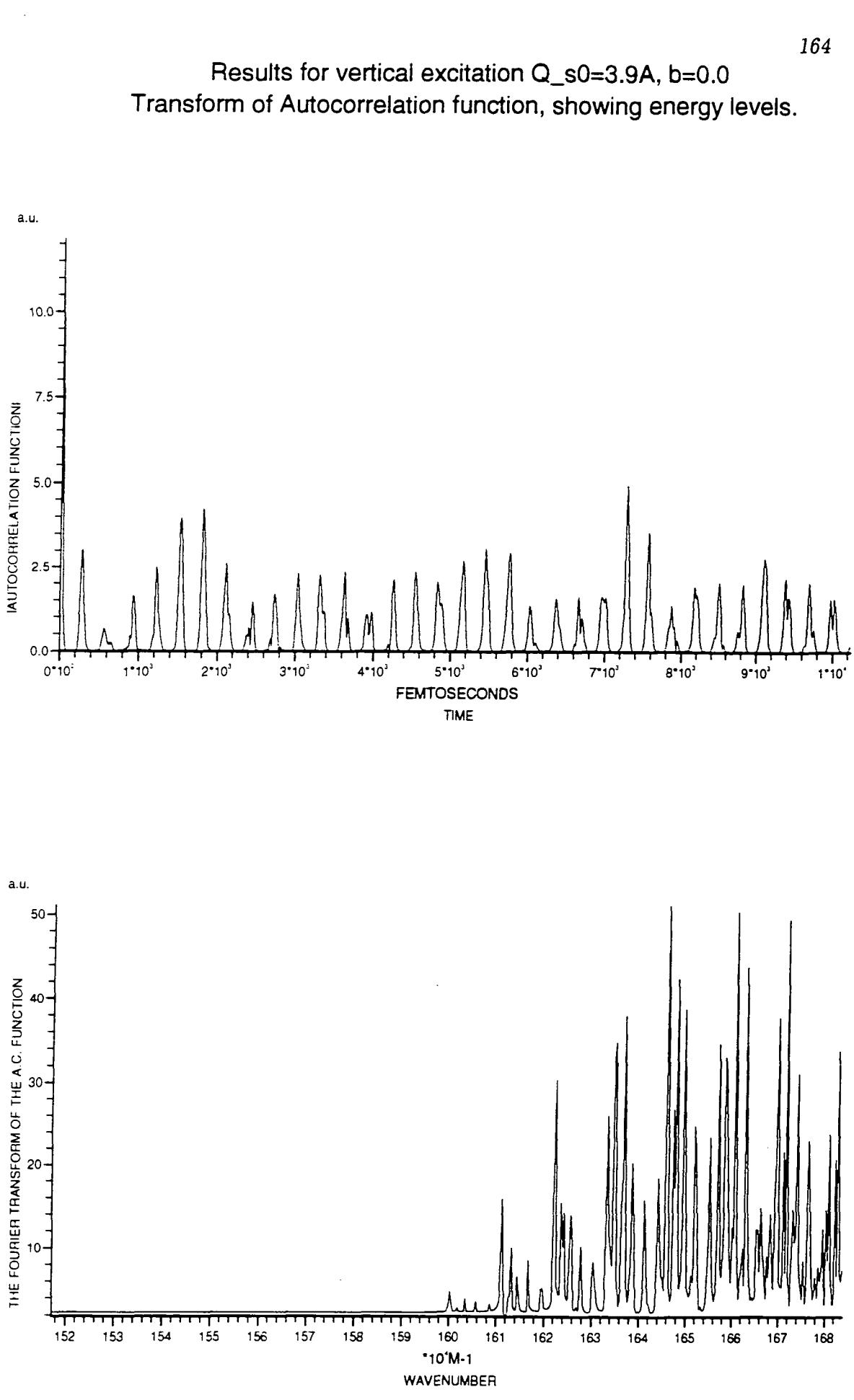

Fig. 64. Graphs showing the autocorrelation function and its Fourier transform for vertical excitation, with $b = 0.0, Q_{s_0} = 3.9$ Å.

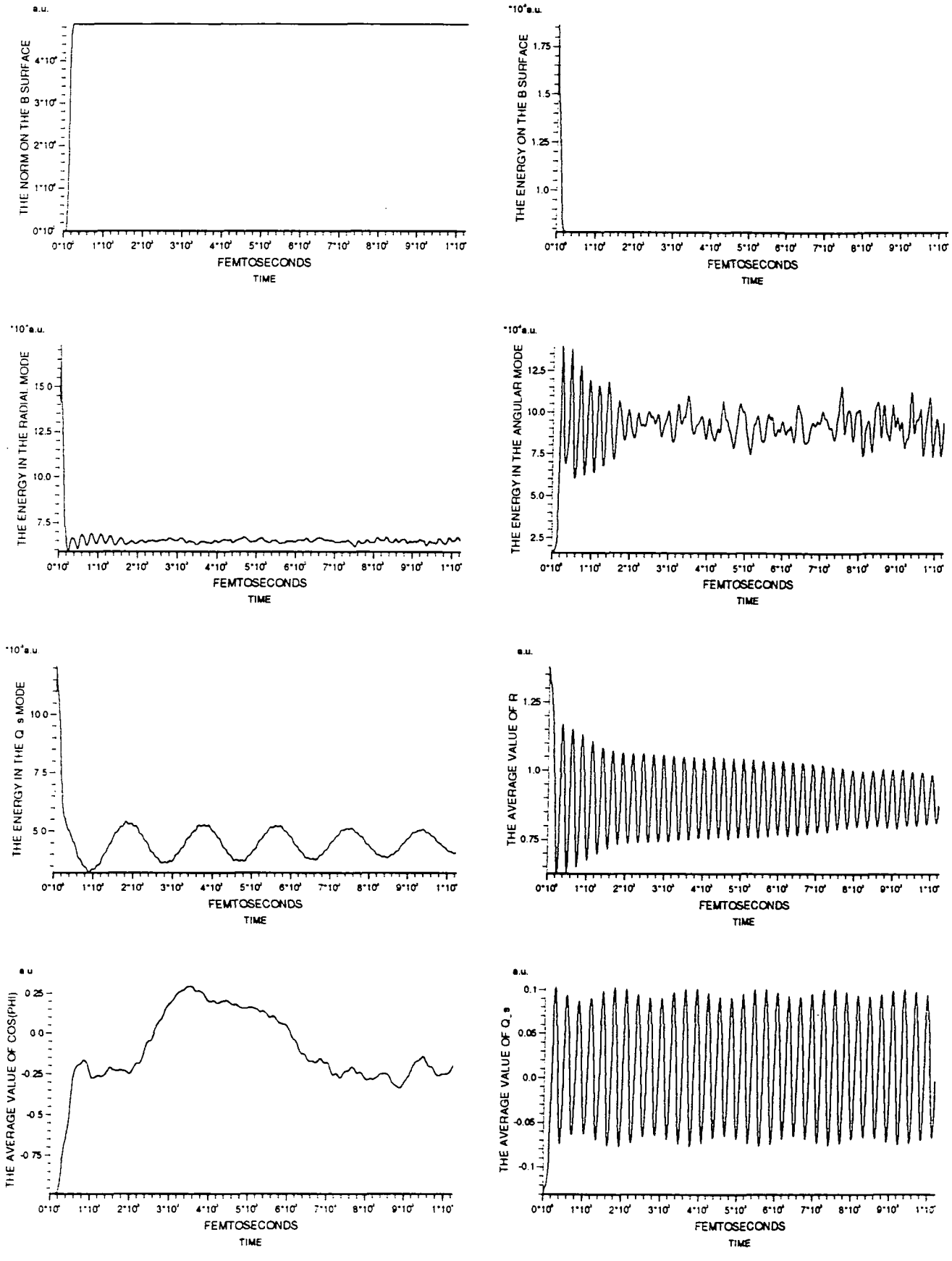

Fig. 65. Graphs showing the variation of the observables over the entire propagation time for the femtosecond experiment, with $b = 0.012/\sqrt{2}, Q_{s_0} = 3.7$ Å.

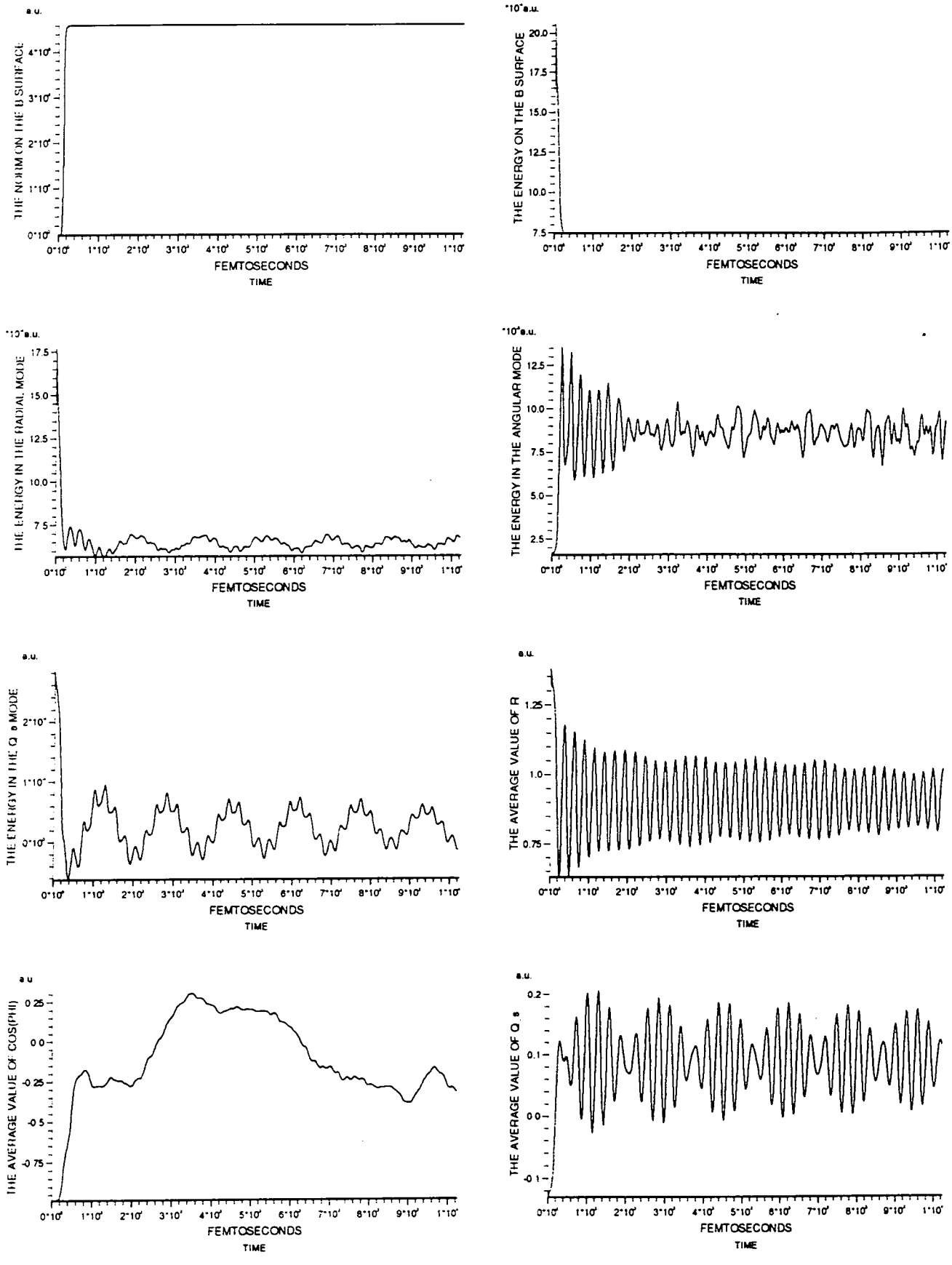

Fig. 66. Graphs showing the variation of the observables over the entire propagation time for the femtosecond experiment, with $b = 0.086/\sqrt{2}, Q_{s_0} = 3.7$ Å.

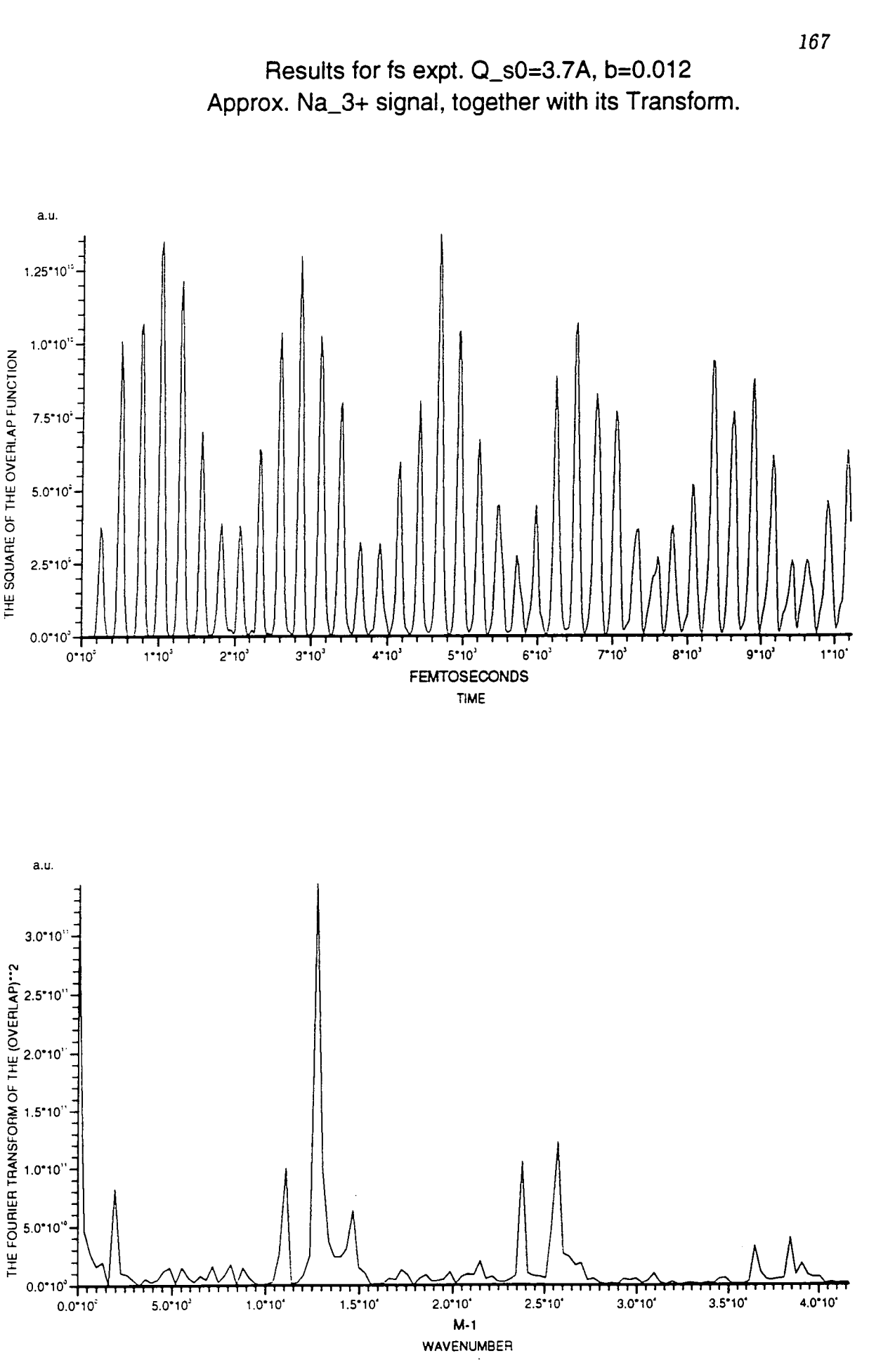

Fig. 67. Graphs showing the *approximate* Na_3^+ signal and its Fourier transform for the femtosecond experiment, with $b = 0.012/\sqrt{2}, Q_{s_0} = 3.7$ Å.

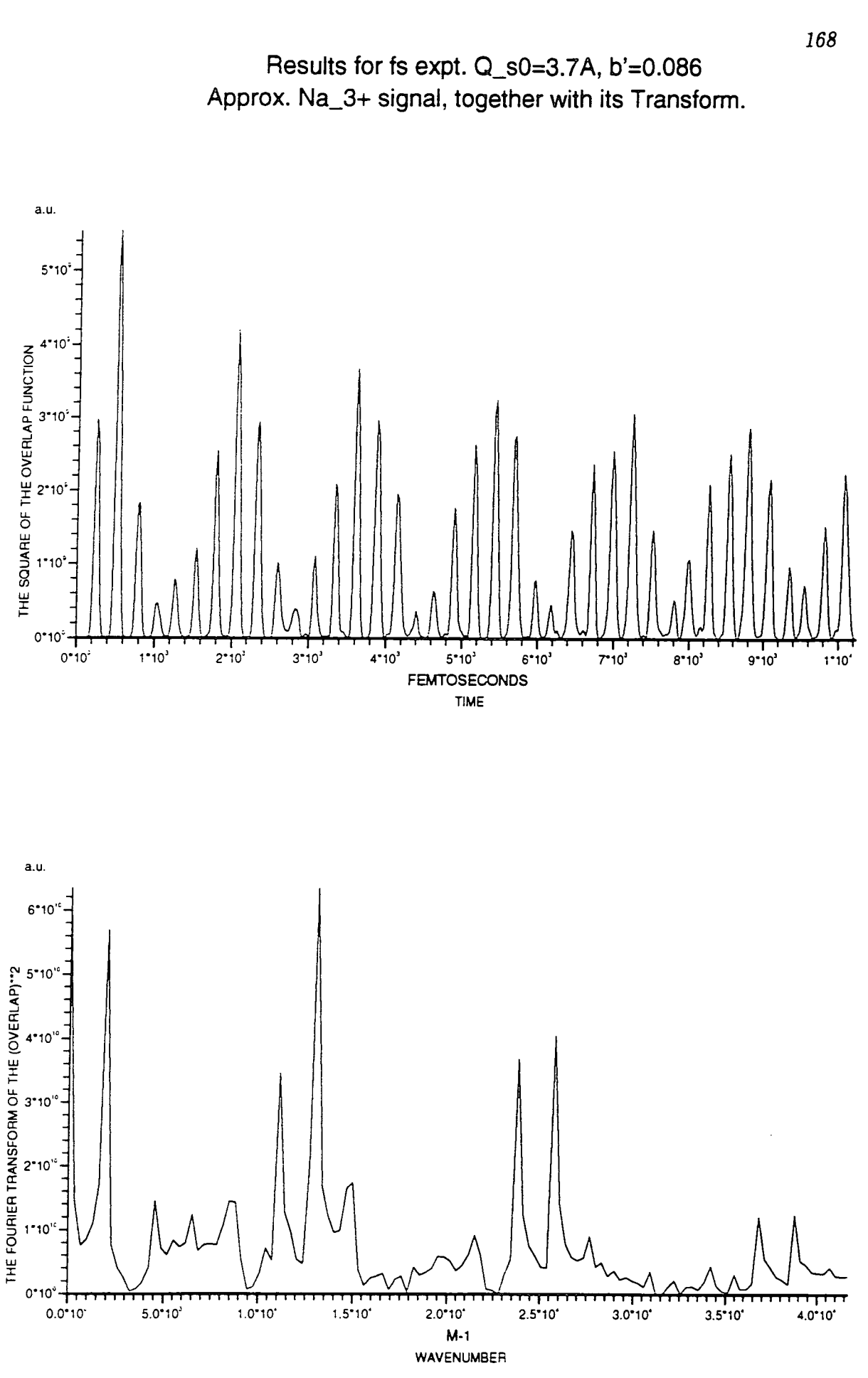

Fig. 68. Graphs showing the *approximate* Na_3^+ signal and its Fourier transform for the femtosecond experiment, with $b = 0.086/\sqrt{2}, Q_{s_0} = 3.7$ Å.

Results for vertical excitation Q_s0=3.7A, b'=0.012.
Transform of Autocorrelation function, showing energy levels.

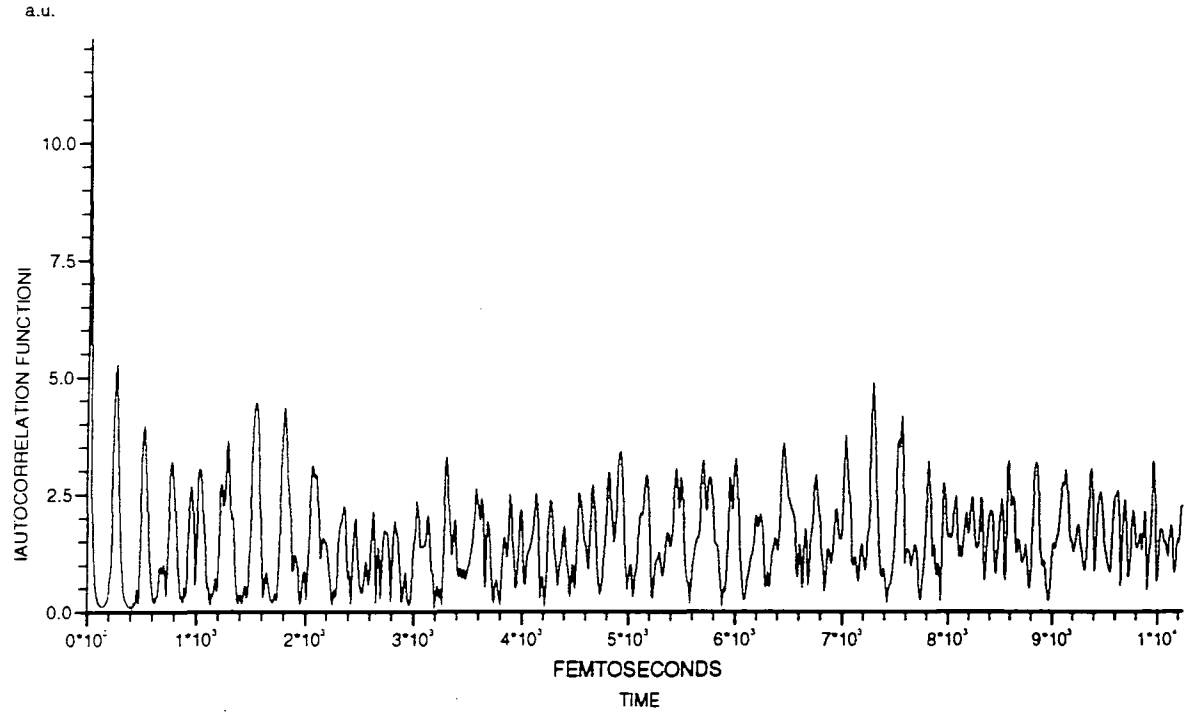

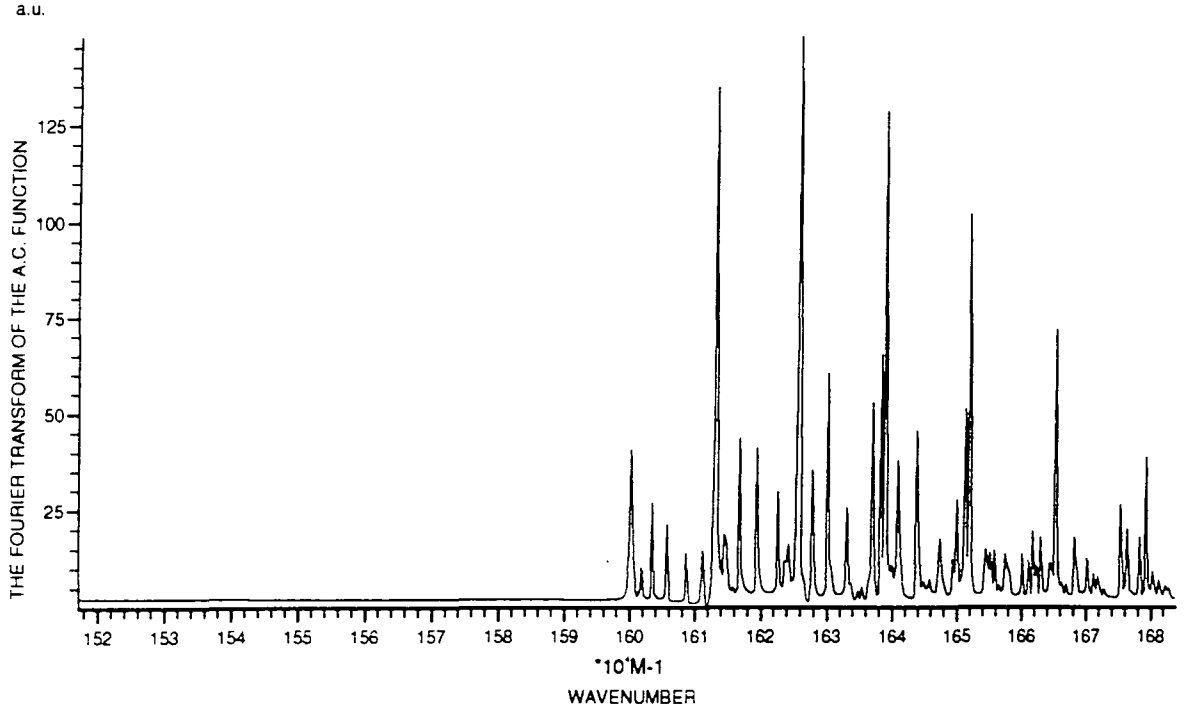

Fig. 69. Graphs showing the autocorrelation function and its Fourier transform for vertical excitation, with $b = 0.012/\sqrt{2}, Q_{s_0} = 3.7$ Å.

Results for vertical excitation Q_s0=3.7A, b'=0.086.
Transform of Autocorrelation function, showing energy levels.

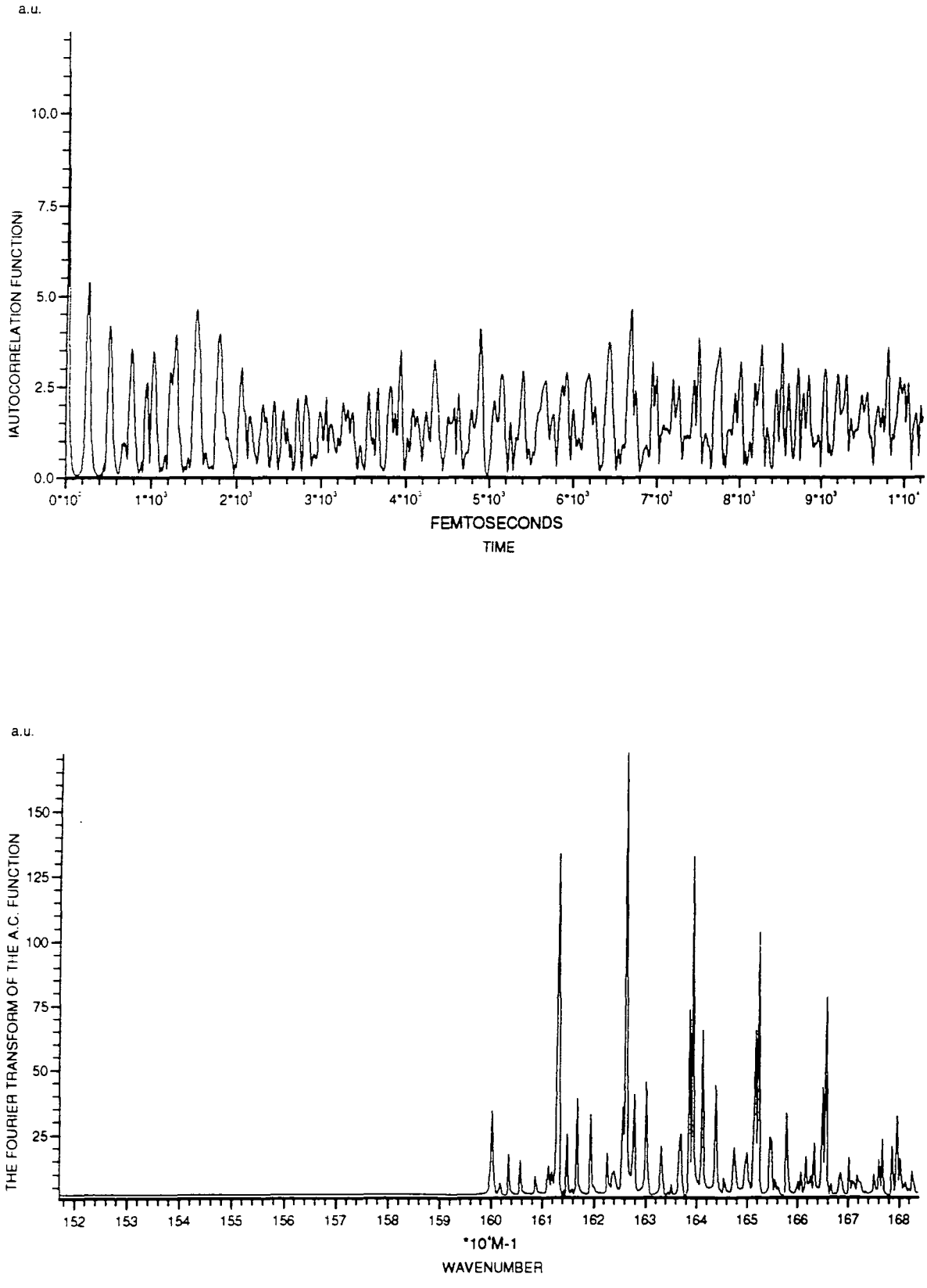

Fig. 70. Graphs showing the autocorrelation function and its Fourier transform for vertical excitation, with $b = 0.086/\sqrt{2}, Q_{s_0} = 3.7$ Å.

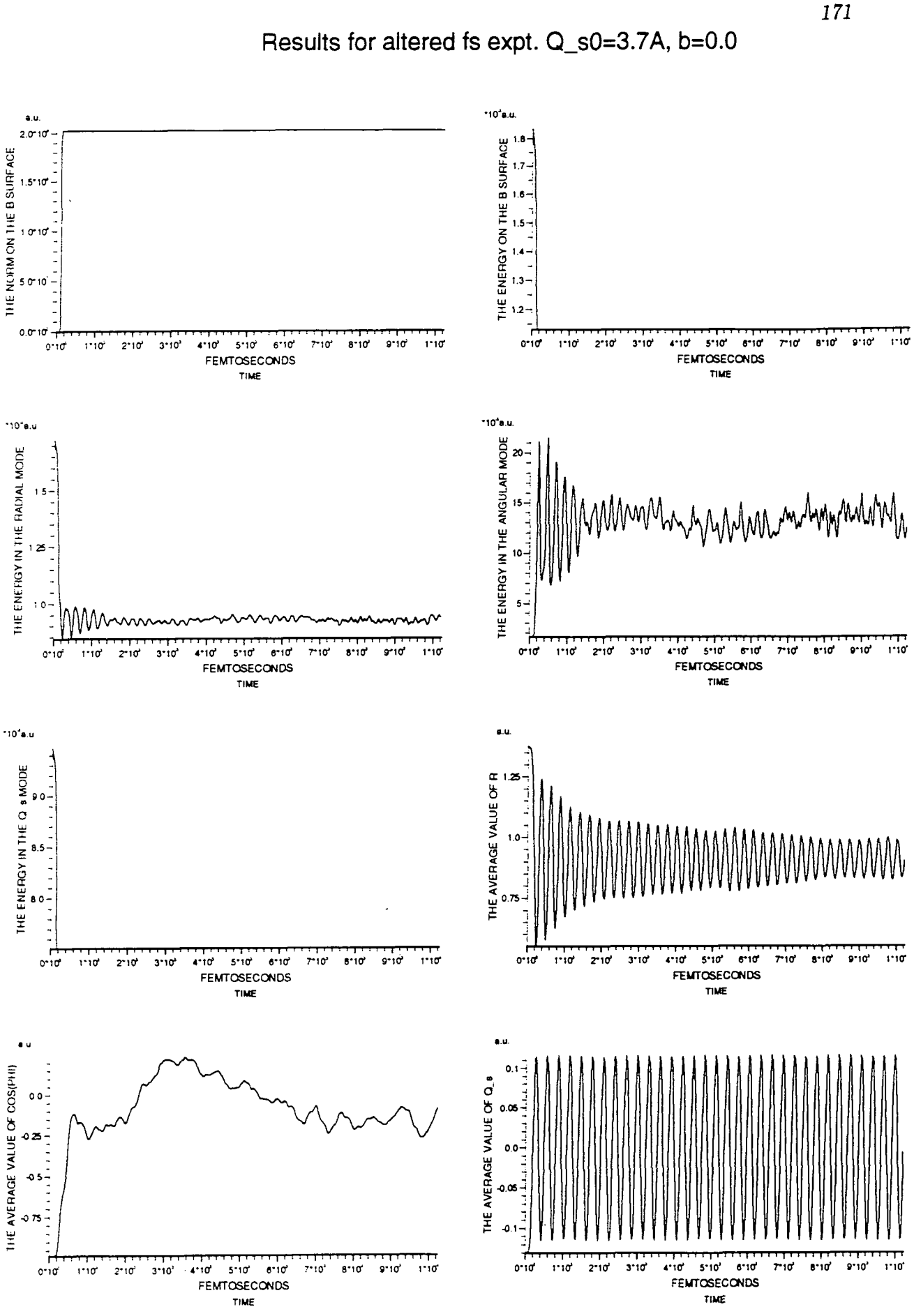

Fig. 71. Graphs showing the variation of the observables over the entire propagation time for the **altered** femtosecond experiment, with $b = 0.0, Q_{s_0} = 3.7$ Å.

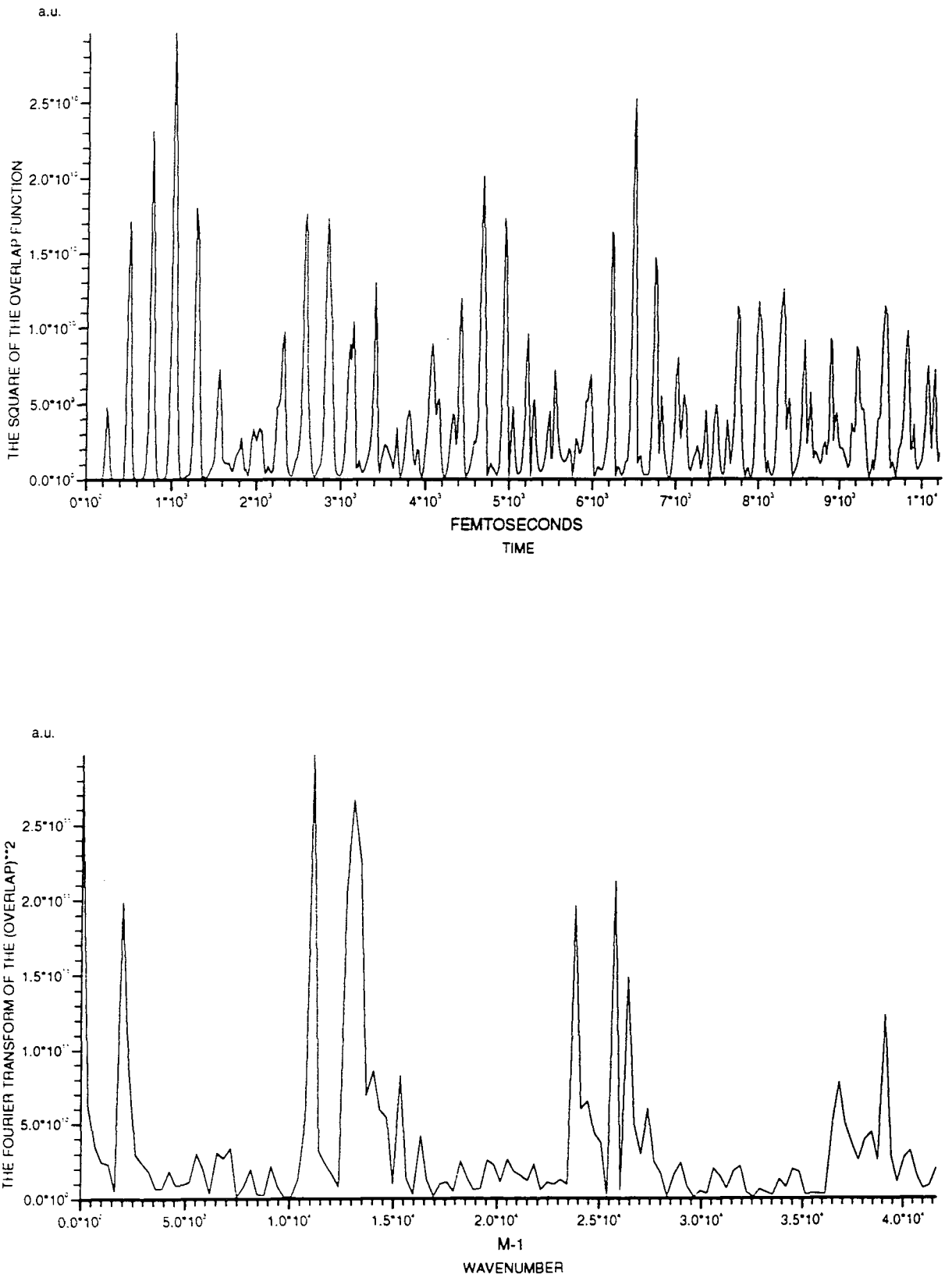

Fig. 72. Graphs showing the *approximate* Na_3^+ signal and its Fourier transform for the **altered** femtosecond experiment, with $b = 0.0, Q_{s_0} = 3.7$ Å.

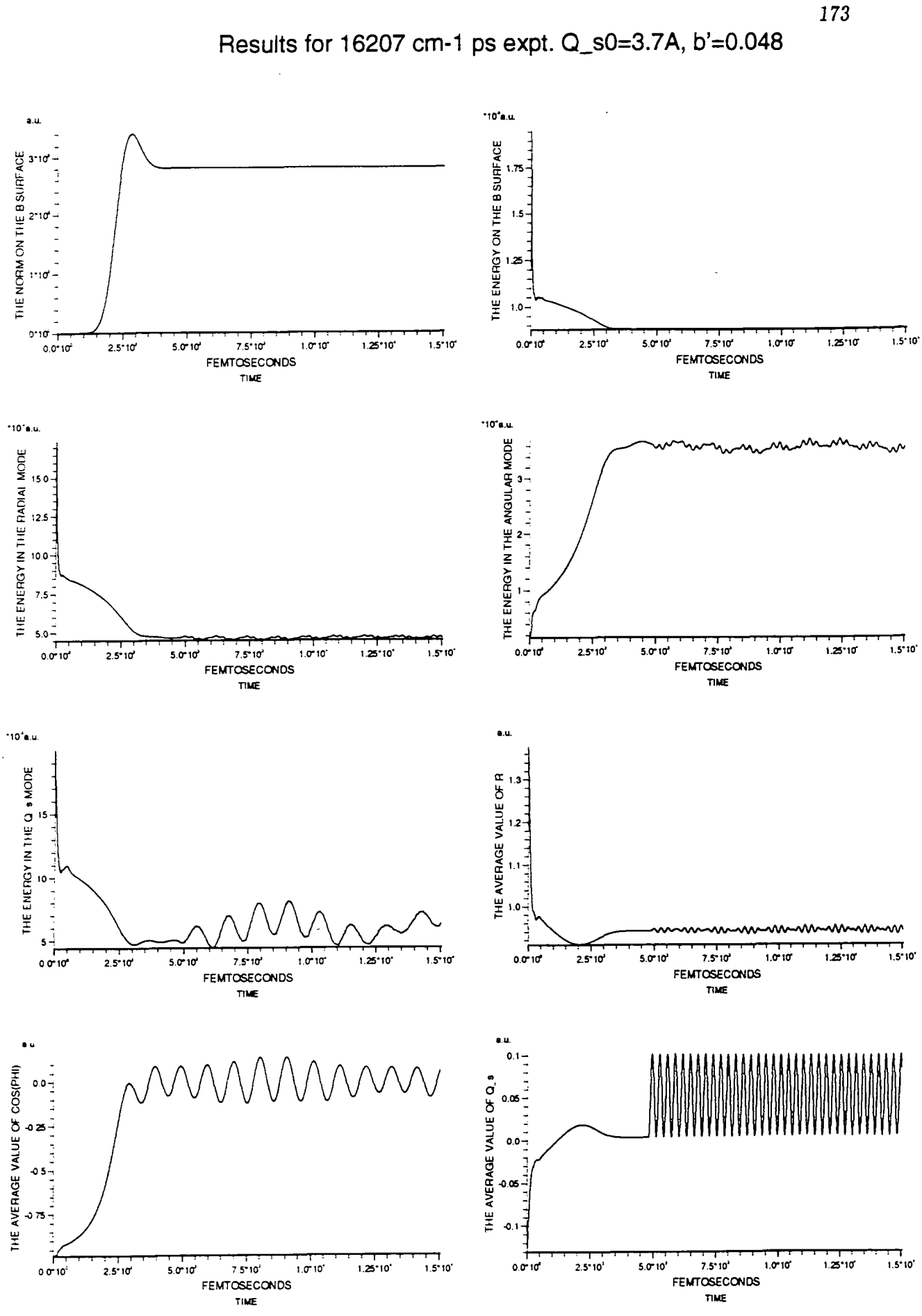

Fig. 73. Graphs showing the variation of the observables over the entire propagation time for the 16207 cm^{-1} picosecond experiment, with $b = 0.048/\sqrt{2}, Q_{s_0} = 3.7$ Å.

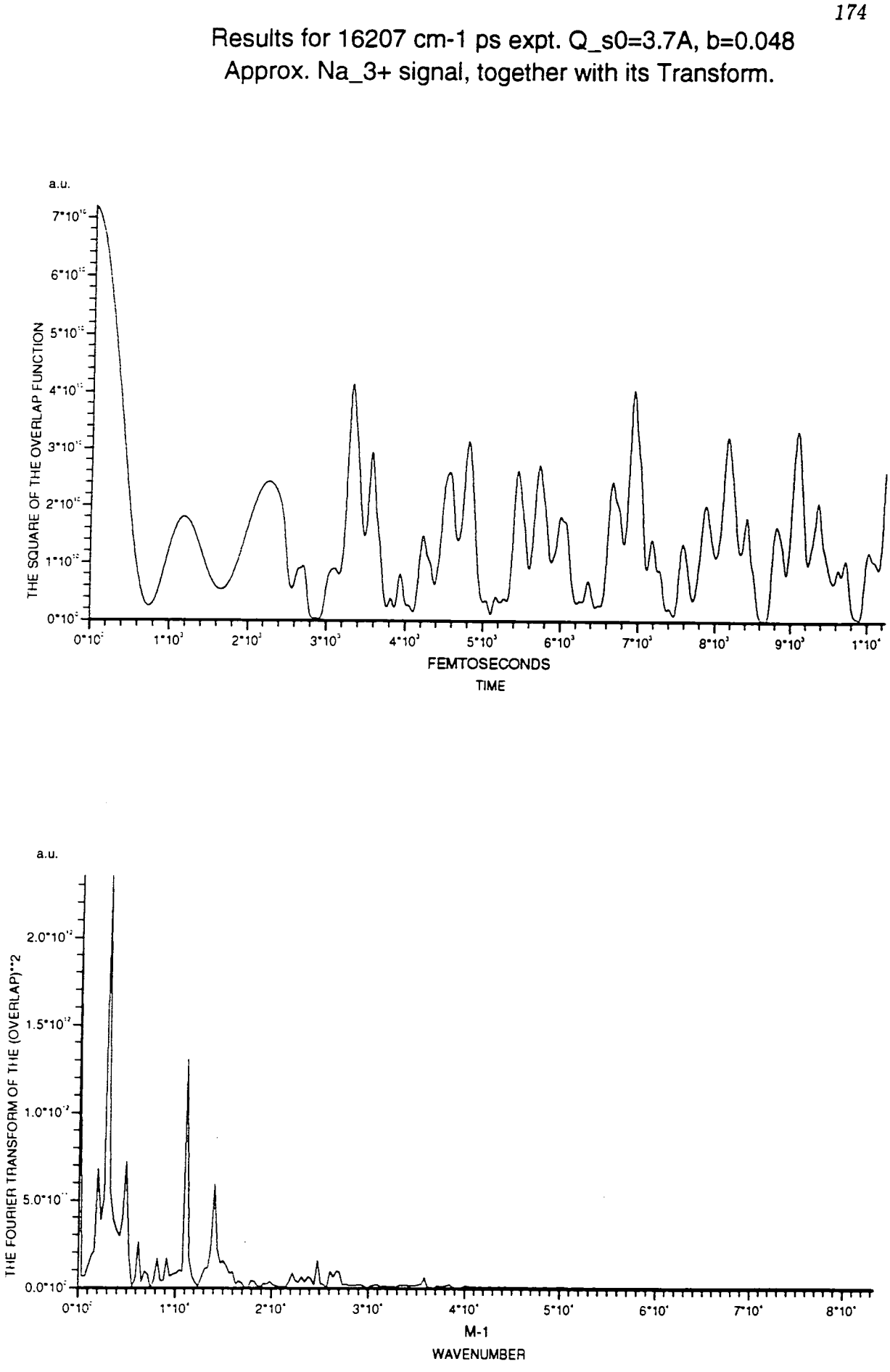

Fig. 74. Graphs showing the *approximate* Na_3^+ signal and its Fourier transform for the 16207 cm^{-1} picosecond experiment, with $b = 0.048/\sqrt{2}, Q_{s_0} = 3.7$ Å.

7: Summary and Conclusions

This thesis is concerned with studying chemical dynamics using time-dependent quantum mechanics and in particular using the Fourier method. The advantages of studying chemical reactions in the time domain were discussed in Chapter 1.

In Chapter 2, the Fourier method for studying one-dimensional problems was introduced. The nature of the initial wavefunction to be used was discussed. It was shown how the Hamiltonian and its operation on the wavefunction can be calculated, and then used to propagate the wavefunction in time. Several different methods for the propagation of the T.D.S.E. were described. Various types of absorbing boundaries were also described.

In Chapter 3, some of the various propagators that were introduced in Chapter 2 were investigated, as was the use of imaginary potentials. It was found that the Chebyshev propagator was the most accurate and efficient, especially when used as a stepping rather than a truly global propagator. However care is needed when using imaginary potentials, since the Chebyshev propagator can become unstable with non-Hermitian Hamiltonians, so that in some cases this may make it preferable to use the Feit/Fleck propagator.

In Chapter 4, the extension of the Fourier method to multi-dimensional problems was described. It was seen that there are many different approaches possible, some of which were similar to the one-dimensional Fourier method, others of which were quite different. The coupled channel wavepacket method was used to describe the fragmentation of Van der Waals molecules. It was seen that the derivation of the set of coupled equations was straightforward. The solution of the equations and the extraction of observables from the channel wavepackets was no more complicated than for the Fourier method. Thus it was seen that this hybrid method of the Fourier method with a more standard basis set expansion can provide a useful tool for multi-dimensional calculations. The two test cases described were shown to produce results which were not at odds with those reported in the literature. Thus, there could be some confidence in the accuracy of the calculations done.

In Chapter 5, two-dimensional calculations were carried out to simulate time-resolved femtosecond and picosecond two-photon ionisation experiments on the sodium trimer. In Chapter 6, the corresponding three-dimensional calculations were carried out, i.e. the symmetric stretch mode was included in the calculations. The simulation of these experiments was divided into three parts:

1. The creation of the initial wavefunction on the B state from the ground-state wavefunction of Na_3. This was done by modelling the effect of the pump laser pulse using

first-order time-dependent perturbation theory.

2. The propagation of the wavefunction in time using the Chebyshev propagator.
3. The extraction of observables from the time-dependent wavefunction. One of the most important observables was the Na_3^+ signal, which was measured in the time-resolved experiments. This was modelled in three different ways:
   1. The first was almost exact, i.e. it modelled the effect of the probe laser pulse using first-order time-dependent perturbation theory. This first method made the assumption that the electrons ejected during ionisation had no kinetic energy.
   2. The second method was approximate. It modelled the ion signal as the overlap of the time-dependent wavefunction with the ground-state vibrational wavefunction of the ion. The second method assumed that there was only just enough energy in the probe laser pulse to ionise the molecule.
   3. The third method was also approximate. This method modelled the ion signal as the overlap of the time-dependent wavefunction with the wavefunction which was present on the B state half way through the pump laser pulse. The third method assumed that the wavefunction present on the B state half way through the pump laser pulse gave the best conditions for ionisation.

The simulation of the time-resolved experiments produced physically plausible results. The correspondence with the experimental results was only fair, but this could be mostly accounted for by the poor quality of the potential energy surfaces used. Thus, even the relatively simple model used here to simulate the time-resolved experiments is useful to gain both a qualitative explanation of the results of these experiments and an insight into the dynamics of systems which are in non-stationary states.

As well as simulating the time-resolved experiments the static spectroscopy was also modelled by using a laser pulse equivalent to 'white light', which moved the wavefunction on the X state vertically to the B state. This simulation of the static spectroscopy was fairly successfully. Thus, there could be a certain amount of confidence in both the potential of the B state and initial wavefunction of the X state, which were used in the calculations.

In the two-dimensional calculations, the initial wavepacket created by the femtosecond laser pulse was made up of many states, which were excited both in the radial mode and in the angular mode. This wavepacket had a large amplitude motion in the radial direction. The angular motion followed no easily discernible pattern. The oscillation of the wavepacket in the radial direction gave rise to an ion signal which oscillated with the frequency of the radial motion. In the three-dimensional calculations, the initial wavepacket was similar to that created in the two-dimensional calculations, but the wavepacket now contained states

which were excited in the symmetric stretch mode. Thus the wavepacket also oscillated in the symmetric stretch coordinate. The oscillation of the wavepacket in both the radial and symmetric stretch coordinates gave rise to an ion signal which oscillated with both the frequency of the radial motion and of the symmetric stretch, as well as with the beat frequencies between the two.

In the two-dimensional calculations, the initial wavepacket created by the picosecond laser pulse was made up of very few states, which were excited in the angular mode, but were in only one radial state. The angular states present interfered with each other to produce a wavefunction which moved angularly. The small coupling of the angular and radial modes, through the quadratic coupling constant, meant that as the wavepacket moved angularly it moved radially as well. This small radial motion gave rise to an ion signal which oscillated with the beat frequencies between the angular modes. In the three-dimensional calculations, the initial wavepacket was almost identical to that created in the two-dimensional calculations.

For the two-dimensional simulation of the femtosecond experiment, the second method of calculating the ion signal, which was approximate, appeared to give satisfactory agreement with the first method of calculation, which was almost exact. This meant that for the picosecond experiments the calculation of the ion signal could be carried out using this approximation. However, it proved more appropriate for a variety of reasons to use vibrational states, other than the ground state, to form the overlap function. In fact, for the simulation of the picosecond experiments, the third method of calculating the ion signal showed slightly better agreement with the experiment than the second method. A useful implication of the success of the approximate methods was that the calculations could be extended to three dimensions, i.e. including the symmetric stretch.

The two-dimensional simulations of the femtosecond experiment showed poor agreement with the experimental results. Superficially, the poor agreement could be attributed to the dominance of the results by the symmetric stretch frequency. The three-dimensional simulations showed some agreement with the experimental results, with the values of the frequencies observed in the calculated spectrum being similar to those in the experimental spectrum. However, the very high intensity of the symmetric stretch frequency relative to the radial frequency was difficult to explain. In order to produce a simulated spectrum which is dominated by the symmetric stretch frequency, a better model of the laser pulse will have to be developed, which allows the spectral width of the pulse to be determined independently of its temporal width.

The picosecond experiments at 625, 620, and 619.7 nm showed some agreement with the experimental results. The results at 617 nm showed less similarity to the reported

experimental results. The calculated ion signals oscillated with frequencies which were similar to those found in the experimental results, but no steady decay of the ion signal was seen. The inclusion of the extra dimension added no extra insight into the results of the picosecond experiments; in particular, it did not lead to an ion signal which showed a fast decay. In order to gain more than the qualitative idea of the experiments given here, it would be necessary to obtain a potential which correctly describes both the energy levels and the coupling between the radial and angular modes.

There is much work that can be done in the future to improve the simulation of these time-resolved experiments. In particular, a great deal of work can be done to improve the modelling of the laser pulses, so that both the temporal width and spectral width of the experimental pulses can be reproduced. It is hoped that in the future better potential surfaces will be available so that any uncertainty regarding the ground-state wavefunction of Na_3, the energy levels of the B state and the coupling between the modes in the B state will be removed. It is also hoped that as more powerful computers become available it will be possible to: first, calculate the ion signal exactly by the explicit treatment of the probe laser pulse for all the simulations, i.e. for the picosecond and femtosecond experiments in both two or three dimensions; and secondly, include the coupling between the X and B states.

Appendix A: Atomic Units

This is a system of units which is *natural* on the atomic scale. The units are defined in the following way:

$$\begin{aligned} m_e &= 1 \\ e &= 1 \\ \hbar &= 1 \\ 4\pi\varepsilon_0 &= 1. \end{aligned} \tag{192}$$

The unit of energy is the Hartree, E_h, and its value is:

$$E_h = \frac{m_e e^4}{4h^2\varepsilon_0^2} \approx 4.359 \times 10^{-18}\text{J}. \tag{193}$$

The unit of distance is the Bohr radius, a_0:

$$a_0 = \frac{h^2\varepsilon_0}{\pi m_e e^2} \approx 5.29 \times 10^{-11}\text{m}. \tag{194}$$

The unit of time is:

$$\tau = \frac{\hbar}{E_h} \approx 2.4 \times 10^{-17}\text{s}. \tag{195}$$

Thus, to convert to atomic units from S.I. units is quite straight forward. For example to convert a force constant:

$$k_{a.u.} = k_{S.I.}\frac{|a_0^2|}{|E_h|}. \tag{196}$$

To convert a distance:

$$x_{a.u.} = \frac{x_{S.I.}}{|a_0|}. \tag{197}$$

To convert a time:

$$t_{a.u.} = \frac{t_{S.I.}}{|\tau|}. \tag{198}$$

To convert a reduced mass:

$$\left[\frac{1}{2\mu}\right]_{a.u.} = \frac{m_e}{m_p}\left[\frac{1}{2\mu}\right]_{a.m.u.}, \tag{199}$$

etc.

Other useful conversions are:

$$1\text{eV} = 8065.47\, hc\,\text{cm}^{-1};$$

and

$$\text{wavenumber}\,(\text{cm}^{-1}) \times hc/E_h \rightarrow \text{energy in Hartrees}\,(E_h).$$

Appendix B: Theoretical Background

One of the most important assumptions involved in trying to solve the Schrödinger equation is the separation of the nuclear and electronic motions. This is justified by the large differences in the masses of the electron and nucleons. What follows is an investigation into some of the consequences of the breakdown of this assumption, and ways in which the theory can be extended to take some account of the deficiences of this assumption [139].

Adiabatic theorem

The separation of the nuclear and electronic motions mentioned above is called the Adiabatic Theorem.

The Hamiltonian can be divided into three parts:

$$\hat{H} = \hat{H}_r + \hat{H}_Q + \hat{V}(r,Q) \tag{200}$$

where r and Q are the electronic and vibrational coordinates respectively. H_r is the electronic component of the Hamiltonian, including the kinetic energy of the electrons and the interelectronic electrostatic interaction, H_Q is the kinetic energy of the nuclei, and $V(r,Q)$ is the energy of interaction between the electrons and nuclei and the internuclear repulsion. The potential can be expressed in a Taylor series about some chosen origin, the point $Q_\alpha = Q_{\alpha 0} = 0$:

$$V(r,Q) = V(r,0) + \sum_\alpha \left(\frac{\partial V}{\partial Q_\alpha}\right)_0 Q_\alpha + \frac{1}{2}\sum_{\alpha\beta}\left(\frac{\partial^2 V}{\partial Q_\alpha \partial Q_\beta}\right)_0 Q_\alpha Q_\beta + \ldots \tag{201}$$

If the first term of this expansion is regarded as the potential energy of the electrons in the field of fixed nuclei, the electronic part of the Schrödinger equation can be solved:

$$\left[\hat{H}_r + V(r,0) - \epsilon_k'\right]\phi_k(r) = 0, \tag{202}$$

and a set of energies ϵ_k' and wavefunctions $\phi_k(r)$ can be obtained for the given nuclear configuration corresponding to the point $Q_{\alpha 0}$.

In order to solve the full Schrödinger equation, and to see how these electronic wavefunctions vary under nuclear displacements, the wavefunction is expanded in these electronic wavefunctions:

$$\Psi(r,Q) = \sum_k \chi_k(Q)\phi_k(r), \tag{203}$$

and then substituted into the Schrödinger equation, which is left multiplied by $\phi_m^*(r)$ and integrated over r to give:

$$\left[\hat{H}_Q + \epsilon_k(Q) - E\right]\chi_k(Q) + \sum_{m\neq k} W_{km}(Q)\chi_m(Q) = 0 \tag{204}$$

where $W(r,Q) = V(r,Q) - V(r,0)$ and $\epsilon_k(Q) = \epsilon_k^l + W_{kk}(Q)$, and is a first order approximation to the adiabatic potential in the absence of electronic degeneracy or pseudodegeneracy. If $W_{km}(Q)$ is set to zero, then the wavefunction is simply separable, $\Psi(r,Q) = \chi_k(Q)\phi_k(r)$. This is called the simple adiabatic or Born-Oppenheimer approximation. Here it is of interest to consider the effect on the wavefunction if some terms in $W_{km}(Q)$ are included in equation (204). In order to limit the complexity of the problem, only harmonic terms in $W(r,Q)$ will be included. $W(r,Q)$ can then be written in terms of normal mode coordinates, Q_{Γ_γ}:

$$W(r,Q) = \sum_{\Gamma_\gamma} \left(\frac{\partial V}{\partial Q_{\Gamma_\gamma}}\right)_0 Q_{\Gamma_\gamma} + \frac{1}{2} \sum_{\Gamma_{\gamma 1}\Gamma_{\gamma 2}} \left(\frac{\partial^2 V}{\partial Q_{\Gamma_{\gamma 1}} \partial Q_{\Gamma_{\gamma 2}}}\right)_0 Q_{\Gamma_{\gamma 1}} Q_{\Gamma_{\gamma 2}} \qquad (205)$$

Vibronic coupling constants

Consider the first term in the expansion of $W(r,Q)$ in equation (205). The matrix elements of the coefficients of Q_{Γ_γ}, $\left(\frac{\partial V}{\partial Q_{\Gamma_\gamma}}\right)_0$, are the constants of vibronic coupling or linear coupling constants. They measure the coupling between the electronic structure and nuclear displacements, i.e. the measure of the influence of the nuclear displacements on the electronic distribution and conversely the effect of the changes in the electronic structure upon nuclear dynamics. This constant is then (for non-degenerate states):

$$F_{\bar{\Gamma}}^{\Gamma_m \Gamma_k} = \int \phi_m(r) \left(\frac{\partial V}{\partial Q_{\bar{\Gamma}}}\right)_0 \phi_k(r)\, dr. \qquad (206)$$

From group theory it can be seen that $F_{\bar{\Gamma}}^{\Gamma_m \Gamma_k}$ will only be non-zero if $\Gamma_m \otimes \Gamma_k \in \bar{\Gamma}$. If Γ_k, Γ_m or both are degenerate electronic states then a set of linear vibronic constants will exist appropriate to all the components γ_m and γ_k of the two representations Γ_m and Γ_k. (Note—This set can be calculated easily if one takes into account the fact that the matrix elements within a degenerate term differ solely in numerical coefficients, their values being known.)

The diagonal constant of the linear coupling $F_{\bar{\Gamma}}^{\Gamma_m \Gamma_m} \equiv F_{\bar{\Gamma}}^{\Gamma_m}$ has the sense of the force with which the electrons in state Γ_m affect the nuclei in the direction of symmetrised displacement Q_{Γ_γ}. For non-degenerate states $F_{\bar{\Gamma}}^{\Gamma_m}$ will be zero, except for $\bar{\Gamma} = A_1$, in which case the electrons can distort the nuclear configuration only in the direction of the totally symmetric displacements, and the symmetry of the system does not change. If Γ_m is a degenerate electronic state then $F_{\bar{\Gamma}}^{\Gamma_m}$ may be non-zero for $\bar{\Gamma} \neq A_1$. In this case $\bar{\Gamma}$ may not be totally symmetric, and under the influence of the electrons the nuclear configuration undergoes appropriate distortions which are not totally symmetric. This is sometimes known as the Jahn-Teller effect.

Now consider the second term in equation (205). In order to investigate this, further group-theoretical transformations are introduced. The tensor convolution of the coefficients of this term:

$$\left[\left(\frac{\partial^2 V}{\partial Q_{\Gamma_1}\partial Q_{\Gamma_2}}\right)_0\right]_{\bar{\Gamma}_{\bar{\gamma}}}, \tag{207}$$

is introduced, which means the linear combination of second derivatives, with respect to the $Q_{\Gamma_{\gamma 1}}$ and $Q_{\Gamma_{\gamma 2}}$ coordinates, transform according to the component $\bar{\gamma}$ of representation $\bar{\Gamma} \in \Gamma_1 \otimes \Gamma_2$. Similarly, the appropriate tensor convolution for the coordinates is $\{Q_{\Gamma_1} \otimes Q_{\Gamma_2}\}_{\Gamma_{\bar{\gamma}}}$, so the second term in equation (205) becomes:

$$\frac{1}{2}\sum_{\bar{\Gamma}_{\bar{\gamma}}}\sum_{Q_{\Gamma_1}Q_{\Gamma_2}}\left\{\left(\frac{\partial^2 V}{\partial Q_{\Gamma_1}\partial Q_{\Gamma_2}}\right)_0\right\}_{\Gamma_{\bar{\gamma}}}\{Q_{\Gamma_1} \otimes Q_{\Gamma_2}\}_{\bar{\Gamma}_{\bar{\gamma}}}. \tag{208}$$

Consider now the matrix elements of the coefficients of this term. For a degenerate state there will be a set appropriate to the lines γ_m and γ_k of the two representations Γ_m and Γ_k and their combinations.

The totally symmetric part of the diagonal matrix elements of these second derivatives (i.e. second term in equation (205)), form the curvature of the adiabatic potential or the force constants (in the equilibrium position). The remaining terms and the non-diagonal matrix elements contain the quadratic vibronic constants, $K_{0\bar{\Gamma}_{\bar{\gamma}}}^{\Gamma_m\Gamma_k}$, which must be distinguished from the force constants.

Consider the diagonal matrix element, $K_{0\bar{\Gamma}_{\bar{\gamma}}}^{\Gamma_m\Gamma_m} \equiv K_{0\bar{\Gamma}_{\bar{\gamma}}}^{\Gamma_m}$. As for the linear coupling constants, for the diagonal matrix element is to be non zero then the representation $\bar{\Gamma} \in \Gamma_m \otimes \Gamma_k$ can only be totally symmetric for nondegenerate states, i.e. $\bar{\Gamma} = A_1$, while for degenerate states $\bar{\Gamma}$ can be both totally symmetric and nontotally symmetric.

These non-symmetric quadratic vibronic constants influence the potential functions of the nuclei. However, in this case the potential function is even, since these vibronic constants are the coefficients of, crudely, Q^2; hence the instability that arises is dynamic, rather than static (as for the Jahn-Teller effect), and is called the Renner-Teller effect.

Adiabatic potentials

From the above it can be seen that if information on the stable configuration, the dynamics, and energy spectra of molecules with degenerate electronic states is required, then more consideration must be given to their adiabatic potential surfaces, (beyond the simple adiabatic approximation described initially).

This involves solving the electronic part of the Schrödinger equation, including the terms in the potential, $V(r, Q)$, which vary with the internuclear displacement, i.e. $W(r, Q)$. To do this:

- First separate out the totally symmetric part of the diagonal matrix elements of the vibronic interactions, which give rise to the force constants K_Γ, since these terms do not change the symmetry of the system;
- Secondly, choose the initial configuration of the system at the point $Q_{\Gamma_\gamma} = 0$, where the adiabatic potential without vibronic interactions has a minimum;
- Thirdly, assume that only linear and quadratic vibronic constants need be included, i.e. proper anharmonicity may be neglected.

This will give an adiabatic potential, for a degenerate electronic state, well separated from other states, i.e. where there is no pseudo-degeneracy:

$$\epsilon_k(Q_{\Gamma_\gamma}) = \frac{1}{2}\sum_{\Gamma_\gamma} K_\Gamma Q^2_{\Gamma_\gamma} + \epsilon^v_k(Q_{\Gamma_\gamma}), \qquad k = 0, 1, \ldots, f \tag{209}$$

where f is the degree of degeneracy of the electronic state and $\epsilon^v_k(Q_{\Gamma_\gamma})$ are the roots of the secular determinant:

$$\left|\left|W^v_{\gamma_m\gamma'_m} - \epsilon^v\right|\right| = 0, \qquad \gamma_m, \gamma'_m = 1, 2, \ldots, f \tag{210}$$

in which, unlike in equation (205), the diagonal matrix elements $W^v_{\gamma_m\gamma'_m}$ do not contain the totally symmetric part of the quadratic terms used in the force constant formation, and are simply combinations of the linear and quadratic vibronic force constants.

Appendix C: Dimensionless Constants and Displacements

All the force constants, coupling constants and coordinates used in the equations to describe the potentials of the sodium trimer have been expressed in the literature, and are used in this work, in dimensionless form [119]. Consider the coordinates and the vibronic coupling constants described in Chapter 5. A dimensionless radial displacement is used such that:

$$r^2 = \frac{r^2 K_E}{\hbar\omega_0}, \tag{211}$$

It is possible to find K_E from ω_0 [140] (ω_0 is the radial vibrational frequency on the lower adiabatic surface):

$$K_E = (2\pi)^2 \omega_E^2 m \tag{212}$$

and

$$\omega_E = \frac{\omega_0}{\sqrt{1 - |G_E|}} \tag{213}$$

hence,

$$K_E = \frac{(2\pi)^2 \omega_0^2}{1 - |G_E|} m. \tag{214}$$

Also,

$$\omega_\phi = \omega_E \times 3\sqrt{\frac{|G_E|}{2}}, \tag{215}$$

where ω_ϕ is the vibrational frequency of the motion perpendicular to the radial. The vibronic coupling constants can be expressed similarly in dimensionless form:

$$G_E = \frac{G_E}{K_E} \qquad \text{and} \qquad F_E = \frac{F_E}{\sqrt{K_E \hbar\omega_0}}. \tag{216}$$

If the displacement and vibronic coupling constants are used in their dimensionless forms, then the potential is measured in multiples of $\hbar\omega_0$. Similar expressions are used to find dimensionless constants for P and f, which are often quoted as $P \times \sqrt{2}$ and $f \times \sqrt{2}$. With the inclusion of the symmetric stretch, dimensionless Q_s and b are also used:

$$Q_s^2 = \frac{Q_s^2 K_{Q_s}}{\hbar\omega_0} \tag{217}$$

and

$$b = \frac{b}{\sqrt{K_E K_{Q_s}}}. \tag{218}$$

In other parts of the literature, other dimensionless constants are used [117] [120], such that the potential is measured in multiples of $\hbar\omega_E$. The definitions of the dimensionless displacements and coupling constants are then altered to take account of this. Thus, the dimensionless coupling constants of Cocchini and co-workers [119] differ from the dimensionless coupling constants of Meiswinkel and Köppel [117] [120].

Appendix C: List of Figures

Appendix D: List of Tables

Appendix E: List of References

[1]. K. C. Kulander and A. E. Orel, J. Chem. Phys. **85**, 834 (1986).

[2]. E. A. McCullough and R. E. Wyatt, J. Chem. Phys. **34**, 3578 (1971), and references [1-3] therein.

[3]. A. Askar and A. S. Cakmak, J. Chem. Phys. **68**, 2794 (1978).

[4]. S. C. Leasure, K. F. Milfeld and R. E. Wyatt, J. Chem. Phys. **51**, 1253 (1981).

[5]. D. Kosloff and R. Kosloff, J. Comp. Phys. **52**, 35 (1983).

[6]. R. Kosloff, J. Phys. Chem. **92**, 2087 (1988).

[7]. E. J. Heller, J. Chem. Phys. **68**, 2066 (1978)

[8]. K. C. Kulander and E. J. Heller, J. Chem. Phys. **69**, 2439 (1978).

[9]. G. G. Balint-Kurti, R. N. Dixon and C. C. Marston, J. Chem. Phys. **93**, 6520 (1990).

[10]. M. Jacon, O. Atabek and C. Leforestier, J. Chem. Phys. **91**, 1585 (1989).

[11]. F. Le Quéré and C. Leforestier, J. Chem. Phys. **92**, 247 (1990).

[12]. S. K. Gray and C. E. Wozny, J. Chem. Phys. **91**, 7671 (1989).

[13]. U. Manthe, H. Köppel and L. S. Cederbaum, J. Chem. Phys. **95**, 1708 (1991).

[14]. R. C. Mowrey and D. J. Kouri, J. Chem. Phys. **87**, 339 (1987).

[15]. C. Leforestier, Chem. Phys. **87**, 241 (1984).

[16]. G. Bergeron, R. Hiberty and C. Leforestier, Chem. Phys. Lett. **125**, 373 (1986).

[17]. D. Neuhauser, M. Baer, R. S. Judson and D. J. Kouri, Chem. Phys. Lett. **169**, 372 (1990).

[18]. R. S. Judson, D. J. Kouri, D. Neuhauser and M. Baer, Phys. Rev. A **42**, 351 (1990).

[19]. R. C. Mowrey and D. J. Kouri, J. Chem. Phys. **84**, 6466 (1986).

[20]. R. C. Mowrey and D. J. Kouri, J. Chem. Phys. **86**, 6140 (1987).

[21]. R. B. Gerber, R. Kosloff and M. Berman, Computer Physics Reports **5**, 59 (1986).

[22]. V. Mohan and N. Sathyamurthy, Computer Physics Reports **7**, 213 (1988).

[23]. K. C. Kulander, thematic issue of Comp. Phys. Commun. **63** (1991).

[24]. G. C. Schatz, V. Buch, R. B. Gerber and M. A. Ratner, J. Chem. Phys. **79**, 1808 (1983).

[25]. A. Garcia-Vela, R. B. Gerber and D. G. Imre, J. Chem. Phys. **97**, 7242 (1992).

[26]. R. B. Gerber and M. A. Ratner, Adv. Chem. Phys. **70**, 97 (1988).

[27]. C. Clay, G. G. Balint-Kurti and R. N. Dixon, Theor. Chim. Acta **79**, 313 (1991).

[28]. J. H. Zhang, Chem. Phys. Lett. **160**, 417 (1989).

[29]. R. C. Mowrey, Y. Sun and D. J. Kouri, J. Chem. Phys. **91**, 6519 (1989).

[30]. S. A. Adelman and J. D. Doll, J. Chem. Phys. **64**, 2375 (1976).

[31]. J. C. Tully, G. H. Gilmer and M. Shugard, J. Chem. Phys. **71**, 1630 (1979).

[32]. Y. Guan, J. T. Muckerman and T. Uzer, J. Chem. Phys. **93**, 4383 (1990).

[33]. Y. Guan, J. T. Muckerman and T. Uzer, J. Chem. Phys. **93**, 4400 (1990).

[34]. S. A. Adelman, J. Chem. Phys. **71**, 4471 (1979).

[35]. D. K. Hoffman, O. A. Sharafeddin, D. J. Kouri, M. Carter, N. Nayar and J. Gustafson, Theor. Chim. Acta **79**, 297 (1991).

[36]. M. D. Feit, J. A. Fleck and A. Steiger, J. Comp. Phys. **47**, 412 (1982).

[37]. G. G. Balint-Kurti, Meeting of C.C.P. 6, Durham, 17th December 1991.

[38]. D. Chasman, R. J. Silbey and M. Eisenberg, Theor. Chim. Acta **79**, 175 (1991).

[39]. J. R. Huber and R. Schinke, J. Phys. Chem. **97**, 3463 (1993).

[39]. M. Quack, Phil. Trans. R. Soc. Lond. A. **332**, 203 (1990).

[40]. R. Marquardt and M. Quack, Large Finite Systems p.31 (1987).

[41]. M. Shapiro, J. Ronkin and P. Brumer, Ber. Bunsenges. Phys. Chem. **92**, 212 (1988).

[42]. M. D. Feit and J. A. Fleck, J. Chem. Phys. **80**, 2578 (1984).

[43]. J. Manz and C. S. Parmenter, special issue of Chem. Phys. **139** (1989).

[44]. D. G. Imre and J. Zhang, Chem. Phys. **139**, 89 (1989).

[45]. D. J. Tannor and S. A. Rice, J. Chem. Phys. **83**, 5013 (1985).

[46]. R. Kosloff, S. A. Rice, P. Gaspard, S. Tersigni and D. J. Tannor, Chem. Phys. **139**, 201 (1989).

[47]. W. Jakubetz, B. Just, J. Manz and H.-J. Schreier, J. Phys. Chem. **94**, 2294 (1990).

[48]. J. E. Combariza, S. Görtler, B. Just and J. Manz, Chem. Phys. Lett. **195**, 393 (1992).

[49]. J. E. Combariza, C. Daniel, B. Just, E. Kades, E. Kolba, J. Manz, W. Malisch, G. K. Paramonov and B. Warmuth, Isotope Effects in Gas-Phase Chemistry, edited by J. A. Kaye, ACS Symposium Series **502**, 310 (1992).

[50]. A. H. Zewail, Faraday Discuss. Chem. Soc. **75**, 315 (1983).

[51]. A. H. Zewail and R. B. Bernstein, p.223, The Chemical Bond, Structure and Dynamics, edited by A. H. Zewail, Academic Press Inc. (1992).

[52]. M. Dantus, M. J. Rosker and A. H. Zewail, J. Chem. Phys. **87**, 2395 (1987).

[53]. M. J. Rosker, M. Dantus and A. H. Zewail, J. Chem. Phys. **89**, 6113 (1988).

[54]. M. J. Rosker, M. Dantus and A. H. Zewail, J. Chem. Phys. **89**, 6128 (1988).

[55]. T. S. Rose, M. J. Rosker and A. H. Zewail, J. Chem. Phys. **88**, 6672 (1988).

[56]. T. S. Rose, M. J. Rosker, A. H. Zewail, J. Chem. Phys. **91**, 7415 (1989).

[57]. M. Dantus, R. M. Bowman, M. Gruebele and A. H. Zewail, J. Chem. Phys. **91**, 7437 (1989).

[58]. M. Dantus, M. H. M. Janssen and A. H. Zewail, Chem. Phys. Lett. **181**, 281 (1991).

[59]. R. M. Bowman, M. Dantus and A. H. Zewail, Chem. Phys. Lett. **161**, 297 (1989).

[60]. N. F. Scherer, C. Sipes, R. B. Bernstein and A. H. Zewail, J. Chem. Phys. **92**, 5239 (1990).

[61]. M. Gruebele, I. R. Sims, E. D. Potter and A. H. Zewail, J. Chem. Phys. **95**, 7763 (1991).

[62]. The proceedings of Femtosecond Chemistry, Berlin, March 1 – 4, 1993.

[63]. N. F. Schrer, R. J. Carlson, A. Matro, M. Du, A. J. Ruggiero, V. Romero-Rochin, J. A. Cina, G. R. Fleming and S. A. Rice, J. Chem. Phys. **95**, 1487 (1991).

[64]. W. Thomas, S-Y. Lee and R. A. Mathies, J. Chem. Phys. **92**, 4012 (1990).

[65]. R. Loudon, The Quantum Theory of Light (2nd ed.), Oxford University Press (1983).

[66]. G. Roberts and A. H. Zewail, J. Phys. Chem. **95**, 7973 (1991).

[67]. V. Engel and H. Metiu, J. Chem. Phys. **91**, 1596 (1989).

[68]. R. Kosloff and D. Kosloff, J. Chem. Phys. **79**, 1823 (1983).

[69]. E. O. Brigham, The Fast Fourier Transform and its Applications, Prentice-Hall International Editions (1988).

[70]. G. S. Rushbrooke, Introduction to Statistical Mechanics, Oxford University Press (1964).

[71]. W. H. Press et al., Numerical Recipes, The Art of Scientific Computing, Cambridge University Press (1988).

[72]. R. Kosloff and D. Kosloff, J. Comp. Phys. **63**, 363 (1986).

[73]. H. Tal-Ezer, R. Kosloff and C. Cerjan, J. Chem. Phys. **100**, 179 (1992).

[74]. R. Kosloff, preprint.

[75]. Numerical Methods, J. H. Mathews, Prentice-Hall International Editions (1987).

[76]. H. Tal-Ezer and R. Kosloff, J. Chem. Phys. **81**, 3667 (1984).

[77]. H. Tal-Ezer, S.I.A.M. J. Numerical Analysis, **23**, 11 (1986).

[78]. C. Leforestier, R. H. Bisseling, C. Cerjan, M. D. Feit, R. Friesner, A. Guldberg, A. Hammerich, G. Jolicard, W. Karrlein, H.-D. Meyer, N. Lipkin, O. Roncero and R. Kosloff, J. Comp. Phys. **94**, 59 (1991).

[79]. T. J. Park and J. C. Light, J. Chem. Phys. **85**, 5870 (1986).

[80]. D. Kohen and D. J. Tannor, J. Chem. Phys. **98**, 3168 (1993).

[81]. J. A. Fleck, J. R. Morris and M. D. Feit, Applied Physics **10**, 129 (1976).

[82]. D. Neuhasuer and M. Baer, J. Chem. Phys. **90**, 4351 (1989).

[83]. M. S. Child, Mol. Phys. **72**, 89 (1991).

[84]. Á. Vibók and G. G. Balint-Kurti, J. Phys. Chem. **96**, 8712 (1992).

[85]. Á. Vibók and G. G. Balint-Kurti, J. Chem. Phys. **96**, 7615 (1992).

[86]. J. H. Zhang, J. Chem. Phys. **92**, 324 (1990).

[87]. R. Bisseling and R. Kosloff, J. Comp. Phys. **59**, 136 (1985).

[88]. U. Manthe and H. Köppel, Chem. Phys. Lett. **178**, 36 (1990).

[89]. R. N. Dixon, Chem. Phys. Lett. **190**, 430 (1992).

[90]. S. K. Gray and C. E. Wozny, J. Chem. Phys. **94**, 2817 (1991).

[91]. W. J. Hovingh and R. Parson, J. Chem. Phys. **96**, 4200 (1992).

[92]. A. Untch, K. Weide and R. Schinke, J. Chem. Phys. **95**, 6496 (1991).

[93]. J. M. Hutson, J. Comp. Phys. **56**, 165 (1984).

[94]. J. M. Hutson, J. Phys. B **14**, 851 (1981).

[95]. S. L. Marple, Digital Spectral Analysis with Applications, Prentice-Hall, Englewood Cliffs (1987).

[96]. S. K. Gray, J. Chem. Phys. **87**, 2051 (1987).

[97]. H. A. Jahn and E. Teller, Proc. Roy. Soc. (London), Ser. A **161**, 220 (1937).

[98]. M. V. Berry, Proc. Roy. Soc. (London), Ser. A **392**, 45 (1984).

[99]. C. A. Mead, Rev. Mod. Phys. **64**, 51 (1992).

[100]. M. J. Riley, A. Furlan, H. U. Güdel and S. Leutwyler, J. Chem. Phys. **98**, 3805 (1993).

[101]. A. Geers, J. Kappert, F. Temps and T. J. Sears, J. Chem. Phys. **98**, 4297 (1993).

[102]. T. Baument, M. Grosser, R. Thalweiser and G. Gerber, Phys. Rev. Lett. **67**, 3753 (1991).

[103]. T. Baument, V. Engel, C. Röttgermann, W. T. Strunz and G. Gerber, Chem. Phys. Lett. **191**, 639 (1992).

[104]. C. Kittrell, E. Abramson, J. L. Kinsey, S. A. McDonald, D. E. Reisner and R. W. Field, J. Chem. Phys. **75**, 2056 (1981).

[105]. M. Boyer, G. Delacrétaz, R. L. Whetten, J. P. Wolf and L. Wöste, J. Chem. Phys. **90**, 4620 (1989).

[106]. M. Boyer, G. Delacrétaz, G. Q. Ni, R. L. Whetten, J. P. Wolf and L. Wöste, Phys. Rev. Lett. **62**, 2100 (1989).

[107]. M. Boyer, G. Delacrétaz, P. Labastie, J. P. Wolf and L. Wöste, Z.Phys.D—Atoms, Molecules and Clusters **3**, 131 (1986).

[108]. G. Delacrétaz, E. R. Grant, R. L. Whetten, L. Wöste and J. W. Zwanziger, Phys. Rev. Lett. **56**, 2598 (1986).

[109]. M. Boyer, G. Delacrétaz, P. Labastie, J. P. Wolf and L. Wöste, J. Phys. Chem. **91**, 2630 (1987).

[110]. T. Baumert, B. Bühler, M. Grosser, R. Thalweiser, V. Weiss, E. Wiedenmann, and G. Gerber, J. Phys. Chem. **95**, 8103 (1991).

[111]. G. Gerber, Private Communication.

[112]. K. Kobe, H. Kühling, S. Rutz, E. Schreiber and L. Wöste, European Meeting on Photons, Beams, and Chemical Dynamics, University of Paris XI at Orsay, July 8–10, 1992.

[113]. S. Rutz, K. Kobe, H. Küling, E. Schreiber and L. Wöste, Z. Phys. D - Atoms, Molecules and Clusters **26**, 276 (1993).

[114]. E. Schreiber, H. Küling, K. Kobe, S. Rutz and L. Wöste, Ber. Bersenges. Phys. Chem. **96**, 1302 (1992).

[115]. J. Gaus, K. Kobe, V. Bonačić-Koutecký, H. Küling, J. Manz, B. Reischl, S. Rutz, E. Schreiber and L. Wöste, Preprint.

[116]. P. P. Bunker, Molecular Symmetry and Spectroscopy, Academic Press (1979).

[117]. R. Meiswinkel and H. Köppel, Chem. Phys. **129**, 463 (1989).

[118]. J. W. Zwanziger and E. R. Grant, J. Chem. Phys. **87**, 2954 (1987).

[119]. F. Cocchini, T. H. Upton and W. Andreoni, J. Chem. Phys. **88**, 6068 (1988).

[120]. R. Meiswinkel and H. Köppel, Chem. Phys. **144**, 117 (1990).

[121]. R. L. Martin and E. R. Davidson, Mol. Phys. **35**, 1713 (1978).

[122]. T. C. Thompson, G. Izmirlian, S. J. Lemon, D. G. Truhlar, J. Chem. Phys. **82**, 5597 (1985).

[123]. H. C. Longuet-Higgins, U. Öpik, M. H. L. Pryce and R. A. Sack, Proc. Roy. Soc. (London), Ser. A **1**, 244 (1958).

[124]. S. Rakowsky, R. F. W. Herrmann and W. E. Ernst, Z. Phys. D - Atoms, Molecules and Clusters **26**, 270 (1993).

[125]. W. E. Ernst and S. Rakowsky, Z. Phys. D - Atoms, Molecules and Clusters **26**, 273 (1993).

[126]. G.-H. Jeung, M. Broyer and P. Labastie, Chem. Phys. Lett. **165**, 494 (1990).

[127]. R. W. Hall, Chem. Phys. Lett. **160**, 520 (1989).

[128]. R. A. Eades, M. L. Hendewerk, R. Frey, D. A. Dixon and J. L. Gole, J. Chem. Phys. **76**, 3075 (1982).

[129]. S. Carter and W. Meyer, J. Chem. Phys. **93**, 8902 (1990).

[130]. F. Spiegelmann and D. Pavolini, J. Chem. Phys. **89**, 4954 (1988).

[131]. B. T. Sutcliffe and J. Tennyson, Mol. Phys. **58**, 1053 (1986).

[132]. J. Tennyson, Comp. Phys. Commun. **42**, 257 (1986)

[133]. J. Tennyson and S. Miller, Comp. Phys. Commun. **55**, 149 (1989).

[134]. V. Engel, Comp. Phys. Commun. **63**, 228 (1991).

[135]. S. O. Williams and D. G. Imre, J. Phys. Chem. **92**, 3363 (1988).

[136]. S. O. Williams and D. G. Imre, J. Phys. Chem. **92**, 6636 (1988).

[137]. S. O. Williams and D. G. Imre, J. Phys. Chem. **92**, 6648 (1988).

[138]. V. Engel, Chem. Phys. Lett. **178**, 130 (1991).

[139]. I. B. Bersuker, The Jahn-Teller Effect and Vibronic Interactions in Modern Chemistry, Penum Press New York (1984).

[140]. T. C. Thompson, D. G. Truhlar and C. A. Mead, J. Chem. Phys. **82**, 2392 (1985).

Appendix F: Conferences and Seminars Attended

The following information is included in compliance with the requirements of the Board of Studies in Chemistry.

Conferences Attended

1. Annual conference of the High Resolution Spectroscopy Group with C.C.P.6, 'Wide amplitude motions: experiment and theory.' University college London, 16-18 December 1990.
2. 'Chemical Dynamics in the Time Domain', organised by C.C.P.6 and M.B.D.G. Oxford University, 21-22 March 1991.
3. C.C.P.6 workshop on parallel computing. Durham University, 17 December 1991.
4. Annual conference of the High Resolution Spectroscopy Group with The Spectroscopy Group of the Institute of Physics, 'Novel Spectroscopic Techniques for High Resolution Spectroscopy.' Heriot Watt University, 18-20 December 1991.
5. European Meeting on Photons, Beams and Chemical Dynamics. University of Paris XI at Orsay, 8-10 July 1992. Poster presented: 'Chemical Dynamics Using Wavepacket Methods.'
6. Physics Computing 1992, 4th International Conference on Computational Physics. Prague, 24-28 August 1992.
7. MOLEC IX, Ninth European Conference on Dynamics of Molecular Collisions. Prague, 30 August-4 September 1992. Poster presented: 'Time-dependent Calculations and Experiments on the Sodium Trimer.'
8. M.B.D.G. Spring Meeting. University of Birmingham, 22nd April 1993.
9. 4th Annual Informal Northern Universities Chemical Physics Meeting, 15th July 1993. Paper presented: 'Wavepacket Calculations on the Sodium Trimer.'

Seminars Attended

Durham and Newcastle Theoretical Atomic and Molecular Physics Group

1. November 5th, 1990 Dr. G. Balint-Kurti, Bristol University, 'Time dependent Quantum Dynamics of Molecular Photodissociation and Reactive Scattering'
2. November 21st, 1990 Dr. J. F. McCann, Durham University, 'Photodissociation of Diatomic Molecules by Intense Lasers'
3. December 10th, 1990 Dr. K. Janda, University of Pittsburgh, 'Structure and dynamics of a series of noble-gas–chlorine Van der Waals complexes'
4. December 10th, 1990 Dr. Z. Bacic, New York University, 'Calculating vibration-rotation energy levels for floppy molecules'
5. November 5th, 1991 Dr. A. Dalgarno, Harvard, 'Molecules in the Universe'
6. March 18th, 1992 Dr. J. Tennyson, University College, London, 'Rovibrational States of H_3^+ - Chaos, Jupiter and the Universe'
7. February 17th, 1993 Dr. C. Leach, Southampton University, 'How close is close enough? The impact parameter dependence of a chemical reaction'

The following pages contain lists of the seminars in the chemistry department from 1990-1993. Those marked with an asterisk were attended.

REVISED VERSION

UNIVERSITY OF DURHAM

Board of Studies in Chemistry

COLLOQUIA, LECTURES AND SEMINARS GIVEN BY INVITED SPEAKERS
1ST AUGUST 1990 TO 31ST JULY 1991

ALDER, Dr. B.J. (Lawrence Livermore Labs., California) — 15th January, 1991
Hydrogen in all its Glory

BELL†, Prof. T. (SUNY, Stoney Brook, U.S.A.) — 14th November, 1990
Functional Molecular Architecture and Molecular Recognition

BOCHMANN†, Dr. M. (University of East Anglia) — 24th October, 1990
Synthesis, Reactions and Catalytic Activity of Cationic Titanium Alkyls

BRIMBLE, Dr. M.A. (Massey University, New Zealand) — 29th July, 1991
Synthetic Studies Towards the Antibiotic Griseusin-A

BROOKHART, Prof. M.S. (University of N. Carolina) — 20th June, 1991
Olefin Polymerizations, Oligomerizations and Dimerizations Using Electrophilic Late Transition Metal Catalysts

BROWN, Dr. J. (Oxford University) — 28th February, 1991
Can Chemistry Provide Catalysts Superior to Enzymes?

BUSHBY†, Dr. R. (Leeds University) — 6th February, 1991
Biradicals and Organic Magnets

COWLEY, Prof. A.H. (University of Texas) — 13th December, 1990
New Organometallic Routes to Electronic Materials

CROUT, Prof. D. (Warwick University) — 29th November, 1990
Enzymes in Organic Synthesis

DOBSON†, Dr. C.M. (Oxford University) — 6th March, 1991
NMR Studies of Dynamics in Molecular Crystals

GERRARD†, Dr. D. (British Petroleum) — 7th November, 1990
Raman Spectroscopy for Industrial Analysis

HUDLICKY, Prof. T. (Virginia Polytechnic Institute) — 25th April, 1991
Biocatalysis and Symmetry Based Approaches to the Efficient Synthesis of Complex Natural Products

JACKSON†, Dr. R. (Newcastle University) — 31st October, 1990
New Synthetic Methods: α-Amino Acids and Small Rings

KOCOVSKY†, Dr. P. (Uppsala University) — 6th November, 1990
Stereo-Controlled Reactions Mediated by Transition and Non-Transition Metals

LACEY, Dr. D. (Hull University) — 31st January, 1991
Liquid Crystals

LOGAN, Dr. N. (Nottingham University) — 1st November, 1990
Rocket Propellants

MACDONALD, Dr. W.A. (ICI Wilton) — 11th October, 1990
Materials for the Space Age

MARKAM, Dr. J. (ICI Pharmaceuticals) — 7th March, 1991
DNA Fingerprinting

PETTY, Dr. M.C. (Durham University) — 14th February, 1991
Molecular Electronics

PRINGLE+, Dr. P.G. (Bristol University) — 5th December, 1990
Metal Complexes with Functionalised Phosphines

PRITCHARD, Prof. J. (Queen Mary & Westfield College, London University) — 21st November, 1990
Copper Surfaces and Catalysts

SADLER, Dr. P.J. (Birkbeck College London) — 24th January, 1991
Design of Inorganic Drugs: Precious Metals, Hypertension + HIV

SARRE, Dr. P. (Nottingham University) — 17th January, 1991
Comet Chemistry

SCHROCK, Prof. R.R. (Massachusetts Institute of Technology) — 24th April, 1991
Metal-ligand Multiple Bonds and Metathesis Initiators

SCOTT, Dr. S.K. (Leeds University) — 8th November, 1990
Clocks, Oscillations and Chaos

SHAW+, Prof. B.L. (Leeds University) — 20th February, 1991
Syntheses with Coordinated, Unsaturated Phosphine Ligands

SINN+, Prof. E. (Hull University) — 30th January, 1991
Coupling of Little Electrons in Big Molecules. Implications for the Active Sites of (Metalloproteins and other) Macromolecules

SOULEN+, Prof. R. (South Western University, Texas) — 26th October, 1990
Preparation and Reactions of Bicycloalkenes

WHITAKER+, Dr. B.J. (Leeds University) — 28th November, 1990
Two-Dimensional Velocity Imaging of State-Selected Reaction Products

+ Invited specifically for the postgraduate training programme.

UNIVERSITY OF DURHAM

Board of Studies in Chemistry

COLLOQUIA, LECTURES AND SEMINARS FROM INVITED SPEAKERS

1991 – 1992 (August 1 – July 31)

1991

October	17	Dr. J.A. Salthouse, University of Manchester Son et Lumiere – a demonstration lecture
October	31	Dr. R. Keeley, Metropolitan Police Forensic Science Modern forensic science
November	6	Prof. B.F.G. Johnson†, Edinburgh University Cluster–surface analogies
November	7	Dr. A.R. Butler, St. Andrews University Traditional Chinese herbal drugs: a different way of treating disease
November	13	Prof. D. Gani†, St. Andrews University The chemistry of PLP–dependent enzymes
November	20	Dr. R. More O'Ferrall†, University College, Dublin Some acid–catalysed rearrangements in organic chemistry
November	28	Prof. I.M. Ward, IRC in Polymer Science, University of Leeds The SCI lecture: the science and technology of orientated polymers
December	4	Prof. R. Grigg†, Leeds University Palladium–catalysed cyclisation and ion–capture processes
December	5	Prof. A.L. Smith, ex Unilever Soap, detergents and black puddings
December	11	Dr. W.D. Cooper†, Shell Research Colloid science: theory and practice

1992

January	22	Dr. K.D.M. Harris†, St. Andrews University Understanding the properties of solid inclusion compounds
January	29	Dr. A. Holmes†, Cambridge University Cycloaddition reactions in the service of the synthesis of piperidine and indolizidine natural products

	January	30	Dr. M. Anderson, Sittingbourne Research Centre, Shell Research Recent Advances in the Safe and Selective Chemical Control of Insect Pests
	February	12	Prof. D.E. Fenton†, Sheffield University Polynuclear complexes of molecular clefts as models for copper biosites
	February	13	Dr. J. Saunders, Glaxo Group Research Limited Molecular Modelling in Drug Discovery
	February	19	Prof. E.J. Thomas†, Manchester University Applications of organostannanes to organic synthesis
	February	20	Prof. E.Vogel, University of Cologne *The Musgrave Lecture* Porphyrins: Molecules of Interdisciplinary Interest
	February	25	Prof. J.F. Nixon, University of Sussex *The Tilden Lecture* Phosphaalkynes: new building blocks in inorganic and organometallic chemistry
	February	26	Prof. M.L. Hitchman†, Strathclyde University Chemical vapour deposition
	March	5	Dr. N.C. Billingham, University of Sussex Degradable Plastics – Myth or Magic?
	March	11	Dr. S.E. Thomas†, Imperial College Recent advances in organoiron chemistry
	March	12	Dr. R.A. Hann, ICI Imagedata Electronic Photography – An Image of the Future
	March	18	Dr. H. Maskill†, Newcastle University Concerted or stepwise fragmentation in a deamination–type reaction
	April	7	Prof. D.M. Knight, Philosophy Department, University of Durham Interpreting experiments: the beginning of electrochemistry
	May	13	Dr. J–C Gehret, Ciba Geigy, Basel Some aspects of industrial agrochemical research

† Invited specially for the postgraduate training programme.

UNIVERSITY OF DURHAM

Board of Studies in Chemistry

COLLOQUIA, LECTURES AND SEMINARS FROM INVITED SPEAKERS

1992 - 1993 (August 1 - July 31)

1992

October 15 — Dr M. Glazer & Dr. S. Tarling, Oxford University & Birbeck College, London
It Pays to be British! - The Chemist's Role as an Expert Witness in Patent Litigation

October 20 — Dr. H. E. Bryndza, Du Pont Central Research
Synthesis, Reactions and Thermochemistry of Metal (Alkyl) Cyanide Complexes and Their Impact on Olefin Hydrocyanation Catalysis

October 22 — Prof. A. Davies, University College London
The Ingold-Albert Lecture The Behaviour of Hydrogen as a Pseudometal

October 28 — Dr. J. K . Cockcroft, University of Durham
Recent Developments in Powder Diffraction

October 29 — Dr. J. Emsley, Imperial College, London
The Shocking History of Phosphorus

November 4 — Dr. T. P. Kee, University of Leeds
Synthesis and Co-ordination Chemistry of Silylated Phosphites

November 5 — Dr. C. J. Ludman, University of Durham
Explosions, A Demonstration Lecture

November 11 — Prof. D. Robins, Glasgow University
Pyrrolizidine Alkaloids : Biological Activity, Biosynthesis and Benefits

November 12 — Prof. M. R. Truter, University College, London
Luck and Logic in Host - Guest Chemistry

November 18 — Dr. R. Nix, Queen Mary College, London
Characterisation of Heterogeneous Catalysts

November 25 — Prof. Y. Vallee. University of Caen
Reactive Thiocarbonyl Compounds

November 25 — Prof. L. D. Quin, University of Massachusetts, Amherst
Fragmentation of Phosphorous Heterocycles as a Route to Phosphoryl Species with Uncommon Bonding

November 26 — Dr. D. Humber, Glaxo, Greenford
AIDS - The Development of a Novel Series of Inhibitors of HIV

December 2 — Prof. A. F. Hegarty, University College, Dublin
Highly Reactive Enols Stabilised by Steric Protection

December 2 — Dr. R. A. Aitken, University of St. Andrews
The Versatile Cycloaddition Chemistry of $Bu_3P.CS_2$

December 3 — Prof. P. Edwards, Birmingham University
The SCI Lecture - What is Metal?

December 9 — Dr. A. N. Burgess, ICI Runcorn
The Structure of Perfluorinated Ionomer Membranes

1993

January 20	Dr. D. C. Clary, University of Cambridge Energy Flow in Chemical Reactions
January 21	Prof. L. Hall, Cambridge NMR - Window to the Human Body
January 27	Dr. W. Kerr, University of Strathclyde Development of the Pauson-Khand Annulation Reaction : Organocobalt Mediated Synthesis of Natural and Unnatural Products
January 28	Prof. J. Mann, University of Reading Murder, Magic and Medicine
February 3	Prof. S. M. Roberts, University of Exeter Enzymes in Organic Synthesis
February 10	Dr. D. Gillies, University of Surrey NMR and Molecular Motion in Solution
February 11	Prof. S. Knox, Bristol University *The Tilden Lecture* Organic Chemistry at Polynuclear Metal Centres
February 17	Dr. R. W. Kemmitt, University of Leicester Oxatrimethylenemethane Metal Complexes
February 18	Dr. I. Fraser, ICI Wilton Reactive Processing of Composite Materials
February 22	Prof. D. M. Grant, University of Utah Single Crystals, Molecular Structure, and Chemical-Shift Anisotropy
February 24	Prof. C. J. M. Stirling, University of Sheffield Chemistry on the Flat-Reactivity of Ordered Systems
March 10	Dr. P. K. Baker, University College of North Wales, Bangor 'Chemistry of Highly Versatile 7-Coordinate Complexes'
March 11	Dr. R. A. Y. Jones, University of East Anglia The Chemistry of Wine Making
March 17	Dr. R. J. K. Taylor, University of East Anglia Adventures in Natural Product Synthesis
March 24	Prof. I. O. Sutherland, University of Liverpool Chromogenic Reagents for Cations
May 13	Prof. J. A. Pople, Carnegie-Mellon University, Pittsburgh, USA *The Boys-Rahman Lecture* Applications of Molecular Orbital Theory
May 21	Prof. L. Weber, University of Bielefeld Metallo-phospha Alkenes as Synthons in Organometallic Chemistry
June 1	Prof. J. P. Konopelski, University of California, Santa Cruz Synthetic Adventures with Enantiomerically Pure Acetals
June 2	Prof. F. Ciardelli, University of Pisa Chiral Discrimination in the Stereospecific Polymerisation of Alpha Olefins
June 7	Prof. R. S. Stein, University of Massachusetts Scattering Studies of Crystalline and Liquid Crystalline Polymers

June 16 Prof. A. K. Covington, University of Newcastle
Use of Ion Selective Electrodes as Detectors in Ion Chromatography

June 17 Prof. O. F. Nielsen, H. C. Ørsted Institute, University of Copenhagen
Low-Frequency IR - and Raman Studies of Hydrogen Bonded Liquids

File Ref. CG137/E(CH)